

Bulk wave transport properties in elastically deformed heterogeneous solids: application to concrete

Cheng, H.

DOI

[10.4233/uuid:2d711db2-1d26-4093-8f12-55ee83365c45](https://doi.org/10.4233/uuid:2d711db2-1d26-4093-8f12-55ee83365c45)

Publication date

2025

Document Version

Final published version

Citation (APA)

Cheng, H. (2025). *Bulk wave transport properties in elastically deformed heterogeneous solids: application to concrete*. [Dissertation (TU Delft), Delft University of Technology]. <https://doi.org/10.4233/uuid:2d711db2-1d26-4093-8f12-55ee83365c45>

Important note

To cite this publication, please use the final published version (if applicable).
Please check the document version above.

Copyright

Other than for strictly personal use, it is not permitted to download, forward or distribute the text or part of it, without the consent of the author(s) and/or copyright holder(s), unless the work is under an open content license such as Creative Commons.

Takedown policy

Please contact us and provide details if you believe this document breaches copyrights.
We will remove access to the work immediately and investigate your claim.

**Bulk wave transport properties in elastically deformed
heterogeneous solids: application to concrete**

Dissertation

for the purpose of obtaining the degree of doctor
at Delft University of Technology
by the authority of the Rector Magnificus, Prof.dr.ir. T.H.J.J. van der Hagen,
chair of the Board for Doctorates
to be defended publicly on
Monday 3 February 2025 at 10:00 o'clock

by

Hao CHENG

Master of Science in Architecture and Civil engineering,
Dalian University of Technology, China
born in Qingdao, China

This dissertation has been approved by the promotor.

Composition of the doctoral committee:

Rector Magnificus,	chairperson
Prof.dr.ir. M.A.N. Hendriks	Delft University of Technology
	Norwegian University of Science and Technology, Norway, promotor
Dr.ir. Y. Yang	Delft University of Technology, promotor
Dr. K. Löer	Delft University of Technology, copromotor

Independent member:

Prof.dr. A.V. Metrikine	Delft University of Technology
Prof.dr. L.J. Jacobs	Georgia Institute of Technology, United States
Prof.dr. E.H. Saenger	Bochum University of Applied Sciences, Germany
Dr. C. Weemstra	Royal Netherlands Meteorological Institute
Prof.dr.ir E.C. Slob	Delft University of Technology, reserve member

All rights reserved. This copy of the dissertation has been supplied on condition that anyone who consults it is understood to recognize that its copyright rests with its author and that no quotation from the dissertation and no information derived from it may be published without the author's prior consent.

ISBN 978-94-6384-725-4

An electronic version of this dissertation is available at <http://repository.tudelft.nl/>. All research data supporting the findings described in this thesis are available in 4TU.Re-searchData with DOI: 10.4121/f4487f35-7fd4-478e-a218-98db79b4a308.

*Dedicated to my beloved parents
my cherished family
and my dear girlfriend*

谨以此书献给我挚爱的父母
珍爱的家人
和亲爱的女友

Summary

As materials degrade over time and traffic loads increase, monitoring the structural health of concrete infrastructures has become crucial. Structural health monitoring (SHM) and non-destructive evaluation (NDE) techniques are gaining attention for their role in maintaining the functionality and safety of these structures. One of the most effective methods is tracking stress changes in concrete, as it allows engineers to detect potential weaknesses and address them proactively, thus preventing catastrophic failures and improving safety. To monitor these changes, bulk wave-based acoustoelasticity is chosen for its promise in long-term monitoring and tracking of internal stress distributions.

However, applying bulk wave-based acoustoelasticity to concrete presents significant challenges. These challenges arise from three main areas: data processing techniques, acoustoelastic theory, and heterogeneity of concrete. First, there is limited research on data processing techniques for extracting bulk wave properties specific to concrete, resulting in a gap in understanding how these techniques apply to this material. Second, the existing acoustoelastic theory is primarily developed for scenarios where bulk waves propagate parallel or orthogonal to the principal deformation directions. This focus limits its applicability to concrete, where the principal deformation directions often vary under different loading conditions. Third, the meso-scale heterogeneity of concrete causes strong interactions between bulk waves, at frequencies of around a hundred kilohertz, and heterogeneities within the concrete. These interactions, known as scattering, significantly impact the propagation and spatial distribution of bulk waves, making interpretation challenging. This dissertation explores solutions to these challenges and offers a theoretical framework for engineers and researchers to monitor stress and strain changes in concrete using acoustoelasticity.

Our investigation into data processing techniques focuses on retrieving two categories of bulk wave properties from experiments: travel time changes and diffusive properties. We use wave interferometry techniques to measure travel time changes resulting from stress changes, comparing the wavelet cross-spectrum (WCS) technique and the stretching technique. The results show consistency in the velocity changes retrieved by both techniques. For diffusive properties like diffusivity and dissipation, we fit these properties through the diffusion equation. Adjustments are made to account for boundary effects by incorporating reflected energy from so-called image sources.

We further revisit the current acoustoelastic theory to address bulk waves propagating at angles to the principal deformation directions. Our findings reveal that while shear strains have a minimal impact on longitudinal wave velocities, they significantly affect transverse wave velocities. Based on this, we propose a simplified acoustoelastic expression for inclined propagating ballistic waves, primarily longitudinal, in a plane stress state, and validate it experimentally.

Summary

Understanding acoustoelastic theory alone is insufficient for interpreting travel time changes of diffuse waves in concrete; the energy ratio between longitudinal and transverse waves is also crucial. To address this, we propose a bulk wave energy transport model to estimate this energy ratio based on the angular frequency of bulk waves, the volume fraction of coarse aggregates, and the characteristic radius of these aggregates. The validity of the proposed model is confirmed by comparing theoretical diffusivities with experimental values, which are fitted from the diffusion equation while accounting for boundary reflections.

To investigate travel time changes of diffuse bulk waves, we integrate the previously discussed acoustoelastic theory with the bulk wave energy transport model. The energy transport model estimates the energy ratio between longitudinal and transverse waves and the time required for this ratio to equilibrate. Using Monte Carlo simulations in conjunction with acoustoelastic theory, we estimate the travel time changes for diffuse longitudinal and transverse waves. These estimates are then weighted by the energy ratio to predict travel time changes, which are compared with experimental observations retrieved using the WCS techniques.

This dissertation provides a theoretical foundation for applying bulk wave-based acoustoelasticity to concrete. Additionally, the revisited acoustoelastic theory may be applicable to other compressible, statistically isotropic solids, such as metals. The scattering theory-based model also offers a valuable tool for investigating scatterer properties in concrete.

Samenvatting

Aangezien materialen in de loop der tijd degraderen en verkeersbelastingen toenemen, is het monitoren van de constructieve toestand van betonconstructies in de infrastructuur cruciaal geworden. Monitoren en niet-destructieve evaluatietechnieken krijgen steeds meer aandacht vanwege hun rol bij het behouden van de functionaliteit en veiligheid van deze constructies. Een van de meest effectieve methoden is het volgen van spanningsveranderingen in beton, omdat dit ingenieurs in staat stelt potentiële zwaktes te detecteren en proactief aan te pakken, waardoor catastrofale storingen worden voorkomen en de veiligheid wordt verbeterd. Voor het monitoren van deze spanningsveranderingen wordt akoesto-elasticiteit van bulkgolven gekozen vanwege het potentieel voor langdurige monitoring en het volgen van interne spanningsverdelingen.

Het toepassen van akoesto-elasticiteit van bulkgolven op beton brengt echter aanzienlijke uitdagingen met zich mee. Deze uitdagingen komen voort uit drie hoofdgebieden: gegevensverwerkingstechnieken, akoesto-elastische theorie en de heterogeniteit van beton. Ten eerste is er beperkte onderzoek naar gegevensverwerkingstechnieken voor het extraheren van bulkgolfeigenschappen die specifiek zijn voor beton, wat resulteert in een tekort aan begrip van hoe deze technieken toepasbaar zijn op dit materiaal. Ten tweede is de bestaande akoesto-elastische theorie voornamelijk ontwikkeld voor scenario's waarin bulkgolven parallel of loodrecht op de belangrijkste vervormingsrichtingen voortbewegen. Deze focus beperkt de toepasbaarheid op beton, waar de belangrijkste vervormingsrichtingen vaak variëren onder verschillende belastingcondities. Ten derde veroorzaakt de heterogeniteit op meso-schaal van beton sterke interacties tussen bulkgolven, bij frequenties van rond de honderd kilohertz, en heterogeniteiten binnen het beton. Deze interacties, bekend als verstrooiing, hebben een significante impact op de voortplanting en ruimtelijke verdeling van bulkgolven, wat de interpretatie bemoeilijkt. Dit proefschrift onderzoekt oplossingen voor deze uitdagingen en biedt een theoretisch kader voor ingenieurs en onderzoekers om spannings- en vervormingsveranderingen in beton te monitoren met behulp van akoesto-elasticiteit.

Ons onderzoek naar gegevensverwerkingstechnieken richt zich op het verkrijgen van twee categorieën bulkgolfeigenschappen uit experimenten: veranderingen van voortplantingssnelheden en diffusiestromen. We gebruiken golf-interferometrietechnieken om reistijdveranderingen als gevolg van spanningsveranderingen te meten, waarbij we de wavelet cross-spectrum (WCS)-techniek en de stretching-techniek vergelijken. De resultaten tonen consistentie in de snelheidsveranderingen die door beide technieken worden verkregen. Voor diffusiestromen zoals diffusiviteit en dissipatie passen we deze eigenschappen aan via de diffusievergelijking. Aanpassingen worden gemaakt om rekening te houden met randeffecten door gereflecteerde energie van zogenaamde beeldbronnen op te nemen.

Verder herzien we de huidige akoesto-elastische theorie om bulkgolven aan te pakken die onder hoeken voortplanten ten opzichte van de hoofdvervormingsrichtingen. Onze bevindingen tonen aan dat, hoewel schuifvervormingen minimale invloed hebben op de snelheden van longitudinale golven, ze een aanzienlijke impact hebben op transversale golf-snelheden. Op basis hiervan stellen we een vereenvoudigde akoesto-elastische uitdrukking voor schuin-voortplantende ballistische golven, welke voornamelijk longitudinaal zijn, in een vlakspanningssituatie en valideren we deze experimenteel.

Het begrijpen van alleen de akoesto-elastische theorie is onvoldoende voor de interpretatie van reistijdveranderingen van diffuse golven in beton; de energieverhouding tussen longitudinale en transversale golven is ook cruciaal. Om dit aan te pakken, stellen we een bulk-golf-energie-transportmodel voor om deze energieverhouding te schatten op basis van de hoeksnelheid van bulkgolven, de volumefractie van grove aggregaten en de karakteristieke straal van deze aggregaten. De geldigheid van het voorgestelde model wordt bevestigd door theoretische diffusiviteiten te vergelijken met experimentele waarden, die worden afgeleid uit de diffusievergelijking, terwijl rekening wordt gehouden met randreflecties.

Om reistijdveranderingen van diffuse bulkgolven te onderzoeken, integreren we de eerder besproken akoesto-elastische theorie met het bulk-golf-energie-transportmodel. Het energie-transportmodel schat de energieverhouding tussen longitudinale en transversale golven en de tijd die nodig is om deze verhouding te stabiliseren. Met behulp van Monte-Carlosimulaties in combinatie met akoesto-elastische theorie schatten we de reistijdveranderingen voor diffuse longitudinale en transversale golven. Deze schattingen worden gewogen door de energieverhouding om reistijdveranderingen te voorspellen, die worden vervolgens vergeleken worden met experimentele observaties verkregen met de WCS-technieken.

Dit proefschrift biedt een theoretische basis voor de toepassing van bulk-golf gebaseerde akoesto-elasticiteit op beton. Daarnaast kan de herziene akoesto-elastische theorie ook toepasbaar zijn op andere comprimeerbare, statistisch isotrope vaste stoffen, zoals metalen. Het op verstrooiing gebaseerde theoretische model biedt ook een waardevol instrument voor het onderzoeken van verstrooiingseigenschappen in beton.

Table of Contents

1. Introduction	1
1.1 Background and scope	1
1.1.1 Concrete structure monitoring	1
1.1.2 Bulk waves in concrete	3
1.2 Existing challenges	4
1.3 Objectives and aims	4
1.4 Outline	5
2. Acoustoelastic theory and experimental observations	7
2.1 Introduction	7
2.2 Development of theoretical framework for acoustoelasticity	7
2.2.1 Linear elasticity-based acoustoelastic theory	7
2.2.2 Proposal of third-order elastic constants	9
2.2.3 Modern acoustoelastic theory	9
2.3 Signal processing techniques in estimating velocities from recorded signals ..	13
2.3.1 Arrival time picking	13
2.3.2 Wave interferometry	14
2.4 Experimental work on acoustoelasticity in solids	16
2.5 Knowledge gaps in applying bulk wave-based acoustoelasticity to concrete	18
3. Bulk wave scattering and energy transport in concrete	19
3.1 Introduction	19
3.2 Theoretical description on single scattering	19
3.3 Theoretical description on energy transport of multiply scattered bulk waves	21
3.3.1 Radiative transfer equation (RTE)	22
3.3.2 Diffusion equation	23
3.4 Application of diffusion equation to concrete	24
3.5 Knowledge gaps in applying the scattering and diffusion equation to concrete	25

4. Techniques for estimating bulk wave properties in concrete.....	27
4.1 Introduction	27
4.2 Estimation of travel time changes	27
4.2.1 Knowledge gap in techniques for estimating stress-induced travel time changes in concrete.....	28
4.2.2 Theoretical background of wave interferometry techniques.....	30
4.2.3 Specimens and experiments.....	33
4.2.4 Comparison between the wavelet cross-spectrum technique and the stretching technique.....	36
4.2.5 Application of the stretching and WCS techniques in subsequent chapters .	52
4.3 Estimation of diffusive properties	53
4.3.1 Knowledge gap in characterizing diffusive properties in concrete structures with boundaries.....	54
4.3.2 Theoretical background of diffusion equation	54
4.3.3 Specimens and experiments.....	59
4.3.4 Diffusive properties in specimens with planar boundaries	61
4.3.5 Diffusive properties in the cylindrical specimen	70
4.3.6 Procedures for fitting diffusive properties in subsequent chapters	75
4.4 Discussion	76
4.4.1 Cycle skipping in the WCS technique	76
4.4.2 Computational efficiency of the stretching technique and the WCS technique	76
4.4.3 Noise reduction using the WCS technique	77
4.4.4 Effect of boundary conditions on diffusivity in concrete cylinder.....	77
5. Response of travel time in ballistic bulk waves to stresses.....	79
5.1 Introduction	79
5.2 Knowledge gap relating theoretical framework of acoustoelasticity.....	79
5.3 Theoretical framework of modern acoustoelasticity	81
5.3.1 Coordinates, deformations and displacements.....	81
5.3.2 Strain and stress	82
5.3.3 Non-linear constitutive equation.....	84
5.3.4 Second- and third-order elastic constants for isotropic materials	85

5.3.5 Equation of motion in the initial frame	87
5.3.6 Equation of motion in the natural frame	89
5.3.7 Plane waves propagation.....	90
5.4 Bulk wave acoustoelasticity in compressible elastic medium subjected to normal and shear deformations.....	91
5.4.1 Governing equation.....	93
5.4.2 Example 1: waves propagating parallel or perpendicular to the principal deformations.....	95
5.4.3 Example 2: waves propagating perpendicular to the shear deformation plane – acoustoelastic birefringence	97
5.4.4 Example 3: Wave propagating on the shear deformation plane	100
5.5 Simplification of longitudinal wave acoustoelasticity in plane stress state .	107
5.5.1 Acoustoelasticity for longitudinal waves propagating along one of the principal stress directions in the plane stress state	108
5.5.2 Acoustoelasticity for longitudinal wave propagating inclined to principal stress directions in the plane stress state	109
5.6 Experimental validation for simplified acoustoelastic expression	111
5.6.1 Concrete specimen, sensor layout and measurement plan	111
5.6.2 Data processing approach	113
5.7 Effective acoustoelastic parameters for longitudinal waves	115
5.8 Comparison of acquired effective acoustoelastic parameters with those from literature	119
5.9 Discussion.....	121
5.9.1 Identified inconsistencies in acoustoelastic theory in the current literature	121
5.9.2 Error estimation in acquiring the acoustoelastic parameters of concrete	122
5.10 Summary.....	126
6. Modelling transportation of bulk wave energy.....	127
6.1 Introduction.....	127
6.2 Knowledge gap in evaluating the energy evolution of bulk waves in concrete .	128
6.3 Total scattering cross-sections and energy equilibration in elastic media ..	128
6.3.1 Definition of scattering cross-section and mean free path	128

Table of Contents

6.3.2 Total scattering cross-sections for elastic bulk waves	130
6.3.3 Energy equilibration and equilibration time	135
6.4 Estimation of total scattering cross-sections in concrete	138
6.4.1 Power spectral density of material property fluctuations in concrete	139
6.4.2 Expressions of total scattering cross-sections for bulk waves in concrete..	144
6.5 Role of dissipation on the equilibration process	146
6.5.1 Numerical analysis setup	146
6.5.2 Impact of dissipation on the global equilibration time	148
6.5.3 Impact of dissipation on the equilibrated energy ratio	150
6.6 Model validation and prediction of wave energy evolution	152
6.6.1 Model validation	152
6.6.2 Wave energy evolution and equilibration predicted from the model	154
6.7 Discussion	156
6.7.1 Equilibration time	156
6.7.2 Possible scatterers in concrete	157
6.7.3 Revisit of assumptions in the derivation of total scattering cross-sections.	158
6.7.4 Possible approaches to improve the performance of the model	162
6.7.5 Effect of boundary conditions on diffusivity in concrete cylinder	164
6.8 Summary	165
7. Response of travel time in diffuse bulk waves to stresses	167
7.1 Introduction	167
7.2 Travel time changes of spatially isotropic diffuse bulk waves	168
7.2.1 Choice of simulation method for acoustoelastic effect of diffuse waves	168
7.2.2 Response function for Monte Carlo simulation	172
7.3 Experimental validation design and parameters for signal processing	176
7.4 Estimation of equilibration time and equilibrated ratio using the bulk wave energy transport model	181
7.5 Estimation of travel time changes of diffuse bulk waves	182
7.5.1 Inputs of the response function	182
7.5.2 Travel time changes determined from the Monte Carlo simulation	184
7.6 Effective acoustoelastic parameters of diffuse waves	186
7.7 Discussion	190

7.7.1 Inconsistencies in acoustoelastic parameters obtained using embedded sensors and surface-bonded sensors	190
7.7.2 Fluctuations of effective acoustoelastic parameters among different samples	193
7.7.3 Travel time change of diffuse longitudinal and transverse waves in biaxial or triaxial stress states.....	195
7.7.4 Long-lasting anisotropy of the wavefield.....	195
7.8 Summary	195
8. Recommendations for applications in concrete structures	197
8.1 Introduction.....	197
8.2 Estimating stress-induced velocity changes in concrete using the stretching technique and the WCS technique	197
8.3 Estimating diffusive properties in concrete members with boundaries	197
8.4 Estimating bulk wave energy transport properties in concrete members ..	198
8.5 Determining acoustoelastic parameters for ballistic waves and effective acoustoelastic parameters for diffuse waves	199
8.6 Estimating biaxial principal stress changes in concrete members.....	201
8.7 Applications in monitoring concrete infrastructures.....	203
9. Conclusions and recommendations for the future work	205
9.1 Conclusions.....	205
9.2 Recommendations for the future work	207
9.2.1 Minimum resolution of the stretching technique and the WCS technique..	207
9.2.2 Mitigation of cycle skipping effect while using the WI techniques	208
9.2.3 Response of diffusive properties of bulk waves to stresses.....	208
9.2.4 Determination of Murnaghan constants of concrete	209
9.2.5 Mapping stress change field using ballistic waves and tomography	209
9.2.6 Mapping stress change field using diffuse waves and sensitivity kernel	210
Notations	211
Appendix A	217
Appendix B	219
Appendix C	221

Table of Contents

Appendix D	227
Appendix E	229
Appendix F	231
Appendix G	235
Reference	241
Acknowledgement	263
Curriculum vitae	267

1. Introduction

1.1 Background and scope

1.1.1 Concrete structure monitoring

Concerns over the safety of concrete infrastructures, such as bridges and viaducts, have been growing in the Netherlands. These concerns stem from three primary factors: the outdated design of structures, the deterioration of materials over time, and the escalating volume and weight of the traffic. Figure 1.1 illustrates the construction years of viaducts and bridges in the Netherlands, revealing that a significant portion was built prior to 1975 and has been in service for five decades. Simultaneously, there has been a substantial increase in traffic load over recent decades, as demonstrated in Table 1.1. Given that bridges and viaducts are primarily engineered to withstand anticipated traffic demands, the outdated designs for old bridges are unable to accommodate current traffic conditions according to the modern design code, which were not anticipated during their initial design and construction. Therefore, reliable structural health monitoring (SHM) or non-destructive evaluation (NDE) techniques are imperative to detect structural damage early. By identifying issues before they lead to catastrophic failure, these techniques enable timely maintenance and repair. This is especially important for critical concrete infrastructures such as bridges, tunnels, and dams, where failure could have severe consequences, including significant loss of life or property.

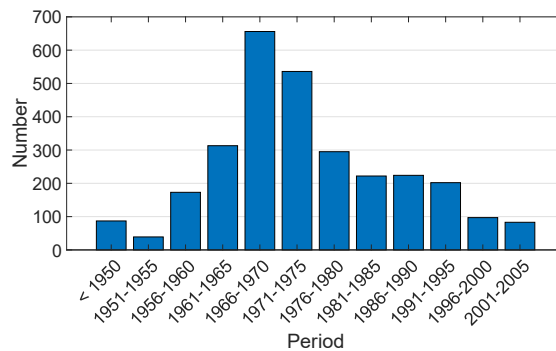


Figure 1.1 Year of construction of viaducts and bridges in the Netherlands (Rijswaterstaat 2007).

Table 1.1 Development of freight traffic mass in the Netherlands (Rijswaterstaat 2007).

Pe- riod	Weight of semi-trailer [t]	Weight of 3- axle vehicle [t]	Weight of 4- axle vehicle [t]	Weight of 5- axle vehicle [t]	Number of vehi- cles with weight over 50 t
1960s	32-36	22	N/A	N/A	Very low
1970s	36-40	23-24	30	N/A	Low
1980s	40-44	26	32	N/A	Moderate
1990s	44-46	26-34.5	34-46	50	High
2000s	46	27-34.5	35-46	50	Very high

1.1 Background and scope

In concrete structures, various features can be monitored to assess the health conditions or the safety of the entire structure. These features include detecting damage through changes in the structure's overall behaviour, such as natural frequency (Salawu 1997) and mode shape (Fayyadh and Abdul Razak 2011), as well as changes in its local behaviour, such as visible cracks (Golewski 2023) and strain/stress alterations (Jiang, Zhang et al. 2017). Given that local changes can lead to global failure, such as shear cracks in the shear-critical zone, which may go undetected when only monitoring global behaviour, this is particularly true for short-span concrete bridges (Sierra, Poliotti et al. 2023). Therefore, monitoring local behaviour changes provides a more effective and proactive approach to ensuring structural safety.

Most current research on monitoring local behaviour has focused on tracking visible crack initiation and propagation, with existing techniques reliably capable of detecting them on the surface of concrete (Zarate Garnica, Lantsoght et al. 2022, Golewski 2023). However, cracks in concrete are not always visible, such as internal cracks. In these cases, monitoring stress or strain changes is preferable, as it allows us to detect potential weaknesses or areas of concern within the structure before cracks become visible, enabling proactive interventions and maintenance to prevent catastrophic failures and enhance safety. Additionally, the measured stress fluctuations within the structure can be used to update the structural model, facilitating predictions of the global structural behaviour through the model. Therefore, this dissertation focuses on tracking strain/stress changes in concrete structures.

In the literature, commonly utilized sensors for tracking strain changes in concrete include strain gauges (Biswal and Ramaswamy 2016) and fibre optic sensors (Majumder, Gangopadhyay et al. 2008, Barrias, Casas et al. 2016). However, both these sensors are restricted to measuring stress either at specific locations or along the sensor itself, and they are generally characterized as time-consuming and expensive. Digital image correlation (Sutton, Orteu et al. 2009) offers a solution for evaluating the global strain field on the surface. However, this technique is unsuitable for long-term monitoring due to its lack of sensitivity to micro-cracking on the surface of concrete. For tracking inner strain/stress distribution, there are only two viable options (Hirao and Ogi 2017): *neutron diffraction* and *acoustoelasticity*. Given the limited accessibility and constraints of laboratory and in-situ studies in the field of concrete structures with neutron diffraction, the acoustoelasticity, which describes how the velocities of an elastic material change if subjected to an initial static stress field, stands as the sole feasible choice. In this dissertation, we further narrow the scope to the analysis of elastic waves travelling through the interior of the medium, commonly referred to as *bulk waves*. Therefore, this dissertation will focus on interpreting the strain/stress changes in concrete by analysing changes in bulk wave properties, i.e., travel time, employing acoustoelasticity.

1.1.2 Bulk waves in concrete

Concrete, being a heterogeneous material, may exhibit anisotropic behaviour at the mesoscale due to the presence of multiple phases, such as the mortar matrix, air bubbles, and coarse aggregates. When bulk waves propagate through this material, interactions between the waves and the different phases may occur. For *ballistic waves*, which denote the first pulse crossing the sample (Derode, Tourin et al. 2001), the wave trajectory is typically short and straightforward, following a direct path from the transmitter to the receiver. Therefore, interactions are likely minimal in this case, and these waves have more deterministic directionality. Please note that the definition of ballistic waves is distinct from that of *coherent waves*, which refer to waves whose energy predominantly propagates in their initial direction (Derode, Tourin et al. 2001).

However, for *coda waves*, which refer to the tail of waveforms (Aki and Chouet 1975), interactions between bulk waves and different phases become inevitable. These interactions, causing the wave energy to deviate from its original trajectory, are known as *scattering*. This is why the term *coda* is synonymous with *later-arriving multiply scattered waves* (Aki and Chouet 1975). Waves in the late coda are typically referred to as *incoherent waves* (Tourin, Derode et al. 2000) or *diffuse waves* (Planès and Larose 2013), where the wave energy transport predominantly occurs within the *diffusive regime* (Elaloufi, Carminati et al. 2002, Zhang and Zhang 2002). Please note that while coda waves indicate the waves in the tail of waveforms, they do not necessarily propagate in the diffusive regime. Therefore, the terms *coda waves* and *diffuse waves* are not always interchangeable.

Due to the much longer wave trajectories in coda waves compared to those in ballistic waves, coda waves are usually more sensitive to minor changes in the medium because of the accumulation of these changes along the wave path. Additionally, coda waves have a broader reach than ballistic waves, potentially allowing for the use of sparser source-receiver arrays (Planès and Larose 2013).

In this dissertation, we will investigate the acoustoelastic effect in both ballistic waves and diffuse waves. The former has a deterministic directionality, which could potentially be applied to determining the orientation of principal stresses, while the latter is more sensitive to minor changes in the medium and may have the potential to map changes in the medium when combined with the sensitivity kernel (Larose, Planès et al. 2010). However, it should be noted that we will not investigate the sensitivity kernel in this dissertation, as this mapping technique is considered a step beyond the scope of this research.

1.3 Objectives and aims

1.2 Existing challenges

Despite that acoustoelastic theory has been applied in various materials for over 70 years (Hughes and Kelly 1953), its implementation in concrete still encounters several significant challenges. These challenges stem from three main aspects: data processing techniques, the acoustoelastic theory, and the heterogeneity of concrete.

Firstly, there is a lack of research on data processing techniques in retrieving bulk wave properties, i.e., travel time changes and diffusive properties, tailored specifically to concrete, resulting in a limited understanding of how to apply these techniques to this material. Consequently, there is no consensus on selecting the appropriate technique and corresponding parameters to estimate travel time changes and diffusive properties in concrete.

Secondly, the current acoustoelastic theory is limited to scenarios where bulk waves propagate either parallel or orthogonal to the principal deformation directions, posing constraints on its application to concrete, where principal deformation directions usually vary across different loading scenarios.

Thirdly, the heterogeneity of concrete at the meso-scale results in strong interactions between bulk waves and various phases in concrete during propagation. These interactions are significant when the frequency of bulk waves is around a hundred kilohertz, which is a typical wave frequency for ultrasonic-based concrete monitoring. Additionally, these interactions significantly affect the spatial distribution of bulk wave energy flux in concrete, presenting a considerable challenge in interpreting wave behaviour in this material. Currently, there is no model or theory to describe travel time changes or energy transport for diffuse waves in concrete.

1.3 Objectives and aims

The main objective of this dissertation is to improve the knowledge about the stress-induced velocity changes in concrete retrieved from bulk waves. Given that such velocity changes may result from a combination of concrete heterogeneity and the acoustoelastic effect, this study aims to develop a means-end approach grounded in acoustoelasticity and scattering theory. To facilitate the problem-solving process, the main objective is divided into five specific sub-goals:

1. **Tailoring data processing techniques:** Employing theoretical analyses and experimental validation to identify or propose suitable techniques capable of acquiring bulk wave properties in concrete, such as travel time changes and diffusive properties.

2. **Refining the acoustoelastic theory:** Employing theoretical analyses to revisit and refine the acoustoelastic theory capable of addressing bulk wave propagation under arbitrary stress conditions.
3. **Interpreting velocity changes in stressed concrete retrieved via ballistic bulk waves:** Employing theoretical analyses and experimental validation to connect stress-induced velocity changes retrieved from ballistic bulk waves to stress changes in concrete.
4. **Modelling bulk wave energy transport in concrete:** Employing theoretical analyses and experimental validation to propose and validate a model that describes the energy transport of bulk waves within concrete.
5. **Interpreting velocity changes in stressed concrete retrieved via diffuse bulk waves:** Employing the refined acoustoelastic theory in conjunction with the bulk wave energy transport model to connect the stress-induced velocity changes retrieved from diffuse bulk waves to stress changes in concrete, with experimental validation required to support the proposed approach.

This study advances the understanding and quantification of stress-induced velocity changes in concrete through a framework grounded in acoustoelasticity and scattering theory. By integrating data processing techniques, the refined acoustoelastic theory, and the tailored model for bulk wave energy transport in concrete, it establishes a comprehensive method for measuring, interpreting, and quantifying stress-induced velocity changes retrieved from bulk waves in concrete, representing a step forward in the non-destructive stress monitoring and structural evaluation of concrete.

1.4 Outline

The outline of this dissertation is illustrated in Figure 1.2. In Chapter 2, a review of acoustoelasticity will be presented, covering its theoretical framework development and its current applications in various materials such as metals, polymers, and concretes. Chapter 3 will introduce the current understanding of bulk wave energy transport in heterogeneous solids. Beginning with the interaction between bulk waves and inhomogeneities, it will progress to the development of elastic scattering theory. Given the focus on energy transport, transport theories applicable to describing scattered bulk waves and their applications in concrete will also be reviewed.

Chapter 4 will address Sub-goal 1, providing the theoretical foundation and experimental demonstration of data processing techniques to be used in subsequent chapters. These techniques primarily aim to extract two types of bulk wave properties: travel time changes and diffusive properties. The techniques for acquiring travel time changes will be applied in Chapters 5 and 7 to determine velocity changes in concrete, while the techniques for

1.4 Outline

acquiring diffusive properties will be used in Chapter 6 and 7 to validate the bulk wave energy transport model.

Chapter 5 will address Sub-goal 2 and Sub-goal 3, concentrating on theoretical and experimental investigations of acoustoelasticity. The acoustoelastic theory will be revisited and refined into a more generalized form capable of accommodating bulk waves propagating under arbitrary stress conditions. This refined theory will be employed to interpret the acoustoelastic effect of ballistic waves, which will then undergo validation via experiments employing data processed techniques for acquiring travel time changes introduced in Chapter 4.

Chapter 6 will address Sub-goal 4, focusing on modelling the energy transport of bulk waves in concrete using scattering theory. The proposed model aims to predict diffusivity, the equilibration energy ratio between longitudinal and transverse waves, and the time required to reach this equilibration. Validation of this model will be performed using diffusive properties obtained through the techniques introduced in Chapter 4.

Chapter 7 will address Sub-goal 5, combining the refined acoustoelastic theory proposed in Chapter 5 with the bulk wave energy transport model proposed in Chapter 6 to interpret the travel time change of diffuse bulk waves. These changes will also be calculated using the techniques introduced in Chapter 4.

In the final two chapters, I will introduce recommendations for applications of the proposed approaches in concrete structures (Chapter 8), followed by a summary of the main conclusions of the dissertation and recommendations for the future work (Chapter 9).

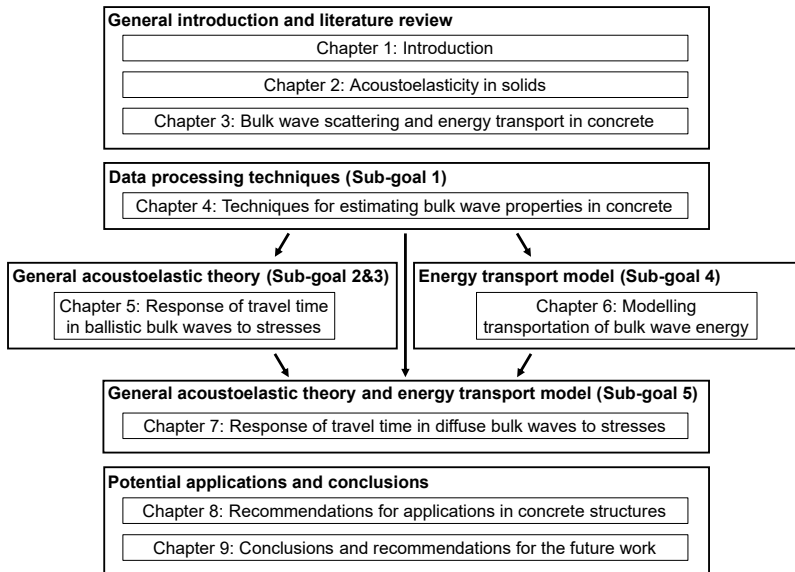


Figure 1.2 Outline of this dissertation.

2. Acoustoelastic theory and experimental observations

2.1 Introduction

Acoustoelasticity, named by Toupin and Bernstein (1961), refers to the change in velocity of an elastic wave within an initially stressed elastic solid. Elastic waves in such media include bulk waves, which are divided into longitudinal and transverse waves, as well as surface waves, such as Rayleigh waves. This chapter provides an overview of the development of acoustoelasticity in solid, covering both bulk waves and Rayleigh waves.

We will first delve into the development of the theoretical framework in Section 2.2, emphasizing the framework for modern acoustoelasticity, which encompasses the non-linear constitutive relation in the equation of motion. Given that the maximum magnitude of stress-induced velocity changes typically fall below 1% (Guz and Makhort 2000), identifying such subtle changes from raw signals requires a signal processing approach with adequate sensitivity. Therefore, before reviewing the experimental work on acoustoelasticity, commonly employed signal processing approaches in literature are firstly presented in Section 2.3. Section 2.4 then proceeds to showcase experimental endeavours in acoustoelasticity. Section 2.5 elucidates the potential challenges that could be encountered during the application of acoustoelastic theory to concrete, which also serve as the knowledge gaps.

Acknowledging space limitations, numerous theoretical works (Birch 1938, Hayes and Rivlin 1961, Green 1963, Hayes 1963, Tang 1967, Ogden 1970, Tverdokhlebov 1983, Pao 1987, Dowaiikh 1990, Degtyar and Rokhlin 1995, Duquenois, Ouafitoh et al. 1999, Shams, Destrade et al. 2011, Abiza, Destrade et al. 2012) and experimental works (Smith 1963, King and Fortunko 1983, Thompson, Lee et al. 1983, Abbasi and Ozevin 2016, Qi and Tan 2018, Pau and Vestroni 2019, Zhong, Zhu et al. 2021, Zhong and Zhu 2022) are not mentioned in this chapter. We extend our sincere respect to these pioneers whose exploration and dedication have propelled the theory and application of acoustoelasticity to its current state. Additionally, we also recommend the review articles by Guz (Guz and Makhort 2000, Guz 2002), whose profound insights and extensive experimental expertise in this domain are invaluable.

2.2 Development of theoretical framework for acoustoelasticity

2.2.1 Linear elasticity-based acoustoelastic theory

The earliest exploration of elastic waves within deformed bodies can be traced back to Cauchy (1829) in 1829. However, despite of his pioneering work, Cauchy's contributions were largely overlooked by subsequent researchers such as Rayleigh (1906), Biot (1940), and Murnaghan (1937). It was not until over a century later that Truesdell (1952) and Man et al. (1987) brought attention back to Cauchy's significance in this field.

2.2 Development of theoretical framework for acoustoelasticity

In the 20th century, progress in this theory was driven by Rayleigh (1906), Brillouin (1925), and Biot (1940). These seminal works all approached the equation of motion using linear elasticity theory, wherein strains are assumed to be small enough to neglect their squares and products in the stress-strain relationship. Detailed explanations of linear elasticity can be found in textbooks on continuum mechanics (Landau, Lifshitz et al. 1986, Aki and Richards 2002, Love 2013). According to linear elasticity, the velocity of elastic waves in isotropic materials is a second-order effect governed by the constitutive relation between stress and strain, characterized by the second-order elastic constants known as *Lamé constants*, denoted by λ and μ .

The main conclusion drawn by Rayleigh was that: *the usual equations* [constitutive equation for materials without external load applied] *may be applied to matter in a state of* [initial] *stress, provided that we allow for altered values of the elasticities*. This conclusion is vague, and Love (1911) gave a detailed explanation to this conclusion (*‘Some Problems of Geodynamics’*, page 89): *The earth ought to be regarded as a body in a state of initial stress; this initial stress may be regarded as a hydrostatic pressure balancing the self-gravitation of the body in the initial state; the stress in the body, when disturbed, may be taken to consist of the initial stress compounded with an additional stress; the additional stress may be taken to be connected with the strain, measured from the initial state as unstrained state, by the same formulae as hold in an isotropic elastic solid body slightly strained from a state of zero stress*. Love's description indicates that the constitutive equations for both the initial and additional stresses are identical in Rayleigh's theory, implying that the rigidity of a material remains unchanged by external loads. This concept is also adopted in Biot's derivation. However, Rayleigh seems to recognize the potential influence of applied stress on the solid's rigidity, as hinted on page 489 of his paper: *But although the initial state is one free of shear, we are not to conclude that the rigidity is the same as it would be without the imposed pressure. On the contrary, there is much reason to think that the rigidity would be increased*.

Building on Rayleigh's conclusion and recognizing that elastic wave velocities are solely determined by rigidity and density ($[(\lambda+2\mu)/\rho]^{1/2}$ for longitudinal waves and $(\mu/\rho)^{1/2}$ for transverse waves), it becomes apparent that the velocities of elastic waves in stressed materials are exclusively influenced by changes in density—or, equivalently, volume—before and after the application of external loads. This essentially encapsulates the fundamental concept behind Brillouin's derivation. His derivation suggested that with increasing pressure, the longitudinal wave velocity decreases, a consequence of the rise in density caused by the applied pressure.

It is important to reiterate that acoustoelastic theory at this stage operated within the framework of linear elasticity. However, elastic waves in a solid with initial stress exhibit a *‘small-on-large’* behaviour, where small strain due to wave motion overlays large strain

caused by initial stress. Compared to the much smaller strain due to wave motion, the initial strain is significantly larger and cannot be considered to be infinitesimal in the constitutive equation. Therefore, the assumption of linear elasticity becomes inadequate. A natural progression from this stage involves proposing a stress-strain relationship considering higher orders of deformation, which will be explored in the subsequent section.

2.2.2 Proposal of third-order elastic constants

As previously noted, linear elasticity assumes infinitesimal strain, allowing higher-order terms in the constitutive equation to be neglected. However, when small strain due to wave motion overlays large strain caused by initial stress, a more accurate portrayal of the constitutive relation between stress and strain is required, involving the incorporation of higher order elastic constants.

The first literature addressing the higher-order elastic constants is attributed to Murnaghan (1937). Through the assumption of energy conservation, Murnaghan demonstrated the necessity of six constants to describe strain energy in isotropic materials: one representing initial hydrostatic pressure, two second-order elastic constants (Lamé constants), and three third-order elastic constants denoted as l , m , and n , commonly known as *Murnaghan constants*.

Murnaghan constants are not the only third-order elastic constants documented in literature. For instance, Landau and Lifshitz's '*Theory of Elasticity*' also acknowledged the existence of third-order elastic constants, though they were presented as an exercise for readers to derive (Landau, Lifshitz et al. 1986). Toupin and Bernstein (1961) introduced v_1 , v_2 and v_3 as third-order elastic constants, labelling them *third-order Lamé constants* in their work. Furthermore, Johnson (1981) discussed a different set of third-order elastic constants denoted as β_1 , β_2 and β_3 .

2.2.3 Modern acoustoelastic theory

Section 2.2.2 introduces the proposal of third-order elastic constants, which proves instruments in addressing scenarios involving finite strain. This section will elaborate the development of modern acoustoelastic theory, which incorporates the constitutive relation involving third-order elastic constants into the equation of motion.

Establishment of fundamental framework

In 1953, Hughes and Kelly (1953) conducted uniaxial compression tests on polystyrene and Pyrex samples. In these experiments, they observed linear changes in rigidity, particularly in the bulk and shear moduli, corresponding to variations in applied stress. This observation confirms the assertion made by Rayleigh that applied stress influences the rigidity of solids (Rayleigh 1906). To quantify these changes in rigidity concerning applied stress, Hughes and Kelly incorporated Murnaghan constants into their analysis. This

2.2 Development of theoretical framework for acoustoelasticity

incorporation led to the development of a new framework for acoustoelasticity, which considers strain-induced modulus changes in the stress-strain relationship, or constitutive relation. This framework, later recognized as the modern theory of acoustoelasticity (Pao and Gamer 1985), aligns with the later proposition by Toupin and Bernstein (1961). Based on the findings reported by Hughes and Kelly, it is evident that the acoustoelastic effect varies between longitudinal and transverse waves. Moreover, this effect appears to be closely tied to the direction of wave propagation and polarization.

The framework proposed by Hughes and Kelly relies on several assumptions which subject to further adjustment for more general cases:

- The wave velocity calculated within this framework represents the pure velocity in the medium. However, in experiments, the measured quantity is the travel time, which depends not only on the medium's velocity but also on its deformation. To ensure alignment between theoretical and experimental results, this deformation must also be taken into account.
- The medium is assumed to be isotropic and its mechanical properties can be described using five elastic constants (two Lamé constants and three Murnaghan constants). As a result, this framework cannot be applied to anisotropic materials.
- The medium is assumed to be compressible, meaning its volume changes under load. However, not all media exhibit compressibility, and for incompressible materials, an alternative description of acoustoelasticity is required.
- Their expressions apply only to situations where bulk waves propagate parallel or perpendicular to the principal stress directions. For wave propagation in other directions, new expressions must be derived based on the existing framework.

Given these assumptions, subsequent researchers have progressively expanded the theoretical framework to accommodate more complex scenarios. Please note that concrete is compressible and statistically isotropic at a sufficiently large scale. Therefore, acoustoelastic theories for incompressible or anisotropic materials will not be used in this dissertation.

Introduction of natural velocity accounting for medium deformation

As mentioned earlier, the framework proposed by Hughes and Kelly (1953) calculates the pure velocity in the medium, which is the quotient of the static stress-induced deformed length in the propagation direction and the time of flight. Consequently, the change in time of flight resulting from static stress-induced deformation is not included in the total time of flight. The velocity change observed in this framework before and after static deformation primarily stems from the rigidity change induced by applied stress,

while stress-induced changes in the wave path are not considered. This finding indicates that applying this framework in experiments necessitates adjusting the path length to account for changes induced by stress.

To streamline the determination of wave velocity in experiments and enhance the comparability between experimental measurements and theoretical frameworks, Thurston and Brugger (1964) extended the existing framework to include the deformation caused by static stress in estimating the wave velocity. This velocity, also known as the natural velocity, is defined as the original length in the propagation direction divided by the time of flight. In their derivation, the framework is established within the natural coordinate system, where no external stress is applied. In contrast, Hughes and Kelly derived the framework within a coordinate system that includes deformation caused by static stresses. In this thesis, we will consider velocities derived from both the natural and initial frames of reference.

Introduction of non-symmetric stiffness tensor for anisotropic compressible materials

In anisotropic compressible materials, the constitutive relations between stress and strain cannot be adequately described using Lamé constants and Murnaghan constants alone. Due to the presence of minor symmetry and major symmetry of elastic tensors, there exist a maximum of 21 distinct second-order elastic constants for anisotropic materials. Here, the major symmetry is associated with the differential equation for determining elastic constants, while the minor symmetry is associated with the stress tensor. Similarly, employing the same symmetry principles, the number of distinct third-order elastic constants is 56 (Thurston 1974). To extend the framework to incorporate these elastic constants, adjustments in the presentation of elastic constants are necessary.

In developing the acoustoelastic framework, Thurston and Brugger (1964) employed stiffness tensors in Voigt notation within the equation of motion. Furthermore, they establish the relationship between these stiffness tensors and both Lamé constants and third-order elastic constants proposed by Toupin and Bernstein (1961) for isotropic materials. The introduction of these stiffness tensors facilitates in describing the acoustoelastic effect of materials with arbitrary symmetry. For example, Pao and Gamer (1985) employed the same stiffness tensors to derive acoustoelastic equations for elastic waves in orthotropic materials. In this thesis, the stiffness tensors for isotropic materials proposed by Thurston and Brugger (1964) will be used in the derivation.

Acoustoelasticity framework of incompressible materials

Incompressible materials typically maintain a constant volume, which implies that their density also remains constant under load—a characteristic observed in certain polymers and soft biological tissues (Ganghoffer 2018). Due to this incompressibility, the strain

2.2 Development of theoretical framework for acoustoelasticity

energy functions of these materials differ from those of compressible materials. To investigate the acoustoelasticity of these materials, the constitutive relation used in the equation of motion needs to be adjusted. For readers interested in exploring the strain energy functions of incompressible materials, we recommend the book *Non-linear Elastic Deformations* by Ogden (1997).

Connor, Destrade, and Ogden (Connor and Ogden 1995, Connor and Ogden 1996, Destrade and Ogden 2005) extended the framework of acoustoelasticity to include incompressible materials by integrating the new strain energy function from the aforementioned book into the derivation of acoustoelastic expressions. Additionally, they examined the influence of static stress-induced deformation on the velocity of surface Rayleigh waves. It is worth noting that Rayleigh waves and bulk waves share the same acoustoelastic framework. The primary difference between these two types of waves in the derivation lies in the type of wave equation substituted into the equation of motion, as demonstrated in the work of Hirao et al. (1981).

Effect of shear deformation in compressible materials

The framework proposed by Hughes and Kelly (1953) is limited to scenarios where waves propagate coincidentally with the axes of principal deformations. However, in engineering applications, it is not always guaranteed that elastic waves will follow these specific directions. For instance, Lamb waves, commonly utilized in non-destructive testing of plate-like structures, often propagate at angles to the principal strain direction (Mi, Michaels et al. 2006). In such cases, shear deformation becomes apparent, and the current acoustoelastic theory fails explain the observed wave velocities.

The earliest reference that considers shear stress in relation to bulk wave acoustoelasticity in compressible materials is found within the context of acoustoelastic birefringence (Tatsuo and Yukio 1968), a special case in the acoustoelastic framework where transverse waves propagate perpendicular to the shear deformation plane. Further details regarding acoustoelastic birefringence can be found in the literature by Tokuoka and Saito (1969). However, it is important to note that acoustoelastic birefringence pertains only to transverse waves and does not offer any general conclusions regarding wave velocities in a shear-deformed solid.

To the best of our knowledge, there exists only one article by Bobrenko et al. (1990) that investigates the influence of shear stresses on bulk wave velocities in compressible materials. However, their study focuses solely on a solid subjected to pure shear deformation, and thus, their research does not lead to general conclusions.

2.3 Signal processing techniques in estimating velocities from recorded signals

Considering that stress-induced velocity changes typically fall below 1% in magnitude (Guz and Makhort 2000), it becomes crucial to select a signal processing approach with adequate sensitivity to detect such changes. Hence, it is practically necessary to delve into the signal processing approaches in the literature. Since the travel time is the actual physical quantity which can be derived from the received signal. This section will use travel time, rather than velocity, to represent the acquired physical quantity. Please note that travel time is a broader term than time of flight, which is often used in the contexts that emphasize the minimum time required for waves to travel through space between two points, typically in relation to the first arrival of waves. Travel time can refer to the time a wave spends moving between two locations, and it does not necessarily correspond to the first arrival.

2.3.1 Arrival time picking

The most straight-forward approach to determine the arrival time is to employ a picker to identify time when a signal arrives. This approach of determining the travel time of elastic waves for acoustoelasticity traces back to the work of Hughes and Kelly (1953). In their study, they measured the time that is taken by elastic waves to travel through a solid to estimate their velocities. This approach is widely adopted in the determination of acoustoelastic effect of various materials, including woods (Sasaki, Iwata et al. 1998) and concrete (Nogueira and Rens 2019).

To measure the travel time accurately, certain criteria are required to determine the onset point of the signal. In the literature, two widely accepted criteria are the Hinkley criterion (Hinkley 1971) and the Akaike information criterion (Maeda 1985). However, determining the onset point also highlights the significance of the sampling rate of the data acquisition system (DAQ), as it greatly impacts the accuracy of this approach. For instance, let us assume the first-arrival is 35 μs . To achieve a resolution of relative travel time change of 0.2%, the sampling rate should be 143 MHz, which far exceeds the requirements for applications in structural health monitoring. Additionally, the accuracy of onset point picking by the arrival time picker is also sensitive to the noise level (Kurz, Grosse et al. 2005).

A variation of the arrival time picking is known as the sing-around method. In this method, the received signal from a pulse transmitted into the solid is used to re-trigger the transmitter continuously, creating a process of the pulse ‘singing-around’ in the sample at a repetition rate (pulse repetition frequency) determined by the total travel time. The pulse repetition frequency can be measured using a counter-type frequency meter. However, an

2.3 Signal processing techniques in estimating velocities from recorded signals

arrival time picker is still necessary to detect the received signal and re-trigger the transmitter.

To ensure measurement accuracy, the duration of the pulse for the sing-around method is typically kept short, as exemplified by Crecraft's adoption of $0.40\text{ }\mu\text{s}$ for longitudinal waves and $0.22\text{ }\mu\text{s}$ for transverse waves (Crecraft 1962). This approach finds numerous applications in literature for determining the acoustoelastic effect (Crecraft 1967, Hirao, Fukuoka et al. 1981, Thompson, Lee et al. 1983, Hasegawa, Sasaki et al. 2000, Hasegawa and Sasaki 2004, Hasegawa and Sasaki 2004, Hasegawa and Sasaki 2004, Sasaki and Hasegawa 2007).

In samples with small dimensions, there is a risk that the previous pulse is not fully attenuated when the new pulse is emitted, potentially resulting in the superposition of multiple pulses at later stages. This superposition can lead to incorrect measurement of travel time. Moreover, the performance of this approach is compromised when dealing with thick heterogeneous solids with strong dissipative properties, such as concrete. The combination of strong dissipation and heterogeneity results in a short transmission path, reducing the accuracy of the sing-around approach in measuring travel time. Additionally, same as the arrival time picking, the accuracy of this approach is heavily dependent on the sampling rate and noise level.

2.3.2 Wave interferometry

Wave interferometry (WI) (Snieder, Gret et al. 2002) presents a relatively new approach for measuring travel time changes in a medium by exploiting the ballistic (Zhong, Zhu et al. 2021) and coda (Stahler, Sens-Schonfelder et al. 2011) segments of elastic waves. The term *coda*, initially proposed by Aki (1969), refers to the tail of seismograms (Aki and Chouet 1975). The resolution of WI in detecting relative travel time change can be up to 0.02% under a sampling rate of 4 MHz and a first-arrival of around $35\text{ }\mu\text{s}$ (Larose and Hall 2009). This travel time change resolution under 4 MHz sampling rate is much higher than those of arrival time picking and sing-around approaches. So far, the WI approach is primarily used in detecting the stress-induced travel time change of elastic waves in heterogeneous materials like concrete (Payan, Garnier et al. 2009, Lillamand, Chaix et al. 2010, Payan, Garnier et al. 2010, Payan, Garnier et al. 2011).

Five WI techniques are seen in literature that are used to estimate the travel time change: the Moving Window Cross-Correlation (MWCC) (Grêt, Snieder et al. 2006, Snieder 2006), which measures time shifts in the time domain using cross-correlation of two windowed signals; the Moving Window Cross-Spectrum (MWCS) (Poupinet, Ellsworth et al. 1984, Frechet, Martel et al. 1989), which measures the time shifts based on phase changes in the frequency domain, derived from the cross-spectrum of two windowed signals obtained through Fourier transform; the stretching technique (Lobkis and Weaver 2003,

Sens-Schönfelder and Wegler 2006), which measures travel time changes in the time domain using cross-correlation between the reference signal and the stretched/compressed signal within the same time window, with a constant stretching factor; the Dynamic Time Warping (DTW) (Mikesell, Malcolm et al. 2015), which measures travel time changes in the time domain by finding the shortest warping path between the reference signal and the stretched/compressed signal, where the stretching factor varies along the lag-time; and the Wavelet Cross-Spectrum (WCS) technique (Mao, Mordret et al. 2020), which measures time shifts using phase changes in the wavelet domain derived from the wavelet cross-spectrum of two signals obtained through wavelet transform.

A performance comparison of these five techniques is reported by Yuan et al. (2021) using numerical simulations (i.e., the correct value is known). They used five criteria to evaluate their performance: operating domain, availability of the *Correlation Coefficient* (CC), frequency resolution, stability, and accuracy. Their conclusions are summarized in Table 2.1.

Table 2.1 Criteria used by Yuan et al. (2021) to compare five techniques for retrieving travel time changes.

WI technique	MWCC	MWCS	Stretching	DTW	WCS
Operating domain	Time	Fourier	Time	Time	Wavelet
Availability of CC	Yes	Yes	Yes	No	Yes
Time-frequency resolution	Low	Medium	Low	Low	High
Stability	Low	Low	Medium	High	Unknown
Accuracy	Low	Low*	High	High	Medium*

Note: * only valid when the signal energy at the frequency of interest is high

The *operating domain* describes which domain the WI technique operates in. The benefit of employing the transform-domain-based technique is the ability to capture changes in travel time for specific frequency components, the importance of which will be emphasized in Section 3.5.

The *availability of CC* indicates whether the ‘correlation coefficient’ between the perturbed and unperturbed signal becomes available using that technique. Although the correlation coefficient, or alternatively the *decorrelation*, is chiefly used for crack localization (Zhang, Planes et al. 2016, Zhang, Larose et al. 2018, Grabke, Clauss et al. 2021), this parameter also quantifies the reliability of the retrieved travel time change (Clauss, Epple et al. 2020). That is, the travel time change is meaningful only when the perturbed and unperturbed signals are sufficiently similar (Mao, Mordret et al. 2020), which is reflected by the magnitude of the correlation coefficient.

The *time-frequency resolution* points to the minimum resolution in both time and frequency that can be resolved. Since time-domain-based techniques operate in the time domain, the frequency resolution of these techniques is poor. For transform-domain-based techniques, WCS has better time-frequency resolution than MWCS (Mao, Mordret et al. 2020).

2.4 Experimental work on acoustoelasticity in solids

The fourth criterion, *stability*, evaluates whether the estimated travel time change is temporally stable. When it comes to this aspect, the performance of the different techniques involves their ability to mitigate *cycle skipping*, a phenomenon that one wiggle in the signal associated with the perturbed medium aligns with a wiggle in the signal associated with the unperturbed state that is displaced by approximately one period (Mikesell, Malcolm et al. 2015).

Finally, the *accuracy* is the degree to which the estimated travel time change corresponds to the correct value. In the article by Yuan et al. (2021), the authors concluded that DTW and the stretching technique have greater accuracy compared to other techniques. They also mentioned that the modest performance of MWCS and the WCS technique is attributed to low energy at specific frequencies. If one operates the WCS technique in a frequency range with sufficient energy, it has a better performance than MWCS according to Mao et al. (2020). It should be noted that the assessment of the accuracy of the WCS technique reported by Yuan et al. (2021) involved the application of this technique to a broad frequency band.

After comparing various techniques, it is evident that the stretching technique stands out among time-domain-based techniques due to its superior balance between accuracy and stability. On the other hand, the WCS technique, offering higher accuracy and improved time-frequency resolution compared to MWCS, demonstrates superior performance among transform-domain-based techniques.

2.4 Experimental work on acoustoelasticity in solids

After outlining the development of acoustoelastic theory and data processing approaches, this section will explore the experimental research dedicated to validating the theory and characterizing elastic constants.

The validation of acoustoelastic theory is closely tied to theoretical work. Studies on this topic primarily focus on validating proposed theoretical expressions through experiments. These validations include the acoustoelastic effect of bulk waves (Hughes and Kelly 1953), the acoustoelastic birefringence of transverse waves (Iwashimizu and Kubomura 1973, Hsu 1974, Imanishi, Sasabe et al. 1982), and the acoustoelastic effect of Rayleigh waves (Hirao, Fukuoka et al. 1981).

In addition to experimental validation, other researchers have focused on characterizing material properties, specifically second- and third-order elastic constants, using the acoustoelastic framework. Some reported elastic constants are summarized in Table 2.2. Please be aware that some experimental works (Clotfelter and Risch 1974, Cantrell and Salama 1991) are not included in Table 2.2 because they focused on acquiring the fractional change in velocity with respect to the applied stress rather than elastic constants. It is

important for readers to exercise caution when utilizing these parameters, as the acousto-elastic equations adopted in some articles may not be consistent with others. For instance, Eq. (4a) in the paper by Egle and Bray (1976) cannot be reproduced from equations reported by Hughes and Kelly (1953).

Table 2.2 Lamé constants and Murnaghan constants of various compressible materials reported in the literature.

Material	Lamé constants [GPa]		Murnaghan constants [GPa]			Source
	λ	μ	l	m	n	
Polystyrene	2.889	1.381	-18.9	-13.3	-10.0	Hughes and Kelly (1953)
Armco iron	110.0	82.0	-348	-1030	1100	
Pyrex	13.53	27.5	14	92	420	
Nickel steel	90.9	78.0	-46	-590	-730	Crecraft (1962)
	109.0	81.7	-56	-671	-785	
Copper	104.0	46.0	542	-372	-401	Crecraft (1967)
Aluminium	61.0	24.9	-47	-342	-248	
Rail steel	115.8	19.9	-248	-623	-714	Egle and Bray (1976)
	110.7	82.4	-302	-616	-724	
Steel Hecla 37	111	82.1	-461	-636	-708	Smith, Stern et al. (1966)*
Steel Hecla 17	110.5	82.2	-328	-595	-668	
Steel Hecla 138A	109	81.9	-426.5	-619	-708	
Steel Rex 535 Ni	109	81.8	-327.5	-578	-676	
Steel Hecla ATV austenitic	87	71.6	-535	-752	-400	
Aluminium alloys 2S	57.0	27.6	-311	-401	-408	
Aluminium alloys B53SM	58.0	26.0	-223.5	-237	-276	
Aluminium alloys B53SP	61.9	26.2	-201.5	-305	-300	
Aluminium alloys D54S	49.1	26.0	-387.5	-358	-320	
Aluminium alloys JH77S	57.5	26.8	-337	-395	-436	
Magnesium tooling plate	25.9	16.6	-90.1	-141.6	-168.4	Nogueira and Rens (2019)
Molybdenum sintered	157	110	-308.5	-669	-772	
Molybdenum resintered	178	124	-301	-852	-908	
Tungsten sintered	75.0	73.0	-250.5	-391	-496	
Tungsten resintered	163	137	-472.5	-792	-1068	
Concrete mixture 1	9.2	12.9	-510.0	-1177.0	-942.6	
	10.3	12.8	-580.0	-846.1	-943.1	
Concrete mixture 2	8.9	13.1	-517.9	-960.5	-771.7	
	9.6	12.3	-741.6	-1183.6	-1115.8	
Concrete mixture 3	6.5	12.9	-783.6	-929.5	-1077.9	
Concrete mixture 4	8.3	13.0	-912.7	-455.0	-432.3	
Concrete mixture 5	6.2	12.9	-677.0	-536.0	-556.2	
Concrete mixture 6	10.7	14.4	-1151.0	-614.9	-571.2	
Concrete mixture 7	9.9	15.2	-563.0	-629.1	-1080.7	
Concrete mixture 8	8.1	12.3	-57.9	-217.3	-1275.0	Nogueira and Rens (2019)
Concrete mixture 9	9.0	12.0	-153.1	-467.5	-416.9	
Mortar	7.8	12.5	-126.9	-830.4	-483.4	
Nylon	9.8	15.8	-1379.3	-1426.6	-497.7	
Aluminium	9.0	9.8	-170.7	-235.8	-280.0	
	4.8	1.4	-13.1	-7.6	-5.6	
	61.6	27.0	-449.8	-384.2	-229.8	

2.5 Knowledge gaps in applying bulk wave-based acoustoelasticity to concrete

Note: * The original third-order elastic constants are converted into the form of Murnaghan constants.

2.5 Knowledge gaps in applying bulk wave-based acoustoelasticity to concrete

In this chapter, we conducted an overview of the development of acoustoelastic theory, commonly used signal processing approaches, and experimental investigations on acoustoelasticity. These endeavours primarily focus on quantifying homogeneous materials such as metals and polymers. Concrete, as the mostly used material in engineering practice, on the other hand, remains relatively underexplored in this regard. Based on the literature review provided in this chapter, there are two main knowledge gaps identified surrounding the application of bulk wave-based acoustoelasticity to concrete.

Acoustoelastic theory for bulk waves in concrete under arbitrary stress conditions

The combination of surface-bonded sensors and ballistic wave components allows for the alignment of the sensors so that the ballistic wave propagation direction could be either parallel or perpendicular to the principal deformation. However, as the recent application shift towards long-term monitoring utilizing permanently deployed ultrasonic sensors within structures, there is no assurance that ballistic waves will consistently propagate along these predetermined directions. Despite the efforts made by several researchers to investigate the influence of shear deformation on acoustoelasticity (Iwashimizu and Kubomura 1973, Bobrenko, Kutsenko et al. 1990), no specific conclusion regarding the response of bulk wave velocity to applied shear deformations can be drawn from the existing theoretical derivations. This knowledge gaps will be tackled in Chapter 5, where we will conduct a revisit of the modern acoustoelastic theory, followed by encompassing arbitrary wave propagation directions and stress conditions in the acoustoelastic theory. Building upon the refined theory, an experimental study will be conducted to validate the conclusions derived from the extended framework.

Signal processing techniques for retrieving stress-induced travel time changes in concrete

After evaluating various techniques based on the criteria outlined in the literature, we selected the stretching technique as the time-domain-based technique and the WCS technique as the transform-domain-based technique. However, it is important to note that the performance of the WCS technique in detecting velocity changes in concrete has not yet been explored. Therefore, before applying this technique to retrieve stress-induced velocity changes in concrete, a thorough comparison with the time-domain technique is necessary to assess their stability against cycle skipping and ensure consistency in retrieving velocity changes. This will be further discussed in Section 4.2.

3. Bulk wave scattering and energy transport in concrete

3.1 Introduction

In an infinite, isotropic, and homogeneous solid, a plane wave can be defined by its frequency, propagation direction, and polarization direction. However, when dealing with a heterogeneous solid, the existence of inhomogeneities leads to interactions with the wave, resulting in deviations in its original propagation direction. This phenomenon is frequently accompanied by conversions of bulk wave modes (Snieder 2002) and is termed *scattering*.

As scattering events increase, the direction of wave propagation undergoes significant alterations. Once a certain threshold of scattering event number is reached, waves are propagating in all directions with equal strength (Curtis, Gerstoft et al. 2006). Simultaneously, the energy ratio between two bulk wave modes stabilizes, leading to the emergence of *diffuse waves*.

The multiply scattered waves are typically not detected in the first arrival since waves which travel directly from the source to the receiver and are unlikely to undergo multiple scattering events (Derode, Tourin et al. 2001). However, in the coda segment, diffuse waves dominate. As mentioned in Section 2.2.3, the acoustoelastic effect differs between longitudinal and transverse waves and is closely related to the directions of wave propagation and polarization. Given the characteristics of diffuse waves, where waves propagate in all directions with equal strength and the energy ratio between longitudinal and transverse waves remains constant, it becomes apparent that understanding bulk wave scattering and transport properties is essential for evaluating the acoustoelastic effect in the coda sector of waves. The bulk wave energy transport properties will be explored in Chapter 6.

This chapter aims to introduce works in the literature on bulk wave energy transport in heterogeneous solids. We will begin by introducing theoretical descriptions of scattering in heterogeneous solids, with an emphasis on multiple scattering, in Section 3.2. Since intrinsic dissipation is not addressed by scattering theory, Section 3.3 will introduce energy transport theories for elastic waves, allowing for the separate analysis of scattering-induced attenuation and intrinsic dissipation-induced attenuation. Section 3.4 will review current applications of scattering and transport theories in the realm of concrete, with Section 3.5 summarizing the identified knowledge gaps.

3.2 Theoretical description on single scattering

When a wave propagates in a heterogeneous solid, the existence of inhomogeneities leads to interactions with the wave, resulting in deviations in its original propagation direction. These deviations are random and cannot be explained by the law of reflection, which states that the incident wave, the reflected wave, and the normal to the surface of the

3.2 Theoretical description on single scattering

mirror all lie in the same plane, and the angle of reflection equals the angle of incidence. This phenomenon is known as scattering, and the inhomogeneities causing scattering are referred to as *scatterers*.

It is essential to recognize that waves in an elastic heterogeneous solid can undergo various phenomena beyond scattering alone. These include refraction due to spatial and/or temporal changes in the solid, such as different layers within the earth, as well as reflection across interfaces between different solids. However, when focusing on wave scattering, simplifications are necessary because it is impractical to simultaneously account for all three phenomena at the interfaces of the scatterers (de Hoop 2001). Consequently, the scattering theories in the literature primarily investigate the interaction between waves and scatterers in a general wave-scatterer interaction relationship, while other phenomena triggered by interfaces and boundaries are typically addressed through numerical calculations (Margerin, Campillo et al. 2000, Heller, Margerin et al. 2022) or by simplifying wave propagation into energy propagation (Trégourès and van Tiggelen 2001, Wan, Wu et al. 2009, Margerin 2017).

Scattering can be broadly categorized into two types according to Sheng (2006): inelastic scattering and elastic scattering. Inelastic scattering alters both frequency and propagation direction, while elastic scattering preserves frequency but alters propagation direction. The primary distinction between these two types lies in whether waves adhere to energy conservation during interaction with scatterers. Since inelastic scattering is mainly observed at subatomic scales, e.g., with electrons and neutrons (Taylor 1991), current literature on the scattering of bulk waves in solids primarily addresses elastic scattering (Weaver 1990, Ryzhik, Papanicolaou et al. 1996, Sheng 2006). This implies that energy conservation holds during the scattering process. Thus, in this dissertation, the interactions between bulk waves and scatterers are also treated as elastic scattering. This means that the attenuation of wave energy due to scattering and dissipation is independent and handled separately.

The concept of wave scattering by individual scatterer was initially formulated by Rayleigh (1896), who recognized that scattering arises primarily from discontinuities in density and elasticity. He formulated the scattered amplitude as a function of wavelength, incident amplitude, bulk modulus difference, and density difference. This formula was adopted by Mason and McSkimin (1947, 1948) to investigate elastic wave scattering in metallic materials, treating each grain as a perturbation within a matrix of other grains. They assessed scattering through measuring wave attenuation and calculated the total scattered energy from multiple scatterers by summing contributions from each scatterer. However, longitudinal and transverse waves are treated separately in their articles, overlooking potential interconversions between two wave modes.

The mode conversion at grain boundaries was incorporated by Lifshits and Parkhomovskii (1950), leading to improved agreement between experimental and theoretical scattering attenuations (Merkulov 1956). They introduced the Green's function rather than plane wave function to extract physical information during scattering. Unlike wave functions, which describe the variation of the displacement in space at every instant and how it varies over time, Green's functions analyse correlation between two locations as a function of time separation. It should be noted that the two locations mentioned above can coincide. In such circumstances, the Green's function encapsulates information equivalent to that found in the wave function (Sheng 2006). Therefore, the Green's function is more general than the wave function and is able to provide a broader understanding of wave propagation.

According to the theoretical description of single scattering, the extent of interaction between waves and scatterers can be categorized into three regimes (Papadakis 1965, Stanke and Kino 1984, Sheng 2006) based on the relationship between wavelength λ_w and average diameter of scatterers d :

- $\lambda_w \gg d$: when the wavelength is 10 times larger than the average diameter of scatterers, the propagating wave encounters limited interactions with scatterers. This regime is known as the **Rayleigh regime** or low-frequency limit.
- $\lambda_w \cong d$: when the wavelength is of a size that is approximately equal to the average diameter of scatterers, the wave has sufficient interactions with scatterers. This regime is known as the **stochastic regime**.
- $\lambda_w \ll d$: when the wavelength is less than one-tenth of the average diameter of the scatterers, the wave strongly interacts with scatterers. This regime is known as the **geometrical regime** or high-frequency limit.

In the geometrical regime, interactions between the wave and scatterers may involve refraction and reflection across interfaces between different solids. Additionally, the Born approximation, which can significantly simplify the derivation of scattered amplitude during the scattering process (Sakurai and Napolitano 2020), is not applicable in this regime. This approximation will be discussed further in Chapter 6.

3.3 Theoretical description on energy transport of multiply scattered bulk waves

In a heterogeneous medium, a wave may interact with multiple scatterers during its propagation. These interactions involve multiple scattering, which requires a theoretical description that accounts for the spatial distribution of scatterers or spatial fluctuations of material properties within the medium. Several researchers have contributed to this topic,

3.3 Theoretical description on energy transport of multiply scattered bulk waves

including Stanke & Kino (1984), Weaver (1990), Ahmed & Thompson (1996), Turner (1999), and Turner & Anugonda (2001).

However, in the above research, the attenuation of wave energy due to scattering and dissipation is treated independently. This implies that intrinsic dissipation, stemming from material viscosity and internal friction (Brunet, Jia et al. 2008), is difficult to be incorporated into the scattering model. Therefore, it is challenging to investigate scattering and intrinsic dissipation simultaneously using the scattering theory. To separately examine scattering-induced attenuation and intrinsic dissipation-induced attenuation, energy transport theories are introduced for bulk waves in heterogeneous solids. These theories focus exclusively on the energy or intensity of bulk waves, without describing individual wave components.

This section will introduce two transport equations: the radiative transfer equation (RTE) (Chandrasekhar 2013), a differential equation used to describe the transport of wave energy through a medium, and its approximation, the diffusion equation (Watson, Fleury et al. 1987), a differential equation modelling the spread of wave energy over time as a result of diffusion.

3.3.1 Radiative transfer equation (RTE)

The RTE is a scalar differential equation that characterizes the propagation of wave energy in a medium, accounting for processes like scattering, intrinsic dissipation, and emission. Originally introduced by Wu (1985) for bulk waves in heterogeneous solids, this equation aimed to separate scattering-induced attenuation from intrinsic dissipation-induced attenuation (Mayeda, Su et al. 1991, Mcsweeney, Biswas et al. 1991, Fehler, Hoshihara et al. 1992).

Initially, RTE did not consider the vector nature of bulk wave motion or possible mode conversions. Numerous research has been done afterwards to enhance the RTE by incorporating wave propagation vectors, mode conversions, and intrinsic dissipations. For example, Weaver (1990) considered wave vectors and mode conversions in RTE, while Sato (1994) and Zeng (1993) incorporated mode conversions and intrinsic dissipation. Later on, Turner and Weaver (1994) and Ryzhik et al. (1996) further developed the RTE to include all three aspects. This improved RTE, considering wave propagation vectors, mode conversions, and intrinsic dissipations, was adopted by Margerin et al. (2000) to numerically study multiple scattering of bulk waves in heterogeneous solids.

Despite the advancements in describing energy transport using the RTE, its direct application to quantify transport properties through measurements is challenging. This difficulty arises from the form of RTE for bulk waves in heterogeneous solids, which is a complex differential equation dependent on wave vectors, locations, and time, often lacking analytical solutions. Consequently, researchers commonly resort to approximating the

RTE with the simpler diffusion equation to quantify transport properties in heterogeneous solids.

3.3.2 Diffusion equation

The diffusion equation (Crank 1979, Watson, Fleury et al. 1987) describes the macroscopic behaviour of energy transport for diffusion process. Its corresponding equation, the diffusion equation, is a parabolic partial differential equation describing the isotropic spreading of energy throughout space. Despite its simplicity, the effectiveness of this equation has been demonstrated in many studies describing energy transport over long distances (Wesley 1965, Freund, Kaveh et al. 1988, Weitz, Pine et al. 1989, Weaver and Sachse 1995).

The energy transport in heterogeneous media using the diffusion equation is characterized by two parameters, namely: diffusivity and dissipation, both frequency-dependent (Weaver and Sachse 1995). Diffusivity measures the rate at which energy spreads within the medium (Planès and Larose 2013), akin to the *spreading velocity* of the diffusion halo (Ramaniraka, Rakotonarivo et al. 2022). Notably, in the absence of dissipation, the pure diffusion or scattering process generally adheres to energy conservation (Anugonda, Wiehn et al. 2001). Dissipation in heterogeneous solids likely involves a combination of viscous dissipation and internal friction (Brunet, Jia et al. 2008), deviating from energy conservation. The diffusion equation will be used in Section 4.3 to quantify the scattering-induced attenuation and intrinsic dissipation-induced attenuation of bulk wave energy in concrete.

Even though the diffusion equation is simple and effective in quantifying energy transport, this equation is valid only within the diffusive regime, where wave energy has undergone numerous scattering events, losing its phase information and original propagation direction (Lai, Cheung et al. 2005). If the energy transport is not in the diffusive regime, then this transport can only be described using RTE.

There were several attempts on determining the range of validity of diffusion approximation (Yoo, Liu et al. 1990, Kop, deVries et al. 1997, Zhang, Jones et al. 1999), but no conclusion for bulk waves until the paper of Ryzhik et al. (1996), who proposed an indirect criterion to determine the validity of diffusion approximation for bulk waves. According to this criterion, the diffusion approximation holds when the energy ratio of transverse waves to longitudinal waves converges to a constant independent of the scattering process during wave propagation (Egle 1981, Weaver 1982, Shapiro, Campillo et al. 2000, Hennino, Tregoures et al. 2001, Wu, Lai et al. 2008, Wan, Wu et al. 2009). Theoretically, this equilibration also implies isotropy of the bulk wave field, where transverse waves are fully depolarized (Margerin, Campillo et al. 2000), and the energy flux of longitudinal and transverse waves is isotropic in space (Paul, Campillo et al. 2005). This theoretical

3.4 Application of diffusion equation to concrete

assertion was supported by Monte Carlo simulations (Margerin, Campillo et al. 2000) and numerical simulations of seismic coda (Paul, Campillo et al. 2005). However, no research has yet addressed the range of validity of the diffusion equation in the context of concrete.

3.4 Application of diffusion equation to concrete

In Section 3.2, we introduced scattering theory, which describes the interactions between elastic waves and scatterers, covering both single and multiple scattering. Scattered waves hold significant potential for monitoring concrete structures due to their extended wave paths and their inherent sensitivity to the properties of heterogeneities in concrete. However, research on elastic wave scattering in concrete remains limited. Notable studies include Anugonda et al.'s (2001) work on multiple scattering and Ramaniraka et al.'s (2019, 2022) studies on single scattering. Despite these efforts, a theoretical model to quantify multiple scattering in concrete is still lacking.

In contrast, the diffusion equation introduced in Section 3.3 has been widely applied to quantify the transport properties of elastic waves in concrete due to its simpler formulation compared to the RTE. These studies can be divided into two categories: global monitoring of a region using diffusive properties (Ahn, Shin et al. 2022) and disturbance localization using sensitivity kernels (Zhang, Larose et al. 2018, Zhan, Jiang et al. 2020).

The former focuses on leveraging changes in diffusive properties, such as diffusivity and dissipation, which are behaviours of diffuse field, to characterize variations in the micro and meso-structure of the material. The latter involves utilizing bulk waves within a specific time window and localizing disturbances in the sensor grid. Both approaches rely on the accurate estimation of diffusive properties. In global monitoring, diffusive properties are directly utilized, while in disturbance localization using the sensitivity kernel, the sensitivity kernel is constructed based on diffusive properties (Rossetto, Margerin et al. 2011). Therefore, obtaining an accurate estimation of the diffusive properties is essential for the application of diffuse waves in concrete structure monitoring.

The diffusive properties of a medium can be extracted by fitting the wave energy profile with a diffusion equations in one-dimensional form (Yim, An et al. 2016, Ramaniraka, Rakotonarivo et al. 2022), two-dimensional form (Becker, Jacobs et al. 2003, Quiviger, Payan et al. 2012) or three-dimensional form (Ahn, Shin et al. 2019, Jiang, Zhan et al. 2019, Tinoco and Pinto 2021, Ahn, Shin et al. 2022). However, it is important to note that the analytical solution of the diffusion equation is derived for an infinite medium. While concrete can be considered as an infinite medium, in certain cases where the boundary is sufficiently far away, as observed in cases reported by Anugonda et al. (2001) and Schubert & Koehler (2004), the direct application of the diffusion equation is limited in most scenarios. To overcome this limitation, Ramamoorthy et al. (2004) proposed an analytical solution of diffusion equation that incorporates the Neumann boundary condition. This

modification, which considers all possible reflected energy, enables a theoretically more accurate estimation of the diffusive property within a two-dimensional rectangular domain (In, Holland et al. 2013, Seher, In et al. 2013, In, Arne et al. 2017) and three-dimensional cuboid domain (Deroo, Kim et al. 2010, Hilloulin, Legland et al. 2016). Nevertheless, the increased complexity in the expression of the diffusion equation makes nonlinear curve fitting more intricate for obtaining diffusivity, rendering it less robust compared to the original diffusion equation in infinite solids (Deroo, Kim et al. 2010). Currently, a simplified diffusion equation that accounts for boundary reflections is necessary to estimate the diffusive properties of elastic waves in concrete.

3.5 Knowledge gaps in applying the scattering and diffusion equation to concrete

In this chapter, we provided an overview of the theoretical descriptions of bulk wave scattering and energy transport, focusing on the RTE and diffusion equation in heterogeneous solids. Additionally, we discussed the applications of scattering and energy transport of bulk waves in concrete. From the literature review, two major knowledge gaps were identified regarding the application of diffuse bulk waves to concrete.

Characterizing diffusive properties in concrete structures with boundaries

Diffusivity and dissipation are transport properties easily measured through experiments, with diffusivity also holding potential for assessing the scattering property of bulk waves in concrete. However, the analytical solution of the diffusion equation is proposed for an infinite medium, posing a challenge for direct application to most concrete structures with boundaries. In such cases, the influence of boundaries on diffusive properties must be considered.

In the presence of complex boundary conditions, solving the diffusion equation for the geometry of system becomes a problem within the field of applied mathematics (Crank 1979). Section 3.4 introduced examples of solving the diffusion equation for two-dimensional rectangular and three-dimensional cuboid domains. However, the increased complexity in the expression of the diffusion equation makes nonlinear curve fitting more intricate for obtaining diffusive properties, rendering it less robust compared to the original diffusion equation in infinite media (Deroo, Kim et al. 2010). Hence, an improved diffusion equation for three-dimensional media is needed to incorporate boundaries without significantly increasing its complexity, enhancing the accuracy of diffusive property estimation. This part will be discussed in Section 4.3.

Evaluating the evolution of bulk wave energy in concrete

In Section 3.3, we introduced two theoretical models for bulk wave energy transport in heterogeneous solids: the RTE and the diffusion equation. While the diffusion equation

3.5 Knowledge gaps in applying the scattering and diffusion equation to concrete

is simpler and more suitable for engineering applications, we emphasized that it is an approximation of the RTE. Therefore, the range of validity, equivalent to detecting energy equilibration, should be verified before application. If wave energy transport can be accurately described by the diffusion equation, it indicates that the bulk waves are in the diffusive regime, where the ratio between longitudinal and transverse waves is equilibrated, and the bulk wave field becomes isotropic.

Furthermore, as discussed in Section 3.2, the scattering process of bulk waves is greatly influenced by the relationship between the wavelength and average diameter of scatterers. Given that the wavelength is closely linked to the frequency of bulk waves, the scattering process inherently relies on wave frequency. Since the evolution of bulk wave energy arises from the scattering process, it can be inferred that energy evolution primarily hinges on wave frequency. Therefore, to effectively leverage the equilibrated energy ratio and the isotropic wave field in interpreting the acoustoelastic effect of diffuse coda waves, travel time changes and energy evolution should be investigated in the same frequency band. This consideration motivates the use of the WI technique in the transform domain.

The equilibrated energy ratio is also critical for understanding the relationship between applied stress and measured travel time changes in the coda, as the travel time shift in the coda is a weighted average of both longitudinal and transverse wave changes (Snieder 2002). Consequently, a bulk wave energy transport model is necessary to describe the equilibration process of wave energy in concrete. This model can help estimate the equilibration time, which can then be used to assess the validity of the diffusion approximation. Additionally, the model allows for estimating the equilibrated energy ratio, which can further aid in interpreting velocity changes retrieved from diffuse waves. This model will be discussed in Chapter 6.

4. Techniques for estimating bulk wave properties in concrete

4.1 Introduction

In Chapters 2 and 3, a literature review is provided on acoustoelasticity and bulk wave energy transport in heterogeneous solids, respectively. This chapter introduces the techniques that will be employed in this research to extract bulk wave properties from the raw signal. Two types of bulk wave properties will be extracted in this chapter: travel time changes, covered in Section 4.2, and diffusive properties, covered in Section 4.3. The first can be used to investigate how travel time of bulk waves responds to applied stress, which will be further used in Chapters 5 and 7 to assess stress-induced velocity changes in concrete. The second is relevant to the scattering and transport properties of bulk waves in heterogeneous media, which will be utilized in Chapters 6 and 7 to analyse diffusive properties of bulk waves in concrete. In this chapter, we will conduct a comprehensive investigation of these techniques, along with necessary enhancements to ensure their desired functionality. The procedures and parameter selections for applying these techniques to the concrete members studied in this dissertation will also be detailed in this chapter.

4.2 Estimation of travel time changes

The first bulk wave property of interest is the travel time change. Historically, the prevalent method for obtaining the travel time involves the usage of arrival time pickers (Karaiskos, Deraemaeker et al. 2015). However, the emergence of wave interferometry (WI) in concrete monitoring (Larose and Hall 2009) has garnered increased attention due to its high sensitivity to weak changes in the medium. This sensitivity stems from the extended propagation path, enabling the accumulation of effects from minor perturbations within the medium. Given that stress-induced velocity changes in the medium are typically subtle, with relative changes often below 1% (Guz and Makhort 2000), WI is well-suited for detecting such nuanced changes. Based on the location of the operational window, WI can be divided into coda wave interferometry (CWI) (Snieder, Gret et al. 2002), which operates in the coda wave regime, and direct wave interferometry (DWI) (Zhong, Zhu et al. 2021), which operates in the direct wave regime.

In this chapter and in the remainder of this dissertation, there will be repeated references to velocity changes and travel time changes. It is important to emphasize that the velocity change is associated with the change in the medium, and this change further results in the travel time change. Assuming a constant wave path, the velocity becomes inversely proportional to the travel time. Based on this assumption, the velocity change in the medium can be retrieved by using the travel time change of the wave signal (Grêt, Snieder et al. 2006). For the remainder of this dissertation, travel time changes will be associated with bulk waves, while velocity changes will be linked to the medium, i.e., stress-induced changes in the material.

4.2 Estimation of travel time changes

WI techniques can be broadly categorized into two types based on their operational domain: time-domain-based techniques and transform-domain-based techniques, both of which are introduced in Section 2.3.2. Time domain techniques are adept at handling signals with short durations, implying lower frequency resolution, while transform domain techniques excel in exploring frequency-dependent changes in travel time. In this section, the stretching technique is chosen as the time-domain approach due to its blend of high accuracy and stability. Meanwhile, within the transform-domain category, the wavelet cross-spectrum (WCS) technique, known for its superior accuracy and time-frequency resolution compared to the moving window cross-spectrum (MWCS), is selected.

Given that the performance of the stretching technique has already been demonstrated for measuring velocity changes in concrete health monitoring (Larose and Hall 2009, Payan, Garnier et al. 2009), while it is not the case for the WCS technique, their consistency in determining velocity changes in concrete and the stability against cycle skipping needs to be assessed. Stability here evaluates whether the estimated travel time change is temporally stable. When it comes to this aspect, the performance of different techniques involves their ability to mitigate cycle skipping, a phenomenon where a wiggle in the signal associated with the perturbed medium aligns with a wiggle in the signal from the unperturbed state, displaced by approximately one period (Mikesell, Malcolm et al. 2015).

This section aims to elaborate and compare the two selected techniques. We will first emphasize the knowledge gap in Section 4.2.1. Theoretical backgrounds of these techniques are discussed in Section 4.2.2. To assess their performance in retrieving velocity changes in concrete, a dedicated experiment is designed, with details provided in Section 4.2.3. The results are compared and discussed in Section 4.2.4, with the parameter selection for applying the stretching and WCS techniques in later chapters introduced in Section 4.2.5.

4.2.1 Knowledge gap in techniques for estimating stress-induced travel time changes in concrete

The literature presents various efforts to retrieve stress-induced velocity changes in concrete using WI techniques, as summarized in Table 4.1. Notably, current studies predominantly rely on time-domain-based techniques. Additionally, the potential frequency dependence of the retrieved velocity changes is ignored and hence cannot be evaluated.

Given that frequency is not explicitly considered in bulk wave-based acoustoelasticity (Hughes and Kelly 1953, Toupin and Bernstein 1961, Thurston and Brugger 1964), some researchers assume that the travel time change remains constant across different frequency components in concrete (Stahler, Sens-Schonfelder et al. 2011). This has not yet been validated. To address this, it is imperative to employ a frequency-domain-based technique to investigate stress-induced velocity changes in concrete thoroughly.

Table 4.1 Recent studies on retrieving the stress-induced velocity changes in concrete using WI.

Specimen dimensions [mm]	WI technique	Time window length [μ s]	Literature
Cylinder $\varnothing 160 \times 285$	Stretching	450	Larose et al. (2009)
Cylinder $\varnothing 75 \times 160$	MWCC*	20	Payan et al. (2009)
Cylinder $\varnothing 75 \times 160$	MWCC	NM**	Payan et al. (2010)
Cylinder $\varnothing 70 \times 135$	MWCC	NM	Lillamand et al. (2010)
Cylinder $\varnothing 75 \times 160$	MWCC	20	Payan et al. (2011)
Prism $305 \times 76 \times 76$	Stretching	NM	Schurr et al. (2011)
Cube $150 \times 150 \times 150$	Stretching	NM	Stähler et al. (2011)
Cylinder 110×450	Stretching	200	Zhang et al. (2012)
Cylinder 110×450	Stretching	200	Zhang et al. (2013)
Beam $6100 \times 1600 \times 800$	Stretching	500	Zhang et al. (2016)
Cube $100 \times 100 \times 100$	Stretching	50/75	Zhang et al. (2018)
Beam $2000 \times 150 \times 400$	Stretching	NM	Clauß et al. (2020)
Beam $5960 \times 870 \times 300$	Stretching	NM	Jiang et al. (2020)
T-beam $29200 \times 1700 \times 1600$	Stretching	NM	Zhan et al. (2020)
Prism $300 \times 150 \times 150$	Stretching	40	Zhan et al. (2020)
Cube $150 \times 150 \times 150$	Stretching	257	Hu et al. (2021)
Beam $5960 \times 870 \times 300$	Stretching	2000/6000	Jiang et al. (2021)
T-beam $29200 \times 1700 \times 1600$	Stretching	320	Xue et al. (2022)
Concrete Containment Cylinder $\varnothing 152 \times 304$	Stretching	14/150	Zhong et al. (2021)
Prism $508 \times 152 \times 152$			
Prism $400 \times 100 \times 100$	Stretching	NM	Diewald et al. (2022)
Bone-shaped cylinder Cube $150 \times 150 \times 150$	Stretching	NM	He et al. (2022)
$100 \times 100 \times 100$ Cylinder $\varnothing 100 \times 200$	Stretching	200	Zhong et al. (2022)

Note: * MWCC: Moving Window Cross-Correlation

** NM: Not Mentioned

In Section 2.3.2, we have introduced five WI techniques and compared them in the context of seismology. After the comparison, it is evident that the stretching technique stands

4.2 Estimation of travel time changes

out among time-domain-based techniques due to its superior balance between accuracy and stability. On the other hand, the WCS technique demonstrates better performance among transform-domain-based techniques. However, it is worth noting that the performance of transform-domain-based techniques in discerning velocity changes in concrete remains unexplored. Therefore, prior to employing the transform-domain technique for retrieving stress-induced velocity changes in concrete, it is essential to conduct a comprehensive comparison with the time-domain technique to ensure their consistency.

4.2.2 Theoretical background of wave interferometry techniques

4.2.2.1 The stretching technique

The stretching technique (Lobkis and Weaver 2003) assumes a linear increase or decrease of the travel time as a result of a homogeneous velocity perturbation of the medium (Sens-Schönfelder and Wegler 2006). This technique calculates correlation coefficients of windowed signals recorded in an unperturbed state, u_{unp} , and after (or during) the perturbation, u_{per} , in the time domain using:

$$CC(t_c, T, \varepsilon) = \frac{\int_{t_c-T}^{t_c+T} u_{\text{unp}}^{(t_c)}(t) u_{\text{per}}^{(t_c)}(t(1-\varepsilon)) dt}{\sqrt{\int_{t_c-T}^{t_c+T} [u_{\text{unp}}^{(t_c)}(t)]^2 dt} \sqrt{\int_{t_c+T}^{t_c+T} [u_{\text{per}}^{(t_c)}(t(1-\varepsilon))]^2 dt}}, \quad (4.1)$$

where the time window is centred at time t_c with a duration of $2T$ and ε denotes the stretching factor. In case of a uniform velocity change dv in the medium, the stretching factor that maximizes $CC(t_c, T, \varepsilon)$, ε_{max} , coincides with the relative change in travel time, dt/t .

The stretching technique does not solely rely on the phase spectrum. This can be proved by representing this technique in the frequency domain. Letting the Fourier transforms of $u_{\text{unp}}^{(t_c)}(t)$ and $u_{\text{per}}^{(t_c)}(t(1-\varepsilon))$ be $U_{\text{unp}}^{(t_c)}(f)$ and $U_{\text{per}}^{(t_c)}(f, \varepsilon)$, and assuming that the magnitude of ε is much smaller than 1, then Zhan et al. (2013) derive the following expression:

$$U_{\text{unp}}^{(t_c)}(f) := F\{u_{\text{unp}}^{(t_c)}(t)\} \\ = A_{\text{unp}}(f) e^{j\varphi_{\text{unp}}(f)}, \quad (4.2a)$$

$$U_{\text{per}}^{(t_c)}(f, \varepsilon) := F\{u_{\text{per}}^{(t_c)}(t(1-\varepsilon))\} \\ = \frac{1}{1-\varepsilon} U_{\text{per}}^{(t_c)}\left(\frac{f}{1-\varepsilon}\right) \\ \approx (1+\varepsilon) U_{\text{per}}^{(t_c)}(f(1+\varepsilon)) \\ = (1+\varepsilon) A_{\text{per}}(f(1+\varepsilon)) e^{j\varphi_{\text{per}}(f(1+\varepsilon))}, \quad (4.2b)$$

where f is the frequency, $A_{\text{unp}}(f)$ and $A_{\text{per}}(f)$ are amplitude spectra, and $\varphi_{\text{unp}}(f)$ and $\varphi_{\text{per}}(f)$ are phase spectra. Equation (4.1) can be rewritten as:

$$\begin{aligned}
 CC(t_c, T, \varepsilon) &= \frac{\int_{-\infty}^{+\infty} U_{\text{per}}^{(t_c)}(f, \varepsilon) [U_{\text{unp}}^{(t_c)}(f)]^* df}{\sqrt{\int_{-\infty}^{+\infty} U_{\text{unp}}^{(t_c)}(f) [U_{\text{unp}}^{(t_c)}(f)]^* df} \sqrt{\int_{-\infty}^{+\infty} U_{\text{per}}^{(t_c)}(f, \varepsilon) [U_{\text{per}}^{(t_c)}(f)]^* df}} \\
 &= \frac{\int_{-\infty}^{+\infty} A_{\text{unp}}(f) A_{\text{per}}(f(1+\varepsilon)) e^{j[\varphi_{\text{per}}(f(1+\varepsilon)) - \varphi_{\text{unp}}(f)]} df}{\sqrt{\int_{-\infty}^{+\infty} A_{\text{unp}}^2(f) df} \sqrt{\int_{-\infty}^{+\infty} A_{\text{per}}^2(f(1+\varepsilon)) df}},
 \end{aligned} \quad (4.3)$$

where the asterisk denotes complex conjugation. Please note that Parseval's theorem is used in the derivation of Equation (4.3) through Equation (4.1). Although Equation (4.3) contains imaginary terms, its absolute value coincides with the value of CC obtained by Equation (4.1). Explicitly, this is written as (Liu 1994):

$$\begin{aligned}
 |CC(t_c, T, \varepsilon)| &= \\
 &= \frac{\sqrt{\int_{-\infty}^{+\infty} A_{\text{unp}}(f) A_{\text{per}}(f(1+\varepsilon)) e^{j[\varphi_{\text{per}}(f(1+\varepsilon)) - \varphi_{\text{unp}}(f)]} df \int_{-\infty}^{+\infty} A_{\text{unp}}(f) A_{\text{per}}(f(1+\varepsilon)) e^{-j[\varphi_{\text{per}}(f(1+\varepsilon)) - \varphi_{\text{unp}}(f)]} df}}{\sqrt{\int_{-\infty}^{+\infty} A_{\text{unp}}^2(f) df} \sqrt{\int_{-\infty}^{+\infty} A_{\text{per}}^2(f(1+\varepsilon)) df}}.
 \end{aligned} \quad (4.4)$$

The quantity $|CC|$ in Equation (4.4) is usually referred to as the ‘coherency’. Equation (4.4) clearly shows that both amplitude and phase spectra are involved in the calculation of the stretching technique.

The stretching technique is adept at handling the retrieval of velocity changes from ballistic waves within very narrow time windows, which is also known as DWI (Zhong, Zhu et al. 2021). The utilization of such short time windows is essential for capturing travel times changes of pure wave modes while minimizing the influence of possible wave mode conversions on the results. As per the frequency-time uncertainty principle (Gabor 1947, Tsao 1984), when a signal has a short duration and fewer sampling points, its frequency resolution tends to be diminished. Consequently, in theory, transform-domain-based techniques are deemed inadequate for this application due to the unreliable nature of the results they yield.

4.2.2.2 The wavelet cross-spectrum (WCS) technique

The WCS technique (Mao, Mordret et al. 2020) relies on the phase of the wavelet cross-spectrum, which is related to the time shift between two signals. In application, a raw signal is firstly transformed to the wavelet domain using the continuous wavelet transform (CWT). In this dissertation, the analytical Morlet wavelet (Morlet, Arens et al. 1982, Morlet, Arens et al. 1982) is chosen as the mother wavelet since it has equal variance in time and frequency. The analytical Morlet-based CWT filter bank $\Phi(f^{(c)}_{i,n})$ is designed in the frequency domain as:

$$\Phi(f^{(c)}_i, f_n) = 2 \times H(f_n) \times e^{-\frac{[S(f^{(c)}_i) f_n - \omega_0]^2}{2}}, \quad n \in [1, N], \quad (4.5a)$$

4.2 Estimation of travel time changes

$$S(f_i^{(c)}) = \omega_0 \frac{f_{\text{Nyquist}}}{f_i^{(c)}}, \quad i \in [1, M], \quad (4.5b)$$

where f_n , f_{Nyquist} and $f_i^{(c)}$ represent the frequency components of the filter, the Nyquist frequency, and the centre frequency of the filter, respectively. The parameter N represents the total number of sampling points of the signal in the time domain. The number of filters in the filter bank is M . The functions $H(\cdot)$ and $S(f_i^{(c)})$ are the Heaviside step function and scale function, respectively. The constant ω_0 is set to 6 to satisfy the admissibility condition, which requires the mother wavelet to be zero-mean (Farge 1992). A typical analytical Morlet-based CWT filter bank is shown in Figure 4.1. It is important to note that the CWT filter bank consists of multiple Gaussian filters in the frequency domain. Consequently, each filter does not isolate a single frequency component but instead captures energy from adjacent frequencies. This leads to less pronounced energy fluctuations between consecutive frequency components.

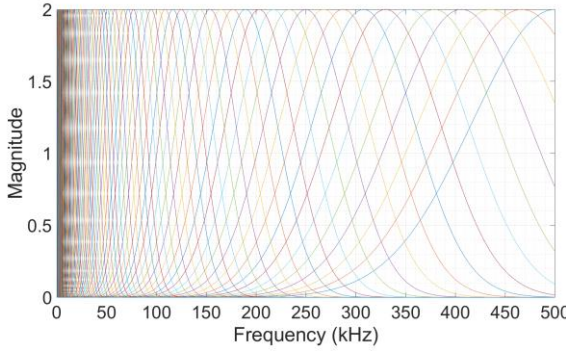


Figure 4.1 Typical analytical Morlet-based CWT filter bank.

The designed CWT filter bank is multiplied with the target signal in the frequency domain, and then transformed back to time domain through the inverse fast Fourier transform (IFFT). The obtained time-frequency spectrum is dubbed the wavelet spectrum $W(f_i^{(c)}, t_n)$, where t_n is the sampling point in the time domain.

After operating the CWT, the wavelet cross-coherency $I(f_i^{(c)}, t_n)$ can be calculated through the obtained wavelet spectra of the signal before perturbation, $W_{\text{unp}}(f_i^{(c)}, t_n)$, and after perturbation, $W_{\text{per}}(f_i^{(c)}, t_n)$:

$$\Gamma(f_i^{(c)}, t_n) = \frac{\zeta \left\{ \left[s(f_i^{(c)}) \right]^{-1} W_{\text{unp,per}}(f_i^{(c)}, t_n) \right\}}{\sqrt{\zeta \left\{ \left[s(f_i^{(c)}) \right]^{-1} W_{\text{unp,unp}}(f_i^{(c)}, t_n) \right\} \zeta \left\{ \left[s(f_i^{(c)}) \right]^{-1} W_{\text{per,per}}(f_i^{(c)}, t_n) \right\}}} \quad (4.6)$$

$$= \frac{\zeta \left\{ \left[s(f_i^{(c)}) \right]^{-1} W_{\text{unp}}(f_i^{(c)}, t_n) W_{\text{per}}^*(f_i^{(c)}, t_n) \right\}}{\sqrt{\zeta \left\{ \left[s(f_i^{(c)}) \right]^{-1} |W_{\text{unp}}(f_i^{(c)}, t_n)|^2 \right\} \zeta \left\{ \left[s(f_i^{(c)}) \right]^{-1} |W_{\text{per}}(f_i^{(c)}, t_n)|^2 \right\}}},$$

where $s(f_i^{(c)})$ represents the wavelet scale (Torrence and Compo 1998) and can be calculated through dividing $S(f_i^{(c)})$ in Equation (4.5b) by the sampling rate. The symbol $\zeta\{\cdot\}$ denotes the smoothing operator for both time and frequency scales to prevent the coherence being identically one (Glaudeaud 1981). The phase angle of the wavelet cross-coherence $\Gamma(f_i^{(c)}, t_n)$ is the phase difference spectrum $\phi_{\text{unp,per}}(f_i^{(c)}, t_n)$. This phase difference spectrum can be converted into the time difference spectrum $\delta t_{\text{unp,per}}(f_i^{(c)}, t_n)$ through dividing by $2\pi f_i^{(c)}$ at each frequency component. The travel time change spectrum $dt/t_{\text{unp,per}}(f_i^{(c)}, t_n)$ can be obtained using the $\delta t_{\text{unp,per}}(f_i^{(c)}, t_n)$ divided by the lapse time t at each lapse time.

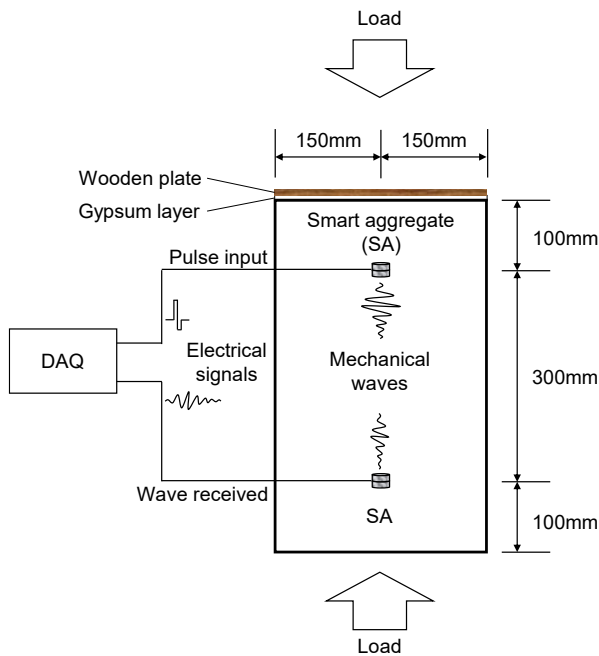
Compared with the Fourier transform-based MWCS, in which the length of the time window is fixed, the time window used in WCS adapts to each frequency through CWT and hence has a better time-frequency resolution (Mao, Mordret et al. 2020). Another advantage of WCS technique is its higher computational speed, especially compared to time-domain-based techniques (Mao, Mordret et al. 2020). A drawback of the WCS technique is poor performance in estimating the velocity change at frequencies with low energy (Mao, Mordret et al. 2020, Yuan, Bryan et al. 2021), which will be further discussed in Section 4.4.1.

4.2.3 Specimens and experiments

The selected WI techniques are further verified and compared in a concrete specimen. To ensure that the propagating waves in the coda within the specimen are predominantly bulk waves, the dimensions of the specimen should be several times larger than the maximum wavelength of transverse waves, which dominate the coda (Snieder 2002). Considering that the maximum wavelength of transverse waves associated with the lowest frequency of interest (50 kHz) is approximately 54 mm (assuming a transverse wave velocity of approximately 2700 m/s, which is typical for concrete), a cylindrical sample with a diameter of 300 mm (approximately 5.6 times the wavelength) and a height of 500 mm (approximately 9.3 times the wavelength) is designed. A typical commercial concrete mixture with a compressive strength grade of C50/60 is used. The load is applied along the axial direction of the cylinder and is uniformly distributed over the cross sectional areas by means of a gypsum layer and a wooden plate on the top surface of the cylinder. A diagram of the experimental setup is shown in Figure 4.2.

4.2 Estimation of travel time changes

Two piezoelectric sensors, namely smart aggregates (SAs), with the polarization direction parallel to the load direction are embedded inside this cylinder to serve as the actuator and receiver. The minimum distance from the SA to the surface of the specimen is 100 mm (top/bottom surface). Considering that the frequencies of interest exceed 50 kHz, and that the Rayleigh wave velocity in concrete is around 2300 m/s (Shin, Yun et al. 2007), the maximum effective depth of penetration of Rayleigh waves, which is equal to one Rayleigh wave wavelength (Giurgiutiu, Bao et al. 2001), is about 46 mm. This is obviously smaller than 100 mm, implying that the presence of Rayleigh wave-related particle velocities in measurements can be neglected. Sensor locations are also depicted in Figure 4.2.



(a) Front view.

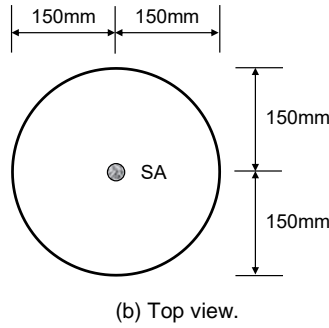


Figure 4.2 Concrete cylindrical specimen with smart aggregate (SA) locations.

In the test, the cylinder is loaded to a stress range between 7 MPa and 12 MPa. The loading and unloading processes are repeated 3 times. The loading protocol is designed based on this stress range and shown in Figure 4.3. The first and second cycles are loaded from 500 kN (7.07 MPa) to 700 kN (9.90 MPa) and back to 500 kN (7.07 MPa) with a 10 kN (0.14 MPa) interval. The third cycle starts from 500 kN (7.07 MPa) but goes up to 800 kN (11.32 MPa) and back to 400 kN (5.66 MPa) with the same interval. The choice of the load interval of 10 kN (0.14 MPa) is determined by two criteria: it should be sufficiently large to ensure detectability of travel time changes and yet small enough to guarantee sufficient resolution in detecting stress changes. The loading and unloading processes are coloured in red and green in Figure 4.3, respectively. There are 151 loading steps in total, as shown on the x -axis, and the first loading step is counted as load step 0. The loading speed during both the loading and unloading processes is maintained at 0.5 kN/s, which translates to 7.07 kPa/s. Upon reaching each load step, there is an initial one-minute waiting period to ensure stability in the loading jack before measurements are taken. The measurement at each loading step is completed in less than one minute.

A portable ultrasonic system is used at each load step to generate and receive wave signals. Considering the resonant frequency of SA, around 80 kHz (Kong 2015), and frequency of interest, higher than 50 kHz, a squared pulse with a frequency of 54 kHz is used as the excitation signal. The sampling rate is 1 MHz. Since the test was carried out in the lab with a small temperature fluctuation, it is supposed that velocity variations are mainly caused by stress changes.

4.2 Estimation of travel time changes

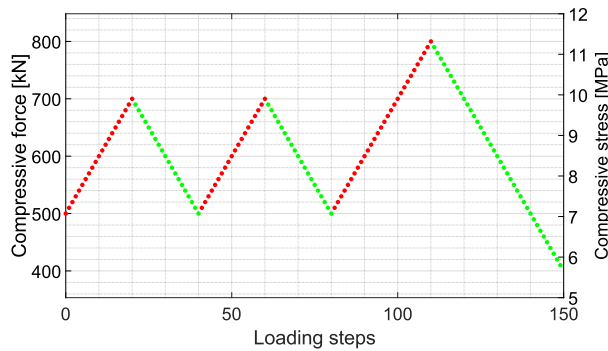


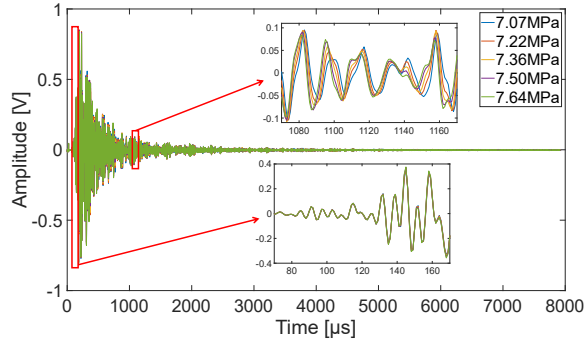
Figure 4.3 Loading protocol (red dots are associated with loading stages, green dots with unloading). The loading speed during both the loading and unloading processes is maintained at 0.5 kN/s, which translates to 7.07 kPa/s. Upon reaching each load step, there is an initial one-minute waiting period to ensure stability in the loading jack before measurements are taken. The measurement at each loading step is completed in less than one minute.

4.2.4 Comparison between the wavelet cross-spectrum technique and the stretching technique

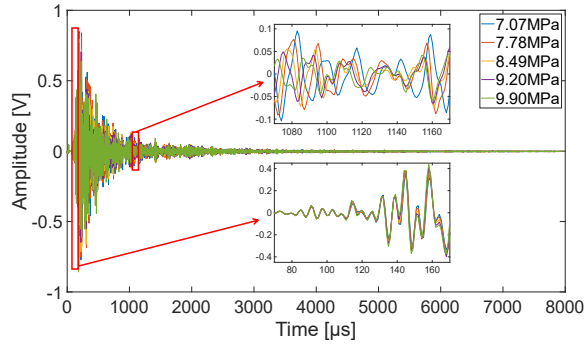
4.2.4.1 Time-frequency characteristics of typical waves received by smart aggregates in concrete

In this section, we will present the characteristics of typical waves received by SAs in concrete. These characteristics will assist in identifying the frequency of interest, which will be used in the frequency-domain analysis, i.e., the WCS technique. As mentioned in Section 4.2.2.2, the WCS technique needs to be applied within frequency bands exhibiting adequate energy levels to ensure its effective performance in retrieving velocity changes. Therefore, a time-frequency analysis is required to identify frequency bands with sufficiently high energy, within which the WCS technique will be implemented.

The time-domain signals measured at the first five loading steps (Step 0-4) are shown in Figure 4.4(a). The stress linearly increases with steps of 0.14 MPa. With such small stress changes, waveforms are almost identical, and time shifts are not visible in direct waves. However, time shifts are evident in the coda, whereas the waveforms still have almost the same form. Upon reaching a higher stress level of approximately 9.90 MPa, as illustrated in Figure 4.4(b), waveforms of direct waves remain relatively indistinguishable, but time shifts become more pronounced compared to Figure 4.4(a). In the coda, time shifts become substantial, and the similarity between waveforms decreases, particularly between the signals recorded at 7.07 MPa and 9.90 MPa. The result shown in Figure 4.4(b) suggests that directly applying WI to signals recorded at 7.07 MPa and 9.90 MPa may result in an unreliable measurement of velocity perturbations, given the relatively low waveform similarity between these two cases in the coda. We will revisit this topic in Section 4.2.4.3.



(a) Signals at Loading Step 0 (7.07 MPa), 1 (7.22 MPa), 2 (7.36 MPa), 3 (7.50 MPa), and 4 (7.64 MPa).



(b) Signals at Loading Step 0 (7.07 MPa), 5 (7.78 MPa), 10 (8.49 MPa), 15 (9.20 MPa), and 20 (9.90 MPa).

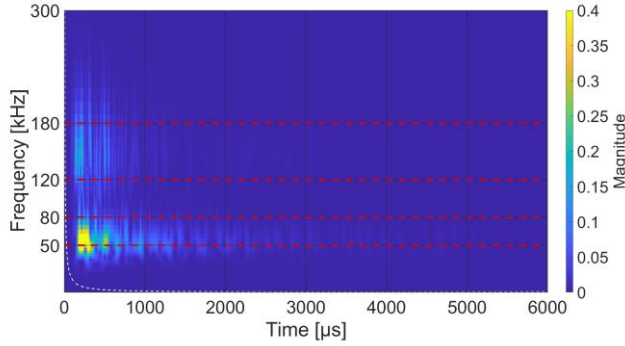
Figure 4.4 Received signals in the time domain. The time window from 70 μs to 170 μs contains the direct wave and the first scattered arrivals, whereas the time window from 1070 μs to 1170 μs contains multiply scattered waves.

In this dissertation, the time-frequency analysis is realized using the CWT (i.e., a filter bank introduced in Section 4.2.2.2). The centre frequencies of the filter bank require the input of the frequency range and the number of voices per octave, a parameter related to the sampling density of the frequency scale. The frequency range is selected from 50 Hz to the Nyquist frequency, 500 kHz, and the number of voices per octave is 10.

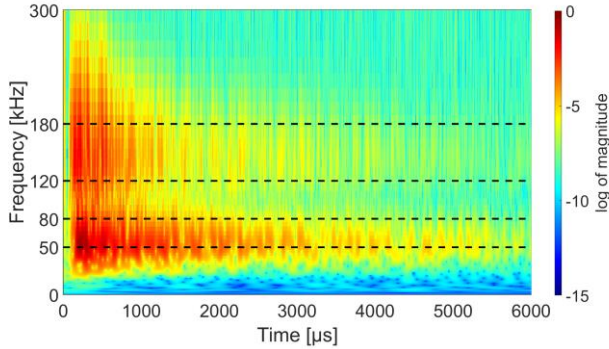
Figure 4.5 shows the time-frequency spectra of the signals at Step 150 (5.66 MPa) and Step 110 (11.32 MPa), respectively. These selected load steps represent the lowest and highest compressive stress levels in this test, respectively. For each load step, there are two time-frequency spectra representing linear and log magnitudes, respectively. The log-magnitude spectra, illustrated in Figure 4.5(b) and Figure 4.5(d), facilitate the examination of wave energy in the late coda (i.e., from 4000 μs to 6000 μs), which is barely discernible in the linear-magnitude spectra in Figure 4.5(a) and Figure 4.5(c). From the

4.2 Estimation of travel time changes

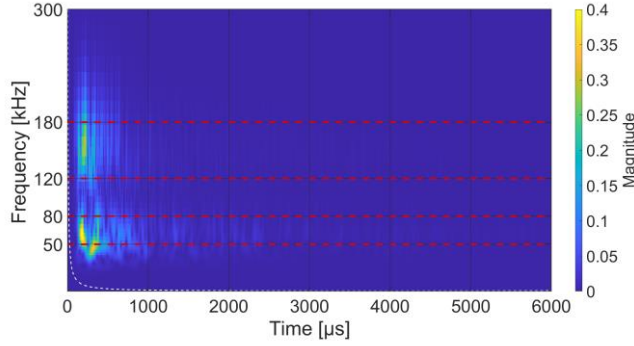
magnitude of the time-frequency spectrum, one can find that the energy concentrates in two frequency bands: one roughly from 50 kHz to 80 kHz, and the other from 120 kHz to 180 kHz. We consistently observe that the frequency characteristics of signals received by SAs fall within these two frequency bands, even across different types of concrete. This may be related to the resonant frequency of the SA, which is around 80 kHz (Kong 2015). Note that the frequency bands may vary when different sensors are used.



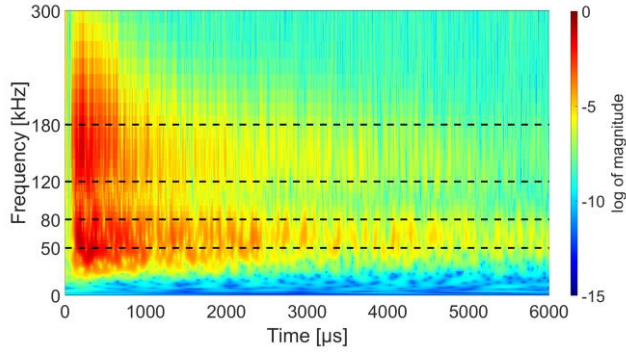
(a) 5.66 MPa (load step 150) with magnitude in the linear scale.



(b) 5.66 MPa (load step 150) with magnitude in the log scale.



(c) 11.32 MPa (load step 110) with magnitude in the linear scale.



(d) 11.32 MPa (load step 110) with magnitude in the log scale.

Figure 4.5 Time-frequency spectra of signals at load step 150 and load step 110. The energy concentrates in two frequency bands, 50-80 kHz and 120-180 kHz, highlighted using red or black dashed lines.

4.2.4.2 Choice of parameters for wave interferometry techniques

For the stretching technique, the time window length is an important parameter. Rossetto et al. (2011) suggested a criterion that time windows in coda should contain at least five periods to prevent cycle skipping and mitigate strong fluctuations of the CC . There is no strict upper limit for the length of the time window. However, it is worth considering that the travel time change obtained through the stretching technique represents an average travel time change within the time window over which the stretching technique is operated. Consequently, a longer time window may result in reduced resolution of the travel time change across the travel time scale. To be on the safe side, the time window length for the stretching technique is therefore set to 200 μs , which is 10 times the reciprocal of 50 kHz and hence a time window contains at least ten periods. The time windows start just before the first arrival, and adjacent time windows overlap by 100 μs (50% overlap) to ensure the continuity of obtained ϵ_{max} or dt/t . In Section 4.2.4.3, the reference signal is fixed as the signal at load step 0 (500 kN). In Section 4.2.4.4, relative dt/t are obtained by

4.2 Estimation of travel time changes

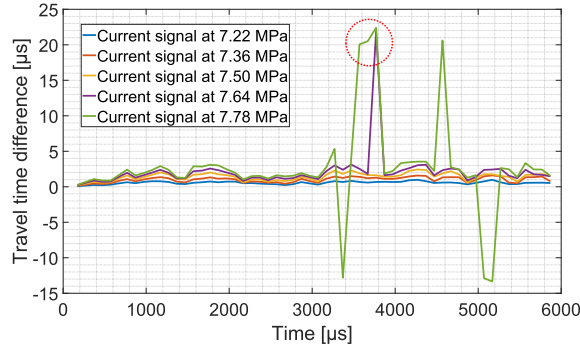
step-wise stretching (Wang, Chakraborty et al. 2020), meaning that the signal at the previous loading step is always taken as the reference. The range of ε is from -1% to 1% with a step of 0.01%. Considering the low signal-to-noise ratio (SNR) in the late coda, only the time windows before 6000 μs are used for the analysis.

As mentioned before, the WCS technique is effective only for obtaining the travel time changes at frequencies for which there is sufficient energy. Based on the time frequency analysis of the typical wave signals, only the frequency bands between 50 and 80 kHz and between 120 and 180 kHz are adopted for the WCS analysis and referred to as the low-frequency regime (50-80 kHz) and the high-frequency regime (120-180 kHz). Just as for the stretching technique, the reference signal is set to be the signal at Step 0 in Section 4.2.4.3. Relative dt/t are obtained by step-wise WCS in Section 4.2.4.4, where the reference signal is always associated with the previous loading step. The mother wavelet is the analytic Morlet wavelet. To prevent the CC from being identically one (Glaubeaud 1981), the smoothing approach as used by Torrence and Webster (1999) is adopted: a boxcar filter with a window length of three scales for scale smoothing and a Gaussian, $\exp(-t^2/(2s^2))$, for time smoothing.

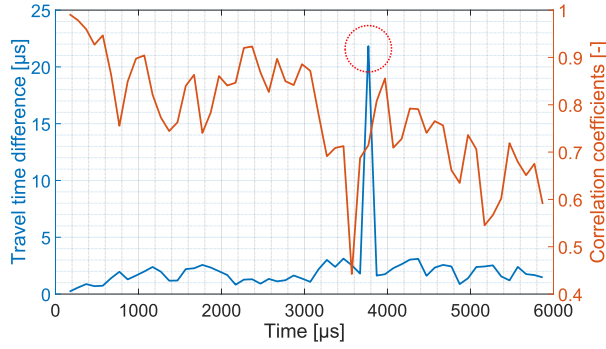
4.2.4.3 Comparison in terms of stability against cycle skipping

As mentioned in Section 2.3.2, the stability analysis of a WI technique determines whether the retrieved velocity changes are stable as a function of time. In case of low stability, anomalously large or small travel time changes can be observed. A lack of stability is due to the alignment of peaks which in reality are offset by approximately one period. This phenomenon is usually referred to as cycle skipping (Mikesell, Malcolm et al. 2015). Effectively, the assessment of a WI technique's stability therefore involves assessing its ability to mitigate cycle skipping.

To ensure the occurrence of cycle skipping (for assessment purposes), the reference signal is set to be the signal at Step 0 (corresponds 7.07 MPa) for all computations in this section. The current signals are associated with loading steps 1 to 5 with magnitudes of compressive stress from 7.22 MPa to 7.78 MPa. The inferred travel time difference relative to the signal at 7.07 MPa are shown in Figure 4.6(a). It is important to emphasize that the stretching technique quantifies the relative travel time change (dt/t) between two traces. The travel time difference in Figure 4.6 is obtained by multiplying this relative travel time change with the travel time (i.e., t_c in Equation (4.1)). An anomalously high/low travel time difference, marked by the red cycle, is observed at around 3800 μs for the coda of the signal associated with the compressive stress of 7.64 MPa. Focussing on the analysis using signal obtained at 7.64 MPa, the travel time difference and CC are shown for all time windows in Figure 4.6(b). It is found that cycle skipping occurs at time window 37, which has a central time t_c of 3780 μs and is marked by a red cycle, and despite the fact that the CC in this time window has a relatively high value of around 0.7.



(a) Travel time difference as a function of travel time (i.e., t_c in Equation (4.1)).



(b) Travel time difference and CC as function of travel time (i.e., t_c in Equation (4.1)) with the current signal being the signal at 7.64 MPa.

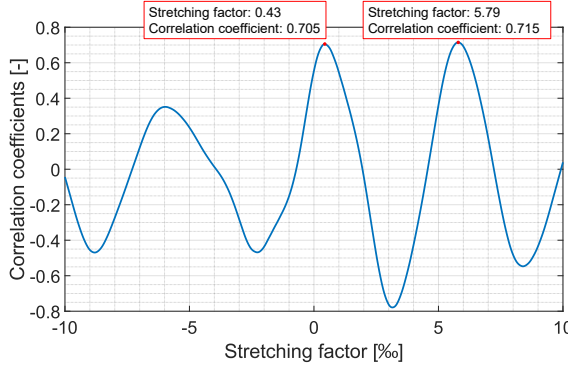
Figure 4.6 Cycle skipping when using the stretching technique. The reference signal is set to be the signal at Step 0 (corresponds to 7.07 MPa). Cycle skipping is indicated by red cycles. The stresses shown in this figure are compressive stresses.

As mentioned in Section 4.2.2.1, the stretching technique selects the stretching factor ε associated with the highest correlation coefficient. Focussing on time window 37 ($t_c=3780 \mu s$) of the signal recorded at 7.64 MPa, we investigate how the correlation coefficient varies for different stretching factors. Figure 4.7(a) therefore displays the CC as a function of the employed stretching factor ε . Two almost equally high peaks can be observed, both with a relatively high correlation coefficient. The second peak is associated with a stretching factor of 5.79%. Since the CC attains its maximum for this value of ε , the stretching factor corresponding to this peak is selected. Plotting the stretched reference signals using the stretching factors associated with the two peaks, 0.43% and 5.79%, together with the current signal, it can be observed that the time difference between the two stretched signals is indeed one cycle (see the yellow and red dotted cycles shown in Figure 4.7(b)). Here ‘one cycle’ corresponds to a time shift just below $20 \mu s$, which corresponds to a frequency just over 50 kHz. Obviously, the true ε is not expected to be 5.79% since this

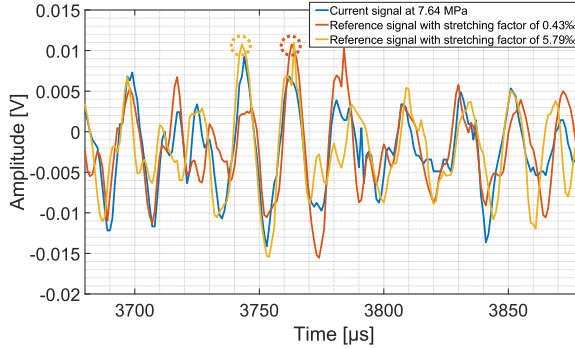
4.2 Estimation of travel time changes

value is significantly higher than the ε inferred for adjacent time windows (see Figure 4.6(b)).

The main reason for the occurrence of cycle skipping is the decrease in SNR owing to the signal's amplitude attenuation. The strong noise masks the similarity between reference and current signals. Furthermore, because higher frequencies attenuate faster, the bandwidth becomes narrower with increasing travel time, further exacerbating cycle skipping (Mikesell, Malcolm et al. 2015). In conclusion, the low SNR is the main trigger of cycle skipping while employing the stretching technique in this case. A similar conclusion can be found by Mikesell et al. (2015).



(a) Variation of the correlation coefficients with stretching factors.

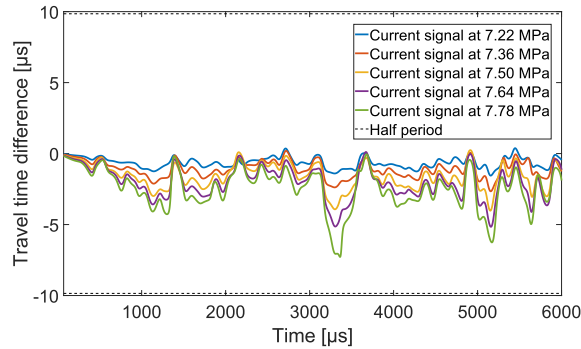


(b) Current signal and stretched signals with stretching factors highlighted in Figure 4.7(a).

Figure 4.7 Stretching factors and stretched signals in the time window 37 ($t_c=3780 \mu s$) when using the signal at 7.64 MPa as the current signal. The stresses shown in this figure are compressive stresses.

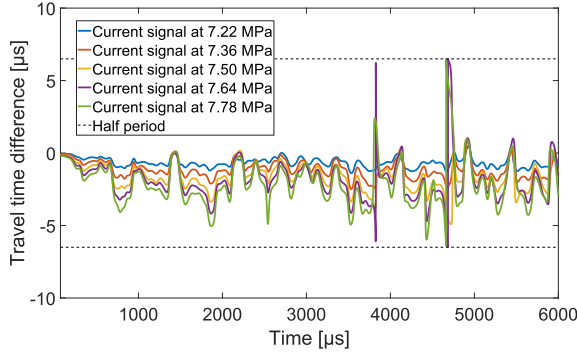
The cause of cycle skipping while employing the WCS technique differs from that of the stretching technique. The WCS technique is based on the phase spectrum in the wavelet domain, which implies that this technique can only measure phase changes from $-\pi$ to $+\pi$. Consequently, travel time differences corresponding to the phase difference spectrum

range from a positive half period to a negative half period. Inferred travel time differences beyond this range will ‘jump’ from the boundary one period to another, resulting in anomalously large travel time differences. Phase-based travel time differences are shown in Figure 4.8 for four specific frequencies. The black dashed lines in Figure 4.8 represent the travel time difference at positive and negative half periods for the considered frequency (equal to half the reciprocal of the frequency). As shown in Figure 4.8(a), no travel time difference jumping from $-\pi$ to $+\pi$ (or vice versa) is observed, which suggests that cycle skipping does not occur at 51 kHz. This is due to the fact that the 51 kHz is the lowest frequency depicted in Figure 4.8, and signals with this frequency have the longest period. Consequently, signals with this frequency component are able to accommodate a larger absolute time shift. However, for the higher frequencies, 77 kHz, 125 kHz and 177 kHz, one can observe that the travel time differences jump from $-\pi$ to $+\pi$ (or vice versa) in the coda part at some travel times, which is typical for cycle skipping. For the wave with a frequency of 177 kHz, cycle skipping is observed when the signal at 7.50 MPa is the current signal, whereas cycle skipping only occurs (first) when signal at 7.64 MPa while employing the stretching technique, see Figure 4.6(a). However, for the wave with a frequency of 77 kHz, cycle skipping is observed for current signals at the same load step (7.64 MPa) as the stretching technique. According to Figure 4.8, the occurrence of cycle skipping in the WCS technique depends on the magnitude of the travel time difference and the wave frequency.

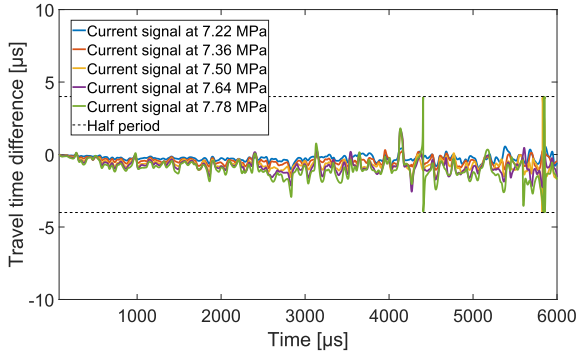


(a) 51 kHz.

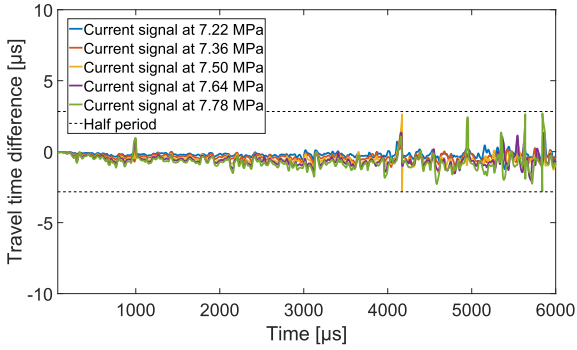
4.2 Estimation of travel time changes



(b) 77 kHz.



(c) 125 kHz.



(d) 177 kHz.

Figure 4.8 Travel time difference of different frequency components as a function of travel time retrieved using the WCS technique. The stresses shown in this figure are compressive stresses.

Based on the results presented in this section, it is evident that the triggers of cycle skipping in the stretching technique and the WCS technique differ. When employing the stretching technique, cycle skipping becomes apparent in time windows with low SNR.

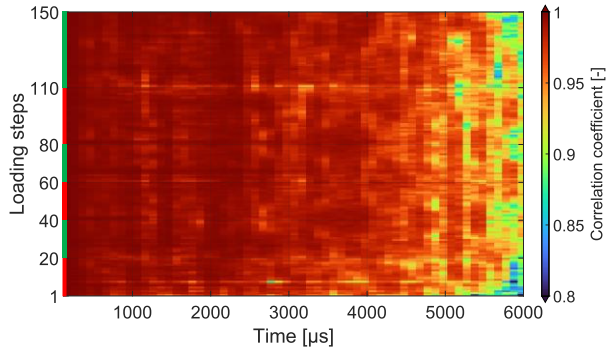
Conversely, using the WCS technique, the occurrence of cycle skipping depends on the wave frequency and the magnitude of the travel time difference because of operating in the wavelet domain. This contrasting trigger mechanism for cycle skipping complicates the determination of which technique provides better stability. When examining the performance of these techniques specifically for wave frequencies ranging from 50 kHz to 80 kHz in this particular case, their stability against cycle skipping is found to be comparable. It should be noticed that the above conclusion is drawn based solely on this experiment and one should be careful generalizing these to other materials and/or significantly higher stress levels.

4.2.4.4 Comparison in terms of retrieved velocity changes

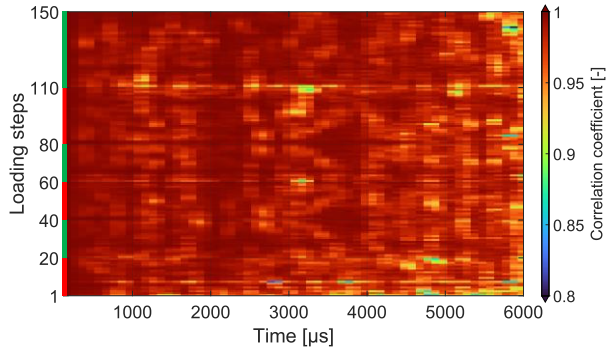
In the previous section, we compared the two techniques in terms of their stability against cycle skipping. Here, we will assess their consistency in retrieving velocity changes within the medium. Consequently, the term ‘velocity change’ will be used throughout this section. To ensure the reliability of the relative velocity change ($d\nu/\nu$), which refers to the travel time changes between two consecutive loading steps, we will first evaluate the *CC* values. Next, the accumulated velocity changes obtained using the two techniques, calculated by summing the relative velocity changes across different load steps, are evaluated and compared to evaluate their consistency in retrieving velocity changes.

The *CC* from the stretching technique is calculated for a specific time window, whereas the *CC* from the WCS technique is associated with a specific travel time and frequency. In order to compare the *CC* and $d\nu/\nu$ obtained from the two techniques as a function of travel time, we use the same time windows as those adopted in the stretching technique. We calculate the mean WCS technique-based relative $d\nu/\nu$ and *CC* by averaging all $d\nu/\nu$ and *CC* values corresponding to travel times within the selected time window. Along the frequency scale, the mean WCS technique-based relative $d\nu/\nu$ and *CC* are calculated by averaging all $d\nu/\nu$ and *CC* values over discrete frequencies within frequency bands 50-80 kHz (low-frequency regime) and 120-180 kHz (high-frequency regime). The averaging across frequency scales is deemed reasonable because the CWT filter bank is based on multiple Gaussian filters in the frequency domain, as discussed in Section 4.2.2.2. The *CC* retrieved using the stretching technique and the WCS technique are shown in Figure 4.9. The *CC* values are generally higher than 0.8 for both techniques, surpassing the threshold 0.7 recommended by Clauss et al. (2020), below which the calculated $d\nu/\nu$ is deemed unreliable. This indicates that the relative $d\nu/\nu$ obtained from both techniques are reliable. The relatively low *CC* values in the coda of the high-frequency regime shown in Figure 4.9(c) are mainly attributed to the attenuation imposed low SNRs of high-frequency waves.

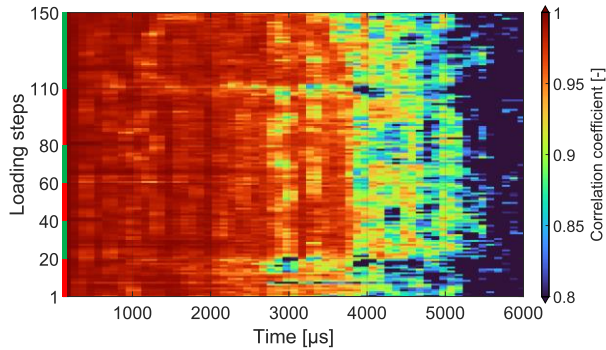
4.2 Estimation of travel time changes



(a) CC obtained using the stretching technique.



(b) CC within the frequency band of 50-80 kHz obtained using the WCS technique.



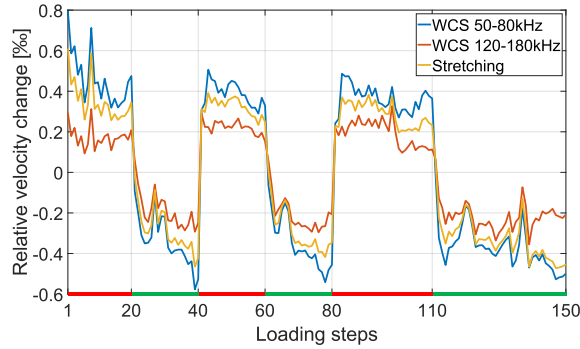
(c) CC within the frequency band of 120-180 kHz obtained using the WCS technique.

Figure 4.9 CC at travel time and loading steps obtained using the stretching technique and the WCS technique (indicated in red on the vertical axis are the loading stages, and indicated in green the unloading stages; note that the CC from the WCS technique represents an average over the discrete frequencies within the frequency band).

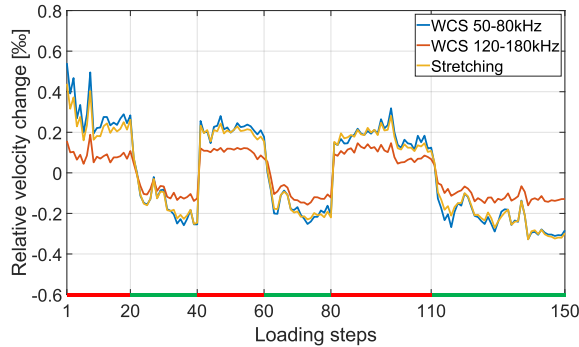
To compare the relative $d\nu/\nu$ retrieved using the stretching technique and the WCS technique, the whole signal is further split into a series of non-overlapping time segments with

a length of around 1 ms (the first time segment is from the first arrival to 1 ms). For the stretching technique and the low-frequency regime WCS, the mean relative dv/v of time windows with CC higher than 0.9 is calculated in each time segment. For the high-frequency regime WCS, the relative dv/v is calculated in each time segment by averaging the relative dv/v of time windows with CC higher than 0.8.

The relative dv/v between signals of the neighbouring load steps during the whole loading program are plotted in Figure 4.10. Here, the three lines are retrieved by stretching technique and WCS technique of the two different frequency ranges in the first four time segments. The relative dv/v is frequency dependent, manifested by higher magnitudes of relative dv/v retrieved from waves in the low-frequency regime compared to those from the high-frequency regime. Additionally, the stretching technique-based relative dv/v , operating in broadband, gives intermediate values in the first time segment and is nearly equal to the dv/v retrieved from the low-frequency regime in the later time segments. This can be explained by the fact that few high-frequency signals remain at greater travel time after 1 ms, as shown in Figure 4.5(b) and Figure 4.5(d).

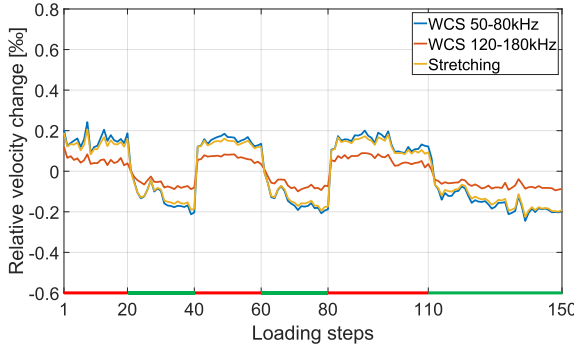


(a) Relative dv/v retrieved from the signal in the first time segment (first arrival-1 ms).



(b) Relative dv/v retrieved from the signal in the second time segment (1 ms-2 ms).

4.2 Estimation of travel time changes



(c) Relative dv/v retrieved from the signal in the third time segment (2 ms-3 ms).

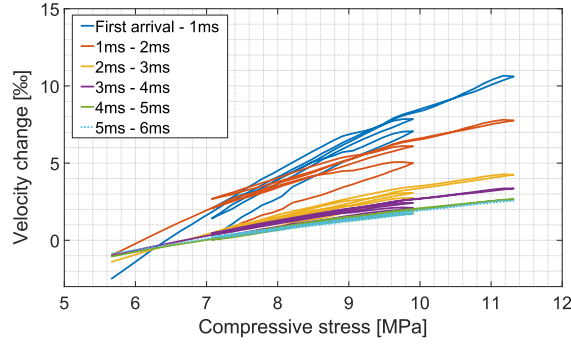


(d) Relative dv/v retrieved from the signal in the fourth time segment (3 ms-4 ms).

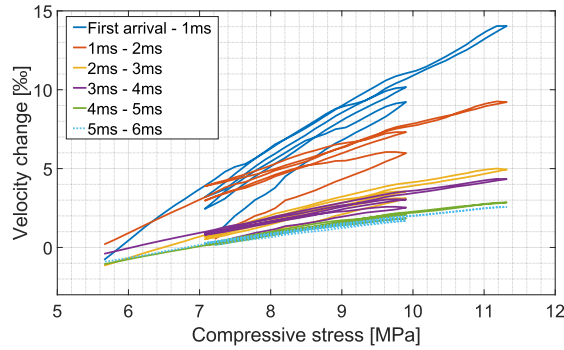
Figure 4.10 Relative dv/v retrieved from the signal in different time segments as a function of loading steps (indicated in red on the horizontal axis are the loading stages, and indicated in green the unloading stages; note that the relative dv/v from the WCS technique represents an average over the discrete frequencies within the frequency band).

The vertical axis in Figure 4.10 represents the relative dv/v , where the signal associated with the previous loading step is used as the reference. By summing these relative dv/v values, one can obtain the accumulated dv/v , reflecting changes relative to the initial stress at load step 0. It is important to note that this operation is only applicable when the magnitude of total velocity change is small. If there is a significant magnitude of total velocity change, we recommend using a similar approach as described in Hu et al. (2021), in which the accumulated velocity change is acquired by multiplying relative velocities. Figure 4.11 displays trajectories of the accumulated dv/v retrieved using the stretching technique and the WCS technique. The accumulated dv/v retrieved from the stretching technique, the low-frequency regime WCS, and the high-frequency regime WCS all demonstrate a linear relationship with increasing compressive stress. Same as the observation in Figure 4.10, the stretching technique-based velocity changes give intermediate values in the first

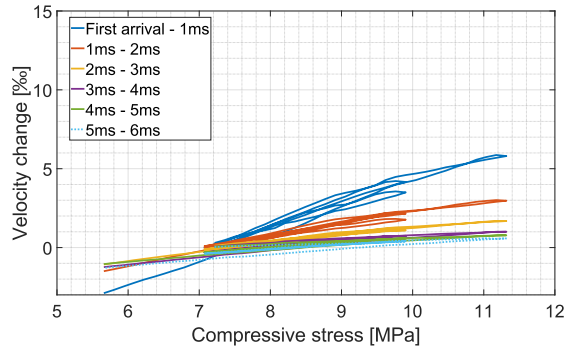
time segment and is nearly equal to those retrieved from the low-frequency regime in the later time segments.



(a) Accumulated dv/v obtained using the stretching technique.



(b) Accumulated dv/v within the frequency band of 50-80 kHz obtained using the WCS technique.



(c) Accumulated dv/v within the frequency band of 120-180 kHz obtained using the WCS technique.

Figure 4.11 Relationship between accumulated dv/v vs. compressive stress in different time segments.

4.2 Estimation of travel time changes

As mentioned earlier, the stretching technique determines the stretching factor, ε_{\max} , that maximizes the CC . Equation (4.4) reveals that both the amplitude spectrum and phase spectrum influence $|CC(t_c, T, \varepsilon)|$ and ε_{\max} . This equation also demonstrates that the relative dv/v retrieved from the stretching technique is weighted by the wave energy. Therefore, it is possible to approximate the stretching technique-based result using the WCS technique-based result by incorporating wave energy information: using the relative dv/v retrieved from the low-frequency regime WCS and high-frequency regime WCS, the estimated dv/v can be calculated using the following equation:

$$\left(\frac{dv}{v}\right)_{\text{estimated}} = \frac{E_{\text{low-frequency}}}{E_{\text{low-frequency}} + E_{\text{high-frequency}}} \left(\frac{dv}{v}\right)_{\text{low-frequency}} + \frac{E_{\text{high-frequency}}}{E_{\text{low-frequency}} + E_{\text{high-frequency}}} \left(\frac{dv}{v}\right)_{\text{high-frequency}}, \quad (4.7)$$

where $(dv/v)_{\text{estimated}}$, $(dv/v)_{\text{low-frequency}}$ and $(dv/v)_{\text{high-frequency}}$ represent the estimated relative dv/v , the relative dv/v retrieved from the low-frequency regime WCS, and the relative dv/v retrieved from the high-frequency regime WCS, respectively. The $E_{\text{low-frequency}}$ and $E_{\text{high-frequency}}$ denote the wave energies (mean squared value of amplitude) of frequency bands in the low-frequency and high-frequency regimes. These energies can be directly obtained from the wavelet time-frequency spectrum. Considering that the stress condition can slightly alter the energies in frequency components of the signal, as depicted in Figure 4.5(b) and Figure 4.5(d), the energy of the current signal is always utilized as the weighting factor. As the intermediate value demonstrated by the stretching technique is more apparent in the first-time segment, this segment is employed to evaluate the estimated relative dv/v . However, the conclusion remains applicable to other time segments as well.

Figure 4.12 presents a comparison between the estimated accumulated velocity change and those retrieved from the stretching and WCS techniques in the first time segment. As shown in this figure, the slope of the estimated result is in closer agreement with the result obtained using the stretching technique. The discrepancy between the stretching technique-based result and the constructed result based on the WCS technique can be attributed to the limited frequency components utilized in Equation (4.7), only 50-80kHz and 120-180kHz. Considering the challenge of including all frequency components due to the potential contamination of travel time changes in frequency bands with low energy (Mao, Mordret et al. 2020, Yuan, Bryan et al. 2021), it is not feasible to incorporate every frequency in the analysis. Nevertheless, the proximity between the estimated result and the result retrieved from the stretching technique indicates that the stretching technique-based velocity change can be approximated using the velocity changes retrieved from the WCS technique.

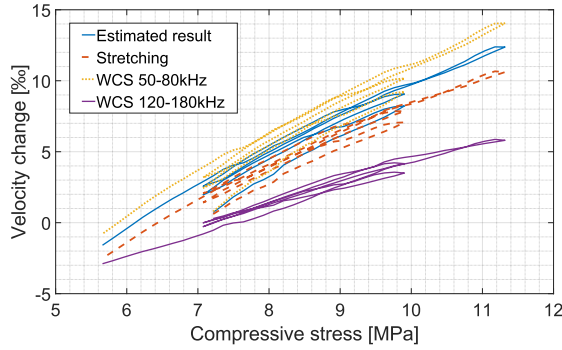
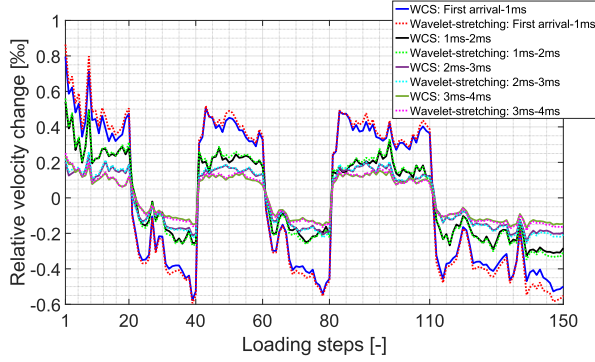


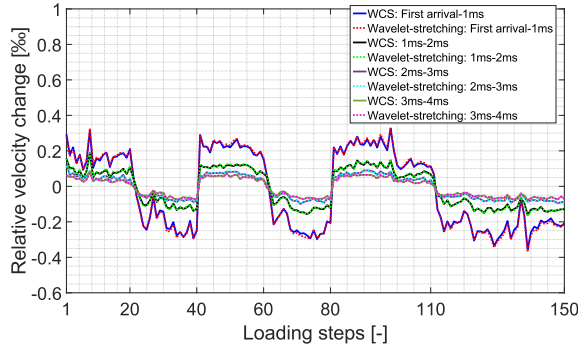
Figure 4.12 Comparison between the estimated accumulated velocity change and those retrieved utilizing the stretching and WCS techniques in the first time segment.

To ensure consistency in the velocity changes retrieved using the stretching technique and the WCS technique, we conduct an additional comparison. In this comparison, the stretching technique is applied to the bandpassed time-series after the CWT, also referred to as the wavelet-stretching technique (Yuan, Bryan et al. 2021). The comparison of velocity changes retrieved using the WCS technique and the wavelet-stretching technique is shown in Figure 4.13. This comparison encompasses two frequency bands previously mentioned: 50-80 kHz and 120-180 kHz. As depicted in Figure 4.13, the results obtained using both techniques demonstrate a high degree of consistency. Therefore, based on findings presented in Figure 4.12 and Figure 4.13, one can conclude that the velocity changes retrieved from the WCS technique and the stretching technique are consistent.

4.2 Estimation of travel time changes



(a) Low-frequency regime: 50-80 kHz.



(b) High-frequency regime: 120-180 kHz.

Figure 4.13 Comparison between the relative velocity changes retrieved utilizing the wavelet-stretching and WCS techniques in different time segments.

4.2.5 Application of the stretching and WCS techniques in subsequent chapters

In the previous sections of Section 4.2, we compared two WI techniques: the stretching technique and the WCS technique. These techniques will be applied in Chapter 5 and 7 to retrieve stress-induced velocity changes in the medium. Based on the comparisons in Section 4.2, the following guidelines are proposed for their use in this dissertation:

- The stretching technique will be used to retrieve velocity changes in the ballistic wave regime, while the WCS technique will be applied to the coda wave regime.
- The time window for the stretching technique should be kept short to ensure it captures a pure wave mode while still containing at least one full cycle of the signal.
- The frequency range for the WCS technique should be 50-80 kHz, where wave energy is highest and persists in the coda.

- The load step should be small enough to maintain stability. In the results shown in Figure 4.8, this value should be smaller than 0.57 MPa. Therefore, in Chapter 7, the load step is set to 0.28 MPa.

4.3 Estimation of diffusive properties

In Section 4.2, we have discussed techniques that can be used to retrieve velocity changes in concrete from bulk waves. However, travel time changes in the coda are resulted from a combination of acoustoelasticity and scattering process. Therefore, understanding the energy transport properties of bulk waves during the scattering process in concrete can greatly aid in interpreting the travel time changes in the coda.

This section will introduce techniques that can be used to estimate energy transport properties of bulk waves in concrete. As mentioned in Section 3.3.1, the energy transport within all regimes can be described by the radiative transfer equation (RTE) (Chandrasekhar 2013). However, the complex nature of RTE presents challenges for its practical application in engineering. As an alternative, the diffusion equation (Watson, Fleury et al. 1987) is commonly used when the energy transport occurs in a diffusive regime (Yoo, Liu et al. 1990, Zhang, Jones et al. 1999, Elaloufi, Carminati et al. 2002). Such a simple scalar equation has been successfully and extensively utilized in describing the energy transport of various phenomena, including electromagnetic waves (Kop, deVries et al. 1997), acoustic waves (Tallon, Brunet et al. 2017) and elastic waves (Jia 2004). This section will delve into the techniques that estimate diffusive properties of concrete medium, specifically, diffusivity and dissipation.

Diffusive properties are generally extracted by fitting the wave energy profile with the diffusion equation in one-dimensional (Yim, An et al. 2016, Ramaniraka, Rakotonarivo et al. 2022), two-dimensional (Becker, Jacobs et al. 2003, Quiviger, Payan et al. 2012), or three-dimensional forms (Ahn, Shin et al. 2019, Jiang, Zhan et al. 2019, Tinoco and Pinto 2021, Ahn, Shin et al. 2022). However, it is crucial to acknowledge that the analytical solution of the diffusion equation is derived for an infinite medium. Although concrete may approximate an infinite medium in certain scenarios with sufficiently distant boundaries (Anugonda, Wiehn et al. 2001, Schubert and Koehler 2004), the direct application of the diffusion equation for infinite media to concrete structures is generally impractical due to the non-negligible energy reflection from boundaries. To address this limitation, improvements to the diffusion equation are made to estimate diffusive properties by incorporating the effect of boundary conditions, which will be elaborated further in this section.

In this section, we will start with the knowledge gap in Section 4.3.1. Then, the theoretical background of the diffusion equation will be introduced in Section 4.3.2. The theoretical background will commence with a presentation of the diffusion equation in infinite media,

4.3 Estimation of diffusive properties

followed by a more precise estimation tailored to consider boundaries. To explore the impact of boundaries on acquired diffusive properties, experimental investigations are conducted on a set of concrete specimens. Section 4.3.3 provides details regarding the specimens and experiments. The subsequent analysis of the experimental results is presented in Section 4.3.4 and 4.3.5. Procedures for fitting diffusive properties in later chapters will be summarized in Section 4.3.6.

4.3.1 Knowledge gap in characterizing diffusive properties in concrete structures with boundaries

Diffusivity and dissipation are transport properties easily measured through experiments, with diffusivity also holding potential for assessing the scattering property of concrete. However, the analytical solution of the diffusion equation is proposed for an infinite medium, posing a challenge for direct application to most concrete structures with boundaries. In such cases, the influence of boundaries on diffusive properties must be considered.

In the presence of complex boundary conditions, solving the diffusion equation for the geometry of system becomes a problem within the field of applied mathematics (Crank 1979). Section 3.4 introduced examples of solving the diffusion equation for two-dimensional rectangular and three-dimensional cuboid domains. However, the increased complexity in the expression of the diffusion equation makes nonlinear curve fitting more intricate for obtaining diffusive properties, rendering it less robust compared to the original diffusion equation in infinite media (Deroo, Kim et al. 2010). Hence, an improved diffusion equation is needed to incorporate boundaries without significantly increasing its complexity.

In situations with planar boundaries, the solution to the diffusion equation can be approximated by superimposing energy from the real source with additional energy reflected from the planar boundary. This method, where reflected energy is treated as originating from the image source (Weaver and Sachse 1995, Rossetto, Margerin et al. 2011), is known as the image source method (Allen and Berkley 1979). By using this method, reflected energy from planar boundaries can be incorporated by adding additional terms to the diffusion equation. However, it is important to note that the image source method is limited to geometries formed by planar boundaries (Habets 2006). In the case of wave propagation in cylindrical samples, this method is not applicable. To acquire diffusive properties in samples with such geometries, the diffusion equation needs to be further adjusted to estimate diffusive properties of bulk waves.

4.3.2 Theoretical background of diffusion equation

4.3.2.1 Diffusion equation in an infinite medium

The governing equation for diffusion is written in the following form (Weaver and Sachse 1995, Weaver 1998):

$$\frac{\partial E(x_i, t)}{\partial t} = D \nabla^2 E(x_i, t) - \alpha E(x_i, t) + E_0, \quad (4.8)$$

where t represents the time and x_i are the spatial coordinates. In a three-dimensional Cartesian coordinate system, i can be 1, 2 and 3. $E(x_i, t)$ is the transport energy at location x_i and time t , and E_0 represents the deposited impulse energy at initial location at time $t = 0$ (Weaver and Sachse 1995). The parameters D and α represent the diffusivity and dissipation, respectively, that describe the characteristics of energy transport.

The diffusivity quantifies how quickly the energy spreads within the medium (Planès and Larose 2013). In this context, the diffusivity can be viewed as a measure similar to the ‘spreading velocity’ of the diffusion halo (Ramaniraka, Rakotonarivo et al. 2022). It is noteworthy that the pure diffusion process, in the absence of dissipation, generally follows the energy conservation (Anugonda, Wiehn et al. 2001). The mechanism of dissipation in concrete is likely a combination of viscous dissipation and internal friction (Brunet, Jia et al. 2008). Unlike the energy-conserving nature of the pure diffusion process, the dissipation process does not follow the energy conservation.

In an infinite n -dimensional medium, the solution of Equation (4.8) is given as (Weaver and Sachse 1995):

$$E(r, t) = \frac{E_0}{(4\pi Dt)^{\frac{n}{2}}} e^{\frac{-r^2}{4Dt} - \alpha t}, \quad (4.9)$$

where r represents the distance between source and receiver. The logarithmic form of Equation (4.9) is commonly employed in fitting the diffusion equation:

$$\ln(E(r, t)) = \ln(E_0) - \frac{n}{2} \ln(4\pi Dt) - \frac{r^2}{4Dt} - \alpha t. \quad (4.10)$$

Taking the partial derivative of Equation (4.10) with respect to t gives:

$$\frac{\partial \ln(E(r, t))}{\partial t} = -\frac{n}{2t} + \frac{r^2}{4Dt^2} - \alpha. \quad (4.11)$$

As indicated in Equation (4.11), when the time t is very small, the slope of the logarithm energy against time is positive and dominated by the term $r^2/4Dt^2$. When t is large, the slope of the energy against time is negative and dominated by α . One can also estimate the arrival time of the maximum energy from Equation (4.11) by setting the equation equal to zero and considering the fact that this arrival time must be positive:

$$t_{\text{maximum energy}} = \frac{-\frac{n}{2} + \sqrt{\frac{n^2}{4} + \frac{\alpha r^2}{D}}}{2\alpha}. \quad (4.12)$$

4.3 Estimation of diffusive properties

When assuming that no dissipation and the initial deposited energy is 1, Equation (4.9) becomes:

$$E(r, t) = \frac{1}{(4\pi Dt)^{\frac{n}{2}}} e^{\frac{-r^2}{4Dt}} . \quad (4.13)$$

Owing to the energy conservation inherent in the pure diffusion process, the integral of Equation (4.13) over space represents the total energy of the wave field, which is equal to the initial deposited energy. However, both Equation (4.9) and (4.13) are derived under the assumption of an infinite medium, which may not be realistic when applying them to concrete specimens with multiple boundaries.

4.3.2.2 Diffusion equation in a medium with multiple planar boundaries

In the presence of complicated boundary conditions, the diffusion equation needs to be solved for the geometry of the system (Crank 1979), and this task presents a problem within the field of applied mathematics (Rossetto, Margerin et al. 2011). In situations where the boundaries of a concrete structural element are predominantly planar, the solution to the diffusion equation can be approximated by superimposing the energy from the real source with the additional energy reflected from the planar boundary. The reflected energy can be considered as originating from the image source (Morse and Feshbach 1954, Weaver and Sachse 1995, Rossetto, Margerin et al. 2011), as illustrated in Figure 4.14. It is essential to underscore that the image source method is constrained to geometries formed by planar boundaries (Habets 2006).

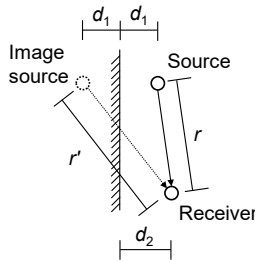


Figure 4.14 Schematic representation of energy superposition in the medium with a planar boundary.

Rossetto et al. (2011) proposed the following equation to account for the energy contribution from an image source:

$$E_{\text{total}}(r, r', t) = a [E(r, t) + bE(r', t)] , \quad (4.14)$$

where r' represents the distance between image source and receiver, and b is a coefficient that is related to the nature of the boundary condition. If the boundary is absorbing, $b=-1$

and if it is fully reflecting, $b=1$. The normalization coefficient a is defined as (Rossetto, Margerin et al. 2011):

$$a^{-1} = \frac{1+b}{2} + \frac{1-b}{2} \operatorname{erf}\left(\frac{d_1}{\sqrt{4Dt}}\right), \quad (4.15)$$

where d_1 is the distance between the source to the boundary, and $\operatorname{erf}(\cdot)$ denotes the error function. Considering that the acoustic impedance of concrete is around 20000 times higher than that of air (Ahn, Shin et al. 2022), the transmitted energy from concrete to the air is in the order of 10^{-5} , which is significantly smaller than the reflected energy. Therefore, the concrete-air boundary can be approximated as the fully reflecting boundary, and b in this case is set to be 1. Equation (4.14) can be simplified into:

$$E_{\text{total}}(r, r', t) = E(r, t) + E(r', t). \quad (4.16)$$

After substituting Equation (4.9) into Equation (4.16), one can get the approximate expression of diffusion equation in a medium with a single planar boundary:

$$E_{\text{total}}(r, r', t) = \frac{E_0}{(4\pi Dt)^{\frac{n}{2}}} e^{\frac{-r^2}{4Dt} - at} \left(1 + e^{\frac{-(r')^2 - r^2}{4Dt}} \right). \quad (4.17)$$

As shown in Equation (4.17), the contribution of an image source to the energy produced by the real source is calculated as $\exp\{-(r')^2 - r^2\}/(4Dt)$ multiplied by the energy produced by the real source. In cases with multiple planar boundaries, the expression becomes:

$$E_{\text{total}}(r, r', t) = \frac{E_0}{(4\pi Dt)^{\frac{n}{2}}} e^{\frac{-r^2}{4Dt} - at} \left(1 + \sum_{j=1}^N e^{\frac{-(r'_j)^2 - r^2}{4Dt}} \right), \quad (4.18)$$

where N represents the number of image sources. The logarithmic form of Equation (4.18) is commonly employed in fitting the diffusion equation:

$$\ln(E_{\text{total}}(r, r', t)) = \ln(E_0) - \frac{n}{2} \ln(4\pi Dt) - \frac{r^2}{4Dt} - at + \ln \left(1 + \sum_{j=1}^N e^{\frac{-(r'_j)^2 - r^2}{4Dt}} \right). \quad (4.19)$$

4.3.2.3 Diffusion equation in a cylindrical medium

As pointed out in Section 4.3.2.2, the conventional image source method is limited to geometries defined by planar boundaries (Habets 2006). In the case of a cylindrical member as depicted in Figure 4.15 hence the method for planar boundaries becomes inapplicable. Therefore, a new approach is proposed to estimate diffusive properties of bulk

4.3 Estimation of diffusive properties

waves in cylindrical members. This approach is further employed in Chapter 7 to understand the evolution of travel time changes over time.

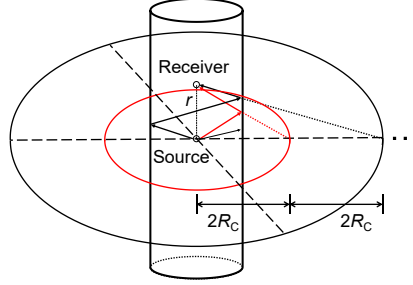


Figure 4.15 Schematic representation of energy reflections and image sources in the cylindrical member. The red and black paths indicate primary and secondary reflections, respectively; circles with the same colours indicate the radii of the corresponding image sources.

To simplify the estimation process, we consider the situation that both the source and receiver are situated along the central axis of an infinitely long cylinder. The diameter of the cylinder is denoted as $2R_C$, and the separation between the source and receiver is represented by the variable r , as illustrated in Figure 4.15. The circular surface, which is a concrete-air boundary, can be approximated as the fully reflecting boundary as discussed in Section 4.3.2.2. The travel distance from the source to the receiver, considering primary boundary reflection (red arrow lines), remains a constant value of $[r^2 + (2R_C)^2]^{1/2}$. It is important to emphasize that the circular boundary causes the reflected energy to converge at a specific point—the location of the receiver. This converged energy is equivalent to the total energy produced by the sources located on the circle centred at the real source with a radius of $2R_C$, shown as the red circle in Figure 4.15. With this consideration in mind, the reflected energy, denoted as $E(r', t)$, can be calculated by integrating along the circle with a radius of $2R_C$ in the polar coordinate system:

$$\begin{aligned} E(r', t) &= \int_C E(r', t) dr \\ &= \int_0^{2\pi} E(r', t) 2R_C d\theta \\ &= 2\pi(2R_C) \frac{E_0}{(4\pi Dt)^{\frac{3}{2}}} e^{\frac{-(r')^2}{4Dt} - at}, \end{aligned} \quad (4.20)$$

where C denotes the curve of integration, and r' represents the distance between image sources and receiver.

The fundamental assumption in this context is the absence of energy leakage at the boundary. The primary reflected energy in Figure 4.15 (red circle) can be calculated through:

$$E\left(\sqrt{r^2 + (2R_C)^2}, t\right) = 2\pi(2R_C) \frac{E_0}{(4\pi Dt)^{\frac{3}{2}}} e^{\frac{-(r^2 + (2R_C)^2)}{4Dt} - at}. \quad (4.21)$$

In the case of secondary reflections, as depicted by the black circle in Figure 4.15, the secondary reflected energy is:

$$E\left(\sqrt{r^2 + (4R_C)^2}, t\right) = 2\pi(4R_C) \frac{E_0}{(4\pi Dt)^{\frac{3}{2}}} e^{\frac{-(r^2 + (4R_C)^2)}{4Dt} - \alpha t} \quad (4.22)$$

For the h -th reflections, the reflected energy is:

$$E\left(\sqrt{r^2 + (2hR_C)^2}, t\right) = 2\pi(2hR_C) \frac{E_0}{(4\pi Dt)^{\frac{3}{2}}} e^{\frac{-(r^2 + (2hR_C)^2)}{4Dt} - \alpha t} \quad (4.23)$$

The expression for the superposition of the main energy from the source and the energy reflected from h reflections can be expressed as:

$$E_{\text{total}} = \frac{E_0}{(4\pi Dt)^{\frac{3}{2}}} e^{\frac{-r^2}{4Dt} - \alpha t} \left[1 + 2\pi \sum_{j=1}^h (2jR_C) e^{\frac{-(2jR_C)^2}{4Dt}} \right] \quad (4.24)$$

Please note that in Equation (4.24), the parameter h approaches infinity when accounting for the infinite reflections within an infinitely long cylinder. The logarithmic representation of Equation (4.24) is as follows:

$$\ln(E_{\text{total}}) = \ln(E_0) - \frac{3}{2} \ln(4\pi Dt) - \frac{r^2}{4Dt} - \alpha t + \ln \left[1 + 2\pi \sum_{j=1}^h (2jR_C) e^{\frac{-(2jR_C)^2}{4Dt}} \right] \quad (4.25)$$

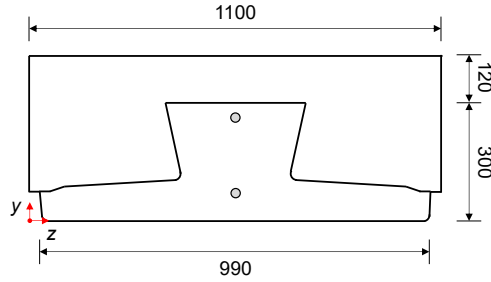
4.3.3 Specimens and experiments

In this chapter, we consider two members. The first member is a prefabricated beam. This member is employed to assess the diffusive properties of bulk waves in a medium with planar boundaries. The prefabricated beam is constructed using an environmental-friendly cementitious material called alkali-activated (geopolymer) concrete (Singh, Ishwarya et al. 2015). The beam comprises two components: prestressed beam with a height of 300 mm, along with a cast-in-situ layer atop the beam. The prestressed beam is manufactured in a prefabricated concrete plant. The cast-in-situ layer is applied 28 days after the beam casting. It is essential to note that the geopolymer concrete used in the topping layer is supplied by a commercial company and features a different composition compared to the mixture used for prestressed beams.

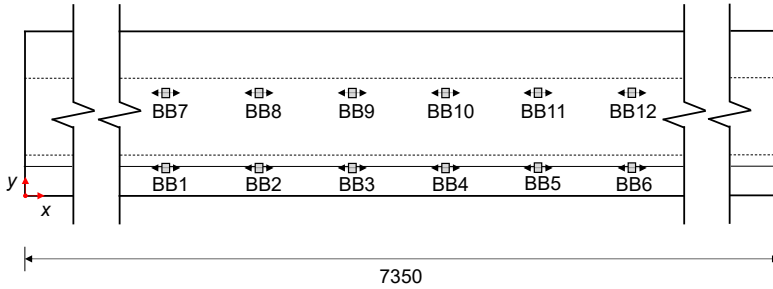
SAs are used to generate and receive elastic waves. These sensors are positioned at the mid-span in the beam. There are 12 SAs, designated from BB1 to BB12, as illustrated in Figure 4.16. Specific sensor locations in this beam can be found in Table 4.2. Measurements are taken between adjacent SAs within each row, where the SAs in the bottom row are not in direct communication with those in the top row. There are a total of ten SA pairs, and each SA pair involves two measurements, swapping the roles of transmitter and

4.3 Estimation of diffusive properties

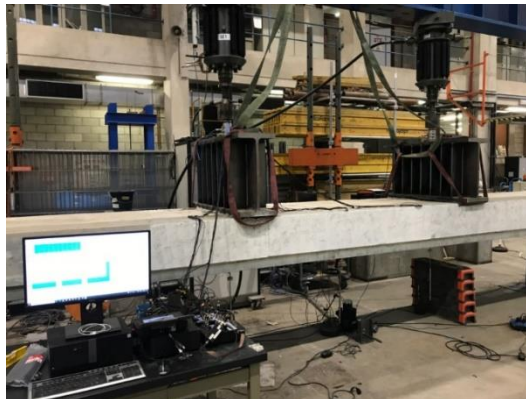
receiver between the first and second measurement. Hence, a total of 20 measurements are conducted. The SAs are situated at a minimum distance of 77 mm from the boundaries. Given that the frequency of interest is higher than 50 kHz and the Rayleigh wave velocity in concrete is approximately 2300 m/s (Shin, Yun et al. 2007), the maximum effective depth of penetration for Rayleigh waves is approximately 46 mm (Giurgiutiu, Bao et al. 2001). This depth is smaller than 77 mm, indicating that the contribution of Rayleigh wave-related energy transport in measurements can be neglected. During the data acquisition, each measurement involves gathering data by stacking five signals. The sampling rate for data acquisition is 3 MHz.



(a) Cross-sectional view.



(b) Front view.



(c) Photo of the beam.

Figure 4.16 Dimensions and photo of the geopolymer concrete and the sensor layout (unit: mm; black arrow on the SA indicates the polarization direction of the sensor).

Table 4.2 Locations of SAs relative to the coordinates in Figure 4.16(a) and Figure 4.16(b).

Sensor	BB1	BB2	BB3	BB4	BB5	BB6	BB7	BB8	BB9	BB10	BB11	BB12
x [mm]	3070	3315	3560	3815	4070	4325	3070	3315	3560	3815	4070	4325
y [mm]	77	77	77	77	77	77	277	277	277	277	277	277
z [mm]	550	550	550	550	550	550	550	550	550	550	550	550

The second category consists of a concrete cylinder, with its height and diameter, as well as the sensor layout, matching that depicted in Figure 4.1. It is worth noting that the concrete mixture compositions in these two cylinders are different. The cylinder utilized in Section 4.2 is cast on the construction site using a commercial mixture with an unknown composition, whereas the one used in this section is cast in our laboratory. The mixture composition is crucial in determining the transport properties of elastic waves, a topic that will be further explored in Chapter 6. Consequently, we use the cylinder cast in our lab to investigate the diffusive properties. Since there is only one pair of sensors embedded in the cylinder, the diffusive properties of bulk waves are investigated during the loading and unloading process. The compressive load is applied from 100 kN (1.41 MPa) to 500 kN (7.07 MPa) and then back to 200 kN (2.83 MPa) with a 20 kN (0.28 MPa) interval.

4.3.4 Diffusive properties in specimens with planar boundaries

In this section, the diffusive properties of elastic waves will be examined in the beam member. The signal energy will be firstly analysed in Section 4.3.4.1 to determine the fitting parameters. Subsequently, we will compare diffusive properties obtained with and without considering boundary reflections in Section 4.3.4.2. Additionally, the impact of the interface between the prestressed beam and the cast-in-situ layer on the diffusive properties will be investigated in Section 4.3.4.3. Finally, we will assess the reliability of the acquired diffusivity and dissipation by examining the arrival time of the maximum energy in Section 4.3.4.4.

4.3.4.1 Signal energy and parameters for fitting the diffusion equation

Since diffusivity and dissipation are functions of frequency, these properties of bulk waves should be acquired for specific frequency bands. Here, the CWT introduced in Section 4.2.2.2 is used to transform the time-domain signal into a time-frequency spectrum. Once the time-frequency spectrum is obtained, the wave energy is calculated by averaging the squared value of the amplitude within a specific time window of a certain length (Weaver and Sachse 1995). The length of the time window is selected to be at least the reciprocal of the frequency of interest to minimize energy fluctuations caused by waveform oscillations. The centre time of the time window is taken as the elapsed time t

4.3 Estimation of diffusive properties

in Equation (4.19). When selecting the beginning and ending time windows for curve fitting, two factors need to be taken into consideration:

- The beginning time window should encompass the first arrival of the wave to smoothen the wave energy, particularly to mitigate any sudden increases caused by the ballistic wave (i.e., Fig. 8 in the paper by Margerin et al. (2000)).
- The declining trend of the logarithmic energy should exhibit linearity or approximate linearity before the ending time window. This ensures the reliability of the fitted dissipation, as energy follows exponential decay when only dissipation is present.

To demonstrate how to determine the beginning and ending time windows, the logarithm of the ensemble-averaged energy at various frequency components, obtained from the signal received by BB2 with BB1 as the transducer, is plotted in Figure 4.17. Eight frequency components ranging from 50 kHz to 400 kHz, with an interval of 50 kHz, are selected. The length of time window is tentatively set as 40 μs (two times reciprocal of 50 kHz) for all frequency components, with an overlap of 20 μs between adjacent time windows. As shown in Figure 4.17, the ensemble-averaged energy of all frequency components initially experiences a rapid rise, followed by a subsequent decrease. The ascending part primarily corresponds to the spreading of energy in space, while the decreasing part is mainly attributed to dissipation. As the frequency of the wave increases, the energy decays at a faster rate. The energy of components with frequencies of 350 kHz and 400 kHz reaches the noise level at around 1100 μs . Similar decay trends can be observed in signals from other transducer-receiver pairs. Moreover, the energy in the high-frequency regime, particularly at 350 kHz and 400 kHz, exhibits significant fluctuations, making the linear decrease associated with dissipation less pronounced. However, it can still be observed that the rate of energy reduction for 350 kHz and 400 kHz slows down after approximately 800 μs . Based on these observations, the centre time of the ending time window for curve fitting is set to around 800 μs .

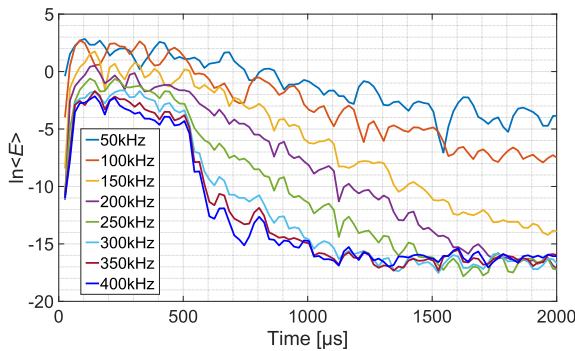


Figure 4.17 Logarithm of the ensemble-averaged energy (denoted as $\ln\langle E \rangle$) at various frequency components as a function of time received by BB2 while BB1 as the actuator.

As reported by Schubert and Koehler (2004), the arrival time of the maximum energy is dominated by diffusivity, while the subsequent decay is closely related to dissipation. However, as revealed in Figure 4.17, using time windows of equal length to capture the wave energy results in an imbalance of data points between the maximum energy arrival and energy decay portions. This disparity in data sampling may lead to an inaccurate estimation of diffusivity. To address this issue, it is crucial to ensure that the number of data points in the energy arrival and decay portions should be relatively comparable. To achieve this, the signal is divided into two parts: the initial part from 25 μs to 225 μs and the latter part from 225 μs to 725 μs . Starting from 25 μs can also help eliminate the influence of cross-talk on the obtained energy. The 1st time window, starting at 25 μs , has a length of 40 μs . The subsequent 10 time windows (2nd to 11th) also have a length of 40 μs , with each overlapping the previous window by 20 μs . The 12th time window, starting at 225 μs , has a length of 100 μs . The subsequent 10 time windows (13th to 22nd) have a length of 100 μs and overlap the previous window by 50 μs .

4.3.4.2 Influence of boundary reflections

Since the SAs are embedded at the midspan, far from the edges, there are four major types of reflections in the beam, illustrated using the SA pair BB1-BB2 in Figure 4.18. These reflections include: reflection from the bottom surface, reflection from the top surface, secondary reflections from bottom and top surfaces, and reflections from the front and back surfaces. Assuming that the diffusivity is 150 m^2/s and the maximum elapsed time is 800 μs , the maximum contributions of the reflected energy from these boundaries to the main energy, as shown in Figure 4.18, can be estimated using Equation (4.17): 95.2% from the bottom surface, 37.5% to the main energy from the top surface, 46.0% to the main energy from the secondary reflections, and 26.0% to the main energy from the front and back surfaces.

4.3 Estimation of diffusive properties

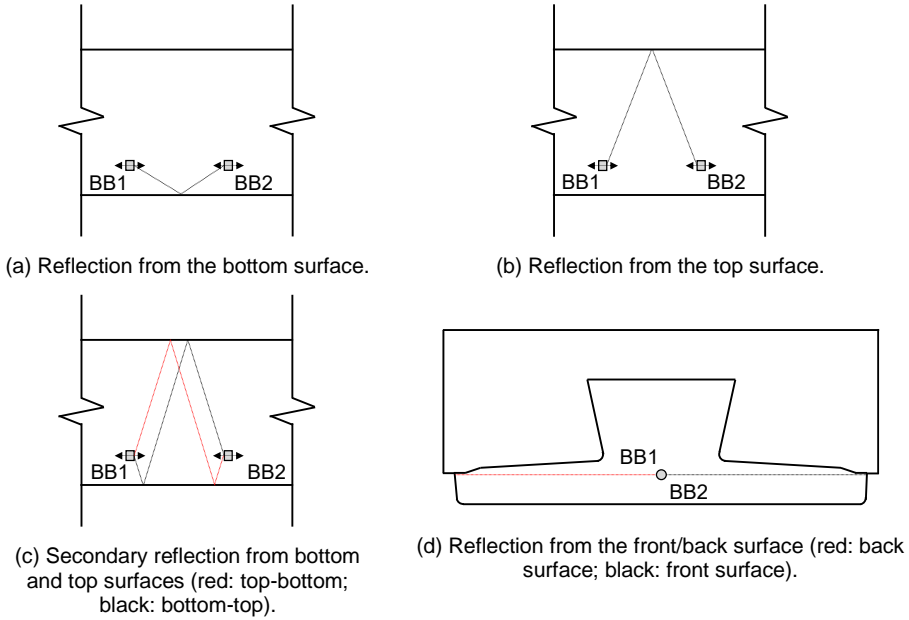


Figure 4.18 Illustration of four types of reflections from boundaries in SA pair BB1-BB2. Figure 4.19 shows a typical experimental result of the signal energy of 200 kHz component received by BB2 while BB1 serves as the actuator. The experimental result is fitted using both the diffusion equation in an infinite medium and the diffusion equation that accounts for reflected energy from top and bottom surfaces and secondary reflections. The curve fitting is evaluated using a least-square criterion to find the best-fit diffusive properties. The energy evolutions constructed using the fitted properties from diffusion equation in an infinite medium and the diffusion equation that accounts for reflected energy from top and bottom surfaces and secondary reflections are nearly identical. However, the acquired diffusivity and dissipation differ, as shown in Table 4.3.

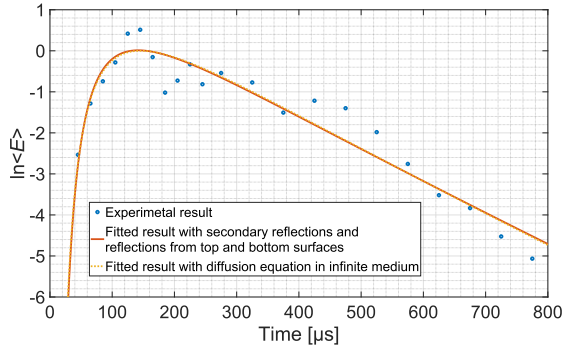


Figure 4.19 Comparison between fitted diffusion curves with and without considering boundary reflections (200 kHz component of the signal received by BB2 while BB1 as the actuator in the beam).

Table 4.3 Fitted results with different amount of image sources.

Diffusion equation used for fitting	Fitted results		
	$\ln E_0$ [-]	Diffusivity D [m^2/s]	Dissipation α [s^{-1}]
Infinite medium (dotted line in Fig. 4.20)	-0.53	44.4	6205
Consider reflections from bottom surface	-0.90	47.4	6465
Consider reflections from bottom and top surfaces	-0.89	47.2	6505
Consider reflections from bottom and top surfaces, and secondary reflections (solid line in Fig. 4.20)	-0.89	47.2	6523
Consider reflections from bottom and top surfaces, secondary reflections, and reflections from front and back surfaces	-0.89	47.2	6525

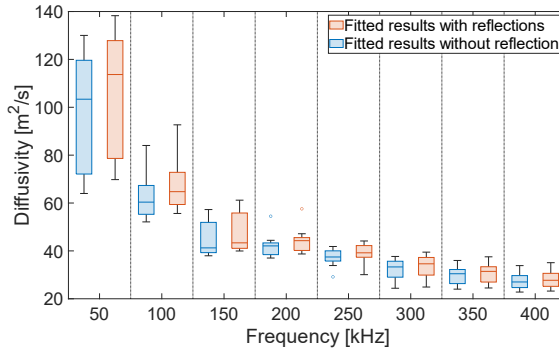
Since a portion of the wave energy reflects back from the boundary, the diffusion equation without considering boundaries interprets this reflected energy as part of the initial energy emitted by the source. Consequently, the calculated deposited energy ($\ln E_0$ in Table 4.3) is higher than when the reflected energy is taken into account. Additionally, the superposition of reflected and diffusive energy introduces a delay in the arrival time of maximum energy and exhibits a slower decay trend in the dissipation phase. If one fits the diffusion equation in such cases without considering the reflection, both diffusivity and dissipation will be underestimated, as indicated in Table 4.3.

Given the limited impact of remote image sources on the main energy, it is not necessary to consider all image sources. In scenarios presented in Table 4.3, taking into account reflections from the bottom and top surfaces, along with secondary reflections, already provides sufficiently accurate results. Consequently, only these image sources will be utilized in the fitting process for the bottom row of SAs in the beam.

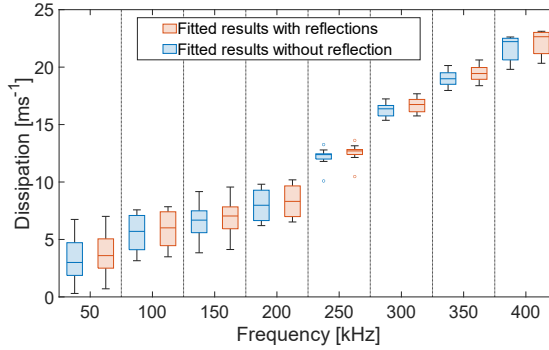
The fitted diffusive properties as a function of frequencies, utilizing the mentioned reflections for the bottom row of SAs (BB1 to BB6), are depicted in Figure 4.20. In these figures, the box plot is employed to visually demonstrate the spread of diffusive properties.

4.3 Estimation of diffusive properties

Each box represents the interquartile range (IQR) of the dataset, with the line inside indicating the median value. The top and bottom edges of the box represent the medians of the upper and lower halves of the dataset, respectively. Outliers, depicted as circles, are values that exceed 1.5 times the IQR above or below the top or bottom of the box. The lines extending from each box connect the median of the upper half to the maximum non-outlier data value and the median of the lower half to the minimum non-outlier data value. Similar to the observations in Table 4.3, neglecting reflections leads to consistently lower estimations of both diffusivity and dissipation. Moreover, the diffusivity of elastic waves in the low-frequency regime, characterized by faster energy spreading, is more affected by boundary reflections.



(a) Diffusivity.



(b) Dissipation.

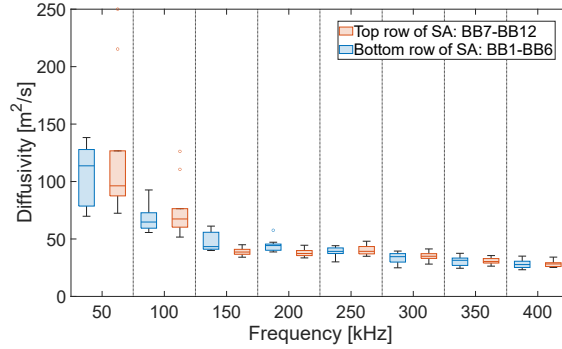
Figure 4.20 Comparison between the fitted diffusive properties with and without considering boundary reflections using signals from BB1 to BB6 in the beam.

4.3.4.3 Influence of concrete-concrete interface

To investigate the influence of concrete-concrete interface on the diffusive properties, Figure 4.21 presents the diffusivity and dissipation obtained from both the top and bottom rows of SAs in the beam. It should be noted here that only reflections from solid-air

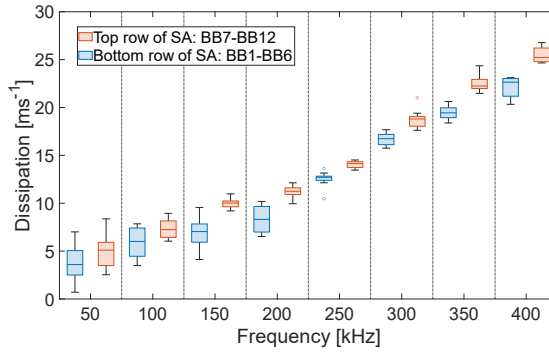
boundaries are considered in the fitting process, neglecting the boundary at the interface between the prestressed beam and the cast-in-situ layer. The fitted results reveal no apparent divergence in diffusivity between different SA rows, despite the small distance of 23 mm between the top row of SAs and the concrete-concrete interface. This suggests that the concrete-concrete interface has limited influence on diffusivity in this specimen. There are several outliers in the fitted results shown in Figure 4.21(a). Specifically, two data points from top row of SAs at 50 kHz show diffusivity values exceeding 200 m²/s. These outliers will be discussed in Section 4.3.4.4.

The dissipation of wave energy shows a consistent faster decay in the region of the top row SAs. This observation can be attributed to three potential explanations. Firstly, the geopolymer concrete in the cast-in-situ topping layer may exhibit higher dissipation compared to the concrete in the prestressed beam, leading to a higher dissipation of elastic waves in this particular region. Secondly, it is possible that a portion of the wave energy leaks to the interface, which is also highlighted by Trégourès and van Tiggelen (2001). Thirdly, the region where the bottom SA row is embedded experiences higher compressive stress, which can lead to lower dissipation. This could happen when the internal friction dominates the dissipation process (Brunet, Jia et al. 2008).



(a) Diffusivity.

4.3 Estimation of diffusive properties



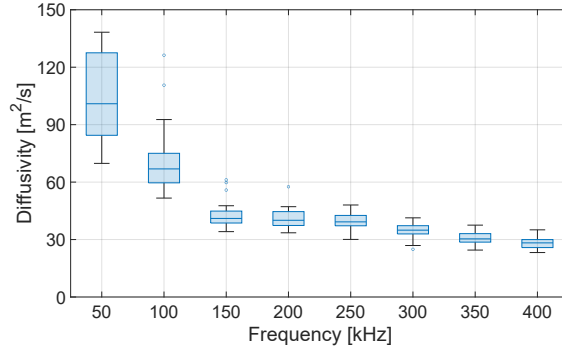
(b) Dissipation.

Figure 4.21 Comparison between the fitted diffusive properties from the top and bottom rows of SAs in the beam.

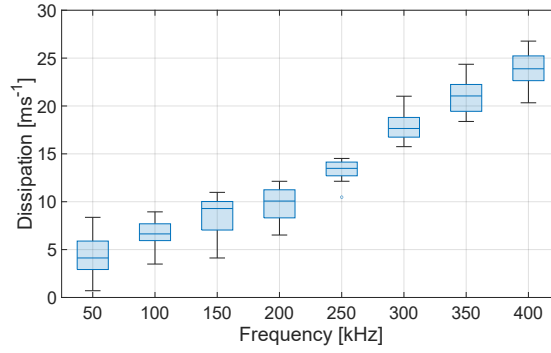
4.3.4.4 Arrival time of maximum energy

In Section 4.3.4.2 and 4.3.4.3, we discussed the influence of boundary reflections and the concrete-concrete interface on the diffusive properties in the beam. In this section, we will present the arrival time of maximum energy estimated through fitted results. The arrival time of maximum energy, which can be calculated using Equation (4.12) in conjunction with the diffusivity and dissipation, can be used to ensure that the fitted diffusive properties are reasonable. In practice, the arrival time of maximum energy cannot precede the first arrival of longitudinal waves. Therefore, any arrival time of maximum energy earlier than this threshold, approximately $55 \mu\text{s}$, is deemed unreliable.

The diffusivity and dissipation of bulk waves in the beam obtained using both the top and bottom rows of SAs are shown in Figure 4.22. The diffusivity exhibits a decreasing trend with increasing wave frequency. The lower diffusivity observed at higher frequencies can be attributed to increased interactions between elastic waves and scatterers in concrete due to the shorter wavelength. These interactions between waves and scatterers will be further investigated in Chapter 6. The dissipation shows a linear increase with the wave frequency, which is in line with the result reported by Anugonda et al. (2001).



(a) Diffusivity.



(b) Dissipation.

Figure 4.22 Diffusive properties of bulk waves in the beam acquired using all SAs.

The arrival time of maximum energy as a function of frequencies is depicted in Figure 4.23, and the arrival time of longitudinal waves is highlighted as a red dotted line. There are few data points observed beyond the arrival time of longitudinal waves. Notably, the corresponding diffusivities of these data points all exceed $200 \text{ m}^2/\text{s}$, and all of them correspond to outliers in Figure 4.21(a). To mitigate the influence of these data points, we focus solely on diffusivities below $180 \text{ m}^2/\text{s}$ in the following chapters. By checking arrival times of maximum energy, the majority of diffusive properties obtained using the improved diffusion equation in geopolymers specimens is deemed reliable and trustworthy.

4.3 Estimation of diffusive properties

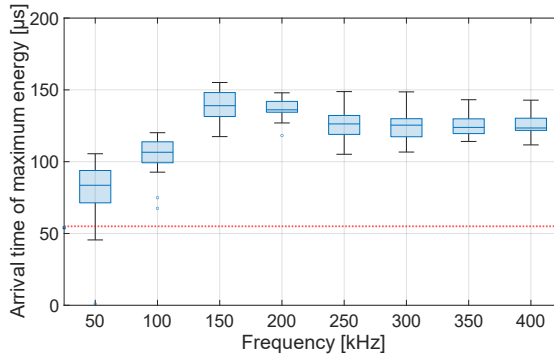


Figure 4.23 Arrival time of maximum energy in the beam (red dotted line indicates the mean arrival time of longitudinal waves).

4.3.5 Diffusive properties in the cylindrical specimen

In Section 4.3.4, diffusive properties of bulk waves in specimens with planar boundaries are determined by fitting them using an improved diffusion equation incorporating reflected energy from planar boundaries. In cases where the boundaries are curved, such as the cylindrical sample, this approximation becomes inadequate. To address this limitation, Section 4.3.2.3 introduced a new diffusion equation tailored for assessing diffusive properties of bulk waves in cylindrical samples. This newly proposed diffusion equation will be employed in this section to evaluate diffusive properties of bulk waves within the cylindrical sample.

4.3.5.1 Signal energy and parameters for fitting the diffusion equation

Figure 4.24 displays the logarithm of ensemble-averaged energy as a function of time for a signal collected in the new cylindrical sample. Consistent with the approach adopted in Section 4.3.4, a total of 22 time windows are employed during curve fitting. The 1st time window, starting at 60 μs , has a length of 40 μs . The subsequent 10 time windows (2nd to 11th) also have a length of 40 μs , with each overlapping the previous window by 20 μs . The 12th time window, starting at 260 μs , has a length of 100 μs . The subsequent 10 time windows (13th to 22nd) have a length of 100 μs and overlap the previous window by 50 μs . The centre time of the 22nd time window is 810 μs ; however, given the exceptionally low energy of the 400 kHz component at this time, the centre time of the last time window of 610 μs is applied specifically for this component, which corresponds to the 18th time window.

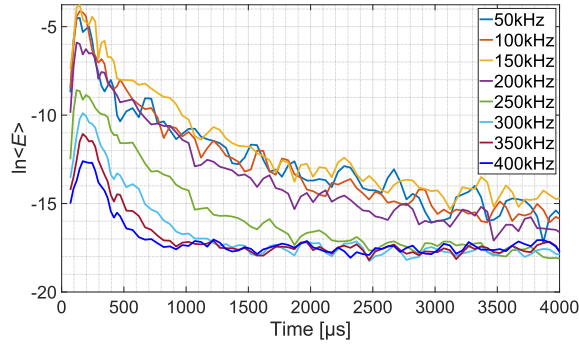
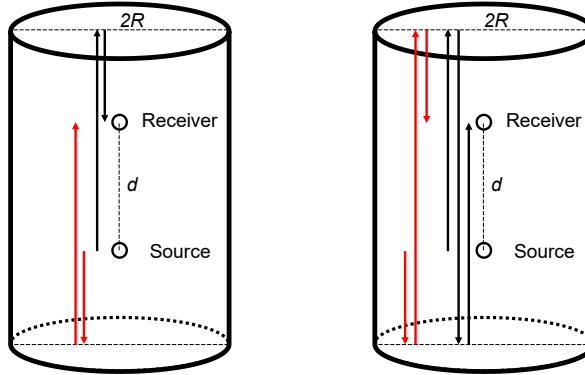


Figure 4.24 Logarithm of the ensemble-averaged energy (denoted as $\ln\langle E \rangle$) as a function of time in the cylindrical sample.

4.3.5.2 Determination of the diffusion equation to fit the diffusive properties

Before fitting diffusive properties using the diffusion equation, it is imperative to assess the contributions of reflected energy. These contributions can be divided into two categories: energy reflected from the planar boundaries (top and bottom surfaces) and energy reflected from the circular surface of the cylinder. To incorporate the reflected energy from planar boundaries, the image source method outlined in Section 4.3.2.2 can be employed. Figure 4.25(a) illustrates two types of primary reflections, both equally represented in this scenario with a constant propagation path of 0.5 m. Secondary reflections, shown in Figure 4.25(b), exhibit varying propagation paths in this sample: the Type I reflection (coloured in red) has a propagation path of 0.7 m, while the Type II reflection (in black) spans 1.3 m.



(a) Two types of primary reflection. (b) Two types of secondary reflection.

Figure 4.25 Illustration of primary and secondary reflections from planar boundaries (note that the dimensions in this figure do not match the actual dimensions).

4.3 Estimation of diffusive properties

Reflections from the circular surface can be classified in the manner discussed in Section 4.3.2.3. The travel distances from the source to the receiver for primary, secondary, tertiary, and quaternary reflections are given by $[d^2+(2R)^2]^{1/2}$, $[d^2+(4R)^2]^{1/2}$, $[d^2+(6R)^2]^{1/2}$, and $[d^2+(8R)^2]^{1/2}$, respectively. Considering a maximum lapse time of 800 μs , the reflected energy to be considered in the diffusion equation can be determined by their maximum contributions to the main energy using Equation (4.24) with a diffusivity of 150 m^2/s . These contributions to the main energy are shown in Table 4.4. For planar reflections, the primary and Type I secondary reflections contribute the most to the main energy, whereas the contributions of Type II secondary reflections, only 3.57%, and higher-order reflections are negligible. Regarding reflections from the circular surface, the first four orders make significant contributions, higher than 30% each of the main energy, and will be considered in the diffusion equation. Therefore, the final expression of the diffusion equation includes diffusion equation components relate to:

- idealized diffusion in infinite medium;
- two image sources related to primary reflections from planar boundaries;
- one image source related to Type I secondary reflections from planar boundaries;
- primary reflection from the circular surface;
- secondary reflection from the circular surface;
- tertiary reflection from the circular surface;
- quaternary reflection from the circular surface.

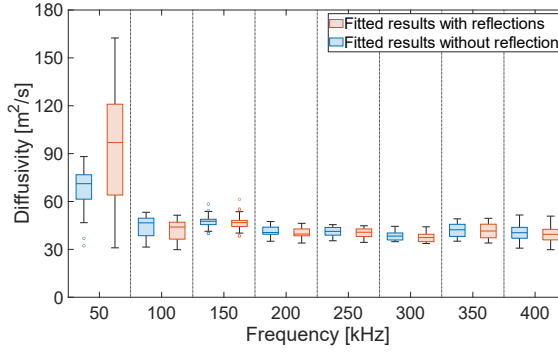
Table 4.4 Contributions of energy reflected from boundaries to the main energy in the cylindrical sample.

Type of reflections	Maximum contribution to the main energy in an infinite medium [%]
Primary reflections from top and bottom surfaces	143.31
Type I secondary reflections from top and bottom surfaces	43.46
Type II secondary reflections from top and bottom surfaces	3.57
Primary reflection from circular surface	156.27
Secondary reflection from circular surface	178.08
Tertiary reflection from circular surface	104.60
Quaternary reflection from circular surface	37.54
Quinary reflection from circular surface	8.68

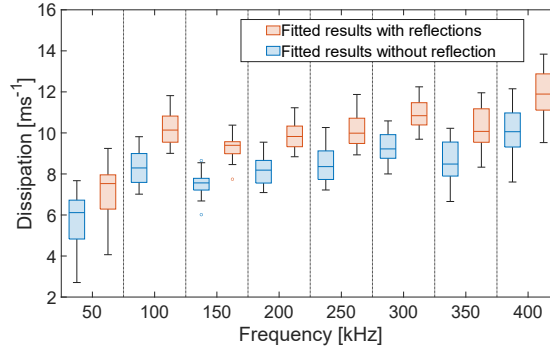
4.3.5.3 Influence of boundary reflections

The comparison of diffusive properties, as determined by the diffusion equation in an infinite medium and the improved diffusion equation accounting for reflections introduced in Section 4.3.5.2, is presented in Figure 4.26. Notably, the presence of reflected energy exerts a significant influence on the diffusivity of the 50 kHz component. This

impact is particularly pronounced due to the inherently higher diffusivity of this component, rendering it more susceptible to reflected energy. Conversely, the influence of reflected energy on diffusive properties of other frequency components is negligible. This observation is different from that in Figure 4.20(a), where diffusivities fitted considering reflections consistently surpass those fitted using the diffusion equation in an infinite medium. A plausible explanation for this discrepancy lies in the increased complexity of the diffusion equation introduced in Section 4.3.5.2 compared to that in Section 4.3.4.2, making curve fitting more challenging. Simultaneously, dissipation, which is closely associated with the exponential decay in the latter stage, consistently exhibits higher values when reflections are taken into account. This observation is consistent with that in Figure 4.20(b).



(a) Diffusivity.



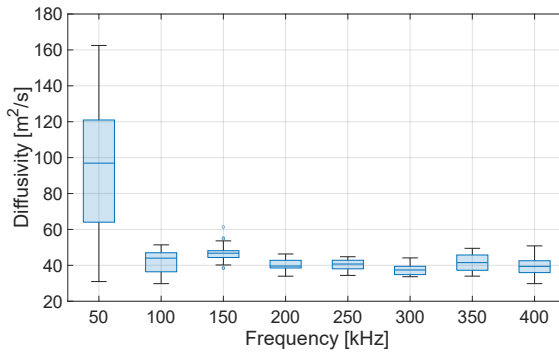
(b) Dissipation.

Figure 4.26 Comparison between the fitted diffusive properties with and without considering boundary reflections in the concrete cylinder.

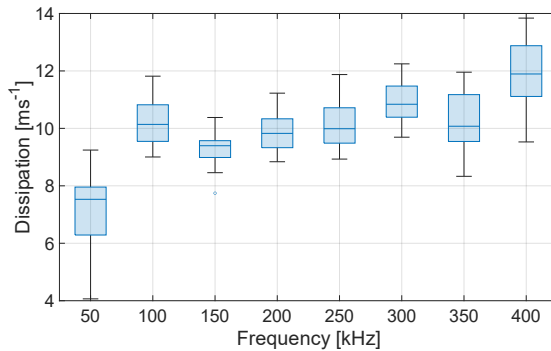
4.3 Estimation of diffusive properties

4.3.5.4 Arrival time of maximum energy

Figure 4.27 illustrates the diffusivity and dissipation obtained using the diffusion equation, considering reflections, in the concrete cylinder. Notably, the diffusivity generally exhibits a decreasing trend with increasing frequency, although the diffusivities of the 100 kHz component are lower than expected. Conversely, dissipation shows an increasing trend with wave frequency, consistent with observations in geopolymer specimens. To ensure the fitted diffusive properties are reasonable, the arrival time of maximum energy is examined. As depicted in Figure 4.28, the arrival time of maximum energy always occurs after the first arrival of longitudinal waves, approximately at 64 μs . Consequently, the diffusive properties obtained using the enhanced diffusion equation in the concrete cylinder are considered reliable.



(a) Diffusivity.



(b) Dissipation.

Figure 4.27 Diffusive properties of bulk waves in the concrete cylinder.

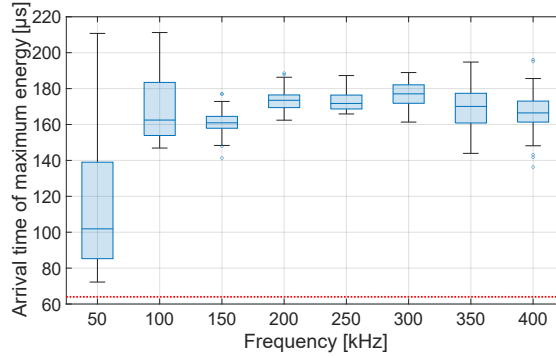


Figure 4.28 Arrival time of maximum energy in the concrete cylinder (red dotted line indicates the mean arrival time of longitudinal waves).

4.3.6 Procedures for fitting diffusive properties in subsequent chapters

In Section 4.3, we demonstrated how to acquire diffusive properties using the improved diffusion equation by taking the reflections from solid-air boundaries into consideration. In Chapter 6 and 7, these diffusive properties will be applied to investigate the scattering properties of bulk waves in concrete. Based on the content of Section 4.3, the following guidelines are proposed for fitting diffusive properties in this dissertation:

- For geopolymers beam: We consider the primary and secondary reflections from the top and bottom surfaces. The 1st time window, starting at 25 μs , has a length of 40 μs . The subsequent 10 time windows (2nd to 11th) also have a length of 40 μs , with each overlapping the previous window by 20 μs . The 12th time window, starting at 225 μs , has a length of 100 μs . The subsequent 10 time windows (13th to 22nd) have a length of 100 μs and overlap the previous window by 50 μs .
- For concrete cylinder: We consider primary reflections and Type I secondary reflections from the bottom and top surfaces, as well as primary, secondary, tertiary, and quaternary reflections from the circular surface. The 1st time window, starting at 60 μs , has a length of 40 μs . The subsequent 10 time windows (2nd to 11th) also have a length of 40 μs , with each overlapping the previous window by 20 μs . The 12th time window, starting at 260 μs , has a length of 100 μs . The subsequent 10 time windows (13th to 22nd) have a length of 100 μs and overlap the previous window by 50 μs . The maximum lapse time is approximately 800 μs ; however, due to the extremely low energy of the 400 kHz component at this time, a maximum lapse time of 600 μs is applied specifically for this component.

4.4 Discussion

4.4 Discussion

4.4.1 Cycle skipping in the WCS technique

In Section 4.2.4.3, we discussed that the causes of cycle skipping in the stretching technique and the WCS technique are different. Cycle skipping observed while employing the stretching technique is predominantly attributed to the low SNR in the coda, while the results of the WCS technique depend explicitly on the magnitude of velocity change and the selected frequency component. In a previous study by Mao et al. (2020), the authors mentioned that cycle skipping in the WCS technique could be mitigated through the process of phase unwrapping. However, they also noted that this approach may not be effective in the coda when the waveform similarity is lost. In another research paper by Mikesell et al. (2015), the authors identified three reasons for the occurrence of cycle skipping in the stretching technique: (i) low SNR, (ii) short time windows, and (iii) significant divergence between the two signals. Based on the experiment conducted in this study and the insights from Mao et al. (2020), one can attribute the occurrence of cycle skipping in the WCS technique to three factors as well: (i) low SNR, (ii) signal dominated by frequencies that have a shorter period compared to the travel time shift, and (iii) significant divergence between the two signals. Reason (i) can also help explain why the WCS technique performs poorly in frequency bands with low energy: the SNR of the signal in these frequency bands is relatively low, making it more susceptible to the cycle skipping and leading to less accurate retrieval of the velocity change.

4.4.2 Computational efficiency of the stretching technique and the WCS technique

In a study given by Yuan et al. (2021), the authors compared the performances of the stretching technique and the WCS technique by applying them to the same signal within a single time window. They concluded that the stretching technique is computationally faster compared to the WCS technique when operating in a single time window. However, in our research, one can observe that the retrieved velocity change exhibits travel time dependence, as reflected in different slopes of velocity change versus stress in different time segments. Therefore, we suggest using multiple overlapping time windows for the stretching operation to capture this travel time-dependent behaviour. However, a drawback of using multiple time windows is the significant increase in computational cost. On the other hand, the WCS technique operates in the wavelet domain and directly retrieves the velocity change at each lapse time from the phase spectrum. Considering the time-dependent nature of retrieved velocity change, the WCS technique offers higher computational efficiency compared to the stretching technique in the application to concrete.

4.4.3 Noise reduction using the WCS technique

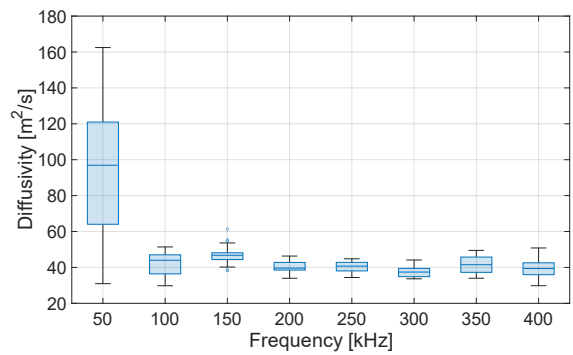
In the work presented by Wang et al. (2021), a possible solution for noise reduction in the application of WI is proposed. This approach involves filtering the signal before applying the stretching technique. While this operation effectively reduces the impact of noise, it introduces additional computational costs due to the signal filtering process, which in turn slows down the computational speed. On the other hand, wavelet decomposition, a tool for time-frequency analysis, implicitly acts as a filter by allowing selective focus on a specific frequency band where the signal energy is sufficiently high. This allows the WCS technique to effectively reduce the influence of noise without the need for additional signal filtering.

4.4.4 Effect of boundary conditions on diffusivity in concrete cylinder

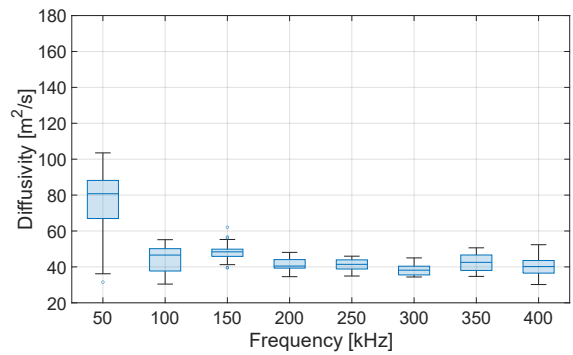
In Section 4.3.5, we investigate the diffusive properties of bulk waves in a concrete cylinder. During the curve fitting process, we account for primary reflections and Type I secondary reflections from the bottom and top surfaces, as well as primary, secondary, tertiary, and quaternary reflections from the circular surface. However, since these diffusive properties are measured during loading, where the top and bottom surfaces are in contact with loading plates rather than being ideal air-solid boundaries, considering these reflections may lead to an overestimation of the diffusivity. Here, our primary focus will be on diffusivity, as it will be used in Chapter 6 to validate the bulk wave energy transport model.

To assess the impact of these reflections on diffusivity, we compare diffusivities fitted using the diffusion equation with (Figure 4.29(a)) and without (Figure 4.29(b)) considering reflections from the top and bottom surfaces. Note that not accounting for these reflections may also lead to an underestimation of diffusivity. For frequencies above 100 kHz, this effect is negligible. However, for the 50 kHz component, considering reflections significantly increases the scattering of diffusivity values. Since these results are obtained from the same sensor pair, the spatial fluctuation of diffusivity can be neglected. Therefore, it can be concluded that the fitted diffusivity at low frequencies—specifically 50 kHz in this dissertation—is highly sensitive to the formulation of the diffusion equation used for fitting, which can also explain the high scattering of diffusivities at 50 kHz shown in Figure 4.27(a). This suggests that diffusivity at low frequencies in concrete should be treated with caution. In Chapter 6, we will use the diffusivity values fitted from the diffusion equation including reflections from the top and bottom surfaces, and will provide further discussion in that chapter.

4.4 Discussion



(a) With reflections from top and bottom surfaces (same with Figure 4.27(a)).



(b) Without reflections from top and bottom surfaces.

Figure 4.29 Comparison of bulk wave diffusivity in the concrete cylinder with and without considering reflections from top and bottom surfaces.

5. Response of travel time in ballistic bulk waves to stresses

5.1 Introduction

The response of travel time of elastic waves to applied stresses is termed as acoustoelasticity. It should be emphasized again here that this process consists of two steps: the applied stress will first lead to velocity changes in the medium, and these velocity changes in the medium in turn lead to changes in the travel time of bulk waves propagating in the medium. However, the application of acoustoelasticity to concrete is limited to cases where the wave propagation direction is either parallel or perpendicular to one of the principal axes of deformation. In practical terms, this limitation implies that the bulk waves must travel either parallel or perpendicular to the principal deformation directions.

This chapter is dedicated to investigating the response of the travel time of ballistic bulk waves to normal and shear stresses in concrete. We will start with the knowledge gap in Section 5.2. Given the identification of certain inconsistencies in acoustoelastic expressions within existing literature, a re-examination of the theory becomes necessary. Building upon this observation, a thorough re-evaluation of the theoretical framework of acoustoelasticity is conducted in Section 5.3. Within this framework, the acoustoelastic theory for bulk waves is extended to encompass a more general scenario involving both shear and normal strains, as detailed in Section 5.4. Within the same chapter, three numerical examples utilizing concrete as the medium are presented to explore the influence of normal and shear strains on the velocity and polarization direction of bulk waves. Leveraging the key insights from Section 5.4, we simplify the expression for acoustoelasticity within the context of inclined propagating ballistic waves in the plane stress state, as demonstrated in Section 5.5. Together with the propagation directions of ballistic waves, this simplification aids in determining the magnitude and direction changes of principal stresses in the plane stress state through an easily calibrated process. The experimental validation for this simplified acoustoelastic expression is detailed in Section 5.6. Section 5.7 provides a detailed discussion on the inconsistencies of acoustoelasticity in the literature and potential errors in acquiring the acoustoelastic parameters of concrete.

5.2 Knowledge gap relating theoretical framework of acoustoelasticity

In the past, experiments investigating the acoustoelastic effect were conducted in laboratories using ultrasonic sensors externally attached to the surface of the sample. Furthermore, ballistic wave components are commonly utilized for data processing due to their straightforward propagation directions—tracing a direct line from the actuator to the receiver—and easier determination of wave modes, characterized by minimal interactions with boundaries and scatterers within the medium. The combination of surface-bonded sensors and ballistic wave components allows for the alignment of the sensors so that the

5.2 Knowledge gap relating theoretical framework of acoustoelasticity

ballistic wave propagation direction could be either parallel or perpendicular to the principal deformation, except in certain cases like Lamb waves, which propagate at an angle to the principal deformation direction (Mi, Michaels et al. 2006). However, as the recent application shift towards long-term monitoring utilizing permanently deployed ultrasonic sensors within structures, there is no assurance that ballistic waves will consistently propagate along these predetermined directions. Consider the scenario of monitoring a concrete bridge deck under the influence of moving vehicle loads, where the stress condition changes over time. In such an instance, it becomes impractical to consistently align the wave propagation direction along the principal deformation directions.

When body waves propagate inclined to the principal deformation in an isotropic elastic medium, it implies an angle between the wave propagation direction and the principal stress direction. By establishing a new coordinate system aligned parallel and perpendicular to the wave propagation direction and computing the stress matrix within this new coordinate system, shear stresses can be identified. Simultaneously, the presence of shear stresses concurrently indicates the existence of shear deformations, which is defined as an isochoric plane deformation in which there are a set of line elements with a given reference orientation that do not change length and orientation during the deformation (Ogden 1997). In this case, the current expressions for acoustoelasticity, which only involves the principal stresses/strains, is not applicable.

Despite the efforts made by several researchers to investigate the influence of shear deformation on acoustoelasticity (Iwashimizu and Kubomura 1973, Bobrenko, Kutsenko et al. 1990), no specific conclusion regarding the response of bulk wave velocity to applied shear deformations can be drawn from the existing theoretical derivations. This limitation stems from the lack of research on the impact of shear deformations on acoustoelasticity in a given material.

Some researchers have made assumptions asserting that shear deformation does not affect either transverse or longitudinal wave velocities (Mi, Michaels et al. 2006, Muir 2009), upon which they derived equations to address cases where waves propagate at an angle to the principal deformation. However, the theoretical basis that support these assumptions were inadequately verified.

Furthermore, inconsistencies exist in the current literature on acoustoelastic theory, necessitating re-examination as they could potentially yield inaccurate descriptions of the acoustoelastic effect. These discrepancies primarily stem from two categories: inconsistent acoustoelastic expressions (Egle and Bray 1976, Payan, Garnier et al. 2011) and the improper utilization of third-order elastic constants (Stahler, Sens-Schonfelder et al. 2011). Hence, it is imperative to re-evaluate the theoretical framework of modern acoustoelasticity for bulk waves in light of these identified inaccuracies.

These two knowledge gaps will be tackled in this chapter, where we will conduct a re-elaboration of the modern acoustoelastic theory, followed by an refinement of the framework to encompass arbitrary wave propagation directions and stress conditions. Building upon that theory, an experimental study will be conducted to validate the conclusions derived from the extended framework.

5.3 Theoretical framework of modern acoustoelasticity

This section provides a thorough re-examination of theoretical framework for modern acoustoelasticity. We will start with the definitions of coordinates, deformations, and displacements in Section 5.3.1 and proceed to expressions for strain and stress in Section 5.3.2. Section 5.3.3 will show the non-linear constitutive equation derived from the strain energy function. This process entails the incorporation of five constants: two second-order elastic constants and three third-order elastic constants, which will be illustrated in Section 5.3.4. The equations of motion in the initial frame and natural frame will be presented in Section 5.3.5 and 5.3.6, respectively. To explore acoustoelastic effects across various wave modes, the integration of a plane wave into the equation of motion will be shown in Section 5.3.7.

5.3.1 Coordinates, deformations and displacements

The concept of *small-on-large* in acoustoelasticity gives rise to three distinct states: the natural state, initial state, and final state. The definitions of the three states are shown in Figure 5.1. The natural state represents the original state of the body without external stress applied. The coordinates associated with this state are referred to as natural coordinates, denoted as \mathbf{a} (with components $a_\alpha, \alpha \in \{1,2,3\}$). The initial state, also known as the deformed state, is a state in which the body has already undergone elastic deformation due to applied stress. The coordinates associated with this state are referred to as initial coordinates or Lagrangian coordinates (Hughes and Kelly 1953), denoted as \mathbf{x} (with components $x_j, j \in \{1,2,3\}$). The final state represents the result from the dynamic disturbances of the pre-deformed body. The position of a material point in this state is described by the coordinates \mathbf{X} (with components $X_J, J \in \{1,2,3\}$). It is important to recognize that the expressions of acoustoelasticity derived from the natural state and the initial state differ due to the consideration of pre-deformation in the natural frame-based acoustoelasticity, whereas it is not considered in the initial frame-based acoustoelasticity (Pao and Gamer 1985).

5.3 Theoretical framework of modern acoustoelasticity

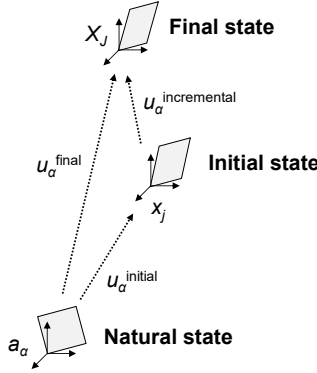


Figure 5.1 Coordinates and displacements at natural, initial, and final states.

The static deformation from natural to the initial state and the dynamic deformation from the initial to the final state are represented by the transformation of coordinates as:

$$\mathbf{x} = \hat{x}(a_1, a_2, a_3) , \quad (5.1)$$

$$\mathbf{X} = \hat{X}(x_1, x_2, x_3, t) , \quad (5.2)$$

where \hat{x} and \hat{X} are two continuous vector functions. The displacements associated with the deformation of the natural state to the initial state, $\mathbf{u}^{\text{initial}}$, and with the deformation of the natural to the final state, $\mathbf{u}^{\text{final}}$, are defined respectively as:

$$\mathbf{u}^{\text{initial}}(\mathbf{a}) = \mathbf{x} - \mathbf{a} , \quad (5.3)$$

$$\mathbf{u}^{\text{final}}(\mathbf{a}, t) = \mathbf{X} - \mathbf{a} . \quad (5.4)$$

Similarly, the incremental displacement from the initial to the final state $\mathbf{u}^{\text{incremental}}$ is given by:

$$\mathbf{u}^{\text{incremental}}(\mathbf{a}, t) = \mathbf{u}^{\text{final}} - \mathbf{u}^{\text{initial}} = \mathbf{X} - \mathbf{x} . \quad (5.5)$$

5.3.2 Strain and stress

In this section, we will specify the strain and stress tensors utilized in the derivation. For the sake of simplicity, we employ the Lagrangian finite strain tensor. The expressions for the Lagrangian finite strain tensors in the initial and final states, in terms of natural coordinates, are given by:

$$e_{\alpha\beta}^{\text{initial}} = \frac{1}{2} \left(\frac{\partial x_k}{\partial a_\alpha} \frac{\partial x_k}{\partial a_\beta} - \delta_{\alpha\beta} \right) , \quad (5.6)$$

and

$$e_{\alpha\beta}^{\text{final}} = \frac{1}{2} \left(\frac{\partial X_K}{\partial a_\alpha} \frac{\partial X_K}{\partial a_\beta} - \delta_{\alpha\beta} \right), \quad (5.7)$$

respectively. Note that here, and in the remainder of this dissertation, Einstein's summation convention applies for repeated indices (k and K in Equation (5.6) and (5.7), respectively). The Kronecker delta δ_{ij} is defined as:

$$\delta_{ij} = \begin{cases} 1, & \text{for } i = j \\ 0, & \text{else} \end{cases}. \quad (5.8)$$

The Lagrangian finite strain tensors in Equation (5.6) and (5.7) quantify how much, locally, the displacement differs from a rigid body displacement, and we can easily tell from these two equations that this strain tensor is symmetry. The incremental strain $e_{\alpha\beta}^{\text{incremental}}$ is:

$$\begin{aligned} e_{\alpha\beta}^{\text{incremental}} &:= e_{\alpha\beta}^{\text{final}} - e_{\alpha\beta}^{\text{initial}} \\ &= \frac{1}{2} \left(\frac{\partial X_k}{\partial a_\alpha} \frac{\partial X_k}{\partial a_\beta} - \frac{\partial x_k}{\partial a_\alpha} \frac{\partial x_k}{\partial a_\beta} \right) \\ &= \frac{1}{2} \left[\frac{\partial (x_k + u_k^{\text{incremental}})}{\partial a_\alpha} \frac{\partial (x_k + u_k^{\text{incremental}})}{\partial a_\beta} - \frac{\partial x_k}{\partial a_\alpha} \frac{\partial x_k}{\partial a_\beta} \right] \\ &= \frac{1}{2} \left(\frac{\partial x_k}{\partial a_\alpha} \frac{\partial x_k}{\partial a_\beta} + \frac{\partial x_k}{\partial a_\alpha} \frac{\partial u_k^{\text{incremental}}}{\partial a_\beta} + \frac{\partial x_k}{\partial a_\beta} \frac{\partial u_k^{\text{incremental}}}{\partial a_\alpha} + \frac{\partial u_k^{\text{incremental}}}{\partial a_\alpha} \frac{\partial u_k^{\text{incremental}}}{\partial a_\beta} - \frac{\partial x_k}{\partial a_\alpha} \frac{\partial x_k}{\partial a_\beta} \right) \\ &\approx \frac{1}{2} \left(\frac{\partial x_k}{\partial a_\alpha} \frac{\partial u_k^{\text{incremental}}}{\partial a_\beta} + \frac{\partial x_k}{\partial a_\beta} \frac{\partial u_k^{\text{incremental}}}{\partial a_\alpha} \right) \\ &= \frac{1}{2} \left(\frac{\partial x_k}{\partial a_\alpha} \frac{\partial u_k^{\text{incremental}}}{\partial x_l} \frac{\partial x_l}{\partial a_\beta} + \frac{\partial x_k}{\partial a_\beta} \frac{\partial u_k^{\text{incremental}}}{\partial x_l} \frac{\partial x_l}{\partial a_\alpha} \right). \end{aligned} \quad (5.9)$$

The approximation stems from the neglect of the terms involving products of spatial derivatives of dynamic displacement in Equation (5.9). This is justified if the condition that the magnitude of the dynamic disturbance is much smaller than the static deformation is fulfilled.

Two stress tensors are considered in the derivation: the Cauchy stress tensor \mathbf{T} , defined over the area of elements in the deformed state, and the second Piola-Kirchhoff stress tensor \mathbf{S} , defined over the area of elements in the undeformed state. Although the stress measured using the ultrasonic method is related to the Cauchy stress tensor (Pao and Gamer 1985, Pao 1987), it is more convenient to use the second Piola-Kirchhoff stress tensor for the subsequent derivation since it forms a conjugate pair with the Lagrangian finite strain tensor (Ogden 1997), which will be shown in Equation (5.15).

The Cauchy stress tensor in the initial state and the second Piola-Kirchhoff stress tensor in the natural state are related by (Pao and Gamer 1985):

5.3 Theoretical framework of modern acoustoelasticity

$$T_{ij} = \frac{\rho^{\text{initial}}}{\rho^0} \frac{\partial x_i}{\partial a_\alpha} \frac{\partial x_j}{\partial a_\beta} S_{\alpha\beta} , \quad (5.10)$$

where ρ^0 and ρ^{initial} are the mass densities in the natural and initial states, respectively. In some literature (Johnson 1981), the ratio of density is expressed as the Jacobian determinant in Equation (5.10). It is important to note that the Jacobian determinant essentially describes the ratio of medium volume between different states. Assuming that the mass of the medium remains constant during elastic deformation, this volume ratio can then be expressed in terms of density ratio. Similarly, the Cauchy stress tensor in the final state and the second Piola-Kirchhoff stress tensors in the initial and natural states are linked by:

$$\begin{aligned} T_{IJ} &= \frac{\rho^{\text{final}}}{\rho^{\text{initial}}} \frac{\partial X_I}{\partial x_i} \frac{\partial X_J}{\partial x_j} S_{ij} \\ &= \frac{\rho^{\text{final}}}{\rho^0} \frac{\partial X_I}{\partial a_\alpha} \frac{\partial X_J}{\partial a_\beta} S_{\alpha\beta} , \end{aligned} \quad (5.11)$$

where ρ^{final} is the mass density in the final state.

Similar to the operations performed on displacement and strain, a second Piola-Kirchhoff stress tensor for the incremental stress is defined in the initial frame as follows:

$$S_{ij}^{\text{incremental}} = S_{ij}^{\text{final}} - S_{ij}^{\text{initial}} , \quad (5.12)$$

Considering that the Cauchy stress tensor is equivalent to the second Piola-Kirchhoff stress tensor for the initial static stress in the initial frame (Pao and Gamer 1985), Equation (5.12) can be further simplified into:

$$S_{ij}^{\text{incremental}} = S_{ij}^{\text{final}} - T_{ij}^{\text{initial}} . \quad (5.13)$$

5.3.3 Non-linear constitutive equation

In order to derive the non-linear equation of motion, it is necessary to specify the constitutive equation. Assuming that the body is elastic and its initial state is unstrained, a strain energy function can be defined and estimated using the following equation (Toupin and Bernstein 1961, King and Fortunko 1983, Pao and Gamer 1985, Janssen 1994):

$$W = \frac{1}{2!} C_{ijkl} e_{ij} e_{kl} + \frac{1}{3!} C_{ijklmn} e_{ij} e_{kl} e_{mn} , \quad (5.14)$$

where the strain tensor e_{ij} can refer to either Lagrangian finite strain tensor in the initial or final state. The tensors C_{ijkl} and C_{ijklmn} are second- and third-order elastic coefficients. The second Piola-Kirchhoff stress tensor can be directly obtained through the strain energy:

$$S_{\alpha\beta} = \frac{\partial W}{\partial e_{\alpha\beta}} . \quad (5.15)$$

The expressions of the second Piola-Kirchhoff stress tensors in the initial and final states are:

$$S_{\alpha\beta}^{\text{initial}} = C_{\alpha\beta\gamma\delta} e_{\gamma\delta}^{\text{initial}} + \frac{1}{2} C_{\alpha\beta\gamma\delta\epsilon\eta} e_{\gamma\delta}^{\text{initial}} e_{\epsilon\eta}^{\text{initial}} , \quad (5.16)$$

and

$$S_{\alpha\beta}^{\text{final}} = C_{\alpha\beta\gamma\delta} e_{\gamma\delta}^{\text{final}} + \frac{1}{2} C_{\alpha\beta\gamma\delta\epsilon\eta} e_{\gamma\delta}^{\text{final}} e_{\epsilon\eta}^{\text{final}} , \quad (5.17)$$

respectively. The incremental second Piola-Kirchhoff stress tensor is then:

$$\begin{aligned} S_{\alpha\beta}^{\text{incremental}} &= S_{\alpha\beta}^{\text{final}} - S_{\alpha\beta}^{\text{initial}} \\ &= C_{\alpha\beta\gamma\delta} e_{\gamma\delta}^{\text{final}} + \frac{1}{2} C_{\alpha\beta\gamma\delta\epsilon\eta} e_{\gamma\delta}^{\text{final}} e_{\epsilon\eta}^{\text{final}} - C_{\alpha\beta\gamma\delta} e_{\gamma\delta}^{\text{initial}} - \frac{1}{2} C_{\alpha\beta\gamma\delta\epsilon\eta} e_{\gamma\delta}^{\text{initial}} e_{\epsilon\eta}^{\text{initial}} \\ &= C_{\alpha\beta\gamma\delta} e_{\gamma\delta}^{\text{incremental}} + \frac{1}{2} C_{\alpha\beta\gamma\delta\epsilon\eta} \left(e_{\gamma\delta}^{\text{final}} e_{\epsilon\eta}^{\text{final}} - e_{\gamma\delta}^{\text{initial}} e_{\epsilon\eta}^{\text{initial}} \right) \\ &\simeq C_{\alpha\beta\gamma\delta} e_{\gamma\delta}^{\text{incremental}} + C_{\alpha\beta\gamma\delta\epsilon\eta} e_{\gamma\delta}^{\text{incremental}} e_{\epsilon\eta}^{\text{initial}} \\ &= \frac{1}{2} \left(\frac{\partial x_k}{\partial a_\gamma} \frac{\partial x_l}{\partial a_\delta} \frac{\partial u_k^{\text{incremental}}}{\partial x_l} + \frac{\partial x_k}{\partial a_\delta} \frac{\partial x_l}{\partial a_\gamma} \frac{\partial u_k^{\text{incremental}}}{\partial x_l} \right) \left(C_{\alpha\beta\gamma\delta} + C_{\alpha\beta\gamma\delta\epsilon\eta} e_{\epsilon\eta}^{\text{initial}} \right) . \end{aligned} \quad (5.18)$$

5.3.4 Second- and third-order elastic constants for isotropic materials

The elastic constants discussed in this section pertain to isotropic materials. It is important to note that these constants are not applicable for materials that are not isotropic. The C_{ijkl} represents the second-order elastic coefficients composed of the second-order elastic constants, also known as Lamé constants, λ and μ . The second-order elastic coefficients can also be expressed using other types of second-order elastic constants, such as any combination pair of Young's modulus, Poisson's ratio, bulk modulus and shear modulus. The expression for C_{ijkl} is as follows:

$$C_{ijkl} = \lambda \delta_{ij} \delta_{kl} + \mu (\delta_{ik} \delta_{jl} + \delta_{il} \delta_{jk}) , \quad (5.19)$$

where δ_{ij} denotes Kronecker delta. The second-order elastic coefficients can be expressed using Voigt notation as C_{IJ} . Then, the second-order elastic coefficients matrix is:

$$\begin{bmatrix} C_{11} & C_{12} & C_{13} & C_{14} & C_{15} & C_{16} \\ C_{21} & C_{22} & C_{23} & C_{24} & C_{25} & C_{26} \\ C_{31} & C_{32} & C_{33} & C_{34} & C_{35} & C_{36} \\ C_{41} & C_{42} & C_{43} & C_{44} & C_{45} & C_{46} \\ C_{51} & C_{52} & C_{53} & C_{54} & C_{55} & C_{56} \\ C_{61} & C_{62} & C_{63} & C_{64} & C_{65} & C_{66} \end{bmatrix} = \begin{bmatrix} \lambda + 2\mu & \lambda & \lambda & 0 & 0 & 0 \\ \lambda & \lambda + 2\mu & \lambda & 0 & 0 & 0 \\ \lambda & \lambda & \lambda + 2\mu & 0 & 0 & 0 \\ 0 & 0 & 0 & \mu & 0 & 0 \\ 0 & 0 & 0 & 0 & \mu & 0 \\ 0 & 0 & 0 & 0 & 0 & \mu \end{bmatrix} . \quad (5.20)$$

5.3 Theoretical framework of modern acoustoelasticity

The third-order elastic coefficients, $C_{\alpha\beta\gamma\delta\epsilon\eta}$, can be expressed using the third-order elastic constants:

$$\begin{aligned}
 C_{\alpha\beta\gamma\delta\epsilon\eta} = & (2l - 2m + n) \delta_{\alpha\beta} \delta_{\gamma\delta} \delta_{\epsilon\eta} \\
 & + \left(m - \frac{1}{2}n \right) [\delta_{\alpha\beta} (\delta_{\gamma\epsilon} \delta_{\delta\eta} + \delta_{\gamma\eta} \delta_{\delta\epsilon}) + \delta_{\gamma\delta} (\delta_{\alpha\epsilon} \delta_{\beta\eta} + \delta_{\alpha\eta} \delta_{\beta\epsilon}) \\
 & + \delta_{\epsilon\eta} (\delta_{\alpha\gamma} \delta_{\beta\delta} + \delta_{\alpha\delta} \delta_{\beta\gamma})] \\
 & + \frac{1}{4} n [\delta_{\alpha\gamma} (\delta_{\beta\epsilon} \delta_{\delta\eta} + \delta_{\beta\eta} \delta_{\delta\epsilon}) + \delta_{\alpha\delta} (\delta_{\beta\epsilon} \delta_{\gamma\eta} + \delta_{\beta\eta} \delta_{\gamma\epsilon}) \\
 & + \delta_{\beta\gamma} (\delta_{\alpha\epsilon} \delta_{\eta\delta} + \delta_{\alpha\eta} \delta_{\epsilon\delta}) + \delta_{\beta\delta} (\delta_{\alpha\epsilon} \delta_{\gamma\eta} + \delta_{\alpha\eta} \delta_{\gamma\epsilon})] ,
 \end{aligned} \tag{5.21}$$

where l , m , and n are Murnaghan constants (Murnaghan 1937), which are a type of third-order elastic constants. The third-order elastic coefficients can also be expressed using other types of third-order elastic constants, such as v_1 , v_2 and v_3 (Toupin and Bernstein 1961):

$$\begin{aligned}
 C_{\alpha\beta\gamma\delta\epsilon\eta} = & v_1 \delta_{\alpha\beta} \delta_{\gamma\delta} \delta_{\epsilon\eta} \\
 & + v_2 [\delta_{\alpha\beta} (\delta_{\gamma\epsilon} \delta_{\delta\eta} + \delta_{\gamma\eta} \delta_{\delta\epsilon}) + \delta_{\gamma\delta} (\delta_{\alpha\epsilon} \delta_{\beta\eta} + \delta_{\alpha\eta} \delta_{\beta\epsilon}) \\
 & + \delta_{\epsilon\eta} (\delta_{\alpha\gamma} \delta_{\beta\delta} + \delta_{\alpha\delta} \delta_{\beta\gamma})] \\
 & + v_3 [\delta_{\alpha\gamma} (\delta_{\beta\epsilon} \delta_{\delta\eta} + \delta_{\beta\eta} \delta_{\delta\epsilon}) + \delta_{\alpha\delta} (\delta_{\beta\epsilon} \delta_{\gamma\eta} + \delta_{\beta\eta} \delta_{\gamma\epsilon}) \\
 & + \delta_{\beta\gamma} (\delta_{\alpha\epsilon} \delta_{\eta\delta} + \delta_{\alpha\eta} \delta_{\epsilon\delta}) + \delta_{\beta\delta} (\delta_{\alpha\epsilon} \delta_{\gamma\eta} + \delta_{\alpha\eta} \delta_{\gamma\epsilon})] .
 \end{aligned} \tag{5.22}$$

It is important to emphasize that in Equation (5.21) and (5.22), the Murnaghan constants l , m , and n cannot be interchangeably replaced by v_1 , v_2 and v_3 , and vice versa. Therefore, Eq. (2) by Stahler et al. (2011) is incorrect since the authors substituted v_1 , v_2 , and v_3 directly with l , m and n . Similar to C_{ijkl} , the third-order elastic coefficients $C_{\alpha\beta\gamma\delta\epsilon\eta}$ can also be represented using Voigt notation as C_{KLM} , which are commonly known as standard third-order elastic coefficients. The standard third-order elastic coefficients exhibit the following symmetry in isotropic materials (Paufler 1988): $C_{IJK} = C_{IKJ} = C_{JIK} = C_{JKI} = C_{KJI} = C_{KIJ}$. Table 5.1 provides a compilation of commonly used third-order elastic constants for isotropic materials reported in the literature.

Table 5.1 Commonly used third-order elastic constants for isotropic materials.

Murnaghan (1937)	Standard Voigt notation (Thurston and Brugger 1964)	Toupin & Bernstein (1961)	Johnson (1981)	Landau & Lifshitz (1986)
l	$C_{111} = C_{222} = C_{333} = 2l + 4m$ $C_{112} = C_{113} = C_{221} = C_{223} =$ $C_{112} = C_{112} = 2l$ $C_{123} = 2l - 2m + n$	$v_1 = 2l - 2m + n$	$\beta_1 = l/3 - m/3 + n/6$	$A = n$
m	$C_{441} = C_{552} = C_{663} = m - n/2$ $C_{442} = C_{443} = C_{551} = C_{553} =$	$v_2 = m - n/2$	$\beta_2 = m - n/2$	$B = m - n/2$
n	$C_{661} = C_{662} = m$ $C_{456} = n/4$	$v_3 = n/4$	$\beta_3 = n/3$	$C = l - m + n/2$

5.3.5 Equation of motion in the initial frame

The equation of motion for the dynamic deformation in the final state is defined as (Pao 1987):

$$\begin{aligned}\frac{\partial T_u^{\text{final}}}{\partial X_j} &= \rho^{\text{final}} \ddot{X}_I \\ &= \rho^{\text{final}} \frac{\partial}{\partial t} \left[\frac{\partial (x_I + u_I^{\text{incremental}})}{\partial t} \right] \\ &= \rho^{\text{final}} \frac{\partial^2 u_I^{\text{incremental}}}{\partial t^2} .\end{aligned}\quad (5.23)$$

Substituting Equation (5.11) into Equation (5.23) gives:

$$\frac{\partial}{\partial x_j} \left(\frac{\rho^{\text{final}}}{\rho^{\text{initial}}} \frac{\partial X_I}{\partial x_i} \frac{\partial X_J}{\partial x_j} S_{ij}^{\text{final}} \right) = \rho^{\text{initial}} \frac{\partial^2 u_I^{\text{incremental}}}{\partial t^2} . \quad (5.24a)$$

Equation (5.24a) can be further written as:

$$\frac{\partial \left(\frac{\partial X_I}{\partial x_i} \right)}{\partial X_J} \frac{\partial X_J}{\partial x_j} S_{ij}^{\text{final}} + \frac{\partial X_I}{\partial x_i} \frac{\partial \left(\frac{\partial X_J}{\partial x_j} \right)}{\partial X_J} S_{ij}^{\text{final}} + \frac{\partial X_I}{\partial x_i} \frac{\partial X_J}{\partial x_j} \frac{\partial S_{ij}^{\text{final}}}{\partial X_J} = \rho^{\text{initial}} \frac{\partial^2 u_I^{\text{incremental}}}{\partial t^2} . \quad (5.24b)$$

The second term on the left side of Equation (5.24b) is equal to zero, while the first and third terms adhere to the chain rule. Therefore, Equation (5.24b) can be simplified into:

$$\frac{\partial}{\partial x_j} \left(S_{ij}^{\text{final}} \frac{\partial X_I}{\partial x_i} \right) = \rho^{\text{initial}} \frac{\partial^2 u_I^{\text{incremental}}}{\partial t^2} . \quad (5.24c)$$

After the substitution of Equation (5.13) and introducing the following equation based on the fact that the deformation from natural to initial state is static in the uniform stress state (Pao and Gamer 1985):

$$\frac{\partial T_{ij}^{\text{initial}}}{\partial x_j} = 0 , \quad (5.25)$$

Equation (5.24c) can be further simplified into:

$$\frac{\partial S_{ij}^{\text{incremental}}}{\partial x_j} + T_{jl}^{\text{initial}} \frac{\partial^2 u_i^{\text{incremental}}}{\partial x_j \partial x_l} = \rho^{\text{initial}} \frac{\partial^2 u_i^{\text{incremental}}}{\partial t^2} . \quad (5.26)$$

Equation (5.26) can also be found in the paper by Pao and Gamer (1985). When deriving Equation (5.26), the products involving the incremental stress tensor and incremental displacement are neglected due to the small magnitude of the dynamic disturbance.

5.3 Theoretical framework of modern acoustoelasticity

Now, we are trying to further simplify the equation of motion by substituting the stress tensor into Equation (5.26). The incremental stress tensor $S_{ij}^{\text{incremental}}$ in the initial frame can be represented by it in the natural frame using the coordinate transformation (Pao and Gamer 1985):

$$\begin{aligned} S_{ij}^{\text{incremental}} &= \frac{\rho^{\text{initial}}}{\rho^0} \frac{\partial x_i}{\partial a_\alpha} \frac{\partial x_j}{\partial a_\beta} S_{\alpha\beta}^{\text{incremental}} \\ &= \frac{1}{2} \frac{\rho^{\text{initial}}}{\rho^0} \frac{\partial x_i}{\partial a_\alpha} \frac{\partial x_j}{\partial a_\beta} \left(\frac{\partial x_k}{\partial a_\gamma} \frac{\partial x_l}{\partial a_\delta} \frac{\partial u_k^{\text{incremental}}}{\partial x_l} + \frac{\partial x_k}{\partial a_\delta} \frac{\partial x_l}{\partial a_\gamma} \frac{\partial u_k^{\text{incremental}}}{\partial x_l} \right) \\ &\quad \times (C_{\alpha\beta\gamma\delta} + C_{\alpha\beta\gamma\delta\epsilon\eta} e_{\epsilon\eta}^{\text{initial}}) . \end{aligned} \quad (5.27)$$

The derivatives of the initial coordinates with respect to natural coordinates in Equation (5.27) can be written as:

$$\frac{\partial x_i}{\partial a_\alpha} = \delta_{i\alpha} + \frac{\partial u_i^{\text{initial}}}{\partial a_\alpha} . \quad (5.28)$$

Therefore, Equation (5.27) can be approximated as:

$$T_{ij}^{\text{incremental}} = \frac{\rho^{\text{initial}}}{\rho^0} \Gamma_{ijkl} \frac{\partial u_k^{\text{incremental}}}{\partial x_l} , \quad (5.29)$$

where

$$\Gamma_{ijkl} = C_{ijkl} + C_{ijklmn} e_{mn}^{\text{initial}} + C_{mjkl} \frac{\partial u_i^{\text{initial}}}{\partial a_m} + C_{imkl} \frac{\partial u_j^{\text{initial}}}{\partial a_m} + C_{ijml} \frac{\partial u_k^{\text{initial}}}{\partial a_m} + C_{ijkn} \frac{\partial u_l^{\text{initial}}}{\partial a_m} . \quad (5.30)$$

Equation (5.30) can also be found in the literature (Pao and Gamer 1985, Janssen 1994).

The initial stress tensor T_{jl}^{initial} can be expressed as:

$$\begin{aligned} T_{jl}^{\text{initial}} &= \frac{\rho^{\text{initial}}}{\rho^0} \frac{\partial x_j}{\partial a_\alpha} \frac{\partial x_l}{\partial a_\beta} S_{\alpha\beta}^{\text{initial}} \\ &= \frac{\rho^{\text{initial}}}{\rho^0} \frac{\partial x_j}{\partial a_\alpha} \frac{\partial x_l}{\partial a_\beta} C_{\alpha\beta\gamma\delta} e_{\gamma\delta}^{\text{initial}} \\ &= \frac{\rho^{\text{initial}}}{\rho^0} C_{jlmn} e_{mn}^{\text{initial}} . \end{aligned} \quad (5.31)$$

The higher-order terms in the constitutive equation are neglected in Equation (5.31). Substituting Equation (5.29) and Equation (5.31) into Equation (5.26) gives the following equation of motion:

$$B_{ijkl} \frac{\partial^2 u_k^{\text{incremental}}}{\partial x_j \partial x_l} = \rho^0 \frac{\partial^2 u_i^{\text{incremental}}}{\partial t^2} , \quad (5.32)$$

where the acoustoelastic moduli B_{ijkl} are defined as

$$\begin{aligned} B_{ijkl} &:= C_{jlmn} e_{mn}^{\text{initial}} \delta_{ik} + \Gamma_{ijkl} \\ &= C_{jlmn} e_{mn}^{\text{initial}} \delta_{ik} + C_{ijkl} + C_{ijklmn} e_{mn}^{\text{initial}} \\ &\quad + C_{mjkl} \frac{\partial u_i^{\text{initial}}}{\partial a_m} + C_{imkl} \frac{\partial u_j^{\text{initial}}}{\partial a_m} + C_{ijml} \frac{\partial u_k^{\text{initial}}}{\partial a_m} + C_{ijkml} \frac{\partial u_l^{\text{initial}}}{\partial a_m} . \end{aligned} \quad (5.33)$$

Equation (5.32) and (5.33) can also be found in the paper by Pao and Gamer (1985). Please note that the strain tensor e_{mn}^{initial} , which is related to the static strain caused by the initial stress, will hereinafter simply referred to as e_{mn} .

5.3.6 Equation of motion in the natural frame

The derivation of the equation of motion in the natural frame is similar to that in the initial frame. Substituting Equation (5.11) into Equation (5.23) gives a similar expression as Equation (5.24):

$$\frac{\partial}{\partial a_\alpha} \left(S_{\alpha\beta}^{\text{final}} \frac{\partial X_I}{\partial a_\beta} \right) = \rho^0 \frac{\partial^2 u_I^{\text{incremental}}}{\partial t^2} . \quad (5.34)$$

Equation (5.34) is the governing equation of motion in the natural frame. Considering that the deformation from natural to the initial state is static, the second Piola-Kirchhoff stress tensor in the natural coordinate system follows (Pao and Gamer 1985):

$$\frac{\partial}{\partial a_\alpha} \left(S_{\alpha\beta}^{\text{initial}} \frac{\partial x_i}{\partial a_\beta} \right) = 0 . \quad (5.35)$$

Therefore, using a similar approach that adopted in deriving the equation of motion in the initial frame, we can obtain:

$$\frac{\partial}{\partial a_\alpha} \left[\left(S_{\alpha\beta}^{\text{initial}} + S_{\alpha\beta}^{\text{incremental}} \right) \frac{\partial (x_I + \partial u_I^{\text{incremental}})}{\partial a_\beta} \right] = \rho^0 \frac{\partial^2 u_I^{\text{incremental}}}{\partial t^2} . \quad (5.36)$$

Considering that the initial second Piola-Kirchhoff stress tensor is static, Equation (5.36) can be written as:

$$S_{\alpha\beta}^{\text{initial}} \frac{\partial^2 u_\xi^{\text{incremental}}}{\partial a_\alpha \partial a_\beta} + \frac{\partial}{\partial a_\beta} \left(S_{\alpha\beta}^{\text{incremental}} \frac{\partial x_\xi}{\partial a_\alpha} \right) = \rho^0 \frac{\partial^2 u_\xi^{\text{incremental}}}{\partial t^2} . \quad (5.37)$$

The initial and incremental second Piola-Kirchhoff stress tensor in Equation (5.37) are:

$$S_{\alpha\beta}^{\text{initial}} = C_{\alpha\beta\epsilon\eta} e_{\epsilon\eta}^{\text{initial}} , \quad (5.38)$$

and

5.3 Theoretical framework of modern acoustoelasticity

$$\begin{aligned}
S_{\alpha\beta}^{\text{incremental}} &= C_{\alpha\beta\gamma\delta} e_{\gamma\delta}^{\text{final}} + \frac{1}{2} C_{\alpha\beta\gamma\delta\epsilon\eta} e_{\gamma\delta}^{\text{final}} e_{\epsilon\eta}^{\text{final}} - C_{\alpha\beta\gamma\delta} e_{\gamma\delta}^{\text{initial}} - \frac{1}{2} C_{\alpha\beta\gamma\delta\epsilon\eta} e_{\gamma\delta}^{\text{initial}} e_{\epsilon\eta}^{\text{initial}} \\
&\simeq C_{\alpha\beta\gamma\delta} e_{\gamma\delta}^{\text{incremental}} + C_{\alpha\beta\gamma\delta\epsilon\eta} e_{\gamma\delta}^{\text{incremental}} e_{\epsilon\eta}^{\text{initial}} \\
&= \frac{1}{2} \left(\frac{\partial x_k}{\partial a_\gamma} \frac{\partial u_k^{\text{incremental}}}{\partial a_\delta} + \frac{\partial x_k}{\partial a_\delta} \frac{\partial u_k^{\text{incremental}}}{\partial a_\gamma} \right) (C_{\alpha\beta\gamma\delta} + C_{\alpha\beta\gamma\delta\epsilon\eta} e_{\epsilon\eta}^{\text{initial}}) \\
&= \frac{1}{2} \left[\left(\delta_{k\gamma} + \frac{\partial u_k^{\text{initial}}}{\partial a_\gamma} \right) \frac{\partial u_k^{\text{incremental}}}{\partial a_\delta} + \left(\delta_{k\delta} + \frac{\partial u_k^{\text{initial}}}{\partial a_\delta} \right) \frac{\partial u_k^{\text{incremental}}}{\partial a_\gamma} \right] (C_{\alpha\beta\gamma\delta} + C_{\alpha\beta\gamma\delta\epsilon\eta} e_{\epsilon\eta}^{\text{initial}}) \\
&\simeq C_{\alpha\beta k\delta} \frac{\partial u_k^{\text{incremental}}}{\partial a_\delta} + C_{\alpha\beta k\delta\epsilon\eta} e_{\epsilon\eta}^{\text{initial}} \frac{\partial u_k^{\text{incremental}}}{\partial a_\delta} + C_{\alpha\beta\gamma\delta} \frac{\partial u_k^{\text{initial}}}{\partial a_\gamma} \frac{\partial u_k^{\text{incremental}}}{\partial a_\delta},
\end{aligned} \tag{5.39}$$

respectively. Accordingly, the term in Equation (5.37) involving the incremental second Piola-Kirchhoff stress tensor is:

$$\begin{aligned}
S_{\alpha\beta}^{\text{incremental}} \frac{\partial x_\xi}{\partial a_\alpha} &= \left(C_{\alpha\beta k\delta} \frac{\partial u_k^{\text{incremental}}}{\partial a_\delta} + C_{\alpha\beta k\delta\epsilon\eta} e_{\epsilon\eta}^{\text{initial}} \frac{\partial u_k^{\text{incremental}}}{\partial a_\delta} + C_{\alpha\beta\gamma\delta} \frac{\partial u_k^{\text{initial}}}{\partial a_\gamma} \frac{\partial u_k^{\text{incremental}}}{\partial a_\delta} \right) \\
&\quad \times \left(\delta_{\xi\alpha} + \frac{\partial u_\xi^{\text{initial}}}{\partial a_\alpha} \right) \\
&\simeq \left(C_{\xi\beta k\delta} + C_{\xi\beta k\delta\epsilon\eta} e_{\epsilon\eta}^{\text{initial}} + C_{\alpha\beta k\delta} \frac{\partial u_\xi^{\text{initial}}}{\partial a_\alpha} + C_{\xi\beta\gamma\delta} \frac{\partial u_k^{\text{initial}}}{\partial a_\gamma} \right) \frac{\partial u_k^{\text{incremental}}}{\partial a_\delta}.
\end{aligned} \tag{5.40}$$

Now, Equation (5.37) can be written as:

$$\begin{aligned}
C_{\beta\delta\epsilon\eta} e_{\epsilon\eta}^{\text{initial}} \frac{\partial^2 u_\xi^{\text{incremental}}}{\partial a_\beta \partial a_\delta} &+ \left(C_{\xi\beta k\delta} + C_{\xi\beta k\delta\epsilon\eta} e_{\epsilon\eta}^{\text{initial}} + C_{\alpha\beta k\delta} \frac{\partial u_\xi^{\text{initial}}}{\partial a_\alpha} + C_{\xi\beta\gamma\delta} \frac{\partial u_k^{\text{initial}}}{\partial a_\gamma} \right) \frac{\partial^2 u_k^{\text{incremental}}}{\partial a_\beta \partial a_\delta} \\
&= \rho^0 \frac{\partial^2 u_\xi^{\text{incremental}}}{\partial t^2}.
\end{aligned} \tag{5.41}$$

Equation (5.41) can be further simplified into:

$$D_{\xi\beta k\delta} \frac{\partial^2 u_k^{\text{incremental}}}{\partial a_\beta \partial a_\delta} = \rho^0 \frac{\partial^2 u_\xi^{\text{incremental}}}{\partial t^2}, \tag{5.42}$$

where the acoustoelastic moduli $D_{\xi\beta k\delta}$ are:

$$D_{\xi\beta k\delta} := C_{\beta\delta\epsilon\eta} e_{\epsilon\eta}^{\text{initial}} \delta_{k\xi} + C_{\xi\beta k\delta} + C_{\xi\beta k\delta\epsilon\eta} e_{\epsilon\eta}^{\text{initial}} + C_{\alpha\beta k\delta} \frac{\partial u_\xi^{\text{initial}}}{\partial a_\alpha} + C_{\xi\beta\gamma\delta} \frac{\partial u_k^{\text{initial}}}{\partial a_\gamma}. \tag{5.43}$$

Equation (5.42) and (5.43) can also be found in the paper by Pao and Gamer (1985). Please note that the strain tensor $e_{\epsilon\eta}^{\text{initial}}$, which is related to the static strain caused by the initial stress, will hereinafter simply referred to as $e_{\epsilon\eta}$.

5.3.7 Plane waves propagation

To investigate the wave velocities among different wave modes, a plane harmonic wave with the following form is introduced into the equation of motion (Hughes and Kelly 1953, King and Fortunko 1983, Pao and Gamer 1985, Cantrell and Salama 1991):

$$u_\gamma = U_\gamma e^{i(kN_\lambda x_\lambda - \omega t)} , \quad (5.44)$$

where N_λ is a unit vector normal to the plane wave that relates to the wave propagation direction, k represents the wavenumber, ω is the angular frequency, and U_γ is the amplitude vector related to the wave polarization direction. The wave mode is dictated by the relation between N_λ and U_γ . When they are orthogonal, indicating that the polarization direction is perpendicular to the wave propagation direction, these waves are identified as transverse or shear waves. Conversely, when the vectors are parallel, signifying that the polarization direction aligns with the wave propagation direction, these waves are termed longitudinal or compression waves. The choice of a harmonic wave is made to simplify the calculations, but the resulting outcome is also applicable to plane waves with a general time function (Pao and Gerner 1985). The second-order partial derivative of Equation (5.44) with respect to time is:

$$\frac{\partial^2 u_i^{\text{incremental}}}{\partial t^2} = (-\omega^2) U_i e^{i(kN_\lambda x_\lambda - \omega t)} . \quad (5.45)$$

The second-order partial derivative of Equation (5.44) with respect to spatial variables is:

$$\frac{\partial^2 u_k^{\text{incremental}}}{\partial x_j \partial x_l} = (\delta_{j\lambda} N_\lambda)(\delta_{l\lambda} N_\lambda)(-k^2) U_k e^{i(kN_\lambda x_\lambda - \omega t)} . \quad (5.46)$$

Therefore, substituting the plane wave propagation into the equation of motion in the initial frame gives:

$$B_{ijkl} (\delta_{j\lambda} N_\lambda)(\delta_{l\lambda} N_\lambda) U_k e^{i(kN_\lambda x_\lambda - \omega t)} = \rho^0 \frac{\omega^2}{k^2} U_i e^{i(kN_\lambda x_\lambda - \omega t)} . \quad (5.47)$$

Equation (5.47) can be further simplified into

$$\left[B_{ijkl} (\delta_{j\lambda} N_\lambda)(\delta_{l\lambda} N_\lambda) - \rho^0 (v^{\text{initial}})^2 \delta_{ik} \right] U_k = 0 , \quad (5.48)$$

where v^{initial} , coinciding with ω/k , denotes the wave velocity in the initial frame. Similarly, substituting the plane wave propagation into the equation of motion in the natural frame gives:

$$\left[D_{\xi\beta k\delta} (\delta_{\beta\lambda} N_\lambda)(\delta_{\delta\lambda} N_\lambda) - \rho^0 (v^{\text{natural}})^2 \delta_{\xi k} \right] U_k = 0 , \quad (5.49)$$

where v^{natural} denotes the wave velocity in the natural frame.

5.4 Bulk wave acoustoelasticity in compressible elastic medium subjected to normal and shear deformations

In Section 5.3, we introduce the theoretical framework of modern acoustoelasticity. This framework holds the potential to accommodate plane waves with arbitrary propagation and polarization directions, as illustrated in Equation (5.48) and (5.49). However, to solve

5.4 Bulk wave acoustoelasticity in compressible elastic medium subjected to normal and shear deformations

these two equations analytically, it is necessary to specify either the propagation vector N_λ or the amplitude vector U_k as known. Both specifying the known propagation vector (Johnson 1981, Pao and Gamer 1985, Duquennoy, Ouafoutou et al. 1999) and the known amplitude vector (King and Fortunko 1983) can be found in the literature. Nevertheless, from an experimental perspective, it is suggested to specify the known propagation vector. This vector, which points in the propagation direction, is easier to determine in experiments than the wave polarization-related amplitude vector. Therefore, we adopt this configuration and propose a governing equation based on Equation (5.48) and (5.49) with a specified unit vector N_λ , while leaving the amplitude vector U_k unspecified. This governing equation will be introduced in Section 5.4.1.

Based on the governing equations, the velocity changes of bulk waves in the medium subject to both normal and shear strains will be investigated through three examples. The classical theory of acoustoelasticity, where the principal stresses coincide with the propagation directions, will be shown as Example 1 in Section 5.4.2. Example 1 consists of acoustoelastic expressions in the both natural and initial frames. Additionally, this example will illustrate the connection between the acoustoelastic expressions in these two frames.

When bulk waves propagate inclined to the principal stress directions in an elastic medium, indicating an angle between the wave propagation direction and principal stress directions, new considerations arise. By establishing a new coordinate system aligned parallel and perpendicular to the wave propagation direction, and calculating the strain matrix within this new coordinate system, we can identify the existence of shear strains. Hence, Example 2 and 3 will illustrate two scenarios depicting the impact of shear strains on wave velocities. Example 2 examines situations where bulk waves travel perpendicular to the shear deformation plane, commonly known as acoustoelastic birefringence. In this example, obtaining analytical solutions is feasible. Example 3 involves bulk waves traveling on the shear deformation plane, posing challenges in deriving analytical forms of acoustoelasticity. Consequently, numerical calculations will be employed to evaluate the effects of shear strain on bulk wave acoustoelasticity in this scenario. Example 2 and 3 will be shown in Section 5.4.3 and 5.4.4, respectively.

As emphasized in the introduction, to the best of our knowledge, there is only one relevant article (Bobrenko, Kutsenko et al. 1990) in the literature that shares similarities with our work. However, this dissertation solely focuses on examining the velocities of bulk waves in a medium subjected to pure shear, without involving any normal deformation.

5.4.1 Governing equation

We specify that the plane wave propagates along the x -axis with the unit vector $\mathbf{N}=(1;0;0)$ and leave the amplitude vector U_k unspecified. Substituting this unit vector into Equation (5.48) and (5.49) gives:

$$\left[B_{ilk1} - \rho^0 \left(v^{\text{initial}} \right)^2 \delta_{ik} \right] U_k = 0 , \quad (5.50)$$

and

$$\left[D_{\xi l k 1} - \rho^0 \left(v^{\text{natural}} \right)^2 \delta_{\xi k} \right] U_k = 0 , \quad (5.51)$$

respectively. The determination of the wave mode relies on the relation between the unit vector N_k and the amplitude vector U_k , as discussed in Section 5.3.7. Equation (5.50) can be expressed in the matrix form as:

$$\begin{bmatrix} B_{1111} & B_{2111} & B_{3111} \\ B_{1121} & B_{2121} & B_{3121} \\ B_{1131} & B_{2131} & B_{3131} \end{bmatrix} \begin{bmatrix} U_1 \\ U_2 \\ U_3 \end{bmatrix} = \rho^0 \left(v^{\text{initial}} \right)^2 \begin{bmatrix} U_1 \\ U_2 \\ U_3 \end{bmatrix} . \quad (5.52)$$

where the acoustoelastic moduli are:

$$\begin{aligned} B_{1111} &= C_{11} + (5C_{11} + C_{111})e_{11} + (C_{12} + C_{112})e_{22} + (C_{13} + C_{113})e_{33} \\ &= \lambda + 2\mu + (5\lambda + 10\mu + 2l + 4m)e_{11} + (\lambda + 2l)(e_{22} + e_{33}) , \end{aligned} \quad (5.53a)$$

$$\begin{aligned} B_{2121} &= C_{66} + (C_{11} + 2C_{66} + C_{661})e_{11} + (C_{12} + 2C_{66} + C_{662})e_{22} + (C_{13} + C_{663})e_{33} \\ &= \mu + (\lambda + 4\mu + m)e_{11} + (\lambda + 2\mu + m)e_{22} + \left(\lambda + m - \frac{n}{2} \right) e_{33} , \end{aligned} \quad (5.53b)$$

$$\begin{aligned} B_{3131} &= C_{55} + (C_{11} + 2C_{55} + C_{551})e_{11} + (C_{13} + 2C_{55} + C_{553})e_{33} + (C_{12} + C_{552})e_{22} \\ &= \mu + (\lambda + 4\mu + m)e_{11} + (\lambda + 2\mu + m)e_{33} + \left(\lambda + m - \frac{n}{2} \right) e_{22} , \end{aligned} \quad (5.53c)$$

$$B_{1121} = B_{2111} = 2(C_{11} + C_{166})e_{12} = (2\lambda + 4\mu + 2m)e_{12} , \quad (5.53d)$$

$$B_{1131} = B_{3111} = 2(C_{11} + C_{155})e_{13} = (2\lambda + 4\mu + 2m)e_{13} , \quad (5.53e)$$

$$B_{2131} = B_{3121} = 2(C_{44} + C_{654})e_{23} = \left(2\mu + \frac{n}{2} \right) e_{23} , \quad (5.53f)$$

where e_{11} , e_{22} and e_{33} represent the normal strains along x -, y - and z -axis, respectively. The shear strains in the x - y , x - z and y - z plane are denoted by e_{12} , e_{13} and e_{23} , respectively. The derivation details of acoustoelastic moduli B_{ijkl} can be found in Appendix A. The second- and third-order elastic coefficients are expressed using the Voigt notations. Please note that in the following sections, we differentiate between strain tensor and principal strains using the following notation: the strain tensor, including normal and shear strains, is represented using e_{ij} , while the principal strain is denoted as e_i .

5.4 Bulk wave acoustoelasticity in compressible elastic medium subjected to normal and shear deformations

Equation (5.52) can be viewed as an eigenvalue equation for the acoustoelastic modulus matrix B_{ijkl} . The eigenvalues of this matrix are equal to $\rho^0(v^{\text{initial}})^2$, with the corresponding eigenvectors being the amplitude vector U_k . Determining the wave velocity necessitates both the eigenvalue and eigenvector: the eigenvector identifies the wave mode, while the eigenvalue provides the velocity of this mode in the initial frame. Thus, eigenvalues and eigenvectors hold equal significance. In the acoustoelastic modulus matrix, the diagonal elements pertain to terms associated with normal strains, while shear strains are hidden within the non-diagonal elements, as depicted in Equation (5.53). In the remainder of this dissertation, the acoustoelastic modulus matrix in Equation (5.52) will be referred to as the B -matrix.

Similarly, in the natural frame, Equation (5.51) can be expressed in the matrix form as:

$$\begin{bmatrix} D_{1111} & D_{2111} & D_{3111} \\ D_{1121} & D_{2121} & D_{3121} \\ D_{1131} & D_{2131} & D_{3131} \end{bmatrix} \begin{bmatrix} U_1 \\ U_2 \\ U_3 \end{bmatrix} = \rho^0 (v^{\text{natural}})^2 \begin{bmatrix} U_1 \\ U_2 \\ U_3 \end{bmatrix}. \quad (5.54)$$

where the acoustoelastic moduli are:

$$\begin{aligned} D_{1111} &= C_{11} + (3C_{11} + C_{111})e_{11} + (C_{12} + C_{112})e_{22} + (C_{13} + C_{113})e_{33} \\ &= \lambda + 2\mu + (3\lambda + 6\mu + 2l + 4m)e_{11} + (\lambda + 2l)(e_{22} + e_{33}), \end{aligned} \quad (5.55a)$$

$$\begin{aligned} D_{2121} &= C_{66} + (C_{11} + C_{661})e_{11} + (C_{12} + 2C_{66} + C_{662})e_{22} + (C_{13} + C_{663})e_{33} \\ &= \mu + (\lambda + 2\mu + m)e_{11} + (\lambda + 2\mu + m)e_{22} + \left(\lambda + m - \frac{n}{2}\right)e_{33}, \end{aligned} \quad (5.55b)$$

$$\begin{aligned} D_{3131} &= C_{55} + (C_{11} + C_{551})e_{11} + (C_{13} + 2C_{55} + C_{553})e_{33} + (C_{12} + C_{552})e_{22} \\ &= \mu + (\lambda + 2\mu + m)e_{11} + (\lambda + 2\mu + m)e_{33} + \left(\lambda + m - \frac{n}{2}\right)e_{22}, \end{aligned} \quad (5.55c)$$

$$\begin{aligned} D_{1121} &= D_{2111} = 2C_{166}e_{12} + C_{66} \frac{\partial u_1^{\text{initial}}}{\partial a_2} + C_{11} \frac{\partial u_2^{\text{initial}}}{\partial a_1} \\ &= 2me_{12} + \mu \frac{\partial u_1^{\text{initial}}}{\partial a_2} + (\lambda + 2\mu) \frac{\partial u_2^{\text{initial}}}{\partial a_1}, \end{aligned} \quad (5.55d)$$

$$\begin{aligned} D_{1131} &= D_{3111} = 2C_{155}e_{13} + C_{55} \frac{\partial u_1^{\text{initial}}}{\partial a_3} + C_{11} \frac{\partial u_3^{\text{initial}}}{\partial a_1} \\ &= 2me_{13} + \mu \frac{\partial u_1^{\text{initial}}}{\partial a_3} + (\lambda + 2\mu) \frac{\partial u_3^{\text{initial}}}{\partial a_1}, \end{aligned} \quad (5.55e)$$

$$D_{2131} = D_{3121} = 2(C_{44} + C_{654})e_{23} = \left(2\mu + \frac{n}{2}\right)e_{23}. \quad (5.55f)$$

Equation (5.54) can be viewed as an eigenvalue equation for the acoustoelastic modulus matrix $D_{\alpha\beta k\delta}$, and the eigenvectors and eigenvalues can be used to determine the wave

mode and its corresponding velocity in the natural frame. The derivation details of acoustoelastic moduli $D_{\varepsilon\beta k\delta}$ can be found in Appendix B. In the remainder of this dissertation, the acoustoelastic modulus matrix in Equation (5.54) will be referred to as the D -matrix.

Please note that two primary distinctions exist between the acoustoelastic moduli in the initial and natural frames. Firstly, the difference between diagonal elements in acoustoelastic moduli obtained in the natural and initial frames is either $2(\lambda+2\mu)e_{11}$ or $2\mu e_{11}$. This value is related to the consideration of pre-deformation, which will be further discussed in Section 5.4.2. Secondly, some acoustoelastic moduli in the natural frame can only be determined through the use of deformation (refer to Equation (5.55d) and (5.55e)), whereas all corresponding moduli in the initial frame can be derived from strains. Therefore, the analytical analysis in Section 5.4.3 and 5.4.4 will primarily rely on expressions in the initial frame, where velocities can be obtained through strains.

5.4.2 Example 1: waves propagating parallel or perpendicular to the principal deformations

The existing modern acoustoelastic assumes that three principal stresses are applied along x -, y - and z -axis, respectively (Hughes and Kelly 1953, Toupin and Bernstein 1961, Thurston and Brugger 1964, Johnson 1981, Pao and Gamer 1985). The principal strains that are induced by these principal stresses are denoted as e_1 , e_2 and e_3 along x -, y - and z -axis, respectively. Therefore, Equation (5.52) can be expressed as:

$$\begin{bmatrix} B_{1111} & 0 & 0 \\ 0 & B_{2121} & 0 \\ 0 & 0 & B_{3131} \end{bmatrix} \begin{bmatrix} U_1 \\ U_2 \\ U_3 \end{bmatrix} = \rho^0 (v^{\text{initial}})^2 \begin{bmatrix} U_1 \\ U_2 \\ U_3 \end{bmatrix}, \quad (5.56)$$

where acoustoelastic moduli B_{1111} , B_{2121} and B_{3131} are:

$$B_{1111} = C_{11} + (5C_{11} + C_{111})e_1 + (C_{12} + C_{112})e_2 + (C_{13} + C_{113})e_3, \quad (5.57a)$$

$$B_{2121} = C_{66} + (C_{11} + 2C_{66} + C_{661})e_1 + (C_{12} + 2C_{66} + C_{662})e_2 + (C_{13} + C_{663})e_3, \quad (5.57b)$$

$$B_{3131} = C_{55} + (C_{11} + 2C_{55} + C_{551})e_1 + (C_{13} + 2C_{55} + C_{553})e_3 + (C_{12} + C_{552})e_2. \quad (5.57c)$$

The diagonal elements are zero since only the principal stresses involved. As the B -matrix in Equation (5.56) is diagonal, its three eigenvectors are $(1;0;0)$, $(0;1;0)$, and $(0;0;1)$. Correspondingly, the three eigenvalues are B_{1111} , B_{2121} and B_{3131} , and three velocities are $(B_{1111}/\rho^0)^{1/2}$, $(B_{2121}/\rho^0)^{1/2}$ and $(B_{3131}/\rho^0)^{1/2}$. Considering that the propagation direction is $(1;0;0)$, the eigenvalue $(B_{1111}/\rho^0)^{1/2}$ corresponds to the velocity of the longitudinal wave, while the remaining $(B_{2121}/\rho^0)^{1/2}$ and $(B_{3131}/\rho^0)^{1/2}$ correspond to the velocities of transverse waves. Moreover, in the absence of externally induced strain in the isotropic medium, the wave velocities are $[(\lambda+2\mu)/\rho^0]^{1/2}$ and $(\mu/\rho^0)^{1/2}$, representing longitudinal and transverse wave velocities, respectively.

5.4 Bulk wave acoustoelasticity in compressible elastic medium subjected to normal and shear deformations

The acoustoelasticity in the natural frame in the scenario that principal stresses are applied along x -, y - and z -axis is shown as follows:

$$\begin{bmatrix} D_{1111} & 0 & 0 \\ 0 & D_{2121} & 0 \\ 0 & 0 & D_{3131} \end{bmatrix} \begin{bmatrix} U_1 \\ U_2 \\ U_3 \end{bmatrix} = \rho^0 (v^{\text{natural}})^2 \begin{bmatrix} U_1 \\ U_2 \\ U_3 \end{bmatrix}, \quad (5.58)$$

where acoustoelastic moduli D_{1111} , D_{2121} and D_{3131} are:

$$D_{1111} = C_{11} + (3C_{11} + C_{111})e_1 + (C_{12} + C_{112})e_2 + (C_{13} + C_{113})e_3, \quad (5.59a)$$

$$D_{2121} = C_{66} + (C_{11} + C_{661})e_1 + (C_{12} + 2C_{66} + C_{662})e_2 + (C_{13} + C_{663})e_3, \quad (5.59b)$$

$$D_{3131} = C_{55} + (C_{11} + C_{551})e_1 + (C_{12} + C_{552})e_2 + (C_{13} + 2C_{55} + C_{553})e_3. \quad (5.59c)$$

The determination of the wave modes and corresponding velocities here follows the same method as described after Equation (5.56), which will not be reiterated in this context.

The difference in longitudinal wave velocity acquired using modern acoustoelasticity between the natural and initial frames can be approximated by employing Taylor expansion, as shown below:

$$\begin{aligned} \sqrt{\frac{B_{1111}}{\rho^0}} - \sqrt{\frac{D_{1111}}{\rho^0}} &\approx \frac{1}{2} \frac{1}{\sqrt{\frac{D_{1111}}{\rho^0}}} \left(\frac{B_{1111}}{\rho^0} - \frac{D_{1111}}{\rho^0} \right) \\ &= \sqrt{\frac{C_{11}^2}{\rho^0 D_{1111}}} e_{11} \\ &\approx \sqrt{\frac{C_{11}}{\rho^0}} e_{11}. \end{aligned} \quad (5.60)$$

The assumption made during the derivation from step 2 to step 3 in Equation (5.60) is that the terms in D_{1111} involving static strain are significantly smaller than C_{11} . Consequently, D_{1111} can be approximated as equal to C_{11} in this scenario. Considering that $(C_{11}/\rho^0)^{1/2}$ is the longitudinal wave velocity in the medium without external load applied, the primary distinction between these two frames lies in whether the travel time in the pre-deformed length in the propagation direction is considered. The natural wave velocity represents the original length in the direction of propagation divided by the time of flight, while the velocity in the initial frame of reference is determined by the quotient of the pre-deformed length in the direction of propagation and the time of flight (Pao and Gamer 1985). This suggests that correcting the wave path at each load step is necessary to obtain the velocity in the initial frame, whereas the velocity in the natural frame does not require such correction.

Please note that the velocity change of the medium measured using WI techniques, such as the stretching and WCS techniques, reflects the velocity change in the natural frame.

The fundamental assumption underlying the interpretation of medium velocity change via WI techniques is that travel time is inversely proportional to velocity, aligning with observations in the natural frame.

5.4.3 Example 2: waves propagating perpendicular to the shear deformation plane – acoustoelastic birefringence

The second example addresses a scenario where the bulk wave travels perpendicular to the shear deformation plane in an isotropic material. In this instance, the polarization directions of two transverse wave modes always align with the principal stress directions. It is worth highlighting that the primary application scenario for the associated theory in this example is in slightly anisotropic materials such as rolled metals (Imanishi, Sasabe et al. 1982) and woods (Hasegawa and Sasaki 2004, Hasegawa and Sasaki 2004, Hasegawa and Sasaki 2004) to decouple the velocity variations induced by material textures and applied stresses (Iwashimizu and Kubomura 1973).

Suppose that the directions of three principal stresses are aligned with the x , y and z axes, respectively, as depicted in Figure 5.2(a). The corresponding principal strains are denoted as e_1 , e_2 and e_3 . The three principal stresses can either be tensile or compressive. Assuming that the wave is propagating along the x -axis. The initial governing equation under the principal strain is:

$$\begin{bmatrix} B_{1111}^0 & 0 & 0 \\ 0 & B_{2121}^0 & 0 \\ 0 & 0 & B_{3131}^0 \end{bmatrix} \begin{bmatrix} U_1 \\ U_2 \\ U_3 \end{bmatrix} = \rho^0 \left(v^{\text{initial}} \right)^2 \begin{bmatrix} U_1 \\ U_2 \\ U_3 \end{bmatrix}, \quad (5.61)$$

where v^{initial} represents the velocity in this state, and the elements in the B^0 -matrix before coordinate transformation are:

$$B_{1111}^0 = \lambda + 2\mu + (5\lambda + 10\mu + 2l + 4m)e_1 + (\lambda + 2l)(e_2 + e_3), \quad (5.62a)$$

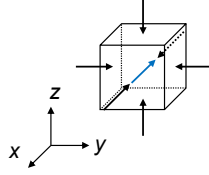
$$B_{2121}^0 = \mu + (\lambda + 4\mu + m)e_1 + (\lambda + 2\mu + m)e_2 + \left(\lambda + m - \frac{n}{2} \right) e_3, \quad (5.62b)$$

$$B_{3131}^0 = \mu + (\lambda + 4\mu + m)e_1 + (\lambda + 2\mu + m)e_3 + \left(\lambda + m - \frac{n}{2} \right) e_2. \quad (5.62c)$$

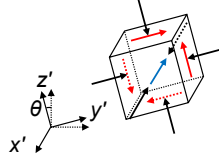
The shear strain in the y - z plane is implemented by transforming the principal strain to a new coordinate system, which can be obtained by rotating around the x -axis with a certain angle θ , as shown in Figure 5.2(b). After the coordinate transformation, the new strain matrix is shown as follows:

5.4 Bulk wave acoustoelasticity in compressible elastic medium subjected to normal and shear deformations

$$\begin{bmatrix} e_{11} & e_{12} & e_{13} \\ e_{21} & e_{22} & e_{23} \\ e_{31} & e_{32} & e_{33} \end{bmatrix} = \begin{bmatrix} 1 & 0 & 0 \\ 0 & \cos(\theta) & \sin(\theta) \\ 0 & -\sin(\theta) & \cos(\theta) \end{bmatrix} \begin{bmatrix} e_1 & 0 & 0 \\ 0 & e_2 & 0 \\ 0 & 0 & e_3 \end{bmatrix} \begin{bmatrix} 1 & 0 & 0 \\ 0 & \cos(\theta) & -\sin(\theta) \\ 0 & \sin(\theta) & \cos(\theta) \end{bmatrix}. \quad (5.63)$$



(a) Triaxial principal stress state for the principal strain condition (black arrow: normal stress direction; blue arrow: wave propagation direction).



(b) Stress state for the strain condition after transforming to a new coordinate system (black arrow: normal stress direction; red arrow: shear stress direction; blue arrow: wave propagation direction).

Figure 5.2 Stress states before and after the rotation of the coordinate system in Example 2.

The governing equation with the wave propagating along the x' -axis (or x -axis) after the rotation can be written as:

$$\begin{bmatrix} B_{1111} & 0 & 0 \\ 0 & B_{2121} & B_{3121} \\ 0 & B_{2131} & B_{3131} \end{bmatrix} \begin{bmatrix} U_1 \\ U_2 \\ U_3 \end{bmatrix} = \rho^0 (\bar{v}^{\text{initial}})^2 \begin{bmatrix} U_1 \\ U_2 \\ U_3 \end{bmatrix}, \quad (5.64)$$

where \bar{v}^{initial} represents the velocity in the new coordinate system, and elements in the B -matrix after the coordinate transformation are:

$$\begin{aligned} B_{1111} &= \lambda + 2\mu + (5\lambda + 10\mu + 2l + 4m)e_{11} + (\lambda + 2l)(e_{22} + e_{33}) \\ &= \lambda + 2\mu + (5\lambda + 10\mu + 2l + 4m)e_1 + (\lambda + 2l)(e_2 + e_3) = B_{1111}^0, \end{aligned} \quad (5.65a)$$

$$\begin{aligned} B_{2121} &= \mu + (\lambda + 4\mu + m)e_{11} + (\lambda + 2\mu + m)e_{22} + \left(\lambda + m - \frac{n}{2}\right)e_{33} \\ &= \mu + (\lambda + 4\mu + m)e_1 + (\lambda + 2\mu + m)[\cos^2(\theta)e_2 + \sin^2(\theta)e_3] \\ &\quad + \left(\lambda + m - \frac{n}{2}\right)[\cos^2(\theta)e_3 + \sin^2(\theta)e_2], \end{aligned} \quad (5.65b)$$

$$B_{3131} = \mu + (\lambda + 4\mu + m)e_{11} + (\lambda + 2\mu + m)e_{33} + \left(\lambda + m - \frac{n}{2}\right)e_{22} \quad (5.65c)$$

$$= \mu + (\lambda + 4\mu + m)e_1 + (\lambda + 2\mu + m)[\cos^2(\theta)e_3 + \sin^2(\theta)e_2] \\ + \left(\lambda + m - \frac{n}{2}\right)[\cos^2(\theta)e_2 + \sin^2(\theta)e_3] ,$$

$$B_{2131} = B_{3121} = \left(2\mu + \frac{n}{2}\right)e_{23} = \left(2\mu + \frac{n}{2}\right)\sin(\theta)\cos(\theta)(e_3 - e_2) . \quad (5.65d)$$

The parameter B_{1111} remains equal to the initial B_{1111}^0 , indicating that the presence of shear strain does not alter the longitudinal wave velocity in this particular strain configuration. The B -matrix in Equation (5.64) is diagonalizable and can be decomposed as:

$$\begin{bmatrix} B_{1111} & 0 & 0 \\ 0 & B_{2121} & B_{3121} \\ 0 & B_{2131} & B_{3131} \end{bmatrix} \quad (5.66)$$

$$= \begin{bmatrix} 1 & 0 & 0 \\ 0 & \cos(\theta) & \sin(\theta) \\ 0 & -\sin(\theta) & \cos(\theta) \end{bmatrix} \begin{bmatrix} B_{1111}^0 & 0 & 0 \\ 0 & B_{2121}^0 & 0 \\ 0 & 0 & B_{3131}^0 \end{bmatrix} \begin{bmatrix} 1 & 0 & 0 \\ 0 & \cos(\theta) & -\sin(\theta) \\ 0 & \sin(\theta) & \cos(\theta) \end{bmatrix} .$$

Notably, Equation (5.66) is strikingly similar to the decomposition of strain matrix in Equation (5.63). The three eigenvectors in Equation (5.66) are $(1;0;0)$, $(0;\cos\theta;\sin\theta)$, and $(0;-\sin\theta;\cos\theta)$, which are exactly the same as those for the strain matrix in Equation (5.63). The first one is aligned with the propagation direction $(1;0;0)$, which represents the longitudinal wave mode. The latter two are orthogonal to the propagation direction, which are relevant to the two transverse wave modes. Given that the eigenvectors specified in Equation (5.63) denote the principal strain directions, it becomes evident that in this particular scenario, the polarization directions of bulk waves consistently align with the principal strain directions.

In addition, as shown in Equation (5.66), the eigenvalues of the B -matrix are solely determined by the B^0 -matrix, which is calculated based on the principal strain. This implies that, in this given configuration, if the magnitudes and directions of the principal strains and the material elastic constants remain constant, the wave velocity, whether it is for the longitudinal or transverse wave, will remain constant regardless of the rotation of the coordinate system or the magnitude of the shear strain. The difference between the second and third eigenvalues of the B -matrix can be determined through:

$$B_{2121}^0 - B_{3131}^0 = \rho^0 \left[\left(v_{S2}^{\text{initial}}\right)^2 - \left(v_{S3}^{\text{initial}}\right)^2 \right] = \left(2\mu + \frac{n}{2}\right)(e_2 - e_3) , \quad (5.67)$$

where v_{S2}^{initial} and v_{S3}^{initial} are the second and third eigenvalue-based transverse wave velocities. Equation (5.67) is the initial frame version of Eq. 44 by Pao and Gamer (1985) under the condition of the isotropic material. This equation reveals that the difference

5.4 Bulk wave acoustoelasticity in compressible elastic medium subjected to normal and shear deformations

between the squared velocities of two transverse waves is proportional to the difference in principal strain, which is commonly referred to as the acoustoelastic birefringence (Iwashimizu and Kubomura 1973, Imanishi, Sasabe et al. 1982, King and Fortunko 1983, Sasaki and Hasegawa 2007).

From this specific instance, one might notice that the influence of shear strains on the transverse wave velocity cannot be ignored. This observation stems from two aspects. Firstly, as the coordinate system rotates, the normal strain undergoes alterations while the transverse wave velocity remains constant. If the transverse wave velocities are exclusively dependent on the normal strains, their values cannot be constant during the rotation. Hence, this observation indicates the involvement of shear strains in the process. Secondly, in this scenario, wave polarization always aligns with principal strain directions. If the effect of shear strains is minimal, the moduli B_{2131} and B_{3121} in Equation (5.66) can be disregarded, resulting in an diagonalized B -matrix. Consequently, the eigenvectors in this matrix, which are $(1;0;0)$, $(0;1;0)$ and $(0;0;1)$, consistently align with the new coordinate system's axes after rotation. However, in reality, polarization remains unchanged during coordinate system rotation, underscoring the significance of shear strain influence on polarization direction.

5.4.4 Example 3: Wave propagating on the shear deformation plane

Example 2 presents a scenario where the bulk wave travels perpendicular to the shear deformation plane within an isotropic material. In this section, we will explore the propagation of bulk waves on the shear deformation plane under a plane stress state, where the out-of-plane principal stress is negligible. Such a stress state is commonly encountered in structural materials like concrete (Mosley, Bungey et al. 1999, Bing, Park et al. 2001).

In this example, the analytical analysis will be presented first in Section 5.4.4.1. As obtaining the analytical solution for acoustoelasticity in this case is challenging, a numerical analysis will be carried out in Section 5.4.4.2. This analysis will utilize the mechanical properties of concrete to explore the influence of shear deformations on acoustoelasticity. Unlike structural or aerospace members made of metallic materials or polymers in which elastic waves are predominantly Lamb and Rayleigh waves due to their thin thickness, concrete elements are usually of comparable dimensions in all axes, making the study of bulk wave acoustoelasticity in concrete important. In this section, we consider concrete as statistically isotropic and statistically homogeneous. Such an assumption is expected to be reasonable for concrete at a sufficiently long length scale (Turner and Anugonda 2001).

5.4.4.1 Analytical analysis

Suppose that the directions of two principal stresses are aligned with the x and y axes, respectively, as depicted in Figure 5.3(a). The corresponding principal strains along the x and y axes are denoted as e_1 and e_2 , respectively. Please note that there exists another principal strain, e_3 , pointed upward, which is not shown in Figure 5.3(a). The two principal stresses can either be tensile or compressive. The bulk wave propagates along the x -axis in this example, same with the configuration in Example 1 and 2. The governing equation for the biaxial strain state is:

$$\begin{bmatrix} B_{1111}^0 & 0 & 0 \\ 0 & B_{2121}^0 & 0 \\ 0 & 0 & B_{3131}^0 \end{bmatrix} \begin{bmatrix} U_1 \\ U_2 \\ U_3 \end{bmatrix} = \rho^0 (v^{\text{initial}})^2 \begin{bmatrix} U_1 \\ U_2 \\ U_3 \end{bmatrix}, \quad (5.68)$$

where the three eigenvalues of the B^0 -matrix, B_1^0 , B_2^0 and B_3^0 , are:

$$B_1^0 = B_{1111}^0 = \lambda + 2\mu + (5\lambda + 10\mu + 2l + 4m)e_1 + (\lambda + 2l)(e_2 + e_3), \quad (5.69a)$$

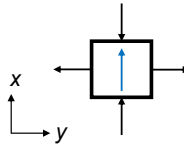
$$B_2^0 = B_{2121}^0 = \mu + (\lambda + 4\mu + m)e_1 + (\lambda + 2\mu + m)e_2 + \left(\lambda + m - \frac{n}{2}\right)e_3, \quad (5.69b)$$

$$B_3^0 = B_{3131}^0 = \mu + (\lambda + 4\mu + m)e_1 + (\lambda + 2\mu + m)e_3 + \left(\lambda + m - \frac{n}{2}\right)e_2. \quad (5.69c)$$

From Equation (5.68), it is apparent that the first eigenvalue, B_1^0 , correlates with the longitudinal wave velocity, whereas the second and third eigenvalues, B_2^0 and B_3^0 , correspond to the transverse wave velocities. The introduction of shear strains in the x - y plane involves rotating the original coordinate system x - y to a new coordinate system x' - y' with a specific angle θ , as illustrated in Figure 5.3(b). Since the direction of principal strain e_3 is along the axis of rotation, its value remains constant during the rotation. Then, the simplified transformation of the strain matrix can be obtained through:

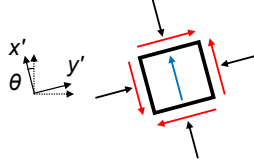
$$\begin{bmatrix} e_{11} & e_{12} \\ e_{21} & e_{22} \end{bmatrix} = \begin{bmatrix} \cos(\theta) & \sin(\theta) \\ -\sin(\theta) & \cos(\theta) \end{bmatrix} \begin{bmatrix} e_1 & 0 \\ 0 & e_2 \end{bmatrix} \begin{bmatrix} \cos(\theta) & -\sin(\theta) \\ \sin(\theta) & \cos(\theta) \end{bmatrix}, \quad (5.70)$$

where θ is the angle between the x -axis and x' -axis after the rotation of the coordinate system.



(a) Biaxial principal stress state for the principal strain condition (black arrow: normal strain direction; blue arrow: wave propagation direction).

5.4 Bulk wave acoustoelasticity in compressible elastic medium subjected to normal and shear deformations



(b) Stress state for the strain condition after transforming to a new coordinate system (black arrow: normal stress direction; red arrow: shear stress direction; blue arrow: wave propagation direction).

Figure 5.3 Stress states before and after the rotation of the coordinate system in Example 3.

After the coordinate rotation, the wave will propagate along the new x' -axis, and the new governing equation is:

$$\begin{bmatrix} B_{1111} & B_{2111} & 0 \\ B_{1121} & B_{2121} & 0 \\ 0 & 0 & B_{3131} \end{bmatrix} \begin{bmatrix} U_1 \\ U_2 \\ U_3 \end{bmatrix} = \rho^0 (\bar{v}^{\text{initial}})^2 \begin{bmatrix} U_1 \\ U_2 \\ U_3 \end{bmatrix}, \quad (5.71)$$

where the acoustoelastic moduli in the B -matrix are:

$$B_{1111} = \lambda + 2\mu + (5\lambda + 10\mu + 2l + 4m)e_{11} + (\lambda + 2l)(e_{22} + e_{33}), \quad (5.72a)$$

$$B_{2121} = \mu + (\lambda + 4\mu + m)e_{11} + (\lambda + 2\mu + m)e_{22} + \left(\lambda + m - \frac{n}{2}\right)e_{33}, \quad (5.72b)$$

$$B_{3131} = \mu + (\lambda + 4\mu + m)e_{11} + (\lambda + 2\mu + m)e_{33} + \left(\lambda + m - \frac{n}{2}\right)e_{22}, \quad (5.72c)$$

$$B_{1121} = B_{2111} = (2\lambda + 4\mu + 2m)e_{12}. \quad (5.72d)$$

Since the B -matrix in Equation (5.71) is symmetrical, the analytical solutions for three eigenvalues of this matrix, denoted as, B_1 , B_2 and B_3 , are:

$$B_1 = \frac{B_{1111} + B_{2121} + \sqrt{(B_{1111} - B_{2121})^2 + 4B_{2111}^2}}{2} \quad (5.73a)$$

$$= B_{1111} + \frac{\sqrt{1 + \frac{4B_{2111}^2}{(B_{1111} - B_{2121})^2}} - 1}{2} (B_{1111} - B_{2121}),$$

$$B_2 = \frac{B_{1111} + B_{2121} - \sqrt{(B_{1111} - B_{2121})^2 + 4B_{2111}^2}}{2} \quad (5.73b)$$

$$= B_{2121} - \frac{\sqrt{1 + \frac{4B_{2111}^2}{(B_{1111} - B_{2121})^2}} - 1}{2} (B_{1111} - B_{2121}),$$

$$B_3 = B_{3131}. \quad (5.73c)$$

The first and second eigenvalues comprise the diagonal elements in the B -matrix, such as B_{1111} and B_{2121} , as well as a term related to shear deformation, B_{2111} . To better understand

the impact of shear deformation-related terms on changes in eigenvalues during coordinate transformations, the difference between the same eigenvalue before and after the coordinate transformation is calculated using:

$$B_1 - B_1^0 = B_{1111} - B_{1111}^0 + \frac{\sqrt{1 + \frac{4B_{2111}^2}{(B_{1111} - B_{2121})^2}} - 1}{2} (B_{1111} - B_{2121}) , \quad (5.74a)$$

$$B_2 - B_2^0 = B_{2121} - B_{2121}^0 - \frac{\sqrt{1 + \frac{4B_{2111}^2}{(B_{1111} - B_{2121})^2}} - 1}{2} (B_{1111} - B_{2121}) . \quad (5.74b)$$

As depicted in Equation (5.74), the change in eigenvalue can be separated into two components: the variation in the diagonal element B_{1111} or B_{2121} due to the alteration in the normal strain, and the change in the term related to the shear strain.

Equation (5.71) indicates that the third eigenvalue, B_3 , is associated with the transverse wave velocity. Since the initial first eigenvalue B_1^0 in Equation (5.69) is related to the velocity of longitudinal waves, it is probable that the first eigenvalue B_1 in Equation (5.73) is also linked to the longitudinal wave velocity, which can be calculated through $(B_1/\rho_0)^{1/2}$. Similarly, the second eigenvalue, B_2 , corresponds to the transverse wave velocity $(B_2/\rho_0)^{1/2}$. Considering the close relationship between the first eigenvalue B_1 and the first diagonal element in the B -matrix B_{1111} shown in Equation (5.73a), there is a potential representation of longitudinal wave velocity through B_{1111} , expressed as $(B_{1111}/\rho_0)^{1/2}$. However, it is important to note that this longitudinal wave velocity is an approximation and may deviate from the exact value $(B_1/\rho_0)^{1/2}$. Likewise, the approximation of the transverse wave velocity can be expressed as $(B_{2121}/\rho_0)^{1/2}$. Utilizing the exact and approximate velocities, we can then calculate four velocity changes using the following equations based on the diagonal elements and the eigenvalues to assess potential discrepancies between exact and approximate velocities:

$$\frac{dv}{v_{P,app}} = \frac{\sqrt{\frac{B_{1111}}{\rho^0}} - \sqrt{\frac{\lambda + 2\mu}{\rho^0}}}{\sqrt{\frac{\lambda + 2\mu}{\rho^0}}} = \frac{\sqrt{B_{1111}} - \sqrt{\lambda + 2\mu}}{\sqrt{\lambda + 2\mu}} , \quad (5.75a)$$

$$\frac{dv}{v_{P,exa}} = \frac{\sqrt{\frac{B_1}{\rho^0}} - \sqrt{\frac{\lambda + 2\mu}{\rho^0}}}{\sqrt{\frac{\lambda + 2\mu}{\rho^0}}} = \frac{\sqrt{B_1} - \sqrt{\lambda + 2\mu}}{\sqrt{\lambda + 2\mu}} , \quad (5.75b)$$

$$\frac{dv}{v_{S,app}} = \frac{\sqrt{\frac{B_{2121}}{\rho^0}} - \sqrt{\frac{\mu}{\rho^0}}}{\sqrt{\frac{\mu}{\rho^0}}} = \frac{\sqrt{B_{2121}} - \sqrt{\mu}}{\sqrt{\mu}} , \quad (5.75c)$$

5.4 Bulk wave acoustoelasticity in compressible elastic medium subjected to normal and shear deformations

$$\frac{dv}{v_{S, \text{exa}}} = \frac{\sqrt{\frac{B_2}{\rho^0}} - \sqrt{\frac{\mu}{\rho^0}}}{\sqrt{\frac{\mu}{\rho^0}}} = \frac{\sqrt{B_2} - \sqrt{\mu}}{\sqrt{\mu}}, \quad (5.75d)$$

where $dv/v_{P, \text{app}}$, $dv/v_{P, \text{exa}}$, $dv/v_{S, \text{app}}$ and $dv/v_{S, \text{exa}}$ represent the approximate velocity changes of longitudinal wave using the first diagonal element B_{1111} , the exact velocity changes of longitudinal wave calculated using the first eigenvalue B_1 , the approximate velocity changes of transverse wave using the second diagonal element B_{2121} , and the exact velocity changes of transverse wave calculated using the second eigenvalue B_2 , respectively.

Unlike Example 2, it is not feasible to draw any conclusions regarding the impact of shear deformation on the wave mode and its corresponding velocity solely through analytical analysis in Example 3. Hence, a numerical analysis is required.

5.4.4.2 Numerical analysis

The Lamé parameters and Murnaghan constants of concrete used in the numerical analysis are obtained from the paper by Nogueira and Rens (2019). To induce large shear stress during the rotation of the coordinate system, the compressive stress σ_1 is applied along the x -axis with a magnitude of 40% of the compressive strength as one of the principal stresses, as shown in Figure 5.3(a). It should be noted that the concrete is still considered to be in the elastic stage under this condition (Materials 2017). Considering the low concrete tensile strength, in the y -axis a tensile stress of 3 MPa is applied. The influence of wave propagation angle θ to the wave velocity is studied by rotating the angle θ from 0° to 90° with steps of 5° , while maintaining the principal stresses unchanged. The shear stress arises immediately as the coordinate rotation commences and reaches its maximum at an angle of 45° .

The static strain is determined by dividing the stress by the elastic modulus or shear modulus. Please be aware here that strain we are using is the tensorial strain. This section exclusively presents the results based on the mechanical properties of Specimen 1 reported by Nogueira and Rens (2019), while the numerical results employing the properties of other specimens can be found in Appendix C. The compressive strength of Specimen 1 is 33.1 MPa, and the magnitude of applied compressive stress is $40\% \times 33.1 \text{ MPa} = 13.24 \text{ MPa}$.

The changes in B_{1111} and shear deformation-related term relative to the original principal stress state calculated based on Equation (5.74a) are shown in Figure 5.4. The horizontal axis represents the angle between the wave propagation direction and x -axis of the coordinate system. As the coordinate system rotates, the changes in B_{1111} (depicted by the solid black line in Figure 5.4) are much more significant than those in the shear defor-

mation-related term (represented by the dash-dotted black line in Figure 5.4). Consequently, the variation in the first eigenvalue, B_1 , is primarily influenced by the changes in B_{1111} . This is evident from the nearly identical absolute values of B_{1111} (shown by the dotted grey line in Figure 5.4) and B_1 (displayed by the dashed grey line in Figure 5.4). Since changes in B_{1111} are solely attributed to variations in the normal strain, it can be concluded that the variation in shear strain has minimal impact on B_1 .

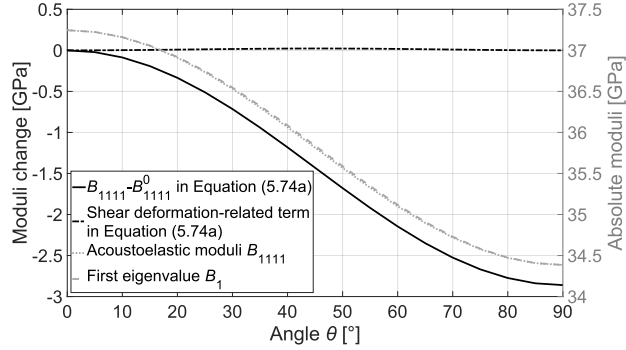


Figure 5.4 The change in B_{1111} and shear deformation-related term relative to the original principal stress state calculated based on Equation (5.74a), and the comparison between the moduli B_{1111} and B_1 during the coordinate transformation.

However, relying solely on the knowledge of the first eigenvalue is insufficient to determine the wave mode it corresponds to. Therefore, it is important to examine the first eigenvector during the coordinate transformation as well. Figure 5.5 displays the first and second scalars in the first eigenvector, while the third scalar (which remains constant at 0) is not included in this figure. The first scalar gradually decreases as the shear strain emerges, yet it remains significantly larger than the second scalar and remains close to 1. Considering that the wave propagates in the direction of (1;0;0), the first eigenvector is not perfectly parallel with the propagation direction. This phenomenon was anticipated by Pao and Gamer (1985) in their article: *in general, neither of obtained polarization direction is parallel to the propagation direction* (page 809). In their article, this type of wave is referred to as a *quasi-longitudinal wave*, and subsequent researchers have adopted this terminology (Bobrenko, Kutsenko et al. 1990).

5.4 Bulk wave acoustoelasticity in compressible elastic medium subjected to normal and shear deformations

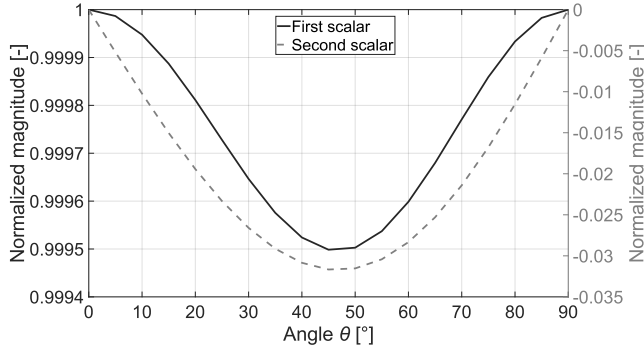


Figure 5.5 The first and second scalars in the first eigenvector of the B -matrix in Equation (5.71) during the coordinate transformation.

Figure 5.6 presents the numerical results of the changes in B_{2121} and the shear deformation-related term relative to the original principal stress state based on Equation (5.74b). Unlike the previous findings in Figure 5.4, the change in the shear deformation-related term (represented by the dash-dotted black line in Figure 5.6) is significant compared to that of B_{2121} (depicted by the solid black line in Figure 5.6). Consequently, there is a noticeable discrepancy between B_{2121} (the dotted grey line in Figure 5.6) and B_2 (the dashed grey line in Figure 5.6) when the shear strain emerges. Moving on to Figure 5.7, we examine the first and second scalars in the second eigenvector of the B -matrix during the coordinate transformation. Similar to the observations in Figure 5.5, it is evident that the wave does not conform to a pure transverse wave mode. This particular type of transverse wave is commonly referred to as a *quasi-transverse wave* (Pao and Gamer 1985).

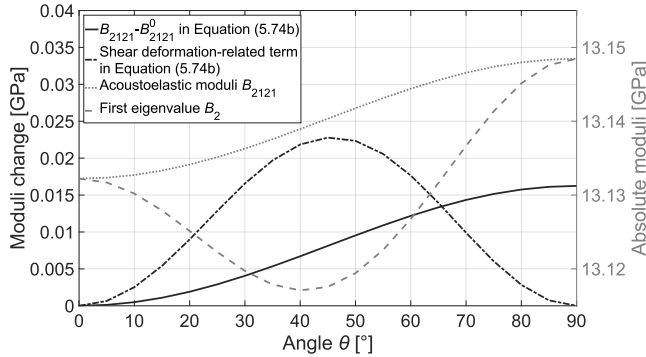


Figure 5.6 Change in B_{2121} and the shear deformation-related term in coordinate transformation relative to the original principal stress condition calculated based on Equation (5.74b), and the comparison between the moduli B_{2121} and B_2 .

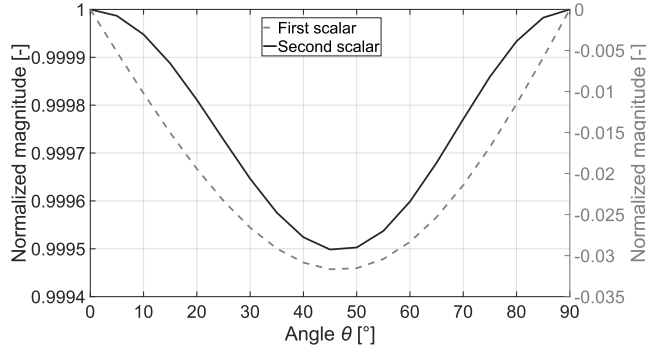


Figure 5.7 The first and second scalars in the second eigenvector of the B -matrix in Equation (5.71) during the coordinate transformation.

The aforementioned results are derived from the elements and eigenvalues of the B -matrix. However, our primary interest lies in the wave velocity obtained from acoustoelasticity. Figure 5.8 presents the velocity change calculated using Equation (5.75). Consistent with the observations in Figure 5.4 and Figure 5.6, the velocity change of the quasi-longitudinal wave can be accurately estimated using the diagonal element B_{1111} . The maximum error occurs when the shear stress reaches its maximum, with an error magnitude of approximately 0.32%. Considering the magnitudes of applied principal stresses, -13.24 MPa and 3 MPa, this difference is very limited. In contrast, the transverse wave velocity cannot be estimated using the diagonal element B_{2121} , confirming our earlier conclusion.

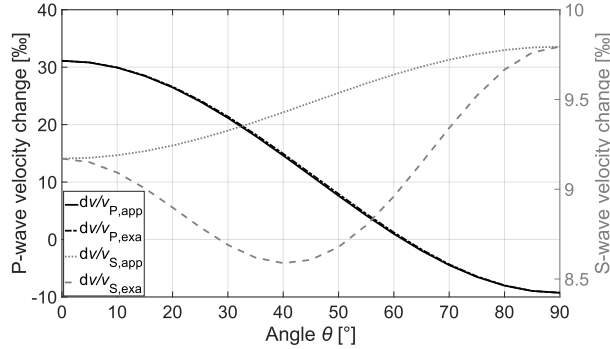


Figure 5.8 Velocity changes of the quasi-longitudinal wave based on the first diagonal element B_{1111} , the quasi-longitudinal wave based on the first eigenvalue B_1 , the quasi-transverse wave based on the second diagonal element B_{2121} and quasi-transverse wave based on the second eigenvalue B_2 using Equation (5.75).

5.5 Simplification of longitudinal wave acoustoelasticity in plane stress state

In Section 5.3 and 5.4, we thoroughly re-examined the theoretical framework of modern acoustoelasticity and proved that the impact of shear stress/strain on longitudinal wave

5.5 Simplification of longitudinal wave acoustoelasticity in plane stress state

velocity in concrete when bulk waves propagate on the shear deformation plane is indeed negligible. This finding allows us to simplify the equations used to describe wave propagation in stressed media, especially when propagating at an angle to the principle direction of stress.

In this section, the simplification of longitudinal wave acoustoelasticity in plane stress state with arbitrary propagation directions will be presented. We will begin by providing the acoustoelastic expression for longitudinal waves in the bi-axial stress state in Section 5.5.1, then progress to the expression for inclined propagating longitudinal waves on the stress plane in Section 5.5.2.

It is important to highlight that equations derived in this section is based on the acoustoelasticity in the natural frame. This option is grounded in the fact that the natural velocity is inversely proportional to the time of travel, eliminating the need to correct the length of wave path using strain measurements (Pao and Gamer 1985).

5.5.1 Acoustoelasticity for longitudinal waves propagating along one of the principal stress directions in the plane stress state

Assuming that a uniaxial stress is applied along the x -axis, and considering the propagation of a longitudinal wave along the same axis. In this case, the velocity of the longitudinal wave can be expressed as follows:

$$\begin{aligned} \rho^0 \left(v_{11}^{\text{natural}} \right)^2 &= \lambda + 2\mu + (3\lambda + 6\mu + 2l + 4m) e_1 + (\lambda + 2l)(e_2 + e_3) \\ &= \lambda + 2\mu + (3\lambda + 6\mu + 2l + 4m) \frac{\sigma_1}{E_s} - 2(\lambda + 2l) \frac{\nu \sigma_1}{E_s}, \end{aligned} \quad (5.76)$$

where e_1 , e_2 and e_3 indicate static principal strains along the x -, y - and out-of-plane z -axis, respectively. The parameter σ_1 represents the static principal stress along the x -axis, while ν represents the static Poisson ratio, and E_s is the static elastic modulus. It is important to note that in viscoelastic materials like concrete, the static Poisson ratio and static elastic modulus cannot be represented using Lamé parameters in Equation (5.76). This is because these Lamé parameters are derived from the constitutive equation for high-frequency ultrasonic waves and may not adequately describe the constitutive relation of viscoelastic materials under static loading conditions, where the strain rate is much lower than that of ultrasonic waves. Equation (5.76) can be further simplified into the following form by introducing the acoustoelastic parameter A_{1111} :

$$v_{11}^{\text{natural}} = v_{11}^{(0)} \sqrt{1 + A_{1111} \sigma_1}, \quad A_{1111} := \frac{3\lambda + 6\mu + 2l + 4m - 2\nu(\lambda + 2l)}{E_s(\lambda + 2\mu)}, \quad (5.77)$$

where the longitudinal wave velocity without external load applied is represented as $v_{11}^{(0)}$, which is equal to $[(\lambda + 2\mu)/\rho^0]^{1/2}$.

When the longitudinal wave propagates along the x -axis while the uniaxial stress is applied along the y -axis, the longitudinal wave velocity is:

$$\begin{aligned}\rho(v_{11}^{\text{natural}})^2 &= \lambda + 2\mu + (3\lambda + 6\mu + 2l + 4m)e_1 + (\lambda + 2l)(e_2 + e_3) \\ &= \lambda + 2\mu - (3\lambda + 6\mu + 2l + 4m)\frac{\nu\sigma_2}{E_s} + (\lambda + 2l)\left(\frac{\sigma_2}{E_s} - \frac{\nu\sigma_2}{E_s}\right).\end{aligned}\quad (5.78)$$

Similarly, Equation (5.78) can be simplified into the form shown in Equation (5.77):

$$v_{11}^{\text{natural}} = v_{11}^{(0)}\sqrt{1 + A_{1122}\sigma_2}, \quad A_{1122} := \frac{\lambda + 2l - \nu(4\lambda + 6\mu + 4l + 4m)}{E_s(\lambda + 2\mu)}. \quad (5.79)$$

When the longitudinal wave propagates along the x -axis and the bi-axial stresses are applied along the x - and y -axis, the longitudinal wave velocity in this stress state is:

$$\begin{aligned}\rho(v_{11}^{\text{natural}})^2 &= C_{11} + (3C_{11} + C_{111})e_1 + (C_{12} + C_{112})(e_2 + e_3) \\ &= \lambda + 2\mu + (3\lambda + 6\mu + 2l + 4m)\left(\frac{\sigma_1}{E_s} - \frac{\nu\sigma_2}{E_s}\right) + (\lambda + 2l)\left(\frac{\sigma_2}{E_s} - \frac{\nu\sigma_1}{E_s} - \frac{\nu\sigma_1}{E_s} - \frac{\nu\sigma_2}{E_s}\right) \\ &= \lambda + 2\mu + (3\lambda + 6\mu + 2l + 4m)\frac{\sigma_1}{E_s} - 2(\lambda + 2l)\frac{\nu\sigma_1}{E_s} \\ &\quad - (3\lambda + 6\mu + 2l + 4m)\frac{\nu\sigma_2}{E_s} + (\lambda + 2l)\left(\frac{\sigma_2}{E_s} - \frac{\nu\sigma_2}{E_s}\right),\end{aligned}\quad (5.80)$$

where σ_1 and σ_2 represent the principal stresses along the x - and y -axis, respectively. Note that Equation (5.80) is similar to the combination of Equation (5.76) and Equation (5.78) and can be simplified into:

$$v_{11}^{\text{natural}} = v_{11}^{(0)}\sqrt{1 + A_{1111}\sigma_1 + A_{1122}\sigma_2}. \quad (5.81)$$

In this section, only the acoustoelastic parameters for longitudinal waves in the natural frame are introduced. The remaining parameters can be found in Appendix D.

5.5.2 Acoustoelasticity for longitudinal wave propagating inclined to principal stress directions in the plane stress state

In a plane stress state, we assume that the principal stresses are applied along the x - and y -axes, as illustrated in Figure 5.9(a), and the stress in z -axis is zero. These two principal stresses can be either compressive or tensile. The propagation direction of a longitudinal wave is indicated by the dotted arrow. To make the acoustoelasticity applicable in this scenario, we need to align the axes of the coordinate system parallel and perpendicular to the wave propagation direction, as depicted in Figure 5.9(b). The normal and shear stresses in the new rotated coordinate system, denoted as x' and y' , can be determined by:

5.5 Simplification of longitudinal wave acoustoelasticity in plane stress state

$$\begin{aligned} \begin{bmatrix} \sigma_{11} & \sigma_{12} \\ \sigma_{21} & \sigma_{22} \end{bmatrix} &= \begin{bmatrix} \cos \theta & \sin \theta \\ -\sin \theta & \cos \theta \end{bmatrix} \begin{bmatrix} \sigma_1 & 0 \\ 0 & \sigma_2 \end{bmatrix} \begin{bmatrix} \cos \theta & -\sin \theta \\ \sin \theta & \cos \theta \end{bmatrix} \\ &= \begin{bmatrix} \cos^2(\theta)\sigma_1 + \sin^2(\theta)\sigma_2 & \sin(\theta)\cos(\theta)(\sigma_2 - \sigma_1) \\ \sin(\theta)\cos(\theta)(\sigma_2 - \sigma_1) & \sin^2(\theta)\sigma_1 + \cos^2(\theta)\sigma_2 \end{bmatrix}, \end{aligned} \quad (5.82)$$

where θ is the inclination of the wave propagation, and σ_{11} and σ_{22} represent the normal stresses along x' - and y' -axes, respectively. The parameters σ_{12} and σ_{21} represent the shear stresses in the x' - y' plane.

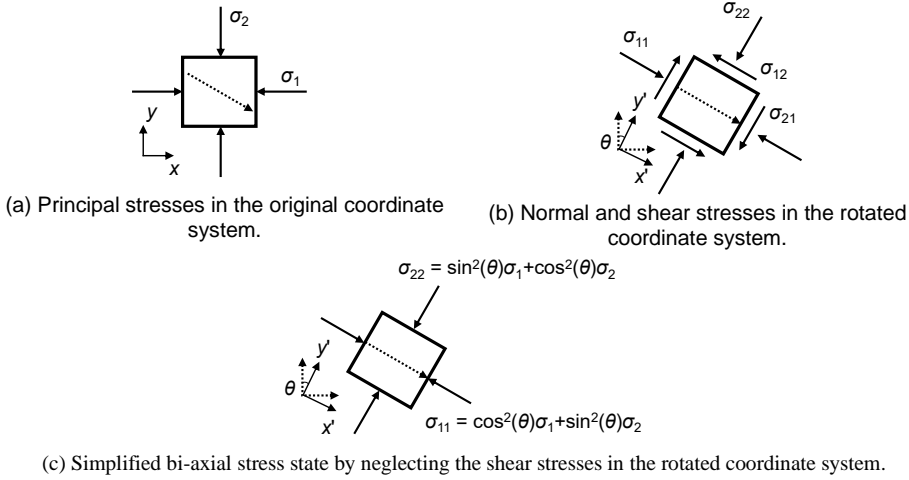


Figure 5.9 Coordinate system transformation (solid arrow: stress direction; dotted arrow: longitudinal wave propagation direction; θ represents the rotation angle to orient the coordinate system according to the propagation direction).

Based on the result presented in Section 5.4.4, it has been established that the velocity change of a longitudinal wave is primarily influenced by the normal stress/strain, while the impact of shear stress/strain on the longitudinal wave velocity can be neglected in the scenario of the plane stress state. As a result, the stress state depicted in Figure 5.9(b) can be simplified to a bi-axial stress state, as illustrated in Figure 5.10. This figure demonstrates that the acoustoelastic parameter associated with an inclined propagating longitudinal wave closely resembles that in a bi-axial stress state with axial stresses of σ_{11} and σ_{22} . Therefore, along with the normal stresses computed in Equation (5.82), the acoustoelastic effect in the bi-axial stress state in Figure 5.9(c) can be formulated as:

$$\begin{aligned}
\rho(v_{11}^{\text{natural}})^2 &= \lambda + 2\mu + (3\lambda + 6\mu + 2l + 4m) \frac{\sigma_{11}}{E_s} - 2(\lambda + 2l) \frac{\nu\sigma_{11}}{E_s} \\
&\quad - (3\lambda + 6\mu + 2l + 4m) \frac{\nu\sigma_{22}}{E_s} + (\lambda + 2l) \left(\frac{\sigma_{22}}{E_s} - \frac{\nu\sigma_{22}}{E_s} \right) \\
&= \lambda + 2\mu + \frac{3\lambda + 6\mu + 2l + 4m - 2\nu(\lambda + 2l)}{E_s} [\cos^2(\theta)\sigma_1 + \sin^2(\theta)\sigma_2] \\
&\quad + \frac{\lambda + 2l - \nu(4\lambda + 6\mu + 4l + 4m)}{E_s} [\sin^2(\theta)\sigma_1 + \cos^2(\theta)\sigma_2] .
\end{aligned} \tag{5.83}$$

Please note that Equation (5.83) is not new, and one can find it in the papers dealing with the acoustoelastic effect of waves propagating inclined to the principal stress directions (Mi, Michaels et al. 2006, Muir 2009, Gandhi 2010, Shi, Michaels et al. 2013, Abbasi and Ozevin 2016). The main assumption in Equation (5.83) is that the influence of shear stresses on wave velocity is negligible, which has not been proven valid in the aforementioned articles. Additionally, we want to emphasize here that the procedure adopted in this section is not applicable to transverse waves since shear stresses significantly affect transverse wave velocity when bulk waves propagate on the shear deformation plane.

5.6 Experimental validation for simplified acoustoelastic expression

To validate the simplified acoustoelastic expression for the longitudinal waves in the plane stress state presented in Section 5.5, an experiment is designed where the longitudinal wave propagates at an angle relative to the coordinate system within a plane stress state. The specifics of the sample used in the experiment, the layout of the ultrasonic sensors, and the loading protocol are detailed in Section 5.6.1, while the data processing approach for obtaining the acoustoelastic parameters for inclined propagating longitudinal waves is explained in Section 5.6.2.

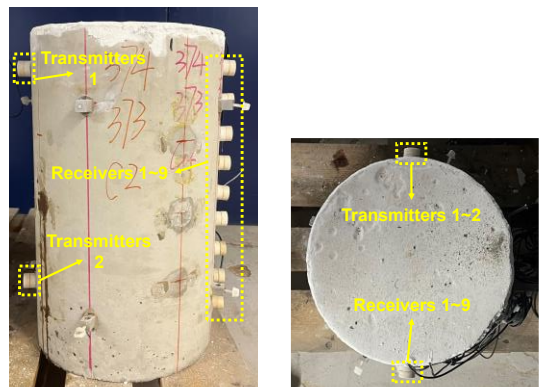
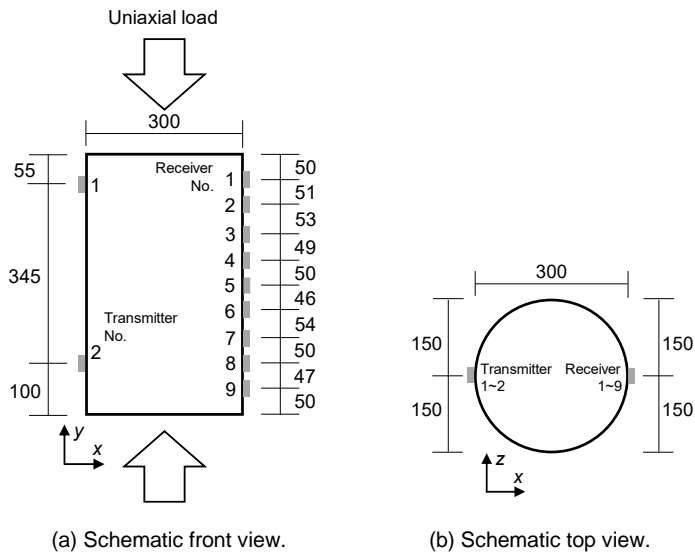
5.6.1 Concrete specimen, sensor layout and measurement plan

The test specimen is a concrete cylinder with dimensions of 300 mm in diameter and 500 mm in height. The cylinder is cast using self-compacting concrete of grade C60/75. The mean cube compressive strength (tested from 150 mm cubes) and mean prism elastic modulus of concrete on the 28th day are 75 MPa and 39 GPa, respectively.

In the experiment, a total of 11 ultrasonic sensors with a central frequency of 80 kHz were employed as transmitters and receivers. Specifically, two sensors were affixed to one side of the concrete cylinder as transmitters, while the remaining sensors were placed on the opposite side as receivers, as illustrated in Figure 5.10. The uniaxial compressive load was applied onto the top and bottom surfaces of the cylindrical sample, aligned with the y-axis according to the coordinate system in Figure 5.10. The transmitter located near the top surface is denoted as Transmitter 1, and the corresponding arrangement of receivers is referred to as SL 1. Likewise, when utilizing the other transmitter, Transmitter 2, the

5.6 Experimental validation for simplified acoustoelastic expression

layout of receivers is termed SL 2. The inclinations of the receivers within SL 1 and SL 2 can be found in Table 5.2.



(c) Photos of the specimen and sensors.

Figure 5.10 Schematic of sensor layout.

Table 5.2 Receiver inclination for SL1 and SL2 with respect to the x-axis on the x-y plane (please be aware that 90° indicates that the propagation direction is parallel to the principal stress direction).

	Re- ceiver	1	2	3	4	5	6	7	8	9
Inclination θ [°]	SL 1	0.96	8.72	18.26	26.26	33.43	39.12	44.81	49.24	52.78
	SL 2	49.40	44.90	39.35	33.29	26.11	18.61	8.90	0.57	9.46

A total of four repetitive ultrasonic tests, numbered as Test 1–4, were conducted on the concrete sample. The age of the concrete during Test 1 is 15 months, while for Test 2, 3 and 4, it is 16 months. All measurements are performed throughout the loading process at a sampling rate for signals of 10 MHz. Prior to the measurement, the sample undergoes three-cycle pre-loading, where the stress ranged from 2.829 MPa to 11.318 MPa, as indicated in Table 5.3. This pre-loading procedure aimed to mitigate the relatively lower slope of the stress-velocity relationship that may occur due to crack formation during the initial loading phase (Stahler, Sens-Schonfelder et al. 2011). For the first three tests, the receiver configuration of SL 1 is utilized, with Transmitter 1 serving as the source. Although the minimum and maximum compressive stresses are the same for all three tests, the stress interval in Test 3 is twice as large as that in Test 1 and Test 2. This variation in stress interval is implemented to assess the sensitivity of the obtained results with different stress intervals. In Test 4, Transmitter 2 is used as the source, while maintaining the same stress range and interval as Test 3. The loading protocols of four tests can be found in Figure 5.11.

Table 5.3 Detailed information for four tests.

Test No.	Sensor layout	Minimum compressive stress [MPa]	Maximum compressive stress [MPa]	Stress interval [MPa]	Number of measurements
1	SL 1	2.829	11.318	0.707	13
2	SL 1	2.829	11.318	0.707	13
3	SL 1	2.829	11.318	1.415	7
4	SL 2	2.829	11.318	1.415	7

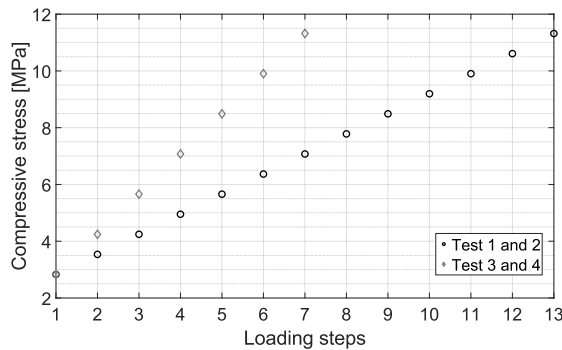


Figure 5.11 Loading protocol of four tests.

5.6.2 Data processing approach

Since the interconversion between longitudinal and transverse waves could occur at each scattering event (Snieder 2002), the longitudinal wave component may contain a certain amount of transverse waves. In order to minimize the impact of transverse waves on the analysis, only the initial one-and-a-half cycles of the signal, which corresponds to a du-

5.6 Experimental validation for simplified acoustoelastic expression

ration of approximately 23.5 μs , will be utilized to retrieve the velocity change of longitudinal waves in concrete. Due to its short duration, the signal cannot be effectively processed using the WCS technique due to the poor frequency resolution of around 42.6 kHz. Therefore, the stretching technique introduced in Section 4.2.2.1 will be used to retrieve the stress-induced velocity change. In addition, the stretching technique used in this section is step-wise, where the signal from the previous load step is taken as the reference. The velocity relative to the measurement at the initial load step is then calculated using the following equation:

$$\begin{aligned} \frac{v_{11,k}}{v_{11,1}} &= \frac{v_{11,2}}{v_{11,1}} \times \frac{v_{11,3}}{v_{11,2}} \times \dots \times \frac{v_{11,k}}{v_{11,k-1}} \\ &= \left[\frac{v_{11,2} - v_{11,1}}{v_{11,1}} + 1 \right] \left[\frac{v_{11,3} - v_{11,2}}{v_{11,2}} + 1 \right] \dots \left[\frac{v_{11,k} - v_{11,k-1}}{v_{11,k-1}} + 1 \right] \\ &= \prod_{i=1}^{k-1} \left[\left(\frac{dv}{v} \right)_{11,i} + 1 \right], \end{aligned} \quad (5.84)$$

where $v_{11,1}$ and $v_{11,k}$ indicate the velocity of longitudinal waves propagating in the x direction measured at the first stress level and the k th stress level, respectively. The parameter $(dv/v)_{11,k-1}$ can be directly obtained using the stretching technique. Since the interconversion between longitudinal and transverse waves could occur at each scattering event (Snieder 2002), the longitudinal wave component may contain a certain amount of transverse waves. In order to minimize the impact of transverse waves on the analysis, only the initial one-and-a-half distinguishable cycles of the signal will be utilized for the stretching calculation. This corresponds to approximately 23.5 μs in duration at a frequency of 64 kHz.

During the experiment, the principal stress is along the y -axis, as shown in Figure 5.10. Based on this information, Equation (5.83) can be simplified as:

$$\begin{aligned} \rho^0 (v_{11}^{\text{natural}})^2 &= \lambda + 2\mu + \frac{3\lambda + 6\mu + 2l + 4m - 2\nu(\lambda + 2l)}{E_s} \sin^2(\theta) \sigma_2 \\ &\quad + \frac{\lambda + 2l - \nu(4\lambda + 6\mu + 4l + 4m)}{E_s} \cos^2(\theta) \sigma_2. \end{aligned} \quad (5.85)$$

Equation (5.85) can be expressed in a form similar to Equation (5.77) and (5.79) as:

$$v_{11}^{\text{natural}} = v_{11}^{(0)} \sqrt{1 + A_{\text{eff}} \sigma_2}, \quad A_{\text{eff}} := \sin^2(\theta) A_{1111} + \cos^2(\theta) A_{1122}, \quad (5.86)$$

where A_{eff} is the effective acoustoelastic parameter for inclined propagating longitudinal waves. As shown in Equation (5.86), this effective acoustoelastic parameters can be calculated through the relationship between applied stress and longitudinal wave velocity. It should be noted that the initial compressive stress level in Equation (5.86) is assumed to be zero. However, during the experiment, the initial compressive stress is 2.82 MPa, as

shown in Table 5.3. Therefore, the following equation is employed to incorporate this non-zero initial compressive stress:

$$\left[\frac{v_{11,k}^{\text{natural}}}{v_{11,1}^{\text{natural}}} \right]^2 = \left(\frac{v_{11}^{(0)} \sqrt{1 + A_{\text{eff}} \sigma_{2,k}}}{v_{11}^{(0)} \sqrt{1 + A_{\text{eff}} \sigma_{2,1}}} \right)^2 \quad (5.87)$$

$$= \frac{A_{\text{eff}}}{1 + A_{\text{eff}} \sigma_{2,1}} \sigma_{2,k} + \frac{1}{1 + A_{\text{eff}} \sigma_{2,1}} ,$$

where $\sigma_{2,1}$ and $\sigma_{2,k}$ indicate the principal compressive stresses in the y direction at the first stress level (2.82 MPa), and stress level at which the measurement k is taken, respectively. The parameter $v_{11,k}$ and $v_{11,1}$ represent the wave velocity at measurement k and the wave velocity at the initial stress state, respectively. The effective acoustoelastic parameter can be calculated by means of the slope of compressive stress-square of relative velocity relation, denoted as s , through:

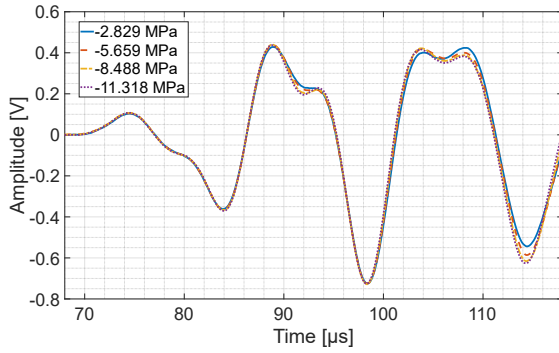
$$A_{\text{eff}} = \frac{s}{1 - s \sigma_{2,1}} . \quad (5.88)$$

The slope s can be determined by performing a linear fit of the square of relative velocity with respect to the compressive stress.

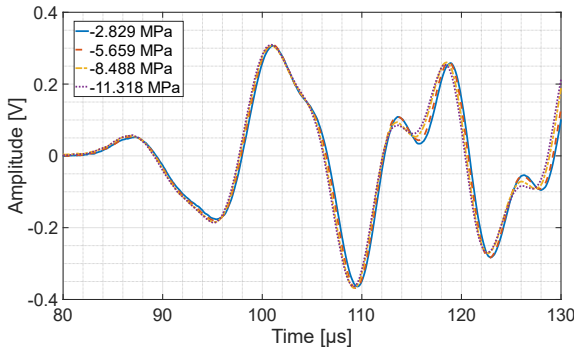
5.7 Effective acoustoelastic parameters for longitudinal waves

The signals received from Receivers 1, 5, and 9 during Test 1 under compressive stresses of 2.829 MPa, 5.659 MPa, 8.488 MPa, and 11.318 MPa are shown in Figure 5.12. In these figures, the waveforms exhibit remarkable similarity across different stress levels, with diminishing amplitudes attributed to increased travel distance. The velocities of ballistic waves in all cases consistently exceed 4000 m/s, indicative of longitudinal waves. As mentioned above, the longitudinal wave component may contain a certain amount of transverse waves because of the interconversion between longitudinal and transverse waves (Snieder 2002). However, since we apply the stretching technique in a very short time window, around 23.5 μs , after the first arrival, we anticipate minimal influence of transverse waves on the obtained results. While phase shifts in the signals received from Receiver 1 remain insignificant, they become progressively more pronounced with greater inclination, as shown in Figure 5.12(b) and Figure 5.12(c). Similar phenomenon as described above are also observable in Tests 2, 3 and 4.

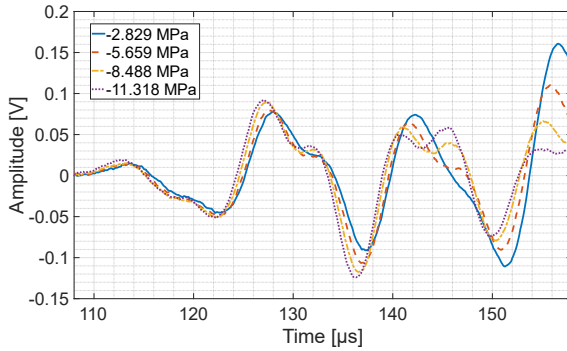
5.7 Effective acoustoelastic parameters for longitudinal waves



(a) Receiver 1 ($\theta=0.96^\circ$).



(b) Receiver 5 ($\theta=33.43^\circ$).

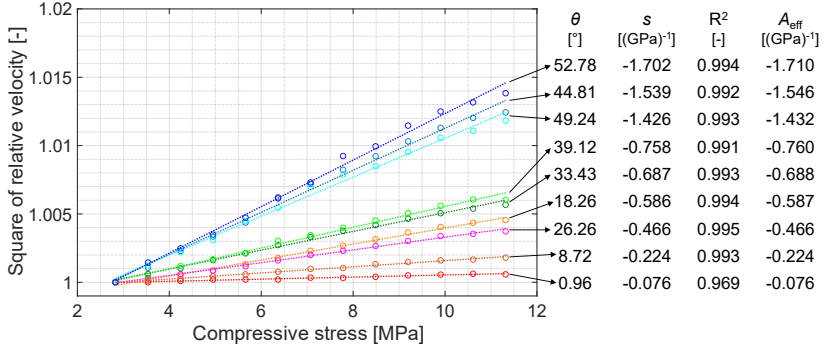


(c) Receiver 9 ($\theta=52.78^\circ$).

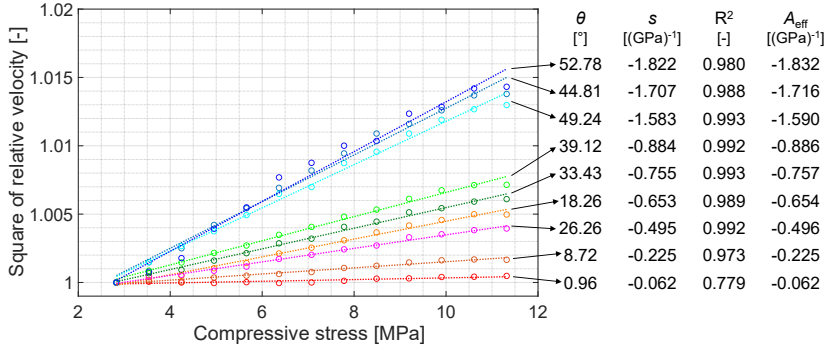
Figure 5.12 Signals from Receiver 1, 5, and 9 during Test 1 under compressive stresses of 2.829 MPa, 5.659 MPa, 8.488 MPa, and 11.318 MPa.

The square of relative velocities obtained using Equation (5.84) as a function of the compressive stress in the four tests are shown in Figure 5.13. When the inclination approaches 0° , the longitudinal wave propagates nearly perpendicular to the principal stress direction,

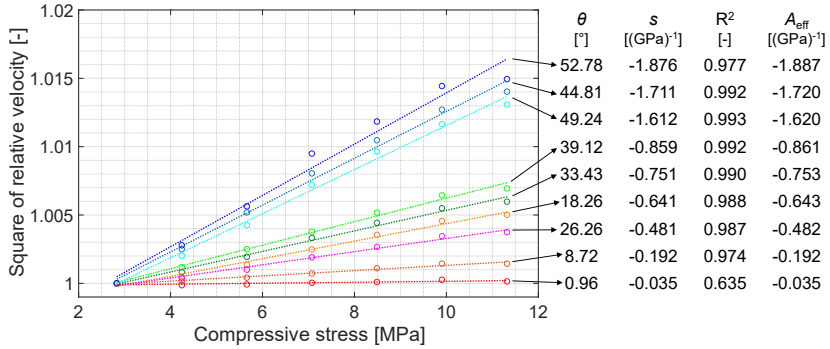
resulting in the lowest slope of the square of relative velocity with respect to the compressive stress. This finding aligns with observations in the literature (Lillamand, Chaix et al. 2010). As the inclination increases, a progressively more significant acoustoelastic effect can be observed, characterized by an increasing slope.



(a) Test 1.

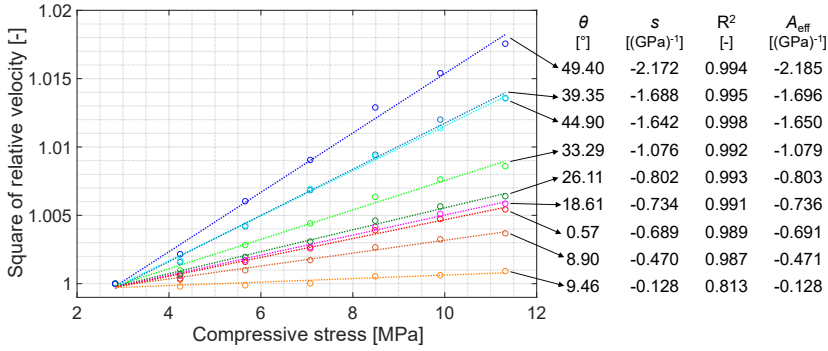


(b) Test 2.



(c) Test 3.

5.7 Effective acoustoelastic parameters for longitudinal waves



(d) Test 4.

Figure 5.13 Square of relative velocity vs. compressive stress. The circles represent the experimental measurements, while the dotted lines indicate the linear fit results. The parameter θ indicates the inclination of sensor-receiver pair with respect to x-axis in Figure 5.10(a). A linear fit of the square of relative velocity with respect to the compressive stress is performed, and the obtained slope is denoted as s . The goodness-of-fit is evaluated using the coefficient of determination R^2 . The effective acoustoelastic parameter A_{eff} is acquired using Equation (5.88) with $\sigma_{2,1} = -2.829$ MPa.

To quantify the relationship between the compressive stress and the square of relative velocity, a linear fit is performed to acquire the slope of this relationship. The goodness-of-fit is evaluated using the coefficient of determination R^2 . It is noteworthy that the majority of these coefficients are high, as shown in Figure 5.13, suggesting a robust linear relationship between compressive stress and the square of relative velocity, which aligns with the theoretical analysis presented in Section 5.5. This observation further reinforces the accuracy and reliability of the measurements.

The obtained slope is then utilized to calculate the effective acoustoelastic parameter using Equation (5.88). These parameters can be found in the legends of Figure 5.13. The consistent outcomes and fluctuations observed in the first three tests, demonstrate the reproducibility of the acoustoelastic effect from the same sensor configuration. One plausible explanation of the fluctuations in the measurements at different inclinations, i.e., the magnitude of the effective acoustoelastic parameter acquired from Receiver 4 ($\theta=26.26^\circ$) is higher than that from Receiver 3 ($\theta=18.26^\circ$) in Test 1 shown in Figure 5.13(a), is the spatial variation of mechanical properties of concrete (Nguyen, Sbartaï et al. 2013). This observation also suggests that relying on a single transmitter-receiver pair to obtain the acoustoelastic parameter may not provide a representative result for the sample. Additionally, examining Test 2 and Test 3 reveals that the effective acoustoelastic parameter is not significantly affected by the magnitude of the load step. Test 4 exhibits slightly different results compared to the initial three tests. Considering that the wave trajectories of transmitter-receiver pairs in Test 4 are different from the previous three tests, this variance could also be ascribed to the spatial variation of mechanical properties of concrete.

Nevertheless, the overall trend of the effective acoustoelastic parameters is evident: the magnitude of effective acoustoelastic parameters increases as the inclination increases.

5.8 Comparison of acquired effective acoustoelastic parameters with those from literature

In Section 5.7, we present the effective acoustoelastic parameters obtained from the experiment for longitudinal waves. To further validate these parameters, we calculate acoustoelastic parameters A_{1111} and A_{1122} based on the results presented in Section 5.7 and compare them with values reported in the literature.

The effective acoustoelastic parameter is determined by three variables as shown in Equation (5.86): A_{1111} and A_{1122} , which are acoustoelastic parameters, and θ , the inclination of wave propagation. Since the inclination of wave propagation can be inferred from the sensor locations in the experiment, only two acoustoelastic parameters remain unknown. Theoretically, these two parameters can be derived using two effective acoustoelastic parameters corresponding to distinct inclinations of wave propagation. In this study, each test involves longitudinal waves propagated at nine distinct inclinations, resulting in nine effective acoustoelastic parameters. Utilizing these nine parameters alongside the minimum norm least-squares criterion facilitates the determination of the two unknown acoustoelastic parameters, A_{1111} and A_{1122} . Once these parameters are obtained, it becomes feasible to reconstruct the effective acoustoelastic parameters for different receivers based on their known inclinations. The deviation between these reconstructed results and the experimental data is evaluated using the root mean square deviation (RMSD). The acoustoelastic parameters, A_{1111} and A_{1122} , and RMSD values comparing experimental and reconstructed results are detailed in Table 5.4. Figure 5.14 illustrates the comparison between the effective acoustoelastic parameters derived from experiments and those reconstructed using the parameters listed in Table 5.4.

Table 5.4 Acoustoelastic parameters obtained using minimum norm least-squares criterion.

Test No.	Acoustoelastic parameters [(GPa) ⁻¹]		RMSD values between experimental and reconstructed results [(GPa) ⁻¹]
	A_{1111}	A_{1122}	
1	-2.4838	-0.1155	0.1698
2	-2.7425	-0.1192	0.1804
3	-2.8100	-0.0859	0.1865
4	-3.2680	-0.3629	0.1909

5.8 Comparison of acquired effective acoustoelastic parameters with those from literature

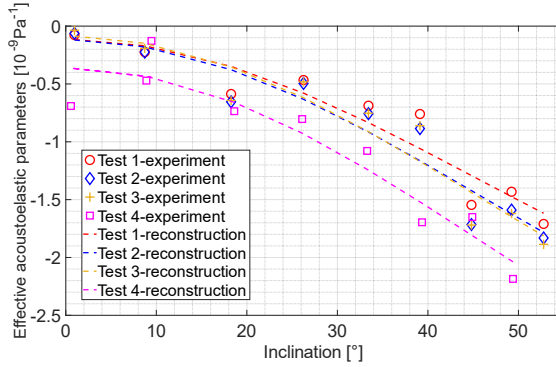


Figure 5.14 Comparison of effective acoustoelastic parameters obtained from experiments and those reconstructed using the acoustoelastic parameters listed in Table 5.4.

In the first three tests, which share the same sensor configuration (SL 1), the reconstructed results are quite consistent. However, the reconstructed effective acoustoelastic parameters in Test 4 consistently manifest a higher magnitude compared to those in Tests 1, 2, and 3. As previously mentioned, this discrepancy could be attributed to the spatial variation of mechanical properties in concrete. The acoustoelastic parameter A_{1122} exhibits a significantly lower magnitude than A_{1111} in all four tests, and the magnitude of A_{1122} obtained from Test 4 is at around three times larger than those from the other tests. Despite some fluctuations, the overall trend of the effective acoustoelastic parameters derived from the experiment aligns with the expectation: when the propagation direction of longitudinal waves approaches closer to the direction of the principal stress, the acoustoelastic effect becomes more significant, and the magnitude of the effective acoustoelastic parameters increases.

The acoustoelastic parameters obtained in this study are further compared with those reported in the literature. To ensure comparability, the slope of the stress-velocity change relationship, which is widely adopted in the literature, is converted into the acoustoelastic parameter A_{1111} and A_{1122} . The following equation, which is derived from Equation (5.77), is adopted for longitudinal waves propagating parallel to the uniaxial principal stress direction:

$$\frac{d\left(\frac{v_{11}^{\text{natural}} - v_{11}^{(0)}}{v_{11}^{(0)}}\right)}{d\sigma_1} = \frac{A_{1111}}{2} \frac{1}{\sqrt{1 + A_{1111}\sigma_1}} \quad (5.89)$$

$$\approx \frac{A_{1111}}{2} .$$

Please note that the approximate equivalence holds as the magnitude of $A_{1111}\sigma_1$, approximately 0.002, is much smaller than 1 in concrete (Nogueira and Rens 2019). A similar expression to Equation (5.89) can be employed to convert the slope of the stress-velocity

change relationship for longitudinal waves propagating perpendicular to the uniaxial principal stress direction into A_{1122} , although it will not be presented here. The comparison between acoustoelastic parameters in this study and those reported in the literature is presented in Table 5.5. The parameters acquired from four tests are consistent with the findings reported by other researchers in the literature, reinforcing the validity of the effective acoustoelastic parameters shown in Section 5.7.

Table 5.5 Comparison between acoustoelastic parameters in this section and those reported in the literature.

		Test 1	Test 2	Test 3	Test 4	Lil- lamand et al. (2010)	Nogueira et al. (2019)	Zhong et al. (2021)
Acoustoelastic parameters [(GPa) ⁻¹]	A_{1111}	-2.48	-2.74	-2.81	-3.27	-1.30	Vary from -0.80 to - 5.26	-2.42
	A_{1122}	-0.12	-0.12	-0.09	-0.36	-0.40	Vary from +0.48 to - 0.74	-0.42

5.9 Discussion

5.9.1 Identified inconsistencies in acoustoelastic theory in the current literature

In Section 5.2, we highlighted the presence of literature producing inconsistent results compared to other publications. These inconsistencies primarily stem from two factors: incorrect acoustoelastic expressions (Egle and Bray 1976, Payan, Garnier et al. 2011) and the improper utilization of third-order elastic constants (Stahler, Sens-Schonfelder et al. 2011). In Section 5.3.4, we have discussed some of them (Stahler, Sens-Schonfelder et al. 2011). Directly applying equations in these papers may yield inaccurate result. Here, we address the concerns in the article by Mi et al. (2006), and Egle and Bray (1976). In this section, we have demonstrated that the longitudinal wave velocity is primarily influenced by the normal stress/strain, while the transverse wave velocity is influenced by both normal and shear stress/strain in the context of concrete. Our numerical results pertaining to the transverse wave velocity raise concerns regarding the accuracy of Eq. 17 in the paper by Mi et al. (2006), as this equation assumes that shear stress/strain does not affect the transverse wave velocity in the aluminium.

We noted that Eq. (1a) in the work by Egle and Bray (1976), directly obtained from expressions reported by Hughes and Kelly (1953) is correct. However, in the derivation of Eq. (2a) in their article, we identified multiple typos. In their article, Eq. (2a) is in the following form (Egle and Bray 1976):

$$\rho^0 (v_{11})^2 = \lambda + 2\mu + \left[4(\lambda + 2\mu) + 2(\mu + 2m) + \nu\mu \left(1 + \frac{2l}{\lambda} \right) \right] \varepsilon, \quad (5.90a)$$

5.9 Discussion

where ε represents the strain in 1-direction in their article. The correct expression should take the following form:

$$\rho^0 (v_{11})^2 = \lambda + 2\mu + \left[5(\lambda + 2\mu) + 2(l + 2m) - 2\nu\lambda \left(1 + \frac{2l}{\lambda} \right) \right] \varepsilon . \quad (5.90b)$$

Based on Eq. (2a) in their article, they proceeded to derive Eq. (4a) for relative changes in wave velocity with axial strain (Egle and Bray 1976):

$$\frac{dv_{11} / v_{11}^0}{d\varepsilon} = 2 + \frac{\mu + 2m + \nu\mu \left(1 + \frac{2l}{\lambda} \right)}{\lambda + 2\mu} . \quad (5.91a)$$

It is crucial to note that this result is incorrect. The correct version of the expression should be in the following form:

$$\frac{dv_{11} / v_{11}^0}{d\varepsilon} = \frac{5}{2} + \frac{l + 2m - \nu\lambda \left(1 + \frac{2l}{\lambda} \right)}{\lambda + 2\mu} . \quad (5.91b)$$

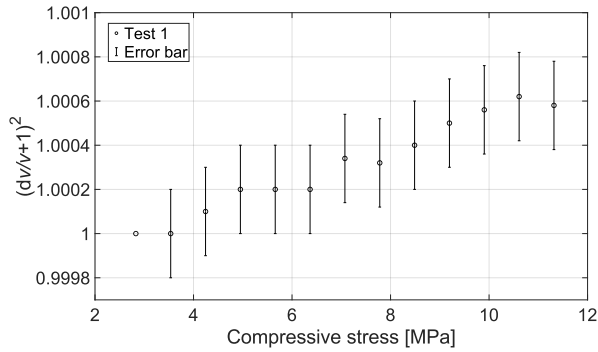
Considering that the magnitude of the third-order elastic constant l is typically much larger than that of the second-order elastic constant m (Hughes and Kelly 1953, Nogueira and Rens 2019), directly utilizing Eq. (4a) reported by Egle and Bray (1976) will underestimate the magnitude of velocity change for a given strain change in a medium with identical elastic constants. In the following up study conducted by Payan et al. (2011), they employed the inaccurate expression of Eq. (4a), which potentially leads to incorrect conclusions.

5.9.2 Error estimation in acquiring the acoustoelastic parameters of concrete

The precision of the acoustoelastic parameters of concrete obtained through the approach proposed in this section is influenced by four main factors: (1) simplification of the acoustoelastic theory, (2) accuracy of the stretching technique to estimate velocity changes in concrete, (3) change of mechanical properties of concrete relating to the age of concrete, and (4) the special variation of mechanical properties of concrete. The first factor stems from neglecting the impact of shear stresses on longitudinal wave velocities. However, this discrepancy in velocity change is very limited, typically less than 0.06‰ per 1 MPa at a 45° inclination (the maximum observed difference) in the plane stress state, based on observations shown in Section 5.4.4.2.

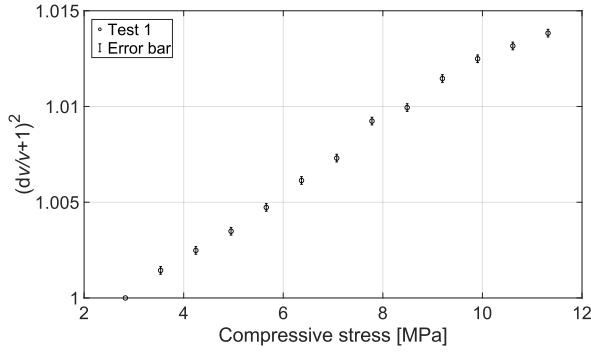
The second type of error arises from the stretching technique. Based on studies by Weaver et al. (2011) and Mao et al. (2020), the error magnitude ranges from 0.01‰ to 0.2‰, similar to the magnitude of velocity change when the longitudinal wave propagates perpendicular to the uniaxial stress direction.

To provide a more intuitive understanding of how errors stemming from the stretching technique affect the acquired effective acoustoelastic parameters, we conducted a preliminary error analysis. Given the absence of research on the precision of the stretching technique specifically applied to concrete thus far, we assume a maximum error of 0.1% in dv/v , a value consistent with findings by Weaver et al. (2011) and Mao et al. (2020). Using Taylor expansion, we estimate the error of $(dv/v+1)^2$ to be approximately 0.2%. In this demonstration, we use Test 1 as an illustration. The acoustoelastic parameter A_{1122} characterizes velocity changes in the medium when longitudinal waves propagate perpendicular to the stress direction. In Test 1, this propagation direction closely aligns with the sensor inclination of 0.96° (Receiver 1). The relationship between the square of relative velocity and compressive stress for this sensor inclination, along with the errors resulting from the stretching technique, can be seen in Figure 5.15(a). The acoustoelastic parameter A_{1111} describes velocity changes in the medium when longitudinal waves travel parallel to the stress direction. However, a sensor inclined in such a manner is lacking. Instead, for illustrative purposes, we utilize the sensor inclination of 52.78° (Receiver 9), which is closest to the scenario of A_{1111} in our tests. The relationship between the square of relative velocity and compressive stress for this sensor inclination, together with the stretching technique-induce error, is displayed in Figure 5.15(b).



(a) Inclination of receivers of 0.96° (Receiver 1).

5.9 Discussion



(b) Inclination of receivers of 52.78° (Receiver 9).

Figure 5.15 Square of relative velocity vs. compressive stress in Test 1 with receivers inclined at 0.96° (Receiver 1) and 52.78° (Receiver 9). The centre circle of the error bar indicates the square of relative velocity acquired from Test 1. The absolute maximum error of dv/v is 0.1‰.

Figure 5.15 clearly illustrates that errors propagated from the stretching technique significantly affect measurements from Receiver 1 but have minimal impact on those from Receiver 9. To further quantify the propagation of these errors to the effective acoustoelastic parameters, the following equation will be employed to estimate the errors in the effective acoustoelastic parameters, denoted as ΔA_{eff} :

$$\begin{aligned} \Delta A_{\text{eff}} &= \frac{\partial}{\partial s} \left(\frac{s}{1 - s\sigma_{2,1}} \right) \Delta s \\ &= \frac{\Delta s}{(1 - s\sigma_{2,1})^2}, \end{aligned} \quad (5.92)$$

where Δs indicates the error in the fitted slope, propagated from the errors in the velocity change acquired using the stretching technique. The slope s can be determined by conducting a linear fit of the square of relative velocity to the compressive stress. The error in the fitted slope Δs can be estimated using the following equation:

$$\begin{aligned} \Delta s &\approx \left| \frac{(y_2 + \Delta) - (y_1 - \Delta)}{x_2 - x_1} - \frac{y_2 - y_1}{x_2 - x_1} \right| \\ &= \left| \frac{2\Delta}{x_2 - x_1} \right|, \end{aligned} \quad (5.93)$$

where x_1 and x_2 represent two query point, while y_1 and y_2 denote corresponding fitted values at these query points. The parameter Δ indicates the absolute error associated with the two fitted values. In this study, Δ is equal to the error of $(dv/v+1)^2$, approximately 0.2‰. The parameters x_1 and x_2 correspond to compressive stresses at the second stress level, -3.54 MPa, and the last stress level, -11.32 MPa, respectively. Utilizing Equation (5.92) and (5.93), the propagated error from the stretching technique to the effective

acoustoelastic parameter is calculated. When the inclination of receivers is 0.96° (Receiver 1), the propagated error is determined as 0.051 GPa. This value is comparable in magnitude to the effective acoustoelastic parameter acquired from the same receiver in Test 1, -0.076 GPa. Furthermore, the effective acoustoelastic parameters of Receiver 1 obtained from Test 2 (-0.062 GPa) and Test 3 (-0.035 GPa), utilizing identical transmitter configuration, fall within the specified error bounds. In contrast, when the inclination of receivers is 52.78° (Receiver 9), the propagated error to the effective acoustoelastic parameter is computed to be 0.052 GPa. Notably, this magnitude is significantly smaller than the effective acoustoelastic parameter acquired from the same receiver in Test 1, -1.710 GPa. The proportion of the magnitude of error to the magnitude of effective acoustoelastic parameter is only 3.0%. However, utilizing effective acoustoelastic parameters obtained from receivers with lower inclinations does not substantially affect the values of acoustoelastic parameters A_{1111} and A_{1122} . Table 5.6 displays the acoustoelastic parameters derived using effective parameters from receivers with inclinations larger than 10° . These parameters exhibit similar magnitudes compared to those in Table 5.4, indicating that the smaller effective parameters from receivers with lower inclinations minimally influence the fitting process based on the minimum norm least-squares criterion.

Table 5.6 Acoustoelastic parameters obtained using minimum norm least-squares criterion.

Test No.	Receivers involved	Acoustoelastic parameters [(GPa) ⁻¹]	
		A_{1111}	A_{1122}
1	Receiver 3~9	-2.4838	-0.1155
2	Receiver 3~9	-2.7425	-0.1192
3	Receiver 3~9	-2.8100	-0.0859
4	Receiver 1~6	-3.2680	-0.3629

Furthermore, the parameters of Receiver 9 in Test 2 (-1.832 GPa) and Test 3 (-1.887 GPa) surpass the error bounds. There is a notable increase in the magnitude of effective acoustoelastic parameters from Test 1 to Test 2 (0.122 GPa), whereas from Test 2 to Test 3, this difference is lower (0.055 GPa). Interestingly, the parameter change between Test 2 and Test 3 slightly exceeds the estimated propagated error, suggesting that the actual error from the stretching technique might be higher than 0.1% in concrete. There is no existing research on the precision of the stretching technique when applied to concrete. Two potential reasons behind the significant jump in the magnitude of effective acoustoelastic parameters acquired from Receiver 9 between Test 1 and Test 2 include the underestimated error while using the stretching technique, as discussed above, and the age of concrete, which will be further explored in the subsequent paragraph. Despite these considerations, it can be concluded that errors stemming from the stretching technique notably affect acoustoelastic parameters when the longitudinal wave propagation direction is perpendicular or nearly perpendicular to the uniaxial stress direction, while their impact is limited when the longitudinal wave propagates parallel or nearly parallel to the uniaxial stress direction.

5.10 Summary

The third aspect to consider is the age of the concrete. The mechanical properties of concrete, which can be represented by second-order elastic constants Lamé parameters, will gradually develop with time, and such a development is called hydration. The increase of Lamé parameters during the hydration process results in an increase of both longitudinal and transverse wave velocities (Carette and Staquet 2016). However, there is no research on the time-dependent behaviour of Murnaghan constants in concrete, but it is certain that these constants must change during hydration. Understanding the evolution of Lamé parameters and Murnaghan constants during concrete hydration could aid in interpreting the notable increase in the magnitude of effective acoustoelastic parameters between Test 1 and Test 2.

The last aspect concerns the spatial variation of mechanical properties of concrete (Nguyen, Sbartai et al. 2013). Our study reveals variations in effective acoustoelastic parameters with changes in transmitter position, suggesting differences in parameters across various transmitter and receiver locations, even within the same concrete sample. Importantly, these differences can be substantial.

To enhance the future application of the proposed approach for concrete stress monitoring, two key issues should be addressed: (1) analysing the source frequency content-induced errors in the stretching technique for retrieving stress-induced velocity changes in concrete through both theory and experiment to establish its minimum resolution in retrieving velocity change, and (2) exploring the impact of spatial variation of mechanical properties of concrete on acoustoelastic parameters through numerous repetitive experiments.

5.10 Summary

This section presents an investigation on the response of the travel time of ballistic bulk waves to normal and shear stresses in concrete. Based on contents presented in this section, we draw a general conclusion regarding the influence of shear strains on bulk wave velocities in concrete: shear strains exert a limited effect on longitudinal wave velocities but significantly alters transverse wave velocities in the context of concrete when bulk waves propagate on or perpendicular to the shear deformation plane. This conclusion suggests that acoustoelasticity can potentially be used to detect both the magnitude and directional changes of principal stresses by using ballistic waves.

According to acoustoelastic theory, the travel time changes of bulk waves in stressed concrete depend on both the wave mode and the propagation direction. The former suggests that the energies of longitudinal and transverse waves are crucial for estimating travel time changes of multiply scattered bulk waves in the diffusive regime, as emphasized by Snieder (2002). In later chapters, we will work on the travel time changes of diffuse bulk waves in concrete, where Equations (5.52) and (5.54) will be mainly used.

6. Modelling transportation of bulk wave energy

6.1 Introduction

According to the acoustoelastic theory detailed in Chapter 5, travel time changes of bulk waves in stressed concrete depend on both the wave mode and the propagation direction. We further demonstrated the impact of propagation direction on the acoustoelastic effect of ballistics waves through experiments in the same chapter. Although ballistic waves have a deterministic directionality, allowing for the determination of principal strain directions in an isotropic medium, methods based on these waves can only examine a limited region between the transducer and the receiver. In contrast, diffuse waves, with their longer trajectories, can cover a larger area with a sparser sensor array (Planès and Larose 2013), making them ideal for detecting changes over a broader region.

Diffuse waves are characterized by an equilibrated energy ratio between longitudinal and transverse waves (Weaver 1982) and an isotropic wavefield in space (Paul, Campillo et al. 2005). Despite this, the distinct acoustoelastic effects of longitudinal and transverse waves suggest that their energies are crucial for estimating travel time changes of multiply scattered bulk waves in the diffusive regime, as emphasized by Snieder (2002). Therefore, interpreting stress-induced travel time changes in diffuse waves requires a model to estimate the bulk wave energy evolution in concrete.

We acknowledge that investigating the acoustoelastic effect of bulk waves before they reach the diffusive regime is challenging due to the complexity of wave propagation directions. The characteristics of diffuse waves can greatly simplify the interpretation of wave properties, such as travel time changes, in the coda. Please note that only after waves enter the diffusive regime the condition where bulk waves arrive at the receiver from all directions with equal strength is met (Curtis, Gerstoft et al. 2006). Otherwise, the wavefield must be considered anisotropic, which significantly complicates the analysis.

This chapter introduces a theoretical framework of modelling the propagation of bulk wave energy in concrete. We will start with the knowledge gap in Section 6.2. After reviewing the scattering theory in elastic media proposed by Weaver (1990), Turner et al. (2001), and Ryzhik et al. (1996) and the theoretical description of the energy equilibration proposed by Snieder (2002), Margerin et al. (2001), and Trégourès et al. (2001), we propose the theoretical framework to estimate the energy evolution in Section 6.3. However, adapting this framework to concrete involves tailoring certain parameters, which is discussed in detail in Section 6.4. The role of intrinsic dissipation in the energy transport model will be investigated in Section 6.5. The resulting theoretical framework, capable of estimating the evolution of bulk wave energy in concrete, will undergo validation utilizing the diffusivity measured in Section 4.3. The validation process and the energy evolution predicted by the model will be elaborated in Section 6.6.

6.3 Total scattering cross-sections and energy equilibration in elastic media

6.2 Knowledge gap in evaluating the energy evolution of bulk waves in concrete

As detailed in Section 2.3.2, the WI method is currently preferred for detecting stress-induced velocity changes in concrete due to its high sensitivity to subtle changes in the medium. However, when applying the WI approach to coda waves, understanding the correlation between applied stress and measured travel time change is challenging due to the complex nature of these waves, which undergo multiple scattering and propagate in random directions. One potential simplification involves evaluating travel time changes when bulk waves reach energy equilibration. In this scenario, the energy ratio is known, and the bulk wave field is theoretically isotropic. Consequently, acoustoelastic effects of longitudinal and transverse waves can be decoupled, and propagation directions can be assumed uniformly distributed in space. However, as of now, no relevant research on the energy evolution of bulk waves has been reported in the realm of concrete.

6.3 Total scattering cross-sections and energy equilibration in elastic media

In this section, theoretical backgrounds of total scattering cross-sections and energy equilibration in elastic media are introduced. Section 6.3.1 gives a brief review on the fundamental definition of mean free path and scattering cross-section. Section 6.3.2 presents analytical expressions for total scattering cross-sections in heterogeneous media with local isotropy reported by Turner and Anugonda (2001). Section 6.3.3 rederives the equilibration time as well as the energy equilibration ratio based on the work of Snieder (2002) and Trégourès et al. (2001).

6.3.1 Definition of scattering cross-section and mean free path

The main purpose of this section is introducing the fundamental definition of mean free path and scattering cross-section, emphasizing the relationship between the classical definition (Chen 1984, Sheng 2006) and the probabilistic-based definition (Snieder 2002). These definitions will be demonstrated using simplified examples without considering the possible mode conversion and scattering angles.

When elastic waves propagate through a heterogeneous medium containing randomly spread scatterers, collisions occur between waves and scatterers. These collisions result in the scattering of a portion of the wave energy into different directions from the wave propagation direction. We assume that all scatterers are in the same spherical shape with a cross-sectional area of σ [m²], which is also known as *scattering cross-section*. Considering that elastic waves are incident upon an element of area A [m²] and thickness dx [m] containing n_s scatterers per m³, as show in Figure 6.1. The fraction of the area of the element being blocked by the total area of scatterers, denoted as A_{sc} , is:

$$\frac{A_{sc}}{A} = \frac{n_s A dx \sigma}{A} = n_s \sigma dx . \quad (6.1)$$

The energy blocked by scatterers can be represented as:

$$\begin{aligned} dE &= E' - E \\ &= E(1 - n_s \sigma dx) - E \\ &= -E n_s \sigma dx , \end{aligned} \quad (6.2)$$

where E and E' represent the energy flux of incident waves and transmitted waves, respectively. The solution of the differential equation in Equation (6.2) is:

$$E = E_0 e^{-\frac{x}{l^s}} , \quad (6.3)$$

where E_0 is the energy at initial location. The characteristic decay length of Equation (6.3) is defined as the *mean free path*, denoted as l^s (Chen 1984):

$$l^s := \frac{1}{n_s \sigma} = \frac{1}{\Sigma} . \quad (6.4)$$

The mean free path can be understood as a plane wave that will have had a good probability, with only 36.8% initial energy remaining, of making a collision after travelling a distance l^s (Chen 1984). Since the product $n_s \sigma$ in Equation (6.4) is related to the total area of scatterers, it is also termed the *total scattering cross-section* (Turner 1998), denoted as Σ . Please note that the physical dimension of Σ is L^{-1} .

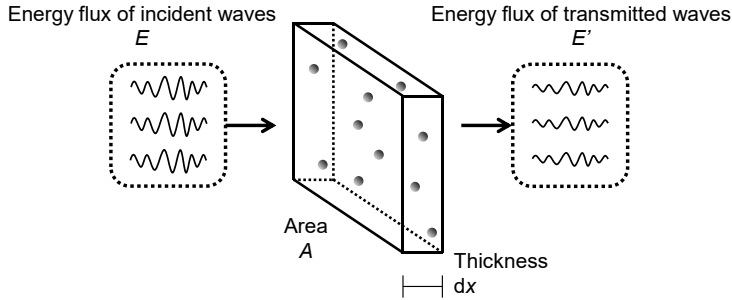


Figure 6.1 Illustration of definitions of scattering cross-section and mean free path.

The mean free path in Equation (6.4) is also known as the *scattering mean free path* (Turner and Anugonda 2001), which gives the decay length of the wave energy that propagates in its initial direction (Tourin, Derode et al. 2000). Energy tends to propagate toward regions with lower energy (Morse and Feshbach 1954). This behavior can be captured using the *weighted total scattering cross-section* (Weaver 1990), denoted as Σ' . Please note that the physical dimension of Σ' is the same as that of Σ , which is L^{-1} . A

6.3 Total scattering cross-sections and energy equilibration in elastic media

transport length l^* over which the wave has lost its initial direction (Busch, Soukoulis et al. 1994) is defined as:

$$l^* := \frac{1}{\Sigma - \Sigma'} . \quad (6.5)$$

The transport length l^* in Equation (6.5) is known as the *transport mean free path* (Turner 1998, Turner and Anugonda 2001). For elastic waves with a forward-scattering tendency, $\Sigma' > 0$ and the transport mean free path is larger than the scattering mean free path. Conversely, $\Sigma' < 0$ when waves have a back-scattering tendency. When the wave propagation is non-preferential, $\Sigma' \approx 0$ and the scattering mean free path is equal to the transport mean free path.

The mean free path can also be defined by means of the fraction of cross-section area blocked by scatterers (Snieder 2002). We assume that scatterers in Figure 6.1 are in the same spherical shape. The mean distance between two adjacent scatterers is defined as x_a [m]. After a wave has travelled the distance x_a , there is a probability that it has interacted with scatterers. This probability, which is dimensionless, is denoted by p . The fraction of energy blocked by scatterers in this case is then:

$$\begin{aligned} dE &= E' - E \\ &= E \left(1 - p \frac{dx}{x_a} \right) - E \\ &= -E \frac{p}{x_a} dx . \end{aligned} \quad (6.6)$$

Equation (6.6) is equivalent to Equation (6.2), and p can be understood as the fraction of cross-section area blocked by scatterers. The scattering mean free path in this case is:

$$l^s = \frac{x_a}{p} . \quad (6.7)$$

6.3.2 Total scattering cross-sections for elastic bulk waves

Definitions of scattering mean free paths and scattering cross-sections mentioned in Section 6.3.1 are provided for simple cases. It is assumed that the scattering cross-section is equivalent to the physical area of the scatterer. However, the scattering cross-section is generally smaller than the physical area of each scatterer (Sheng 2006). Additionally, the previous definition does not account for the scattering angle between incident and scattered waves. In reality, the scattering cross-section should account for the energy flux scattered in a specific direction at a certain angle relative to the incident wave (Boyd, Gaeta et al. 2008).

Figure 6.2 demonstrates a more realistic scattering scenario. The scattering angle, denoted as θ_s , is defined as the angle between the incident unit wave vector, denoted as \mathbf{p} , and the

scattered unit wave vector, denoted as \mathbf{p}' . Please note that \mathbf{p} and \mathbf{p}' are unit vectors pointing to the propagation directions. Obviously, the cosine of the scattering angle, $\cos\theta_s$, is equal to the dot product between \mathbf{p} and \mathbf{p}' . The scattering plane is determined by \mathbf{p} and \mathbf{p}' with the scattered spherical wave being locally considered a plane wave (Newton 2013). The scattering cross-section is angle dependent, and the total scattering cross-section is defined as the integral of the scattering cross-sections over all angles (Turner 1998):

$$\Sigma := \int_{-1}^{+1} \sigma(\cos\theta_s) d(\cos\theta_s) , \quad (6.8)$$

where $\sigma(\cos\theta_s)$ denotes the scattering cross-section that is related to the dot product between \mathbf{p} and \mathbf{p}' . The total scattering cross section that is related to the propagation preference, or weighted total scattering cross-section, is defined as (Turner 1998):

$$\Sigma' := \int_{-1}^{+1} (\cos\theta_s) \sigma(\cos\theta_s) d(\cos\theta_s) . \quad (6.9)$$

As shown in Equation (6.9), Σ' contains a weighting factor of the cosine of the scattering angle in the integral.

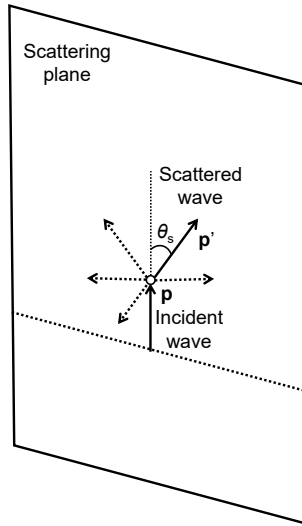


Figure 6.2 Sketch of a scattering event with a scattering angle θ_s between the incident and scattered waves. The parameters \mathbf{p} and \mathbf{p}' indicate the unit wave vectors for incident and scattered waves, respectively.

The total scattering cross-sections of elastic wave in the case of longitudinal (P) and transverse (S) waves are defined separately due to their distinct propagation characteristics. In this dissertation, the total scattering cross-section for longitudinal waves is denoted as Σ_P , while the total scattering cross-section for transverse waves is denoted as Σ_S . When elastic waves propagate through a medium like concrete, there is a probability of collision with

6.3 Total scattering cross-sections and energy equilibration in elastic media

scatterers. During such collisions, the wave mode may convert to another mode. Therefore, the scattering cross-section of a certain wave mode can be subdivided into two categories: those in which the waves retain their original mode after the collision and those in which the waves convert to another mode. For longitudinal waves, scattering cross-sections associated with mode transitions are denoted as σ_{PP} and σ_{PS} . The first P in the subscript σ_{PP} and σ_{PS} represents the original longitudinal wave mode, and the second letter represents the mode it converts into. Accordingly, total scattering cross sections, also known as longitudinal wave attenuations (Turner and Anugonda 2001), are denoted as Σ_{PP} and Σ_{PS} . By utilizing Equation (6.8), the following relation can be obtained:

$$\begin{aligned}\Sigma_P &= \int_{-1}^{+1} \sigma_P(\cos \theta_s) d(\cos \theta_s) \\ &= \Sigma_{PP} + \Sigma_{PS} \\ &= \int_{-1}^{+1} \sigma_{PP}(\cos \theta_s) d(\cos \theta_s) + \int_{-1}^{+1} \sigma_{PS}(\cos \theta_s) d(\cos \theta_s) .\end{aligned}\tag{6.10a}$$

An analogous definition is used for mode transition-related total scattering cross-sections of transverse waves:

$$\begin{aligned}\Sigma_S &= \int_{-1}^{+1} \sigma_S(\cos \theta_s) d(\cos \theta_s) \\ &= \Sigma_{SS} + \Sigma_{SP} \\ &= \int_{-1}^{+1} \sigma_{SS}(\cos \theta_s) d(\cos \theta_s) + \int_{-1}^{+1} \sigma_{SP}(\cos \theta_s) d(\cos \theta_s) .\end{aligned}\tag{6.10b}$$

Equation (6.10) can also be represented by means of the probabilistic-based definition:

$$\Sigma_P = \frac{P_P}{x_a} = \Sigma_{PP} + \Sigma_{PS} = \frac{P_{PP} + P_{PS}}{x_a} ,\tag{6.11a}$$

$$\Sigma_S = \frac{P_S}{x_a} = \Sigma_{SS} + \Sigma_{SP} = \frac{P_{SS} + P_{SP}}{x_a} ,\tag{6.11b}$$

where p_{PP} represents the probability of longitudinal waves converting to longitudinal waves. Similar definitions apply to p_{PS} , p_{SS} and p_{SP} . As shown in Equation (6.11a), the total scattering cross-section of longitudinal waves depends on both probabilities of P-P and P-S scattering.

Equation (6.10) provides a generic relationship between the total scattering cross-section and the scattering cross-section of different wave modes. To obtain explicit expressions of the total scattering cross-sections in heterogeneous media with local isotropy, rigorous derivations are required. In this dissertation, derivations given by Turner and Anugonda (2001) are adopted. The whole derivation is based on three assumptions (Ryzhik, Papanicolaou et al. 1996, Turner and Anugonda 2001):

- (1) the medium is statistically isotropic and statistically homogeneous;

- (2) the phase velocity remains unchanged during the scattering;
- (3) spatial fluctuations of heterogeneities are weak.

Assumption 1 implies that heterogeneities in the medium are uniformly distributed. This assumption is expected to be reasonable for geophysical materials and concrete (Turner and Anugonda 2001). Assumption 2 is known as the Born approximation (Stanke and Kino 1984), which assumes that scattering events only change the propagation direction and wave mode, while the phase velocities, or more specifically, the frequency and wave number, of longitudinal and transverse waves remain constant. This simplification allows expressing the total scattered field as a sum of scattered waves emitted by each individual scatterer (Margerin, Campillo et al. 2000). By adopting the Born approximation, the scattered amplitude can be directly calculated using the three-dimensional Fourier transform of the potential energy function, with respect to the difference of the incident and scattered wave vectors, $\mathbf{p}-\mathbf{p}'$ (Sakurai and Napolitano 2020). In the context of elastic wave scattering in statistically isotropic and statistically homogeneous media, the potential energy function relates to spatial fluctuations of Lamé constants, λ and μ , as well as density, ρ (Ryzhik, Papanicolaou et al. 1996), which govern the propagation of elastic waves in these media. The use of the Born approximation also explains the power spectral densities involved in the expressions shown below: the spatial fluctuations are transformed into the power spectral densities in the Fourier domain when applying the Born approximation (Ryzhik, Papanicolaou et al. 1996). The Born approximation fails when the wavelength is much smaller than the diameter of scatterers (Weaver 1990), or in other words, the scattering is in the geometrical regime (Papadakis 1965). Assumption 3 is to avoid the occurrence of localization (Anderson 1985, Weaver 1990, Sheng 2006), a phenomenon in which energy propagation is hindered within a confined region due to significant interferences from scatterers. The validity of Assumption 2 and 3 will be discussed in Section 6.7.3.

The mode transition-related total scattering cross-sections are shown as follows (Turner and Anugonda 2001):

$$\begin{aligned} \Sigma_{pp} &= \int_{-1}^{+1} \sigma_{pp}(\chi) d\chi, \\ \sigma_{pp}(\chi) &= \frac{\pi^2 \omega^4}{v_p^4} \left[\frac{\lambda^2}{(\lambda + 2\mu)^2} \tilde{R}_{\lambda\lambda}^{pp}(\chi) + \frac{4\lambda\mu}{(\lambda + 2\mu)^2} (\chi)^2 \tilde{R}_{\lambda\mu}^{pp}(\chi) + \frac{4\mu^2}{(\lambda + 2\mu)^2} (\chi)^4 \tilde{R}_{\mu\mu}^{pp}(\chi) \right. \\ &\quad \left. + (\chi)^2 \tilde{R}_{\rho\rho}^{pp}(\chi) + \frac{2\lambda}{\lambda + 2\mu} \chi \tilde{R}_{\lambda\rho}^{pp}(\chi) + \frac{4\mu}{\lambda + 2\mu} (\chi)^3 \tilde{R}_{\rho\mu}^{pp}(\chi) \right], \end{aligned} \quad (6.12a)$$

$$\begin{aligned} \Sigma_{ss} &= \int_{-1}^{+1} \sigma_{ss}(\chi) d\chi, \\ \sigma_{ss}(\chi) &= \frac{\pi^2 \omega^4}{2v_s^4} \left[(1 - 3\chi^2 + 4\chi^4) \tilde{R}_{\mu\mu}^{ss}(\chi) + (\chi^2 + 1) \tilde{R}_{\rho\rho}^{ss}(\chi) + 4\chi^3 \tilde{R}_{\rho\mu}^{ss}(\chi) \right], \end{aligned} \quad (6.12b)$$

6.3 Total scattering cross-sections and energy equilibration in elastic media

$$\begin{aligned}\Sigma_{\text{PS}} &= \int_{-1}^{+1} \sigma_{\text{PS}}(\chi) d\chi, \\ \sigma_{\text{PS}}(\chi) &= \frac{\pi^2 \omega^4}{v_s^3 v_p} \left[\frac{4\mu}{(\lambda + 2\mu)} \chi^2 (1 - \chi^2) \tilde{R}_{\mu\mu}^{\text{PS}}(\chi) + (1 - \chi^2) \tilde{R}_{\rho\rho}^{\text{PS}}(\chi) \right. \\ &\quad \left. + 4\sqrt{\frac{\mu}{\lambda + 2\mu}} \chi (1 - \chi^2) \tilde{R}_{\rho\mu}^{\text{PS}}(\chi) \right],\end{aligned}\tag{6.12c}$$

$$\begin{aligned}\Sigma_{\text{SP}} &= \int_{-1}^{+1} \sigma_{\text{SP}}(\chi) d\chi, \\ \sigma_{\text{SP}}(\chi) &= \frac{\pi^2 \omega^4}{2v_p^3 v_s} \left[\frac{4\mu}{(\lambda + 2\mu)} \chi^2 (1 - \chi^2) \tilde{R}_{\mu\mu}^{\text{SP}}(\chi) + (1 - \chi^2) \tilde{R}_{\rho\rho}^{\text{SP}}(\chi) \right. \\ &\quad \left. + 4\sqrt{\frac{\mu}{\lambda + 2\mu}} \chi (1 - \chi^2) \tilde{R}_{\rho\mu}^{\text{SP}}(\chi) \right],\end{aligned}\tag{6.12d}$$

where ω represents the angular frequency, μ and λ are Lamé parameters of the heterogeneous medium (average among different phases), v_p and v_s denote longitudinal wave and transverse wave velocities in the heterogeneous medium (average among different phases), and ρ is the density of the heterogeneous medium (average among different phases). The parameter χ is defined as the cosine of the scattering angle, $\cos\theta_s$, between the incident wave vector $\mathbf{k}_K = (\omega/v_K)\mathbf{p}$ and scattered wave vector $\mathbf{k}_L = (\omega/v_L)\mathbf{p}'$, where superscripts K ($K \in \{P, S\}$) and L ($L \in \{P, S\}$) represent the modes of incident and scattered waves, respectively. The power spectral density (PSD) of material property fluctuation $\tilde{R}_{ij}^{\text{KL}}(\chi)$ involved in Equation (6.12) is defined as (Turner and Anugonda 2001):

$$\tilde{R}_{ij}^{\text{KL}}(\chi) := \tilde{R}_{ij}^{\text{KL}}(|\mathbf{k}_K - \mathbf{k}_L|),\tag{6.13}$$

where subscripts i and j can be material parameters ρ , μ and λ . For example, $\tilde{R}_{\lambda\lambda}$ is the PSD of fluctuations of λ , and $\tilde{R}_{\lambda\mu}$ is the cross power spectral density (CPSD) of fluctuations of λ and μ . Calculating the PSD and CPSD of material property fluctuations in concrete is a complex task. To make this feasible, certain simplifications are required, which will be explained in detail in Section 6.4.1.

It should be noted that expressions in Equation (6.12) correspond to the wave energy, which are twice the expressions associated with displacement (Turner and Anugonda 2001). As shown in Equation (6.12c) and (6.12d), the ratio of Σ_{SP} and Σ_{PS} is a constant independent of the scattering mechanism:

$$\frac{\Sigma_{\text{SP}}}{\Sigma_{\text{PS}}} = \frac{v_s^2}{2v_p^2}.\tag{6.14}$$

6.3.3 Energy equilibration and equilibration time

In this section, the time required to reach the energy equilibration between longitudinal and transverse waves, as well as the two transverse wave modes, based on the probabilistic model proposed by Snieder (2002) will be derived. Although the derivation is conducted in infinite media, these theoretical expressions can also be applied to concrete components with boundaries, as long as the influence of Rayleigh waves is limited (Tréguerès and van Tiggelen 2001).

6.3.3.1 Energy equilibration between longitudinal and transverse waves

Take the notations E_P for longitudinal wave energy and E_S for transverse wave energy. The probability of a longitudinal wave converting to a transverse wave can be represented by the fraction of total cross-section area blocked by scatterers that enforce this conversion. This probability can be denoted as p_{PS} . Similarly, p_{SP} represents the probability of a transverse wave converting to a longitudinal wave. Please note here that $p_{PS} \neq p_{SP}$, as also indicated in Equation (6.14). The number of cross-sections with scatterers encountered by a longitudinal wave in a time interval dt is defined as $v_P \times dt / x_a$. Consequently, the reduction of the longitudinal wave energy due to conversion into the transverse wave energy can be defined as $p_{PS} \times E_P \times v_P \times dt / x_a$. Using the same definitions, the total change in the longitudinal and transverse wave energies during a time interval dt can be expressed as (Snieder 2002):

$$\begin{aligned} \frac{dE_P}{dt} &= \frac{1}{x_a} (p_{SP} v_S E_S - p_{PS} v_P E_P) \\ &= \Sigma_{SP} v_S E_S - \Sigma_{PS} v_P E_P \quad , \end{aligned} \quad (6.15a)$$

$$\begin{aligned} \frac{dE_S}{dt} &= \frac{1}{x_a} (p_{PS} v_P E_P - p_{SP} v_S E_S) \\ &= \Sigma_{PS} v_P E_P - \Sigma_{SP} v_S E_S \quad . \end{aligned} \quad (6.15b)$$

By substituting Equation (6.14) into Equation (6.15), one can get:

$$\frac{dE_P}{dt} = -v_P \Sigma_{PS} E_P + \frac{v_S^3}{2v_P^2} \Sigma_{PS} E_S \quad , \quad (6.16a)$$

$$\frac{dE_S}{dt} = -\frac{v_S^3}{2v_P^2} \Sigma_{PS} E_S + v_P \Sigma_{PS} E_P \quad , \quad (6.16b)$$

or in a matrix form:

6.3 Total scattering cross-sections and energy equilibration in elastic media

$$\begin{pmatrix} \frac{dE_p}{dt} \\ \frac{dE_s}{dt} \end{pmatrix} = -v_p \Sigma_{ps} \begin{pmatrix} 1 & -\frac{v_s^3}{2v_p^3} \\ -1 & \frac{v_s^3}{2v_p^3} \end{pmatrix} \begin{pmatrix} E_p \\ E_s \end{pmatrix}. \quad (6.17)$$

By setting dE_p/dt to 0, which indicates that the rate of change of longitudinal wave energy over time is zero, one can further obtain the energy equilibration ratio between longitudinal and transverse waves (Weaver 1990, Ryzhik, Papanicolaou et al. 1996, Turner 1998, Snieder 2002):

$$\frac{E_p}{E_s} = \frac{v_s^3}{2v_p^3}. \quad (6.18)$$

One can also estimate the energy evolution over time by solving the differential equation in Equation (6.16a). Since the dissipation is not considered here, the total energy E follows the energy conservation and can be expressed as a sum of E_p and E_s . This energy conservation can be used to eliminate E_s in Equation (6.16a), and one can obtain:

$$\frac{dE_p}{dt} = \frac{v_s^3}{2v_p^2} \Sigma_{ps} E - \frac{2v_p^3 + v_s^3}{2v_p^2} \Sigma_{ps} E_p. \quad (6.19)$$

The analytical solution of Equation (6.19) is:

$$E_p = \frac{v_s^3}{2v_p^3 + v_s^3} E \pm E_p^{(0)} \frac{2v_p^2}{2v_p^3 + v_s^3} \frac{1}{\Sigma_{ps}} e^{-\frac{t}{\frac{2v_p^2}{2v_p^3 + v_s^3} \frac{1}{\Sigma_{ps}}}}, \quad (6.20)$$

where $E_p^{(0)}$ is related to the initial energy of longitudinal waves at $t=0$. Solutions for both longitudinal and transverse wave energies can be represented in a matrix form as:

$$\begin{pmatrix} E_p \\ E_s \end{pmatrix} = \begin{pmatrix} \frac{v_s^3}{2v_p^3 + v_s^3} \\ \frac{2v_p^3}{2v_p^3 + v_s^3} \end{pmatrix} E \pm \begin{pmatrix} E_p^{(0)} \frac{2v_p^2}{2v_p^3 + v_s^3} \frac{1}{\Sigma_{ps}} \\ -E_s^{(0)} \frac{2v_p^2}{2v_p^3 + v_s^3} \frac{1}{\Sigma_{ps}} \end{pmatrix} e^{-\frac{t}{\frac{2v_p^2}{2v_p^3 + v_s^3} \frac{1}{\Sigma_{ps}}}}. \quad (6.21)$$

The time required for the energy equilibration between longitudinal and transverse waves is determined by the exponential function in Equation (6.21). This function can be interpreted as an exponential decay, and the characteristic equilibration time τ_{ps} is defined as (Margerin, van Tiggelen et al. 2001):

$$\tau_{ps} := \frac{2v_p^2}{v_s^3 + 2v_p^3} \frac{1}{\Sigma_{ps}}. \quad (6.22)$$

As the equilibration time in Equation (6.22) is a characteristic value of exponential decay shown in Equation (6.21), this time represents the global energy equilibration of the entire

wave field (Trégourès and van Tiggelen 2001) and does not indicate local energy equilibration (Margerin, van Tiggelen et al. 2001). It is important to note that not all waves necessarily achieve equilibration at time τ_{PS} ; however, they attain equilibration in a statistical sense at this moment. The equilibration time shown in Equation (6.22) is in line with the finding reported by Trégourès and van Tiggelen (2001) (see page 30 in their paper).

It should be noted that the previous derivation does not consider the intrinsic dissipation. This term can be taken into consideration by adding an additional dissipation matrix in Equation (6.17) (Trégourès and van Tiggelen 2001):

$$\begin{aligned} \begin{pmatrix} \frac{dE_p}{dt} \\ \frac{dE_s}{dt} \end{pmatrix} &= -v_p \Sigma_{PS} \begin{pmatrix} 1 & -\frac{v_s^3}{2v_p^3} \\ -1 & \frac{v_s^3}{2v_p^3} \end{pmatrix} \begin{pmatrix} E_p \\ E_s \end{pmatrix} - \begin{pmatrix} \frac{1}{\tau_p^{(a)}} & 0 \\ 0 & \frac{1}{\tau_s^{(a)}} \end{pmatrix} \begin{pmatrix} E_p \\ E_s \end{pmatrix} \\ &= -(\mathbf{J} + \mathbf{A}) \begin{pmatrix} E_p \\ E_s \end{pmatrix}, \end{aligned} \quad (6.23)$$

where \mathbf{J} is the mode conversion matrix and \mathbf{A} is the dissipation matrix. The parameters $\tau_p^{(a)}$ and $\tau_s^{(a)}$ are characteristic dissipation times of longitudinal and transverse waves, respectively. There is no analytical solution for Equation (6.23), but one can get an asymptotic approximation by using the perturbation method with the assumption that the dissipation time is much larger than the scattering mean free time (Margerin, van Tiggelen et al. 2001). However, in this dissertation, we will address it using a different approach.

The matrix $\mathbf{J} + \mathbf{A}$ is essentially a matrix that describes dynamics of elastic wave energy. To clarify the physical meaning of eigenvalues in the matrix $\mathbf{J} + \mathbf{A}$, here, we will consider the non-dissipative case, in which the dissipation matrix is a zero matrix and the energy motion is governed by the conversion matrix \mathbf{J} . The eigenvalues λ_i ($i \in \{1, 2\}$) and corresponding eigenvectors \mathbf{V}_i of the conversion matrix are:

$$\lambda_1 = 0, \quad \mathbf{V}_1 = \begin{pmatrix} 1 \\ \frac{2v_p^3}{v_s^3} \end{pmatrix}, \quad (6.24a)$$

$$\lambda_2 = \frac{2v_p^3 + v_s^3}{2v_p^2} \Sigma_{PS}, \quad \mathbf{V}_2 = \begin{pmatrix} 1 \\ -1 \end{pmatrix}. \quad (6.24b)$$

The first eigenvector corresponds to the energy equilibration ratio, indicating the equilibration of energy between the two wave modes. The corresponding eigenvalue signifies that, statistically, there is no energy conversion when the whole system reaches the equilibration. The second eigenvector indicates the energy conservation between two wave

6.4 Estimation of total scattering cross-sections in concrete

modes. The second eigenvalue coincides to the reciprocal of the equilibration time, describing the speed of energy conversion. Thus, as shown in the non-dissipative case, the equilibration time and equilibration ratio can be estimated by numerically calculating the eigenvalues and eigenvectors of the dynamic matrix $\mathbf{J}+\mathbf{A}$. This approach will be employed to determine the equilibration time and equilibration ratio in the presence of dissipation.

6.3.3.2 Energy equilibration between two transverse waves

Using a similar definition mentioned in Section 6.3.3.1, energy changes in horizontal transverse (SH) waves and vertical transverse (SV) waves are:

$$\begin{aligned} \frac{dE_{SV}}{dt} &= \frac{1}{x_a} \left[p_{ss} v_s E_{SH} + \frac{1}{2} p_{ps} v_p E_p - (p_{ss} + p_{sp}) v_s E_{SV} \right] \\ &= \Sigma_{ss} v_s E_{SH} + \frac{1}{2} \Sigma_{ps} v_p E_p - (\Sigma_{ss} + \Sigma_{sp}) v_s E_{SV} , \end{aligned} \quad (6.25a)$$

$$\begin{aligned} \frac{dE_{SH}}{dt} &= \frac{1}{x_a} \left[p_{ss} v_s E_{SV} + \frac{1}{2} p_{ps} v_p E_p - (p_{ss} + p_{sp}) v_s E_{SH} \right] \\ &= \Sigma_{ss} v_s E_{SV} + \frac{1}{2} \Sigma_{ps} v_p E_p - (\Sigma_{ss} + \Sigma_{sp}) v_s E_{SH} . \end{aligned} \quad (6.25b)$$

The factor 1/2 in the term with the longitudinal wave energy denotes the equivalent possibility of a longitudinal wave converting into SH and SV waves. Taking the difference of the two equations in Equation (6.25) gives:

$$\frac{d(E_{SV} - E_{SH})}{dt} = -(\Sigma_{ss} + \Sigma_{sp}) v_s (E_{SV} - E_{SH}) . \quad (6.26)$$

By taking $d(E_{SV} - E_{SH})/dt = 0$, it can be observed that the energy of SH and SV waves becomes equal once they reach equilibration. Therefore, the equilibration ratio between two transverse waves is equal to one. The characteristic decay time for the differential equation in Equation (6.26) is:

$$\tau_{ss} := \frac{1}{(\Sigma_{ss} + \Sigma_{sp}) v_s} . \quad (6.27)$$

This decay time is the equilibration time between SH and SV wave energy. Considering that the dissipation of SH waves and SV waves is the same, the dissipation does not affect the equilibration ratio (Margerin, van Tiggelen et al. 2001, Trégourès and van Tiggelen 2001) but the equilibration time shown in Equation (6.27) will change.

6.4 Estimation of total scattering cross-sections in concrete

As shown in Equation (6.22), Equation (6.23) and Equation (6.27), total scattering cross-sections are crucial for understanding the energy equilibration process. As indicated in

Equation (6.12), calculating these scattering cross-sections first requires determining the PSD and CPSD of material property fluctuations. However, this calculation is challenging in the case of concrete. To address this complexity, certain simplifications are necessary, which will be explained in detail in Section 6.4.1. Moving forward to Section 6.4.2, analytical expressions of both total scattering cross-sections and weighted total scattering cross-sections will be provided for bulk waves in concrete.

6.4.1 Power spectral density of material property fluctuations in concrete

6.4.1.1 Spatial correlation function of material property fluctuations

It is crucial to underscore that obtaining the PSD of material property fluctuations directly in the Fourier domain is not feasible. Hence, a more viable approach involves initially acquiring the spatial correlation function of material property fluctuations and subsequently transforming it into PSD or CPSD through Fourier transform operation. Spatial correlation function, which quantifies the spatial statistics of material properties in the heterogeneous medium, is utilized to link spatial fluctuations of elastic parameters and the dynamic properties of elastic waves, i.e., velocity and scattering-induced attenuation (Calvet and Margerin 2012). In this section, the acquisition of spatial correlation function of material property fluctuations in concrete will be introduced.

To simplify the concrete material in the following derivation, this material is treated as a two-phase or binary material: scatterers and the matrix. Investigating the spatial or two-point correlation function in a binary material is not a new topic. The earliest attempt can be dated back to 1949 (Debye and Bueche 1949). Since then, the related theory has been further developed (Frisch 1965) and been widely applied in the construction of random media (Yeong and Torquato 1998, Rozman and Utz 2001, Koutsourelakis and Deodatis 2005).

For the assumed two-phase concrete, the entirely occupied three-dimensional space can be divided into two non-intersecting parts: scatterer K_s and matrix K_m . Recent studies by Ramaniraka et al. (2019, 2022) have yielded insights into the scattering behaviour of elastic waves with frequencies of several hundred kilohertz in concrete. Through a combination of numerical simulations and experimental observations, these studies have established that the scattering phenomenon is mainly attributed to the interfacial transition zone (ITZ) surrounding the coarse aggregates. In Section 6.7.2, a further discussion is given on this topic.

The random field for the scatterers is:

$$I_s(\mathbf{x}) = \begin{cases} 1, & \text{if } \mathbf{x} \in K_s \\ 0, & \text{otherwise} \end{cases} \quad (6.28)$$

6.4 Estimation of total scattering cross-sections in concrete

Consequently, the random field for the matrix is $I_m(\mathbf{x})=1-I_s(\mathbf{x})$. The ensemble average of $I_s(\mathbf{x})$ and $I_m(\mathbf{x})$ are equivalent to the volume fraction of scatterers ϕ_s and matrix ϕ_m :

$$\langle I_s(\mathbf{x}) \rangle = \phi_s, \quad (6.29a)$$

$$\langle I_m(\mathbf{x}) \rangle = \phi_m = 1 - \phi_s, \quad (6.29b)$$

where $\langle \cdot \rangle$ indicates the ensemble average operation. The correlation function of material property fluctuations in the medium is in the following form (Liu and Turner 2008):

$$R_{ij}(r) = \frac{(A_i^{(m)} - A_i^{(s)})(A_j^{(m)} - A_j^{(s)})}{\langle A_i \rangle \langle A_j \rangle} [\langle I_s(\mathbf{x}_1) I_s(\mathbf{x}_2) \rangle - \phi_s^2], \quad (6.30)$$

where r represents the spatial distance between \mathbf{x}_1 and \mathbf{x}_2 . The parameters $A_i^{(s)}$ and $A_i^{(m)}$ denote magnitudes of material property i (i and j can be density ρ , Lamé second parameter μ and Lamé first parameter λ) of the scatterer and matrix, respectively. For example, $R_{\lambda\lambda}$ is the auto-correlation function of fluctuations of λ , and $R_{\lambda\mu}$ is the cross-correlation function of fluctuations of λ and μ . The derivation of Equation (6.30) can be found in Appendix E.

By introducing a normalized correlation function $R(r)$, the second-order statistics of the fluctuations in Equation (6.30) can be defined as (Debye, Anderson Jr et al. 1957, Torquato 1999):

$$\begin{aligned} \langle I_s(\mathbf{x}_1) I_s(\mathbf{x}_2) \rangle - \phi_s^2 &= \phi_s \phi_m R(|\mathbf{x}_1 - \mathbf{x}_2|) \\ &= \phi_s \phi_m R(r). \end{aligned} \quad (6.31)$$

Substituting Equation (6.31) into Equation (6.30) gives:

$$\begin{aligned} R_{ij}(r) &= \frac{(A_i^{(m)} - A_i^{(s)})(A_j^{(m)} - A_j^{(s)})}{\langle A_i \rangle \langle A_j \rangle} \phi_s \phi_m R(r) \\ &= A_{ij}^2 \phi_s \phi_m R(r), \end{aligned} \quad (6.32)$$

where A_{ij} is the contrast of the properties for the two phases. The form for the normalized correlation function $R(r)$ is assumed to be an exponential function, which is able to describe correlation of continuous and discrete materials fairly well (Debye and Bueche 1949, Stanke 1986):

$$R(r) = e^{-\frac{r}{H}}, \quad (6.33)$$

where H is the characteristic correlation length. Equation (6.33) can be interpreted as a formula describing the probability that two points separated by a distance r are in the same phase within a binary material. When r exceeds H , this probability becomes low.

From this perspective, the characteristic correlation length H can be seen as the average distance between regions of the phase with the lower volume fraction in the binary materials. It is noteworthy that the characteristic correlation length in concrete differs from that in polycrystalline metals or ceramics. In polycrystals, the medium is dominated by grains (Zavattieri, Raghuram et al. 2001). As a result, the characteristic correlation length in this medium is closely tied to the size of the grains. However, in concrete, the matrix component, the mortar, constitutes a larger portion, leading to the characteristic correlation length being primarily influenced by the spacing between scatterers, the coarse aggregates.

The most challenging aspect in calculating the correlation function of material property fluctuations through Equation (6.32) lies in determining the contrast of properties for the two phases. Since scattering events happen on the surface of scatterers, material properties of scatterers refer to the properties of the ITZ. Hence, the average material property can be written as:

$$\langle A_i \rangle = \phi_s A_i^{(s)} + \phi_m A_i^{(m)} . \quad (6.34)$$

To simplify the contrast of properties for the two phases, the following relation between material properties of two phases is proposed:

$$A_i^{(s)} = \frac{\phi_s}{1 + \phi_s} A_i^{(m)} . \quad (6.35)$$

By doing this, A_{ij}^2 in Equation (6.32) is a constant 1. Considering that the volume fraction of coarse aggregates in concrete is usually lower than 0.5, Equation (6.35) implies that the material properties of ITZ are at most 33% of those of matrix. Experimental studies reported in the literature indicate that the Poisson ratio of the ITZ is generally comparable to that of the matrix (Keinde, Kamali-Bernard et al. 2014, Li, Li et al. 2019), while the elastic modulus of the ITZ ranges from 40% to 85% of the matrix (Lutz, Monteiro et al. 1997, Li, Zhao et al. 1999, Mondal, Shah et al. 2009, Keinde, Kamali-Bernard et al. 2014). These observations imply that ratios of Lamé parameters μ and λ are approximately proportional to the ratio of the elastic moduli. Hence, employing Equation (6.35) could potentially result in an overestimation of the amplitude of the correlation function in Equation (6.32), consequently leading to an overestimation of total scattering cross-sections. Please note that the ratio of density in Equation (6.35) is assumed to be comparable to that of Lamé parameters. The reason for this is that no available research exists working on the density of ITZ to the best of our knowledge. Anticipated to have a lower density than the matrix due to its porous structure, the exact density ratio between the ITZ and the matrix proves challenging to quantify.

6.4 Estimation of total scattering cross-sections in concrete

6.4.1.2 Power spectral density of material property fluctuations

In Section 6.4.1.1, the spatial correlation function of material property fluctuations is defined. In the calculation of total scattering cross-sections, the spatial correlation function should be transformed into the Fourier domain. The spatial Fourier transform of normalized correlation function $R(r)$ in Equation (6.33) is given as (Turner and Anugonda 2001):

$$\tilde{R}(q) = \frac{H^3}{\pi^2 (1 + H^2 q^2)^2}, \quad (6.36)$$

where q represents the angular wavenumber with a physical dimension of L^{-1} . Together with Equation (6.32) and Equation (6.35), the PSD or CPSD of material property fluctuation is given as follows:

$$\tilde{R}_{ij}(q) = \frac{\phi_s \phi_m H^3}{\pi^2 (1 + H^2 q^2)^2}, \quad (6.37)$$

where i and j can be density ρ , Lamé second parameter μ and Lamé first parameter λ . Therefore, Equation (6.13) can be written as:

$$\begin{aligned} \tilde{R}_{ij}^{KL}(\chi) &= \tilde{R}_{ij}^{KL}(|\mathbf{k}_K - \mathbf{k}_L|) \\ &= \frac{\phi_s (1 - \phi_s) H^3}{\pi^2 [1 + H^2 (|\mathbf{k}_K - \mathbf{k}_L|)^2]^2} \\ &= \frac{\phi_s (1 - \phi_s) H^3}{\pi^2 (1 + x_K^2 + x_L^2 - 2x_K x_L \chi)^2}, \end{aligned} \quad (6.38)$$

where x_K or x_L is the dimensionless frequency defined as $x_K = \omega H / v_K$ or $x_L = \omega H / v_L$. As shown in Equation (6.38), the physical dimension of PSD or CPSD is L^3 . For bulk waves, Equation (6.38) can be expanded to include three possible combinations of wave mode transitions: P-P, S-S, and S-P (P-S). After incorporating these wave mode transitions, Equation (6.38) can be expressed as follows:

$$\tilde{R}_{ij}^{PP}(\chi) = \frac{\phi_s (1 - \phi_s) H^3}{\pi^2 [1 + 2x_P^2 (1 - \chi)]^2}, \quad (6.39a)$$

$$\tilde{R}_{ij}^{SS}(\chi) = \frac{\phi_s (1 - \phi_s) H^3}{\pi^2 [1 + 2x_S^2 (1 - \chi)]^2}, \quad (6.39b)$$

$$\tilde{R}_{ij}^{PS}(\chi) = \tilde{R}_{ij}^{SP}(\chi) = \frac{\phi_s (1 - \phi_s) H^3}{\pi^2 (1 + x_P^2 + x_S^2 - 2x_P x_S \chi)^2}. \quad (6.39c)$$

There are three key parameters in Equation (6.39): angular frequency ω , characteristic correlation length H , and volume fraction of coarse aggregates ϕ_s . The angular frequency is related to the property of bulk waves and is independent of the medium itself. The volume fraction of coarse aggregates can be directly obtained from the mixture composition of concrete. Consequently, to apply Equation (6.39) to concrete, it is essential to define the characteristic correlation length H . The details of this specification will be presented in the subsequent section.

6.4.1.3 Determination of characteristic correlation length in concrete

In binary materials, there exists a correlation between the volume fraction of scatterers ϕ_s and the characteristic correlation length H when the diameter of scatterers is a constant. This correlation is evident in the inverse relationship: as the volume fraction of scatterers increases, the characteristic correlation length decreases. Therefore, a similar method as for determining the mean free path in Section 6.3.1 is employed to estimate the characteristic correlation length through the volume fraction of coarse aggregates.

Assuming that all coarse aggregates (scatterers) have a spherical shape with the same radius of r_s . This assumption allows us to consider a uniform size for all coarse aggregates, making the estimation of the correlation length more straightforward. A differential equation analogous to Equation (6.2) is formulated to describe the area of the medium blocked by coarse aggregates:

$$\begin{aligned} dA &= -\frac{\phi_s A dx}{\frac{4}{3}\pi r_s^3} \frac{\pi r_s^2}{A} A \\ &= -A \frac{3\phi_s}{4r_s} dx . \end{aligned} \quad (6.40)$$

Therefore, the characteristic correlation length H can be given as:

$$H = \frac{4r_s}{3\phi_s} . \quad (6.41)$$

For the remainder of this dissertation, we will refer to it as the characteristic aggregate distance. Similar to the mean free path, the characteristic aggregate distance H can be thought of as the distance with a high probability of separating two coarse aggregates.

By using Equation (6.41), the three unknowns in Equation (6.39) become independent variables: angular frequency of elastic waves ω , volume fraction of coarse aggregates in concrete ϕ_s , and characteristic radius of coarse aggregates r_s . Determining the first two unknowns is relatively straightforward, while the third one requires utilizing sieving information for coarse aggregates. The following expression is adopted for calculating the characteristic radius of coarse aggregates (Alderliesten 2005):

6.4 Estimation of total scattering cross-sections in concrete

$$\frac{4}{3}\pi r_s^3 = \frac{V}{\frac{Vn_1}{\frac{4}{3}\pi r_1^3} + \frac{Vn_2}{\frac{4}{3}\pi r_2^3} + \frac{Vn_3}{\frac{4}{3}\pi r_3^3} \dots + \frac{Vn_g}{\frac{4}{3}\pi r_g^3}}, \quad (6.42a)$$

where V represents the total volume of coarse aggregates, n_i denotes the volume ratio within the grading interval i , and r_i is the characteristic radius within this grading interval. The subscript g denotes the total number of grading intervals. The expression of the characteristic radius of coarse aggregates is then:

$$r_s = \left(\frac{V \frac{1}{\frac{4}{3}\pi}}{\frac{Vn_1}{\frac{4}{3}\pi r_1^3} + \frac{Vn_2}{\frac{4}{3}\pi r_2^3} + \frac{Vn_3}{\frac{4}{3}\pi r_3^3} \dots + \frac{Vn_g}{\frac{4}{3}\pi r_g^3}} \right)^{\frac{1}{3}} \quad (6.42b)$$

$$= \left(\frac{1}{\sum_{i=1}^g \frac{n_i}{r_i^3}} \right)^{\frac{1}{3}},$$

The usage of Equation (6.42) allows for determining the characteristic radius of coarse aggregates without altering the number of scatterers.

6.4.2 Expressions of total scattering cross-sections for bulk waves in concrete

This section aims to integrate the PSD or CPSD of material property fluctuations into expressions for total scattering cross-sections. It is important to note that these total scattering cross-sections are not directly measurable through experiments. An alternative validation method involves indirect validation through diffusivity, which can be acquired from the average intensity of signals. Considering that the theoretical prediction of diffusivity requires not only total scattering cross-sections but also weighted total scattering cross-sections, this section will also provide expressions for the latter.

The expressions for total scattering cross-sections can be simplified by substituting Equation (6.39) into Equation (6.12):

$$\Sigma_{PP} = \frac{\phi_s(1-\phi_s)H^3\omega^4}{v_p^4} \times \int_{-1}^{+1} \frac{\left(\frac{v_p^2-2v_s^2}{v_p^4}\right)^2 + \frac{2(v_p^2-2v_s^2)}{v_p^2}\chi + \left[\frac{4v_s^2(v_p^2-2v_s^2)}{v_p^4} + 1\right]\chi^2 + \frac{4v_s^2}{v_p^2}\chi^3 + \frac{4v_s^4}{v_p^4}\chi^4}{(1+2x_p^2-2x_p^2\chi)^2} d\chi, \quad (6.43a)$$

$$\Sigma_{SS} = \frac{\phi_s(1-\phi_s)H^3\omega^4}{v_s^4} \int_{-1}^{+1} \frac{1-\chi^2+2\chi^3+2\chi^4}{(1+2x_s^2-2x_s^2\chi)^2} d\chi, \quad (6.43b)$$

$$\Sigma_{PS} = \frac{\phi_s(1-\phi_s)H^3\omega^4}{v_p v_s^3} \int_{-1}^{+1} \frac{(1-\chi^2)\left(1+\frac{4v_s}{v_p}\chi+\frac{4v_s^2}{v_p^2}\chi^2\right)}{(1+x_p^2+x_s^2-2x_px_s\chi)^2} d\chi, \quad (6.43c)$$

$$\Sigma_{SP} = \frac{\phi_s(1-\phi_s)H^3\omega^4}{2v_p^3 v_s} \int_{-1}^{+1} \frac{(1-\chi^2)\left(1+\frac{4v_s}{v_p}\chi+\frac{4v_s^2}{v_p^2}\chi^2\right)}{(1+x_p^2+x_s^2-2x_px_s\chi)^2} d\chi. \quad (6.43d)$$

As shown in Equation (6.43), the physical dimension of Σ is L^{-1} . The Lamé parameters in Equation (6.43) are expressed by means of longitudinal and transverse wave velocities. Upon acquiring Equation (6.43), the weighted total scattering cross-sections can be obtained by incorporating a weighting factor of the cosine of the scattering angle in the integral used to calculate total scattering cross-sections, as shown in Equation (6.9). Therefore, the expressions for weighted total scattering cross-sections are shown as follows:

$$\Sigma'_{PP} = \frac{\phi_s(1-\phi_s)H^3\omega^4}{v_p^4} \times \int_{-1}^{+1} \frac{\left(\frac{v_p^2-2v_s^2}{v_p^4}\right)^2 + \frac{2(v_p^2-2v_s^2)}{v_p^2}\chi + \left[\frac{4v_s^2(v_p^2-2v_s^2)}{v_p^4} + 1\right]\chi^2 + \frac{4v_s^2}{v_p^2}\chi^3 + \frac{4v_s^4}{v_p^4}\chi^4}{(1+2x_p^2-2x_p^2\chi)^2} \chi d\chi, \quad (6.44a)$$

$$\Sigma'_{SS} = \frac{\phi_s(1-\phi_s)H^3\omega^4}{v_s^4} \int_{-1}^{+1} \frac{1-\chi^2+2\chi^3+2\chi^4}{(1+2x_s^2-2x_s^2\chi)^2} \chi d\chi, \quad (6.44b)$$

$$\Sigma'_{PS} = \frac{\phi_s(1-\phi_s)H^3\omega^4}{v_p v_s^3} \int_{-1}^{+1} \frac{(1-\chi^2)\left(1+\frac{4v_s}{v_p}\chi+\frac{4v_s^2}{v_p^2}\chi^2\right)}{(1+x_p^2+x_s^2-2x_px_s\chi)^2} \chi d\chi, \quad (6.44c)$$

6.5 Role of dissipation on the equilibration process

$$\Sigma'_{SP} = \frac{\phi_s(1-\phi_s)H^3\omega^4}{2v_p^3v_s} \int_{-1}^{+1} \frac{(1-\chi^2) \left(1 + \frac{4v_s}{v_p} \chi + \frac{4v_s^2}{v_p^2} \chi^2 \right)}{(1+x_p^2+x_s^2-2x_px_s\chi)^2} \chi d\chi . \quad (6.44d)$$

After acquiring both total scattering cross-sections and weighted total scattering cross-sections, transport mean free paths can be obtained through (Weaver and Sachse 1995, Turner 1998, Turner and Anugonda 2001):

$$l_p^* = \frac{\Sigma_{SS} + \Sigma_{SP} - \Sigma'_{SS} + \Sigma'_{PS}}{(\Sigma_{PP} + \Sigma_{PS} - \Sigma'_{PP})(\Sigma_{SS} + \Sigma_{SP} - \Sigma'_{SS}) - \Sigma'_{PS}\Sigma'_{SP}} , \quad (6.45a)$$

$$l_s^* = \frac{\Sigma_{PP} + \Sigma_{PS} - \Sigma'_{PP} + \Sigma'_{SP}}{(\Sigma_{PP} + \Sigma_{PS} - \Sigma'_{PP})(\Sigma_{SS} + \Sigma_{SP} - \Sigma'_{SS}) - \Sigma'_{PS}\Sigma'_{SP}} , \quad (6.45b)$$

and the diffusivity is given by (Weaver and Sachse 1995, Ryzhik, Papanicolaou et al. 1996, Turner 1998, Turner and Anugonda 2001):

$$D = \frac{v_s^3 \left(\frac{1}{3} v_p l_p^* \right) + 2v_p^3 \left(\frac{1}{3} v_s l_s^* \right)}{2v_p^3 + v_s^3} . \quad (6.46)$$

As shown in Equation (6.46), the diffusivity of elastic waves is a weighted average of the diffusivities of longitudinal and transverse waves.

6.5 Role of dissipation on the equilibration process

In Section 6.3, we discussed the theoretical background of the energy equilibration process. To enable its calculation in concrete, we then adapted the expressions of total scattering cross-sections specifically for concrete. In this section, a numerical analysis will be conducted to explore the impact of dissipation on both the equilibrated energy ratio and the time required for global energy equilibration.

6.5.1 Numerical analysis setup

We present three numerical cases for the analysis, and the parameters for these numerical cases are provided in Table 6.1. In each case, one parameter is intentionally tuned to investigate its influence on the energy equilibration. In Case I, the influence of wave frequency on the equilibration process is investigated. The frequency range is chosen from 40 kHz to 200 kHz, a typical frequency band utilized in ultrasonic-based concrete monitoring. Since the dissipation of elastic waves is a function of their frequency, it is concurrently adjusted with the frequency within this range. The dissipation of the transverse wave is estimated based on the relationship between the dissipation and frequency reported in beam member in Figure 4.22. Here, it should be noted that the dissipation measured from the experiment is assumed to be solely attributed to that of transverse waves,

which may lead to a slight underestimation of the transverse wave dissipation due to the presence of longitudinal waves within the measured coda waves. The experimentally derived dissipation is a combination of both transverse and longitudinal wave dissipation. Since longitudinal wave dissipation is lower than that of transverse waves (Margerin, van Tiggelen et al. 2001), attributing the entire measured dissipation to transverse waves could lead to a slight underestimation of their actual dissipation. No existing research has addressed the determination of longitudinal wave dissipation in concrete. Therefore, the following relation, commonly used in geophysics, is adopted to estimate the longitudinal wave dissipation: $\tau^{(a)}_P/\tau^{(a)}_S=10/3$ (Margerin, van Tiggelen et al. 2001).

The coarse aggregate diameter range embraced in the current concrete industry in the Netherlands is typically 4 mm to 16 mm. However, in Case II, this range is adjusted to 2 mm to 16 mm. It is important to note that this adjustment includes fine aggregates with diameters between 2 mm and 4 mm, primarily aimed at assessing the equilibration process in scenarios involving smaller scatterers. Considering that the volume fraction of coarse aggregates in concrete typically remains below 0.5, the volume fraction of aggregates in Case III is specified within the range of 0.1 to 0.5. The calculation steps can be found in Algorithm 6.1.

Table 6.1 Parameters for numerical cases.

Properties	Case I	Case II	Case III
P-wave velocity [m/s]*	4500	4500	4500
S-wave velocity [m/s]**	2745	2745	2745
Frequency of elastic waves [kHz]	From 40 to 200	80	80
Characteristic radius of aggregates [mm]	5	From 1 to 8	5
Volume fraction of aggregates [-]	0.4	0.4	From 0.1 to 0.5
P-wave dissipation [s ⁻¹]	From 600 to 3000	1200	1200
S-wave dissipation [s ⁻¹]***	From 2000 to 10000	4000	4000

Note: * P-wave velocities are estimated through measurements reported in Section 4.2.

** S-wave velocities are estimated through P-wave velocity and the velocity ratio in concrete.

*** S-wave dissipation is estimated from Figure 4.22.

Algorithm 6.1 Calculation of energy equilibration ratio and global equilibration time

- 1: Initialize P-wave velocity v_P , S-wave velocity v_S
 $v_P \leftarrow 4500$
 $v_S \leftarrow 2745$
- 2: Initialize angular frequency ω , characteristic radius of aggregates r_s , volume fraction of aggregates ϕ_s , P-wave dissipation $1/\tau^{(a)}_P$, and S-wave dissipation $1/\tau^{(a)}_S$ based on Table 6.1
- 3: Calculate total scattering cross sections:
 $\Sigma_{SS} \leftarrow \text{Eq. 6.43(b)}$
 $\Sigma_{SP} \leftarrow \text{Eq. 6.43(d)}$
 $\Sigma_{PS} \leftarrow \text{Eq. 6.43(c)}$
- 4: Calculate the global equilibration time for P-S and S-S without dissipation:
 $\tau_{PS} \leftarrow \text{Eq. 6.22}$
 $\tau_{SS} \leftarrow \text{Eq. 6.27}$
- 5: Calculate the P-S equilibration ratio without dissipation:
 $E_P/E_S \leftarrow \text{Eq. 6.18}$
- 6: Calculate eigenvalues and eigenvectors for the matrix $\mathbf{J}+\mathbf{A}$ in Eq. 6.23:

6.5 Role of dissipation on the equilibration process

- $\lambda_i \leftarrow \text{ComputeEigenvalues}(\mathbf{J} + \mathbf{A}), i \in \{1, 2\}$
 $\mathbf{V}_i \leftarrow \text{ComputeEigenvalues}(\mathbf{J} + \mathbf{A}), i \in \{1, 2\}$
 - 7: Calculate the P-S equilibration ratio with dissipation:
 $\mathbf{V}_1 \leftarrow \text{Find } \mathbf{V}_i \text{ with the ratio of two components greater than 0, } V_{i,1}/V_{i,2} > 0$
 $(E_P/E_S)^{(a)} \leftarrow V_{1,1}/V_{1,2}$
 - 8: Calculate the global equilibration time for P-S with dissipation:
 $\lambda_2 \leftarrow \text{Find the minimum value of } \lambda_i$
 $\tau^{(a)}_{PS} \leftarrow 1/\lambda_2$
 - 9: Return $\tau_{PS}, \tau_{SS}, E_P/E_S, \tau^{(a)}_{PS}$, and $(E_P/E_S)^{(a)}$.
-

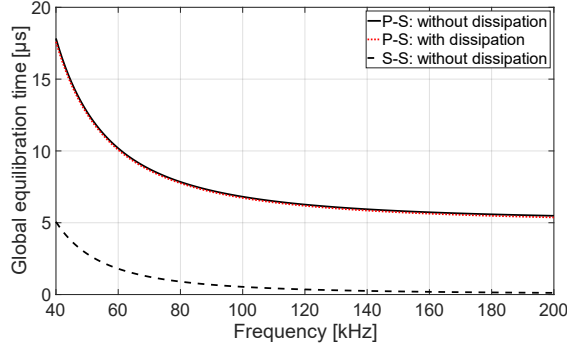
6.5.2 Impact of dissipation on the global equilibration time

The global energy equilibration time (calculated using Equation (6.22) and (6.27)) as a function of the characteristic radius of aggregates, volume fraction of aggregates, and elastic wave frequency are presented in Figure 6.3. In Case I, the global equilibration time for P-S conversion exhibits a declining trend with the rise in wave frequency. This can be attributed to the shorter wavelength of high-frequency waves, facilitating collisions between elastic waves and aggregates. Similarly, for the P-S global equilibration time in Case III, the higher volume fraction of aggregates promotes an increased occurrence of collisions between elastic waves and aggregates, thus contributing to the observed reduction in the global equilibration time.

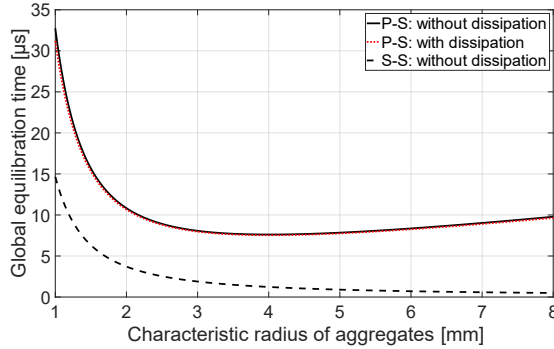
In Case II, the P-S global equilibration time initially experiences a decrease with an increase in the characteristic radius of aggregates, followed by a subsequent slight increase. This two-stage phenomenon stems from the intricate interplay between elastic waves and scatterers. When the volume fraction of aggregates is held constant, smaller aggregates are positioned more closely to each other, yet their small size results in a weaker interaction with elastic waves. Conversely, as the characteristic radius grows, the interaction between elastic waves and scatterers intensifies. Consequently, there is a pronounced decrease in energy equilibration time as the aggregate size increases. These enhanced interactions or collisions play a crucial role in facilitating the equilibration process, with the size of the aggregates primarily determining their interference on propagating waves during this stage. With the continued increase in the characteristic aggregate radius, there is a decrease in the number of aggregates, accompanied by an increase in their characteristic distance. Consequently, elastic waves experience fewer collisions, necessitating a longer time for energy equilibration. During this phase, the interference of aggregates on propagating waves is primarily dictated by the characteristic distance between aggregates. The minimum equilibration time is observed when the aggregate diameter is 8 mm (a radius of 4 mm), signifying that the elastic wave undergoes the highest number of collisions in this scenario. It is noteworthy that this diameter is smaller than both the longitudinal wave wavelength (56.3 mm) and the transverse wave wavelength (34.3 mm).

When considering dissipation, the global equilibration time is consistently reduced in all three cases, which aligns with the trend predicted by the asymptotic solution provided by

Margerin et al. (2001) (see Eq. 12 in their article), in which the existence of dissipation will expedite the reaching of equilibration. For S-S equilibration, the equilibration time is significantly shorter than that of P-S equilibration in all three cases. Consequently, focusing on P-S equilibration is sufficient for the concrete monitoring.

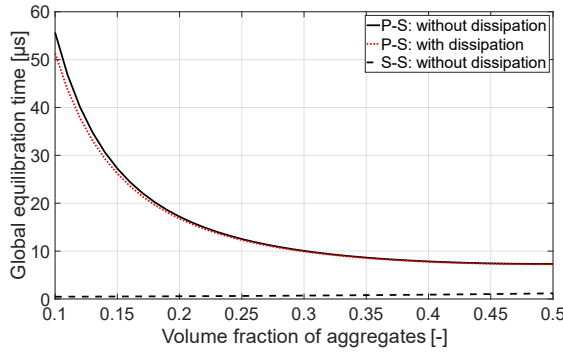


(a) Case I: elastic wave frequency.



(b) Case II: characteristic radius of aggregates.

6.5 Role of dissipation on the equilibration process

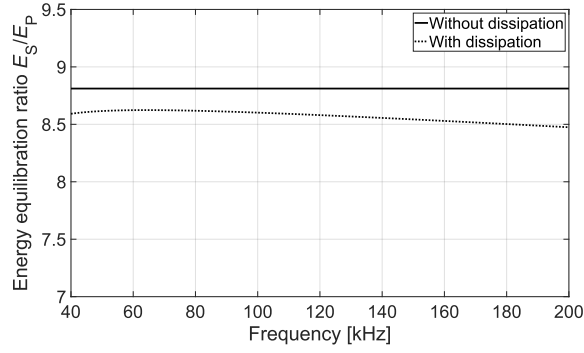


(c) Case III: volume fraction of aggregates.

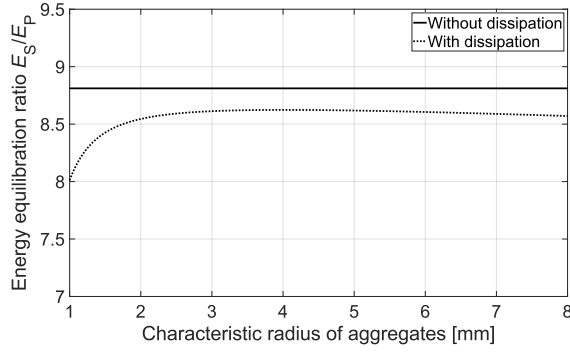
Figure 6.3 Numerical results of global equilibration time as a function of elastic wave frequency, characteristic radius of aggregates, and volume fraction of aggregates. Calculation procedures can be found in Algorithm 6.1.

6.5.3 Impact of dissipation on the equilibrated energy ratio

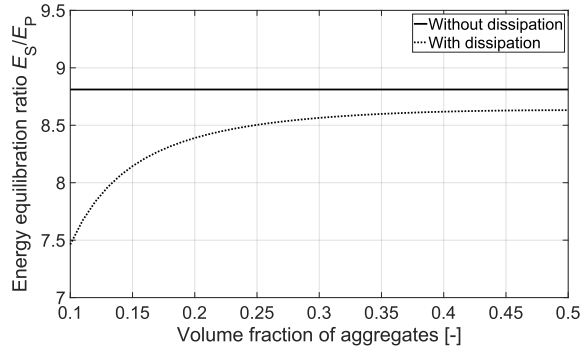
The energy equilibration ratio E_S/E_P as a function of elastic wave frequency, characteristic radius of aggregates and volume fraction of aggregates are presented in Figure 6.4. The incorporation of dissipation causes a shift in favour of the least absorbed longitudinal wave mode in the energy equilibration ratio E_S/E_P . This finding is consistent with the asymptotic solutions presented by Margerin et al. (2001) (see Eq. 11 in their article) and Trégourès et al. (2001) (Eq. 68). Furthermore, the energy equilibration ratio E_S/E_P , when considering dissipation, is found to be sensitive to the volume fraction of aggregates but not significantly influenced by the wave frequency. Since the equilibration ratio is slightly lower when considering dissipation, it is worth noting that when assessing the wave energy and velocity changes observed in the coda, directly utilizing the equilibrated energy ratio suggested by Snieder (2002), where E_S/E_P is around 10.4, assuming $v_P = \sqrt{3} \times v_S$ and no dissipation, may result in a slight overestimation of the contribution from transverse wave energy.



(a) Case I: elastic wave frequency.



(b) Case II: characteristic radius of aggregates.



(c) Case III: volume fraction of aggregates.

Figure 6.4 Numerical results of energy equilibration ratio as a function of elastic wave frequency, characteristic radius of aggregates, and volume fraction of aggregates. Calculation procedures can be found in Algorithm 6.1.

6.6 Model validation and prediction of wave energy evolution

In Section 6.5, we investigated the role of dissipation in the energy equilibration process. We have noted that S-S equilibration process is significantly faster than the P-S equilibration process, which suggests that focusing on P-S equilibration is sufficient for concrete monitoring. In this section, the proposed model is validated by the diffusivities acquired from experiments introduced in Chapter 4. Detailed information regarding the acquisition of diffusivities can be found in Section 4.3. The model validation is provided in Section 6.6.1. The validated model is then employed to estimate the evolution of bulk wave energy in concrete structures, as shown in Section 6.6.2.

6.6.1 Model validation

To ensure the reliability of the theoretical model in predicting energy evolution, this model should be validated first before applying to concrete. In this section, the validation is conducted by comparing diffusivities calculated from the model with those acquired from experiments.

The theoretical model relies on three key inputs: the angular frequency of the elastic wave (ω), the volume fraction of coarse aggregate in concrete (ϕ_s), and the characteristic radius of coarse aggregates (r_s). The choice of these three parameters in the theoretical model are discussed first. The angular frequency is derived from the frequency in Hz.

The experimental results involve those for geopolymers concrete members and those for the concrete cylinder. The diffusivities in the concrete cylinder can be found in Figure 4.27(a). For geopolymers concrete members, there are three members involved, including two beams and one slab. In Section 4.3.4, one beam was introduced and used to demonstrate the extraction of diffusive properties in a medium with planar boundaries. The geometries and sensor layouts in the remaining geopolymers concrete members are introduced in Appendix F. The procedure and parameter selection for fitting the diffusivity through received signals can be found in Section 4.3.6. To ensure comparability between experimental results and theoretical predictions, the frequencies incorporated into the model align with those used in the signal processing of experimental data, ranging from 50 kHz to 400 kHz with a 50 kHz interval. The dry density of coarse aggregates used in all concrete specimens is 2630 kg/m³. The volume fraction of coarse aggregate in concrete can be directly deduced from the mixture composition, as shown in Table 6.2 and Table 6.3. The volume fractions of coarse aggregates are equal to 0.257 for geopolymers concrete specimens and 0.278 for concrete cylinder. The characteristic radius of coarse aggregates is computed using Equation (6.42), and the sieving of coarse aggregates for all concrete specimens is provided in Table 6.4. Within each grading interval, there exist two characteristic radii: the maximum radius and the minimum radius, which are related to the range of particle sizes that can be effectively separated. To explore the impact of the choice of

the characteristic radii on diffusivities predicted by the model, both the maximum and minimum radii within grading intervals are employed as the characteristic radii of coarse aggregates for respective calculations. The average longitudinal wave velocities measured in geopolymer concrete beams and the concrete cylinder are 4544 m/s and 4688 m/s, respectively. The transverse wave velocities can be estimated from the longitudinal wave velocities with a factor of 0.61 (Nogueira and Rens 2019).

Table 6.2 Mixture composition of the geopolymer concrete in prestressed beams.

Materials	Content (kg/m ³)
Blast furnace slag	550.0
NaOH solution (50.0 wt%)	36.9
Sodium silicate solution (48.0 wt%)	80.4
Water	191.0
Admixture/Retarder	1.375
Sand: 0-4 mm	762.0
Gravel: 4-16 mm	676.0

Table 6.3 Mixture composition of the concrete in the cylindrical specimen.

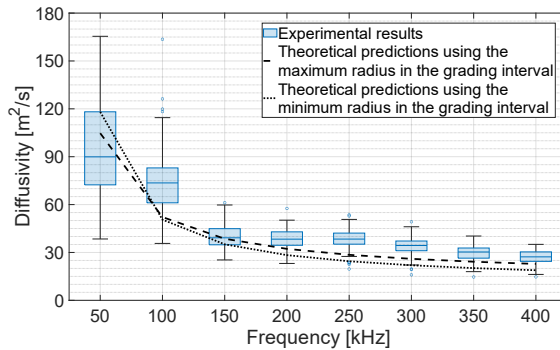
Materials	Content (kg/m ³)
CEM IIIB	285.0
CEM IIIA	285.0
Fillers (fly ash)	45.0
Water	192.0
Super plasticizer	4.3
Sand: 0-4 mm	830.0
Gravel: 4-16 mm	730.0

Table 6.4 Sieving of gravel 4-16 mm in the mixture composition.

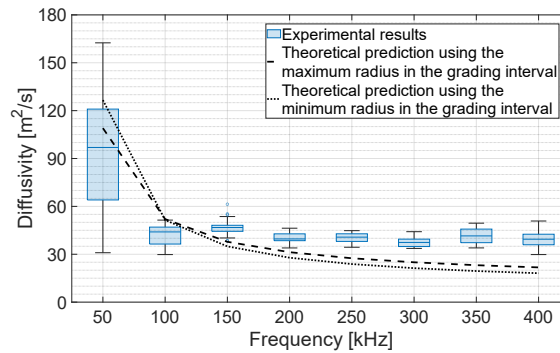
Aggregate diameter	Volume ratio
12 - 16 mm	22.6%
8 - 12 mm	38.9%
5.6 - 8 mm	28.1%
4 - 5.6 mm	10.4%

The comparisons between experimental results and theoretical predictions as functions of frequency are shown in Figure 6.5. Theoretical predictions are generally consistent with experimental results, which suggests that proposed model is reliable. Furthermore, the results obtained using the maximum and minimum radii within the grading interval as the characteristic radius do not exhibit significant divergence. Throughout the remainder of this dissertation, the maximum radius within grading intervals will be utilized as the characteristic radii of coarse aggregates for calculations.

6.6 Model validation and prediction of wave energy evolution



(a) Geopolymer concrete specimens.



(b) Concrete cylinder (experimental results can be found in Figure 4.27(a)).

Figure 6.5 Comparison of experimental results and theoretical predictions by the model as functions of frequency. Theoretical predictions are calculated using Equation (6.46), where transport mean free paths are calculated through Equation (6.45), (6.44) and (6.43). The characteristic correlation length in Equation (6.43) and (6.44) is calculated using Equation (6.41) and (6.42b).

6.6.2 Wave energy evolution and equilibration predicted from the model

In Section 6.6.1, the model underwent validation using diffusivities. The current section shifts its focus to examining the energy evolution of bulk waves during transport, leveraging the insights gained from the validated model for geopolymer concrete members.

A longitudinal wave source is adopted here, indicating that the primary energy contribution comes from longitudinal waves. The selection of the longitudinal wave source directly aligns with the sensor employed for data collection—the compressive mode SA. This sensor predominantly generates longitudinal waves upon vibration. The excitation signal is a squared pulse with a frequency of 54 kHz. Considering the central frequency of the smart aggregate (SA) sensor is around 80 kHz, all subsequent calculations are based on this frequency. Upon normalizing the total energy as 1, Equation (6.21) can be expressed as follows:

$$\begin{pmatrix} E_p \\ E_s \end{pmatrix} = \begin{pmatrix} \frac{v_s^3}{2v_p^3 + v_s^3} \\ \frac{2v_p^3}{2v_p^3 + v_s^3} \end{pmatrix} + \begin{pmatrix} \frac{2v_p^3}{2v_p^3 + v_s^3} \\ \frac{-2v_p^3}{2v_p^3 + v_s^3} \end{pmatrix} e^{-\frac{t}{\frac{2v_p^3}{2v_p^3 + v_s^3} \frac{1}{\omega_{ps}}}} \quad (6.47)$$

One can also use Equation (6.23) to compute the equilibration ratio, taking into account the influence of dissipation. This analysis will not delve into the equilibration time when dissipation is present. The reason lies in the fact that the presence of dissipation expedites the achievement of energy equilibration. By neglecting dissipation, one can obtain a more conservative estimate for the equilibration time. In the calculation of the equilibrated energy ratio in the scenario with dissipation, the dissipation of transverse waves at a frequency of 80 kHz is determined to be 5635 s^{-1} . This value is derived from dissipation measurements of geopolymer concrete specimens shown in Figure 4.22, assuming that the dissipation measured in the experiment is exclusively associated with transverse waves. It is worth noting that this approach might slightly underestimate the dissipation of transverse waves, as discussed earlier. The dissipation of longitudinal waves is estimated using the same equation adopted in Section 6.5.1, $\tau^{(a)}_p/\tau^{(a)}_s=10/3$ (Margerin, van Tiggelen et al. 2001).

Figure 6.6 depicts the energy evolution of a longitudinal wave source utilizing Equation (6.47). Initially, the energy consists of solely longitudinal wave energy produced by the source. As time progresses, this energy experiences a significant decrease, reaching a plateau at approximately $80 \mu\text{s}$. In contrast, the transverse wave energy increases and also reaches a plateau around the same time. The red dotted line in the figure indicates the global equilibration time calculated using Equation (6.22), which is roughly $14.2 \mu\text{s}$. Notably, this time slightly exceeds the period of the longitudinal wave at the 80 kHz frequency, which stands at $12.5 \mu\text{s}$.

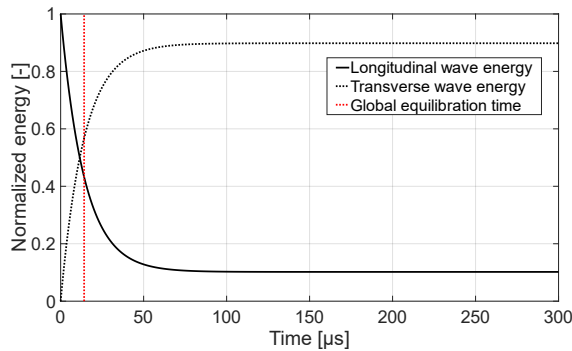


Figure 6.6 Theoretical longitudinal and transverse energy evolutions generated by a longitudinal wave source in concrete using Equation (6.47).

6.7 Discussion

For a more in-depth comparison between the global equilibration time and the time required for full energy equilibration, the energy ratio evolution between transverse and longitudinal waves is presented in Figure 6.7. This figure illustrates that the energy ratio does not fully equilibrate at the global equilibration time indicated by the red dotted line, which can also be seen from Figure 6.6. Instead, the global equilibration time should be interpreted as a characteristic time for energy to approach equilibration, as highlighted in Section 6.3.3.1. The complete equilibration is observed at approximately 120 μs , achieving an equilibration ratio of around 8.81. Taking dissipation into account and following the calculation provided in Algorithm 6.1, one can acquire the equilibration ratio when considering dissipation. In this case, this ratio is reduced to 8.32, as denoted by the black dotted line.

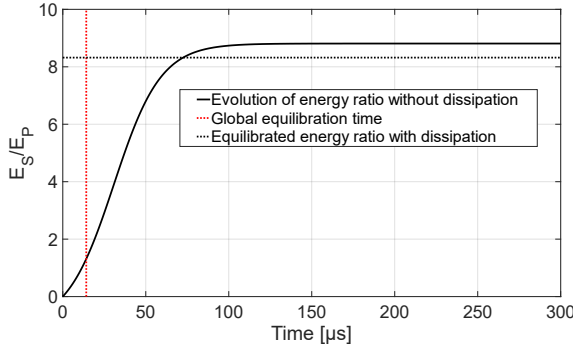


Figure 6.7 The evolution of energy ratio between transverse waves and longitudinal waves using Equation (6.47). The equilibrated ratio considering dissipation is calculated using Equation (6.23).

6.7 Discussion

6.7.1 Equilibration time

In Section 6.3.3, we gave the expressions of global equilibration time for P-S and S-S in Equation (6.22) and Equation (6.27), respectively. However, we noted that Equation (6.22) is not fully consistent with the Eq. (25) proposed by Snieder (2002). This is because Snieder distinguished between two transverse wave modes. Therefore, there is a coefficient 2 in the denominator of Snieder's derivation.

Additionally, the global equilibration time does not indicate complete equilibration of wave energy; rather, it signifies a characteristic time that indicates the mean value of the exponential decay demonstrated in Equation (6.21). This assertion finds support in the observations from Section 6.6.2, where the energy ratio does not reach equilibration at the global equilibration time.

The diffusion approximation theoretically becomes applicable when bulk wave energy achieves full equilibration (Ryzhik, Papanicolaou et al. 1996). It is important to note that

this full equilibration is in a statistical sense. It does not imply that the energy distribution at a specific location and time remains constant once equilibration is reached. Instead, the energy ratio continues to fluctuate around a constant value until the signal-to-noise ratio is met, as observed in previous seismological studies (Shapiro, Campillo et al. 2000, Hennino, Tregoures et al. 2001). Consequently, when fitting the diffusive properties, the initiation of time windows is expected to occur after the time needed for the energy to reach complete equilibration, approximately 100 μ s as depicted in Figure 6.7. However, selecting this time as the initial time of the first time window for fitting diffusive properties may fail to encompass the energy rise segment, which is closely linked to diffusivity, as emphasized by previous researchers (Quiviger, Payan et al. 2012) and also highlighted in Section 4.3.2.1. Consequently, the diffusivity derived from such diffusion curves without including the segment before the arrival time of the maximum energy might be inaccurate. Given this consideration, it is suggested for using the global equilibration time as a criterion for evaluating the validity of the diffusion approximation. This criterion implies that the initial few windows, spanning from the arrival time of longitudinal waves to the time required for full equilibration, can be taken into account when fitting diffusive properties from the experimental data. Moreover, for sensitivity kernel-based crack mapping, it is advisable to choose the time window until the energy is fully equilibrated. The key consideration here is that the accuracy of crack mapping is sensitive to the effective velocity (Zhang, Planes et al. 2016, Zhang, Larose et al. 2018), which remains nearly constant after reaching equilibration.

6.7.2 Possible scatterers in concrete

In this paper, the concrete is treated as a two-phase material: scatterers and mortar matrix. The scattering process of elastic waves in concrete is influenced by three key parameters: the material property difference between the matrix and scatterers, the volume fraction of scatterers, and the diameter of scatterers. There are several possible scatterers in concrete, namely, air voids, reinforcement, boundaries, and the ITZ outside coarse aggregates. Certain criteria need to be met for scatterers to have a significant contribution to the scattering process. The scatters should have:

- a significant different mechanical property compared to the matrix;
- a non-negligible volume fraction;
- sufficiently large diameter comparing to the wavelength considered.

Regarding air voids, their small diameters, typically smaller than 3 mm (Punurai, Jarzynski et al. 2007), suggest a generally limited contribution to the scattering process of elastic waves with frequencies lower than 500 kHz, despite the significant material property difference with the matrix. When considering concrete with an extremely high

6.7 Discussion

volume fraction and extremely large diameters of air voids, the air voids can also be accounted for by treating the concrete as a three-phase material (Baniassadi, Garmestani et al. 2011).

Reinforcement, on the other hand, is limited in volume fraction and distribution within concrete, such as the maximum longitudinal reinforcement area ratio in a beam being 4% (Eurocode 2. 2005), and it is mostly located at localized locations. Consequently, its impact on the scattering process is theoretically limited.

The influence of boundaries, including solid-solid boundaries and solid-air boundaries, on the scattering process remains an open question. In acquiring the diffusivity, solid-air boundaries can be considered by incorporating image sources; however, the model is based on the assumption that the medium is statistically isotropic and statistically homogeneous. Therefore, it is difficult to consider possible mode conversions when reflections happen on boundaries. While boundaries may have limited impact on the energy equilibration ratio (Trégourès and van Tiggelen 2001), the presence of mode conversions on boundaries increases total scattering cross-sections, leading to an earlier attainment of energy equilibration. Solid-solid boundaries, in contrast, have an effect on both equilibration time and equilibration ratio (Trégourès and van Tiggelen 2001). Further studies are necessary to incorporate boundaries into the theoretical framework.

The ITZ, which is tightly attached to the coarse aggregates, is characterized by high porosity, resulting in lower mechanical properties compared to the mortar or other matrix (Königsberger, Hlobil et al. 2018). Specifically, the elastic modulus of the ITZ ranges from 40% to 85% of that of the matrix, as reported by various studies (Lutz, Monteiro et al. 1997, Li, Zhao et al. 1999, Mondal, Shah et al. 2009, Keinde, Kamali-Bernard et al. 2014). The maximum thickness of ITZ has been determined to be only 150 μm (Prokopski and Halbiniak 2000), significantly smaller than the diameter of coarse aggregates, which exceeds 4 mm. Since scattering events happen on the ITZ, as a result of discontinuity in material properties, diameters of scatterers in concrete are assumed the same as those of coarse aggregates in this dissertation. Please note that this simplification may overestimate the contribution of the ITZ to scattering (underestimate the diffusivity), as it assumes that the mechanical properties of the whole coarse aggregate are identical to those of the ITZ.

6.7.3 Revisit of assumptions in the derivation of total scattering cross-sections

In Section 6.3.2, we indicated that there are three main assumptions involved in the derivation of expressions for the total scattering cross-sections: (1) the medium is statistically isotropic and statistically homogeneous; (2) the phase velocity remains unchanged during the scattering; (3) spatial fluctuations of heterogeneities are weak. In this section, we will

revisit the validity of Assumption 2 and 3 in concrete using the validated model for geopolymer concrete members.

As mentioned in Section 6.3.2, Assumption 2 is known as the Born approximation. This approximation fails when the wavelength is much smaller than the diameter of scatterers (Weaver 1990). The scattering regime is defined by the relationship between the wavenumber k and diameter of coarse aggregates r_a using kr_a . Wavenumber k is linked to frequency f and velocity v by $k=2\pi f/v$. In elastic wave-based concrete monitoring, frequencies typically range from 50 kHz to 400 kHz. For a constant frequency, transverse waves have a larger wavenumber due to their lower velocity v_s in concrete, typically around 2700 m/s. Given that the maximum diameter of coarse aggregates (r_a) is 16 mm and the maximum wavenumber of transverse waves (k_s) with a maximum frequency of 400 kHz is around 930 m^{-1} ($2 \times \pi \times 400 \times 10^3 / 2700$), it is evident that the maximum $k_s r_a$ is around 10. Please note that this is the upper bound estimation, and the value for longitudinal and transverse waves in reality should be smaller than 10. Therefore, the scattering of elastic waves is generally in the Rayleigh regime (Papadakis 1965), where $k_s r_a$ is smaller than one, or Rayleigh-Gans regime (Margerin, Campillo et al. 2000), where $k_s r_a$ and 1 are in the same order of magnitude. In both regimes, the Born approximation is applicable (Stanke and Kino 1984, Calvet and Margerin 2018).

Assumption 3 is to avoid the occurrence of bulk wave transport in concrete falling within the localization regime. Given the inherent challenge in directly evaluating the existence of localization of bulk waves in concrete, which requires the measurement of the backscattering effect (Sheng 2006), the validity of this assumption is assessed through checking the self-consistency of the proposed model, in which the strong backscattering effect should not be observed from the results predicted by the model.

Scattering cross-sections serve to illustrate the differential amount of energy lost by the propagating wave into another direction from one mode into another. Figure 6.8 displays the dimensionless scattering cross-sections predicted by the fitted model when $k_p r_a = 0.709$, which corresponds to the frequency component of 50 kHz. Other frequency components are not considered here since the increase of wave frequency will facilitate the forward-scattering tendency, which can also be observed from the work reported by Margerin et al. (2000). The scattering event occurs at the origin, with the incident wave assumed to approach from the left. Since these scattering cross-sections are normalized by their total scattering cross-sections, the dimensionless P-S and S-P scattering cross-sections are identical. Observations from Figure 6.8(a) depict that the predominant portion of energy from an incident longitudinal wave is scattered in the forward direction. A similar phenomenon can be observed in the S-S scattering cross-section shown in Figure 6.8(b). In the case of P-S (or S-P) scattering, the maximum scattering occurs around 30° relative to

6.7 Discussion

the incident direction and is minimal in the forward-scattering direction. There is no significant backscattering observed. Given the established link between backscattering and localization (Sheng 2006), the findings from scattering cross-sections suggest that the localization is unlikely to occur in this model.

The scattering cross-sections presented here are produced by the model and may not accurately reflect real-world events. These cross-sections serve only to verify the consistency of the model, and no conclusions related to reality should be drawn from them. Notably, Ramaniraka et al. (2019) also report the scattering cross-sections in their article acquired from the numerical simulations, and the strong backscattering effect can be observed in their results (refer to Fig. 5 in their paper with k_{Pa} around 8). In the case shown in Figure 6.8, the backscattering is very limited. These inconsistent outcomes probably due to the setup of simulation done by Ramaniraka et al. (2019), where only the single scattering is simulated. In our case, the scattering cross-section is derived from the spatial correlation of the medium. Therefore, this scattering cross-section represents the multiple scattering process in the medium, which involves a dense set of single scattering angles (De Abajo, Van Hove et al. 2001). To have a better understanding of scattering cross-sections in concrete, a well-designed experiment is needed to measure the pressure field of elastic waves inside concrete, as proposed by Tourin et al. (2000).

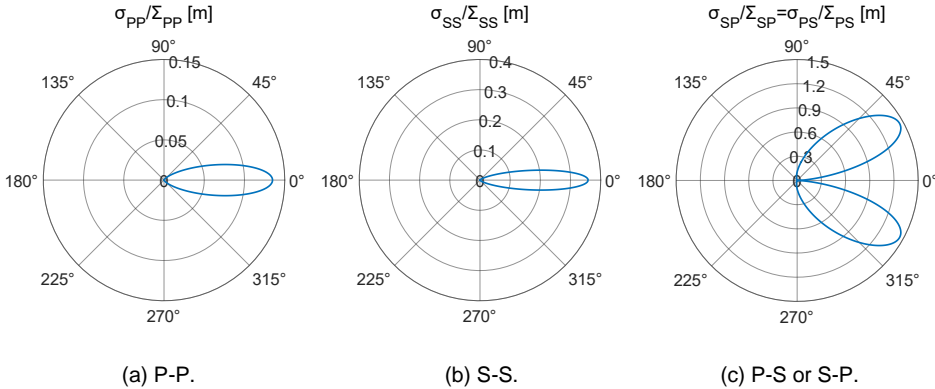


Figure 6.8 Polar plot of dimensionless scattering cross-section when $k_{Pa} = 0.709$.

Another essential metric in characterizing energy transport is the transport mean free path. In Figure 6.9, the transport mean free path of longitudinal and transverse waves is depicted as functions of wavelength. For longitudinal waves, the wavelength is typically larger than the corresponding transport mean free path, signifying strong interactions between longitudinal waves and scatterers. Conversely, with transverse waves, these interactions appear weaker due to the relatively larger transport mean free path. The strong interaction between longitudinal waves and scatterers may lead to localization, in which the diffusivity of longitudinal wave needs to be renormalized (Sheng 2006).

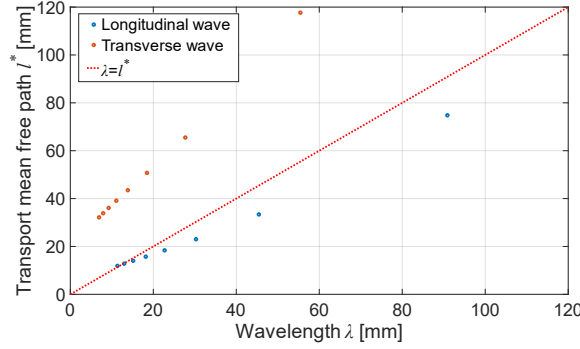


Figure 6.9 Transport mean free path of longitudinal and transverse waves as functions of wavelength calculated using Equation (6.45).

To further verify the potential presence of localization, the diffusivity is renormalized using the following equation proposed by Sheng (Sheng 2006):

$$D_M \equiv D_M^{(0)} - \delta D_M, \quad (6.48)$$

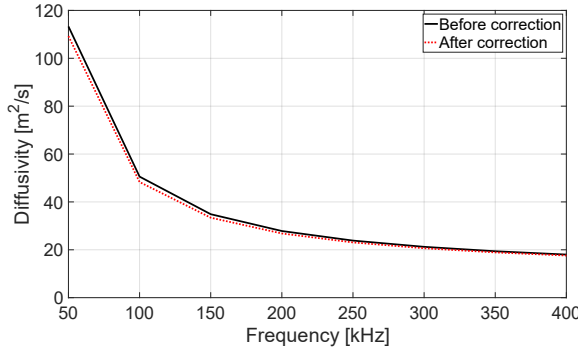
where D_M represents the corrected or renormalized diffusivity, and $D_M^{(0)}$ is the elastic diffusivity, which is equal to $l_M^* v_M / 3$. The parameter M denotes the wave mode ($M \in \{P, S\}$). The term δD_M is defined as:

$$\delta D_M = \frac{v_M^3}{\pi \omega_M^2} \left(\frac{1}{l_M^*} - \frac{1}{L} \right), \quad (6.49)$$

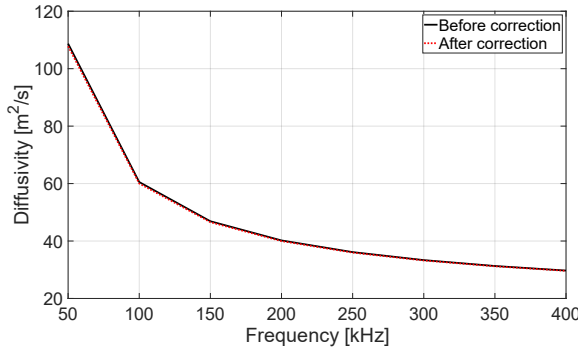
where ω represents the angular frequency, and L denotes the energy transport distance. The condition $D_M = 0$ defines the localization length, beyond which diffusive transport is no longer an accurate description (Sheng 2006). Additionally, the condition for localization is determined by setting $D_M^{(0)} = \delta D_M$ with $L = \infty$ (Sheng 2006). Consequently, the criterion for localization becomes $l_M^* \omega_M / v_M \leq \sqrt{3/\pi} \cong 1$, which is also known as the Ioffe–Regel criterion (Ioffe and Regel 1960). Please note that the mean free path in Equation (6.49) is the transport mean free path, which corresponds to the minimum length scale of the diffusive behaviour (Sheng 2006).

The comparison between elastic diffusivities and renormalized diffusivities for longitudinal and transverse waves, assuming an infinite energy transport distance, is shown in Figure 6.10. Upon comparing the data illustrated in these figures, there is no discernible distinction between the elastic diffusivity and the renormalized diffusivity for both longitudinal and transverse waves. This suggests that transport properties predicted by the theoretical model are unlikely to fall within localization regime. While these specific outcomes do not conclusively establish that bulk waves in concrete are definitively outside the localization regime, they do, however, indicate the self-consistency of the theory concerning localization.

6.7 Discussion



(a) Longitudinal wave.



(b) Transverse wave.

Figure 6.10 Comparison of elastic diffusivity and renormalized diffusivity with infinite energy transport distance calculated using Equation (6.48) and (6.49).

6.7.4 Possible approaches to improve the performance of the model

As introduced in previous sections, the model relies on many assumptions that could potentially affect its performance. In this section, we will introduce two potential approaches that can be used to improve the performance of the model.

The first approach focuses on enhancing the normalized correlation function. In this dissertation, we assume that the normalized correlation function $R(r)$ follows an exponential form. However, this assumption may not hold for the two-phase concrete assumed in this paper. To obtain a more accurate estimation of the correlation function, a numerical model specific to concrete is required. Those interested in this topic can refer to the article by Liu and Turner (2008) for further details.

The second approach employs fitting the model using experimental data to enhance alignment between model outputs and experimental results. The discrepancy between experimental and theoretical results may arise from the use of Equation (6.35), which tends to

overestimate total scattering cross-sections. To address this, the model fitting can be improved by adjusting the volume fraction of coarse aggregates in concrete (ϕ_s) and the characteristic radius of coarse aggregates (r_s) to achieve better consistency between experimental and theoretical results. This can be done by intentionally neglecting the effect of smaller coarse aggregates on scattering, which is anticipated to result in a lower total scattering cross-section, compensating for the overestimation caused by Equation (6.35) and potentially leading to better alignment between theoretical and experimental results.

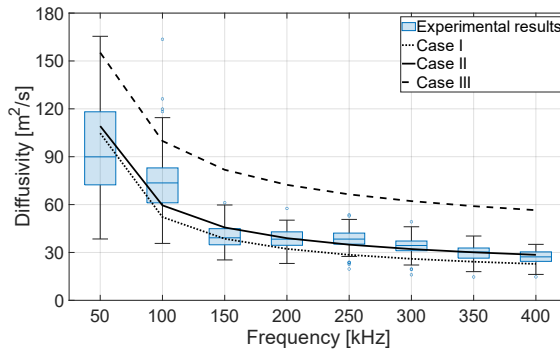
To illustrate this approach, three cases are utilized to fit the theoretical predictions. It is crucial to note that the maximum radius in each grading interval is considered as the characteristic radius for that interval in subsequent calculations in this section. In Case I, encompassing all grading intervals of coarse aggregates serves as the baseline for fitting. In Case II and Case III, only coarse aggregates with diameters larger than 5.6 mm and 8 mm, respectively, are taken into account, as shown in Table 6.5. Consequently, the volume fractions for Case II and Case III are 0.230 and 0.158 in geopolymer concrete specimens, respectively. In the concrete cylinder, the volume fractions in Case II and Case III are 0.249 and 0.171, respectively.

Table 6.5 Sieving of coarse aggregates in Case I, Case II and Case III for model fitting.

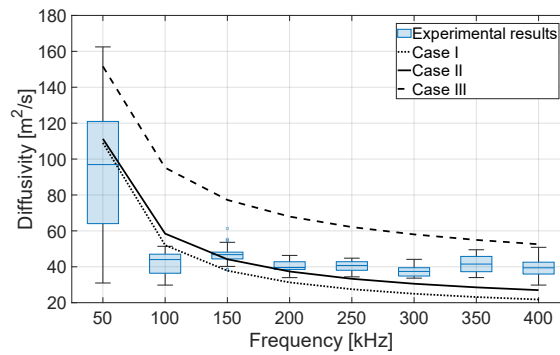
Aggregate diameter	Volume ratio of gravel in Case I	Volume ratio of gravel in Case II	Volume ratio of gravel in Case III
12 - 16 mm	22.6%	25.2%	36.75%
8 - 12 mm	38.9%	43.4%	63.25%
5.6 - 8 mm	28.1%	31.4%	-
4 - 5.6 mm	10.4%	-	-

Figure 6.11 illustrates the comparison between diffusivity values obtained from experiments and those predicted by the theoretical model under different sieving cases in Table 6.5. Notably, the theoretical diffusivities derived from Case II exhibit the closest agreement with the experimental data in both geopolymer concrete members and concrete cylinder. Consequently, parameters from this case can be considered as the fitted input for the model.

6.7 Discussion



(a) Geopolymer concrete members.



(b) Concrete cylinder.

Figure 6.11 Comparison of experimental results and theoretical predictions using different sieving cases. Theoretical predictions are calculated using Equation (6.46), where the transport mean free paths are calculated through Equation (6.45), (6.44) and (6.43). The characteristic aggregate distance is calculated using Equation (6.41) and (6.42).

6.7.5 Effect of boundary conditions on diffusivity in concrete cylinder

In Section 4.3.5, we examine the diffusive behaviour of bulk waves within a concrete cylinder. During the curve fitting process, we account for primary reflections and Type I secondary reflections from the top and bottom surfaces, as well as primary through quaternary reflections from the circular surface. However, since these diffusive properties are measured under loading conditions, where the top and bottom surfaces are in contact with loading plates rather than ideal air-solid boundaries, including these reflections might lead to an overestimation of diffusivity. To address this, a comparison was made in Section 4.4.4 to assess the impact of reflected energy from the top and bottom surfaces on diffusivity.

In Figure 6.11(b), we present a comparison of diffusivities in the concrete cylinder obtained from experiments and theoretical predictions across different sieving scenarios. These experimental results account for reflections from the top and bottom surfaces. Figure 6.12 shows diffusivities acquired from experiments without considering reflections from the top and bottom surfaces. Additionally, we compare the experimentally obtained diffusivities with theoretical predictions for three sieving cases outlined in Table 6.5. As shown in Figure 6.12, the theoretical predictions overestimate diffusivity at 50 kHz when reflections from the top and bottom surfaces are excluded. However, at frequencies above 100 kHz, the theoretical predictions align more closely with the experimental results. Therefore, we consider the proposed model to be reliable.

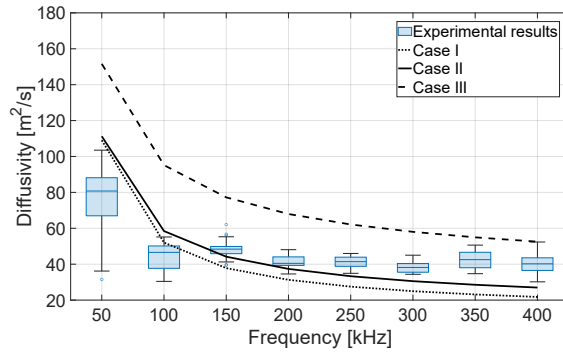


Figure 6.12 Comparison of experimental results acquired from the concrete cylinder without considering reflections from top and bottom surfaces, and theoretical predictions using different sieving cases.

6.8 Summary

This chapter introduces a theoretical framework for modelling the transport of bulk wave energy in concrete. The proposed model requires three independent inputs: the angular frequency of bulk waves, the volume fraction of coarse aggregates, and the characteristic radius of coarse aggregates. This model is capable of estimating the equilibrated energy ratio and the time required to achieve equilibration, which can help us interpret travel time changes of multiply scattered bulk waves in stressed concrete combined with the acoustoelastic theory introduced in Chapter 5. For the applications of this model in the next chapter, there are four main steps:

1. Determine the frequency of interest, the characteristic radius of coarse aggregates (through Equation (6.42b)), the volume fraction of coarse aggregates, and the average longitudinal and transverse wave velocities.
2. Calculate the total scattering cross-sections and weighted total scattering cross-sections using Equations (6.43) and (6.44).

6.8 Summary

3. Estimate energy evolution using Equation (6.20). The time required to reach bulk wave energy equilibration can be predicted through this energy evolution.
4. Determine the equilibrated energy ratio using Equation (6.23), taking into account the dissipation.

7. Response of travel time in diffuse bulk waves to stresses

7.1 Introduction

In Chapter 5, we introduced the acoustoelastic theory and examined how the travel time of ballistic bulk waves responds to stress. Since the trajectory of ballistic waves is a straight line from sender to receiver, evaluating spatial changes in the medium with high resolution requires a dense sensor array. In contrast, diffuse waves travel through much longer paths and can detect medium changes with larger spatial reach using a sparser sensor array (Planès and Larose 2013). Additionally, due to their longer wave paths, these waves are more sensitive to minor changes in the medium compared to ballistic waves. As mentioned in Chapter 6, diffuse waves exhibit two key characteristics: the equilibration of body wave energy and the arrival of waves from all directions with equal strength. Furthermore, the time required to reach equilibration is important, as it determines the validity of the diffusion approximation, where the two previously mentioned characteristics of diffuse waves are applicable.

In Section 4.2.4.4, we qualitatively demonstrated that the travel time changes in diffuse waves vary linearly with stress changes. Yet, this qualitative insight does not suffice to infer specific stress changes based on observed travel time changes. It is important to note that coda waves represent the tail of the waveform, which undergo multiple scattering but may not necessarily be in the diffusive regime. If it is confirmed by the equilibration time that coda waves are in the diffusive regime, then only in this context can the terms *coda wave* and *diffuse wave* be used interchangeably.

The knowledge gap that hinders the interpretation of stress-induced travel time changes in concrete is related to the scattering process of bulk waves. Specifically, we do not know when bulk waves reach equilibration or what the equilibration ratio is. To address this, we introduced a model in Chapter 6 that describes bulk wave energy transport in concrete, including the energy equilibration process and the time required to achieve this.

Building upon previous chapters, our aim in this chapter is to interpret the travel time changes of waves within the diffusive regime, defined as coda wave, by leveraging the acoustoelastic theory and energy transport model. This process entails two primary steps: (1) estimating equilibrated energy ratio of the diffuse wave and the time required to reach equilibration using the energy transport model, and (2) integrating the diffuse wave properties with acoustoelastic theory to construct stress-induced travel time changes in coda. Understanding how travel time in diffuse waves reacts to applied stress can provide the theoretical basis to further apply diffuse wave-based stress monitoring in concrete structures.

The wavefield in the diffuse regime is usually considered to be isotropic, which implies that all propagation and polarization directions are equally represented in space (Paul,

7.2 Travel time changes of spatially isotropic diffuse bulk waves

Campillo et al. 2005). Therefore, the acquired travel time change is a sum of changes from waves traveling in various directions, which forms a uniform distribution in space. The uniformity of this propagation will be simulated using Monte Carlo methods. The methodology for obtaining the acoustoelastic effect of diffuse waves is detailed in Section 7.2. Section 7.3 will outline the experimental validation design, while Section 7.4 and 7.5 will provide estimations of diffuse wave properties and stress-induced travel time changes of diffuse waves with the help of experimental results. Finally, Section 7.6 will focus on constructing time-lapse effective acoustoelastic parameters for diffuse waves, utilizing acquired diffuse wave properties and travel time changes. It is important to emphasize that acoustoelastic parameters are properties of the medium itself. In the case of diffuse waves, what we refer to as the effective acoustoelastic parameters are not true acoustoelastic parameters but rather a related concept. They serve to quantitatively describe the relationship between wave velocity and stress of diffuse waves using methods that are similar to those used for calculating acoustoelastic parameters.

7.2 Travel time changes of spatially isotropic diffuse bulk waves

This section presents a method of computing travel time changes of diffuse bulk waves. First, we will introduce a simulation method that is capable of calculating the acoustoelastic effect of diffuse bulk waves in Section 7.2.1. Subsequently, in Section 7.2.2, we will introduce a simplified response function tailored for this simulation method.

7.2.1 Choice of simulation method for acoustoelastic effect of diffuse waves

The acoustoelastic effect of a bulk wave propagating in an arbitrary direction in a stressed medium can be calculated by rotating the coordinate system in alignment with its propagation direction. The coordinate rotation is achieved using the following stress matrix transformation equation:

$$\boldsymbol{\sigma}' = \mathbf{Q}\boldsymbol{\sigma}\mathbf{Q}^T, \quad (7.1)$$

where $\boldsymbol{\sigma}$ and $\boldsymbol{\sigma}'$ denote the stress matrix in the original stress state and the stress state after coordinate rotation, respectively. The superscript 'T' denotes the transpose operation applied to a matrix. The transformation matrix \mathbf{Q} is defined as:

$$\mathbf{Q} := \begin{bmatrix} \cos(\gamma) & \sin(\gamma) & 0 \\ -\sin(\gamma) & \cos(\gamma) & 0 \\ 0 & 0 & 1 \end{bmatrix} \begin{bmatrix} \cos(\beta) & 0 & -\sin(\beta) \\ 0 & 1 & 0 \\ \sin(\beta) & 0 & \cos(\beta) \end{bmatrix} \begin{bmatrix} 1 & 0 & 0 \\ 0 & \cos(\alpha) & \sin(\alpha) \\ 0 & -\sin(\alpha) & \cos(\alpha) \end{bmatrix}, \quad (7.2)$$

where α , β , and γ are rotation angles as elucidated in Figure 7.1. In the first step, the coordinate system undergoes a rotation around the z -axis, as depicted in Figure 7.1(a), with the rotation angle denoted as $-\gamma$. The negative sign corresponds to the rotation adhering to the right-hand rule, where right thumb pointing in the positive direction of the axis

and right fingers curled in the direction of rotation. Therefore, counterclockwise rotation is considered positive. Following this step, the coordinate system transits from (x,y,z) to (x',y',z') , or equivalently, to (x',y',z) . In the second step, the entire system is then rotated around the y' -axis, resulting in the new coordinate system (x'',y'',z'') , or equivalently, (x'',y',z'') , as shown in Figure 7.1(b). Finally, the rotation is applied around the x'' -axis, defining the new coordinate system as (X,Y,Z) , or equivalently, (x'',Y,Z) , as illustrated in Figure 7.1(c). In the following calculation, the propagation direction of the wave remains consistently fixed along the X -axis.

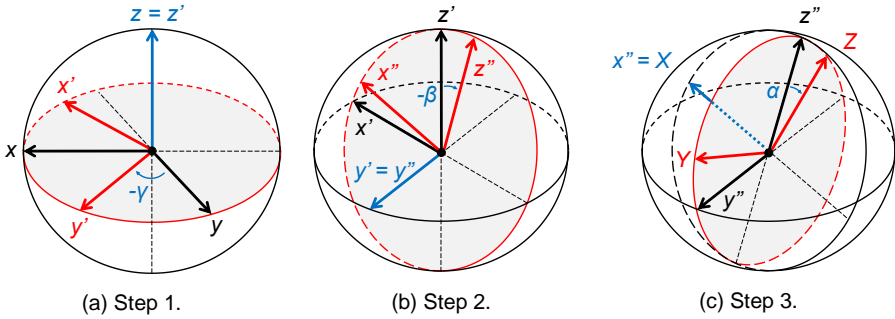


Figure 7.1 Visualisation of coordinate rotation (blue arrow: axes of rotation; black arrow: axes before rotation; red arrow: axes after rotation).

The new stress matrix, σ' , can be substituted into Equation (5.52) and (5.54)—the governing equations for acoustoelasticity in the initial and natural frames for wave propagation along the X -axis—to determine the velocity in that particular propagation scenario in the initial or natural frame of acoustoelasticity. Theoretically, one can simulate all propagation scenarios in arbitrary stress states when combining Equation (7.1) and acoustoelasticity.

When it comes to estimating the velocity change of diffuse bulk waves, there are two possible methods that can be used to simulate the acoustoelastic effect of the spatially isotropic waves. The first method is the exhaustive search, wherein all conceivable combinations of rotation angles from predefined rotation angle sets are systematically explored. Given that the energy flux of the diffuse bulk waves is uniformly distributed in space, this method scrutinizes all potential scenarios. The observed velocity change, which can be determined through experiments using wave interferometry, is an average of velocity changes across all scenarios. The second method employs the Monte Carlo simulation (Metropolis and Ulam 1949), wherein a group of waves propagating in random directions, following a uniform distribution in space, is generated to estimate the velocity change based on these random results.

7.2 Travel time changes of spatially isotropic diffuse bulk waves

In this section, the performance of the exhaustive search and Monte Carlo simulation are compared numerically. The numerical calculations are based on a test in which a uniaxial principal stress is applied along the original x -axis. The wave propagation direction is determined by rotating the coordinate system through three angles: α , β , and γ , as shown in Figure 7.1. The pseudocodes for these two approaches are presented in Algorithm 7.1 and Algorithm 7.2, respectively.

In the exhaustive search, rotation angles α , β , and γ are uniformly sampled at a fixed interval for different cases within the range of 0 to 2π , allowing for different sampling points by adjusting the interval. A velocity change can be determined for each rotation scenario, and the observed velocity change is computed by averaging these individual changes. Rotation angle intervals and the total number of rotation angle combinations or samples, denoted as M^3 in Algorithm 7.1, utilized in different calculation cases for exhaustive search can be found in Table 7.1.

In the Monte Carlo simulation, rotation angles α , β , and γ are randomly selected from 0 to 2π for varying sample sizes, which can be found in Table 7.1. The observed velocity change is also determined by averaging these individual changes. The uniaxial compressive stress is applied along the original x -axis before rotation with a constant magnitude of 9.93 MPa in both exhaustive search and Monte Carlo simulation. Equation (5.52) (acoustoelasticity in the initial frame) is used as the response function to estimate velocity changes since the acoustoelastic moduli matrix can be directly calculated through strains or stresses. The material parameters are from Specimen 1 reported by Nogueira and Rens (2019).

Algorithm 7.1 Estimating observed velocity changes of longitudinal waves propagating in arbitrary directions using exhaustive search

Initialization:

- 1: Initialize principal stress matrix σ
 $\sigma \leftarrow [-9.93e6 \ 0 \ 0; 0 \ 0 \ 0; 0 \ 0 \ 0]$
- 2: Initialize elastic constants λ , μ , l , m , and n based on Concrete mixture 1 in Table 2.2
- 3: Generate rotation angles:
Generate M sets for α values with an interval of $2\pi/(M-1)$ in the range of $[0, 2\pi]$
Generate M sets for β values with an interval of $2\pi/(M-1)$ in the range of $[0, 2\pi]$
Generate M sets for γ values with an interval of $2\pi/(M-1)$ in the range of $[0, 2\pi]$
- 4: **Repeat** for all possible values of $(\alpha_p, \beta_q, \gamma_r)$ using nested loops, where $p \in [1, M]$, $q \in [1, M]$, $r \in [1, M]$
The total number of combinations $(\alpha_p, \beta_q, \gamma_r)$ is M^3
Each individual combination is identified by a unique index k , where $k \in [1, M^3]$
- 5: Compute transformation matrix based on rotation angles:
 $\mathbf{Q} \leftarrow \text{Eq. 7.2}((\alpha_p, \beta_q, \gamma_r))$
- 6: Compute new stress matrix based on transformation matrix:
 $\sigma' \leftarrow \text{Eq. 7.1}(\sigma, \mathbf{Q})$
- 7: **if** ($i=j$)
 $e'_{ij} \leftarrow \sigma'_{ij} / [\mu(3\lambda+2\mu)/(\lambda+\mu)]$, i and $j \in \{1, 2, 3\}$
- 8: **else**
 $e'_{ij} \leftarrow \sigma'_{ij} / 2\mu$, i and $j \in \{1, 2, 3\}$
- 9: Set the wave propagation direction as $(1, 0, 0)$:
 $\mathbf{N} \leftarrow (1, 0, 0)$
- 10: Compute the acoustoelastic modulus matrix:
 $\mathbf{B} \leftarrow \text{Eq. 5.53}(e'_{ij})$, i and $j \in \{1, 2, 3\}$
- 11: Compute eigenvalues of \mathbf{B} :

	$B_I \leftarrow \text{ComputeEigenvalues}(\mathbf{B}), I \in \{1,2,3\}$
12:	Compute three eigenvectors of the acoustoelastic modulus matrix: $\mathbf{V}_I \leftarrow \text{ComputeEigenvectors}(\mathbf{B}), \mathbf{V}_I = (V_{I1}, V_{I2}, V_{I3}), I \in \{1,2,3\}$
13:	Compute the velocity change of longitudinal wave using the eigenvalue: $\mathbf{V}_1 \leftarrow \text{Find } \mathbf{V}_I \text{ with maximum } \mathbf{V}_I \cdot \mathbf{N} $ $B_1 \leftarrow \text{Find the eigenvalue corresponding to } \mathbf{V}_1$ $(dv/v)^{(P)}_k \leftarrow [(B_1)^{1/2} \cdot (\lambda + 2\mu)^{1/2}] / (\lambda + 2\mu)^{1/2}$
14:	Until all (α, β, γ) sets are iterated over
15:	Compute the average of longitudinal wave velocity change: $(dv/v)^{(P, \text{ob})} \leftarrow \text{average}((dv/v)^{(P)}_k)$
16:	Result: Return the observed velocity change for longitudinal wave, $(dv/v)^{(P, \text{ob})}$.

Algorithm 7.2 Estimating observed velocity changes of longitudinal waves propagating in arbitrary directions using Monte Carlo simulation

	Initialization:
1:	Initialize principal stress matrix $\boldsymbol{\sigma}$ $\boldsymbol{\sigma} \leftarrow [-9.93e6 \ 0 \ 0 \ 0 \ 0 \ 0 \ 0 \ 0 \ 0]$
2:	Initialize elastic constants λ, μ, l, m , and n based on Concrete mixture 1 in Table 2.2
3:	Generate N random sets for (α, β, γ) values, where α, β , and $\gamma \in [0, 2\pi]$
4:	Repeat for each random set of $(\alpha_k, \beta_k, \gamma_k), k \in [1, N]$
5:	Compute transformation matrix based on rotation angles: $\mathbf{Q} \leftarrow \text{Eq.7.2}(\alpha_k, \beta_k, \gamma_k)$
6:	Compute new stress matrix based on transformation matrix: $\boldsymbol{\sigma}' \leftarrow \text{Eq.7.1}(\boldsymbol{\sigma}, \mathbf{Q})$
7:	if $(i=j)$ $e'_{ij} \leftarrow \sigma'_{ij} / [\mu(3\lambda + 2\mu) / (\lambda + \mu)], i \text{ and } j \in \{1,2,3\}$
8:	else $e'_{ij} \leftarrow \sigma'_{ij} / 2\mu, i \text{ and } j \in \{1,2,3\}$
9:	Set the wave propagation direction as $(1,0,0)$: $\mathbf{N} \leftarrow (1,0,0)$
10:	Compute the acoustoelastic modulus matrix: $\mathbf{B} \leftarrow \text{Eq.5.53}(e'_{ij}), i \text{ and } j \in \{1,2,3\}$
11:	Compute eigenvalues of \mathbf{B} : $B_I \leftarrow \text{ComputeEigenvalues}(\mathbf{B}), I \in \{1,2,3\}$
12:	Compute three eigenvectors of the acoustoelastic modulus matrix: $\mathbf{V}_I \leftarrow \text{ComputeEigenvectors}(\mathbf{B}), \mathbf{V}_I = (V_{I1}, V_{I2}, V_{I3}), I \in \{1,2,3\}$
13:	Compute the velocity change of longitudinal wave: $\mathbf{V}_1 \leftarrow \text{Find } \mathbf{V}_I \text{ with maximum } \mathbf{V}_I \cdot \mathbf{N} $ $B_1 \leftarrow \text{Find the eigenvalue corresponding to } \mathbf{V}_1$ $(dv/v)^{(P)}_k \leftarrow [(B_1)^{1/2} \cdot (\lambda + 2\mu)^{1/2}] / (\lambda + 2\mu)^{1/2}$
14:	Until all (α, β, γ) sets are iterated over
15:	Compute the average of longitudinal wave velocity change: $(dv/v)^{(P, \text{ob})} \leftarrow \text{average}((dv/v)^{(P)}_k)$
16:	Result: Return the observed velocity change for longitudinal wave, $(dv/v)^{(P, \text{ob})}$.

Table 7.1. Parameters for exhaustive search and Monte Carlo simulation.

ES*	1	2	3	4	5	6	7	8	9	10	11
$2\pi/(M-1)$ **	$2\pi/1$	$2\pi/39$	$2\pi/59$	$2\pi/79$	$2\pi/99$	$2\pi/11$	$2\pi/13$	$2\pi/15$	$2\pi/17$	$2\pi/19$	$2\pi/21$
[$^\circ$]	9					9	9	9	9	9	9
M^3	0.008	0.064	0.22	0.51	1	1.73	2.74	4.09	5.83	8.00	10.64
$[\times 10^6]$											
MC*	1	2	3	4	5	6	7	8	9	10	
N	0.001	0.002	0.007	0.022	0.060	0.17	0.46	1.29	3.59	10	
$[\times 10^6]$		8	7								

Note: * ES indicates exhaustive search, and MC indicates Monte Carlo simulation

** $2\pi/(M-1)$ indicates the interval shown in Algorithm 7.1. Please note that both 0 and 2π are sampled in the exhaustive search and Monte Carlo simulation. M indicates the amount of samples for each rotation steps shown in Figure 7.1.

7.2 Travel time changes of spatially isotropic diffuse bulk waves

In Figure 7.2, we present a comparison of these two methods in terms of calculating the velocity change of spatially isotropic longitudinal waves and the corresponding calculation time. The computational efficiency of both methods is comparable, as evidenced by the nearly linear relationship observed between the number of samples and the logarithm of the calculation time. However, the Monte Carlo simulation converges much faster than the exhaustive search, as indicated by blue circles in Figure 7.2. This faster convergence arises from the stochastic nature of the Monte Carlo simulation, which inherently provides a better representation of diffuse waves propagating in arbitrary directions with isotropic energy flux in space simulated here. Consequently, in the remainder of this chapter, the Monte Carlo simulation is adopted as the simulation method for acquiring the acoustoelastic effect of diffuse waves.

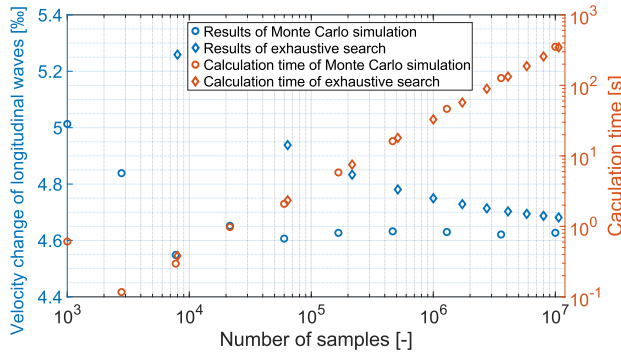


Figure 7.2 Comparison of the velocity change for spatially isotropic longitudinal waves obtained through Monte Carlo simulation (Algorithm 7.2) and exhaustive search (Algorithm 7.1). The mechanical properties of concrete utilized in the calculation is from Specimen 1 reported by Nogueira and Rens (2019).

7.2.2 Response function for Monte Carlo simulation

In Section 7.2.1, we demonstrated the efficiency of the Monte Carlo simulation for simulating the acoustoelastic effect of diffuse bulk waves. Moreover, the integration of these random propagation directions with acoustoelastic theory allows us to further estimate the velocity change of spatially isotropic waves. However, the earlier calculations employed a response function that necessitates seven elastic constants: two static Lamé parameters, two dynamic Lamé parameters, and three Murnaghan constants. In this section, we will simplify the previous response function and introduce an approximate response function that involves only five acoustoelastic parameters A_{ijkk} , two for longitudinal waves and three for transverse waves. The advantage of using these acoustoelastic parameters is that they can be directly obtained through experiments with applied uniaxial loads. The efficiency of the approximate response function will be checked by comparing it with the exact response function adopted in Section 7.2.1. The acoustoelasticity in the initial frame will be used in this section.

It is important to distinguish between the exact and approximate velocity changes discussed in this section. The exact velocity change is derived by solving the eigenvalues of the acoustoelastic moduli matrix (the B -matrix in Equation (5.52)), which includes both normal and shear stresses. On the other hand, the approximate velocity change is determined using only five acoustoelastic parameters and accounts solely for normal stresses. The exact one offers the most precise theoretical results by incorporating both shear and normal stresses. In contrast, the approximate one, which disregards shear stresses, provides a less accurate estimate of the acoustoelastic effect. Nonetheless, because shear stress-induced velocity changes are difficult to measure experimentally, the calculation of approximate velocity changes requires simplified calculation and calibration, making it a practical alternative when applying acoustoelastic theory to diffuse waves in concrete.

The approximate response function of a longitudinal wave propagating in an arbitrary direction, considering only normal stresses, can be formulated based on Equation (D.3) in Appendix D as follows:

$$\left(\frac{dv}{v}\right)_P^{(i)} = \frac{\sqrt{1 + A_{1111}^{(i)}\sigma_{11}^{(r)} + A_{1122}^{(i)}\sigma_{22}^{(r)} + A_{1122}^{(i)}\sigma_{33}^{(r)}} - \sqrt{1 + A_{1111}^{(i)}\sigma_{11}^{(0)} + A_{1122}^{(i)}\sigma_{22}^{(0)} + A_{1122}^{(i)}\sigma_{33}^{(0)}}}{\sqrt{1 + A_{1111}^{(i)}\sigma_{11}^{(0)} + A_{1122}^{(i)}\sigma_{22}^{(0)} + A_{1122}^{(i)}\sigma_{33}^{(0)}}}, \quad (7.3)$$

where $(dv/v)_P^{(i)}$ represents the velocity change of longitudinal wave in the initial frame; $\sigma_{11}^{(r)}$, $\sigma_{22}^{(r)}$ and $\sigma_{33}^{(r)}$ denote the three normal stresses in the current stress state after rotation using Equation (7.1) along X -, Y -, and Z -direction (as shown in Figure 7.1(c)), respectively; $\sigma_{11}^{(0)}$, $\sigma_{22}^{(0)}$ and $\sigma_{33}^{(0)}$ represent three normal stresses in the original stress state along x -, y -, and z -direction, respectively. Please note that in an isotropic material, the acoustoelastic parameters $A_{1122}^{(i)}$ and $A_{1133}^{(i)}$ are equal. The details of acoustoelastic parameters, $A_{ijkk}^{(i)}$, in Equation (7.3) can be found in Appendix D.

For transverse waves, it has been shown in Chapter 5 that shear deformations wield a substantial influence on their velocities. It is important to note, however, that this observation is specifically pertinent to the transverse waves in the ballistic regime, where the propagation and polarization directions are known. For spatially isotropic transverse waves, the effect of shear deformations on transverse wave velocity change might be cancelled out due to waves propagating in various directions. Consequently, we introduce the following equations based on Equation (D.3) in Appendix D to estimate velocity changes of transverse waves propagating in an arbitrary direction considering only normal stresses:

$$\left(\frac{dv}{v}\right)_{s1}^{(i)} = \frac{\sqrt{1 + A_{1211}^{(i)}\sigma_{11}^{(r)} + A_{2311}^{(i)}\sigma_{22}^{(r)} + A_{2311}^{(i)}\sigma_{33}^{(r)}} - \sqrt{1 + A_{1211}^{(i)}\sigma_{11}^{(0)} + A_{2311}^{(i)}\sigma_{22}^{(0)} + A_{2311}^{(i)}\sigma_{33}^{(0)}}}{\sqrt{1 + A_{1211}^{(i)}\sigma_{11}^{(0)} + A_{2311}^{(i)}\sigma_{22}^{(0)} + A_{2311}^{(i)}\sigma_{33}^{(0)}}}, \quad (7.4a)$$

$$\left(\frac{dv}{v}\right)_{s2}^{(i)} = \frac{\sqrt{1 + A_{1211}^{(i)}\sigma_{11}^{(r)} + A_{2311}^{(i)}\sigma_{22}^{(r)} + A_{2111}^{(i)}\sigma_{33}^{(r)}} - \sqrt{1 + A_{1211}^{(i)}\sigma_{11}^{(0)} + A_{2311}^{(i)}\sigma_{22}^{(0)} + A_{2111}^{(i)}\sigma_{33}^{(0)}}}{\sqrt{1 + A_{1211}^{(i)}\sigma_{11}^{(0)} + A_{2311}^{(i)}\sigma_{22}^{(0)} + A_{2111}^{(i)}\sigma_{33}^{(0)}}}, \quad (7.4b)$$

7.2 Travel time changes of spatially isotropic diffuse bulk waves

where $(dv/v)^{(i)}_{S1}$ and $(dv/v)^{(i)}_{S2}$ represent the velocity change of the first and second transverse wave modes in the initial frame, respectively. The details of acoustoelastic parameters, $A_{ijk}^{(i)}$, in Equation (7.4) can be found in Appendix D.

To validate the proposed Equation (7.3) and (7.4), the Monte Carlo simulation is conducted. The details of calculation steps can be found in Algorithm 7.3. The simulation comprises 21 uniaxial compressive stress cases ranging from 0 to 10 MPa, with intervals of 0.5 MPa. The compressive stress is applied along the x -axis before the rotation of coordinate system. Within each stress case, rotation angles α , β , and γ are randomly selected from 0 to 2π across 10^6 samples. For each sample within a stress case, the wave is set to propagate along the X -axis after rotation. The exact velocity change, relative to the velocity without stress applied, is computed using the exact response function by solving the eigenvalues and eigenvectors in the acoustoelastic modulus matrix shown in Equation (5.52). The observed exact velocity change is calculated by averaging all individual velocity changes across 10^6 samples within the same stress case. Simultaneously, the approximate velocity change, also relative to the velocity without stress applied, is calculated using Equation (7.3) and (7.4). The observed approximate velocity change is also calculated by averaging all individual velocity changes across 10^6 samples within the same stress case. The material parameters utilized for these calculations are from the measurement given by Nogueira and Rens (2019). It is important to highlight that employing material parameters from other samples will yield comparable results, as indicated in Appendix G.

Algorithm 7.3 Estimating observed approximate and observed exact velocity changes of longitudinal and transverse waves propagating in arbitrary directions using Monte Carlo simulation

Initialization:
1: Initialize elastic constants λ, μ, l, m , and n based on Concrete mixture 1 in Table 2.2
2: Compute acoustoelastic parameters, $A_{ijk}^{(i)}$, using Eq.(D.4) in Appendix D
3: Initialize stress matrix for iteration:
 $\sigma_{(p)} \leftarrow [\sigma_{11,p} \ 0 \ 0; 0 \ 0 \ 0; 0 \ 0 \ 0]$, $\sigma_{11,p} = [0:0.5e6:-10e6]$, $p \in [1,21]$
4: **Repeat** for each principal stress matrix $\sigma_{(p)}$
5: Generate 10^6 random sets for (α, β, γ) values, where α, β , and $\gamma \in [0, 2\pi]$
6: **Repeat** for each random set of $(\alpha_k, \beta_k, \gamma_k)$, $k \in [1, 10^6]$
7: Compute transformation matrix based on rotation angles:
 $\mathbf{Q} \leftarrow \text{Eq. 7.2}((\alpha_k, \beta_k, \gamma_k))$
8: Compute new stress matrix based on transformation matrix:
 $\sigma' \leftarrow \text{Eq. 7.1}(\sigma_{(p)}, \mathbf{Q})$
9: Compute normal stress components required in Eq.7.3 and Eq.7.4:
 $\sigma_{11}^{(i)} \leftarrow \sigma'_{11}$
 $\sigma_{22}^{(i)} \leftarrow \sigma'_{22}$
 $\sigma_{33}^{(i)} \leftarrow \sigma'_{33}$
 $\sigma_{11}^{(0)} \leftarrow 0$
 $\sigma_{22}^{(0)} \leftarrow 0$
 $\sigma_{33}^{(0)} \leftarrow 0$
10: **if** ($i=j$)
 $e'_{ij} \leftarrow \sigma'_{ij} / [\mu(3\lambda+2\mu)/(\lambda+\mu)]$, i and $j \in \{1,2,3\}$
11: **else**
 $e'_{ij} \leftarrow \sigma'_{ij} / 2\mu$, i and $j \in \{1,2,3\}$
12: Set the wave propagation direction as $(1,0,0)$:
 $\mathbf{N} \leftarrow (1,0,0)$
13: Compute the acoustoelastic modulus matrix:

```

14:         B ← Eq.5.53( $e'_{ij}$ ),  $i$  and  $j \in \{1,2,3\}$ 
        Compute approximate velocity changes:
        ( $dv/v$ )(P, app) $k$  ← Eq.7.3
        ( $dv/v$ )(S1, app) $k$  ← Eq.7.4(a)
        ( $dv/v$ )(S2, app) $k$  ← Eq.7.4(b)
15:        Compute eigenvalues of B:
         $B_I$  ← ComputeEigenvalues(B),  $I \in \{1,2,3\}$ 
16:        Compute three eigenvectors of the acoustoelastic modulus matrix:
         $V_I$  ← ComputeEigenvectors(B),  $V_I = (V_{I1}, V_{I2}, V_{I3})$ ,  $I \in \{1,2,3\}$ 
17:        Compute the exact velocity change of longitudinal wave:
         $V_1$  ← Find  $V_I$  with maximum  $|V_I \cdot N|$ 
         $B_1$  ← Find the eigenvalue corresponding to  $V_1$ 
        ( $dv/v$ )(P, exa) $k$  ←  $[(B_1)^{1/2} - (\lambda + 2\mu)^{1/2}] / (\lambda + 2\mu)^{1/2}$ 
18:        Compute the exact velocity change of first-mode transverse wave:
         $V_2$  ← Find  $V_I$  (excluding  $V_1$ ) with  $|V_{I2}| \geq |V_{I3}|$ 
         $B_2$  ← Find the eigenvalue corresponding to  $V_2$ 
        ( $dv/v$ )(S1, exa) $k$  ←  $[(B_2)^{1/2} - (\mu)^{1/2}] / (\mu)^{1/2}$ 
19:        Compute the exact velocity change of second-mode transverse wave:
         $V_3$  ← Find the rest  $V_I$  (excluding  $V_1$  and  $V_2$ )
         $B_3$  ← Find the eigenvalue corresponding to  $V_3$ 
        ( $dv/v$ )(S2, exa) $k$  ←  $[(B_3)^{1/2} - (\mu)^{1/2}] / (\mu)^{1/2}$ 
20:        Until all ( $\alpha, \beta, \gamma$ ) sets are iterated over
21:        Compute the observed longitudinal wave velocity change in each stress case:
        ( $dv/v$ )(P, exa_ob) $p$  ← average( $(dv/v)^{(P, exa)}_k$ )
        ( $dv/v$ )(P, app_ob) $p$  ← average( $(dv/v)^{(P, app)}_k$ )
        ( $dv/v$ )(S, exa_ob) $p$  ← average( $[(dv/v)^{(S1, exa)}_k; (dv/v)^{(S2, exa)}_k]$ )
        ( $dv/v$ )(S, app_ob) $p$  ← average( $[(dv/v)^{(S1, app)}_k; (dv/v)^{(S2, app)}_k]$ )
22:        Until all  $\sigma_{(p)}$  sets are iterated over
23:        Result: Return observed exact velocity changes in  $21 \times 1$  vectors for longitudinal waves, ( $dv/v$ )(P, exa_ob),
        and transverse waves, ( $dv/v$ )(S, exa_ob). Also, return observed approximate velocity changes in
         $21 \times 1$  vectors for longitudinal waves, ( $dv/v$ )(P, app_ob), and transverse waves, ( $dv/v$ )(S, app_ob).
    
```

Simulation results are shown in Figure 7.3. As shown in this figure, observed approximate velocity changes using Equation (7.3) and (7.4) demonstrate a good agreement with the observed exact values in both transverse and longitudinal wave scenarios. The maximum error occurs in the longitudinal wave case at 10 MPa, amounting to only 0.08‰ in magnitude. This result suggests that the velocity change of spatially isotropic transverse or longitudinal waves can be accurately estimated by using the proposed response equations.

7.3 Experimental validation design and parameters for signal processing

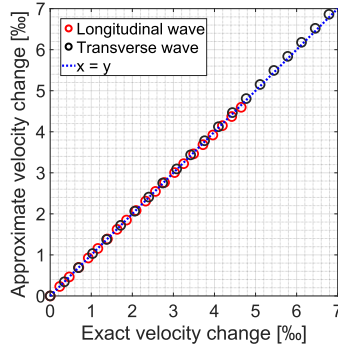


Figure 7.3 Comparison of observed exact velocity change obtained from the exact response function, Equation (5.52), and observed approximate velocity change obtained from approximate response functions, Equation (7.3) and (7.4), in 21 uniaxial stress cases ranging from 0 MPa to 10 MPa. The calculation steps can be found in Algorithm 7.3. The mechanical properties of concrete utilized in the calculation is from Specimen 1 reported by Nogueira and Rens (2019).

The comparison depicted in Figure 7.3 is based on the acoustoelasticity in the initial frame. Given that acoustoelasticity in the natural frame is derived from the same theoretical principles as in the initial frame, the conclusions drawn should be similarly applicable to the natural frame. The response functions can also be expressed by means of acoustoelastic parameters in the natural frame, A_{ijkk} , as follows:

$$\left(\frac{dt}{t}\right)_P = \frac{\sqrt{1 + A_{1111}\sigma_{11}^{(r)} + A_{1122}\sigma_{22}^{(r)} + A_{1122}\sigma_{33}^{(r)}} - \sqrt{1 + A_{1111}\sigma_{11}^{(0)} + A_{2211}\sigma_{22}^{(0)} + A_{2211}\sigma_{33}^{(0)}}}{\sqrt{1 + A_{1111}\sigma_{11}^{(0)} + A_{2211}\sigma_{22}^{(0)} + A_{2211}\sigma_{33}^{(0)}}}, \quad (7.5a)$$

$$\left(\frac{dt}{t}\right)_{S1} = \frac{\sqrt{1 + A_{1211}\sigma_{11}^{(r)} + A_{2111}\sigma_{22}^{(r)} + A_{2311}\sigma_{33}^{(r)}} - \sqrt{1 + A_{1211}\sigma_{11}^{(0)} + A_{2111}\sigma_{22}^{(0)} + A_{2311}\sigma_{33}^{(0)}}}{\sqrt{1 + A_{1211}\sigma_{11}^{(0)} + A_{2111}\sigma_{22}^{(0)} + A_{2311}\sigma_{33}^{(0)}}}, \quad (7.5b)$$

$$\left(\frac{dt}{t}\right)_{S2} = \frac{\sqrt{1 + A_{1211}\sigma_{11}^{(r)} + A_{2311}\sigma_{22}^{(r)} + A_{2111}\sigma_{33}^{(r)}} - \sqrt{1 + A_{1211}\sigma_{11}^{(0)} + A_{2311}\sigma_{22}^{(0)} + A_{2111}\sigma_{33}^{(0)}}}{\sqrt{1 + A_{1211}\sigma_{11}^{(0)} + A_{2311}\sigma_{22}^{(0)} + A_{2111}\sigma_{33}^{(0)}}}. \quad (7.5c)$$

For acoustoelastic parameters in the natural frame, only four distinct parameters exist: A_{1111} , A_{2211} , A_{2311} , and A_{2111}/A_{1211} , as shown in Appendix D. In Equation (7.5), we employ the travel time change dt/t rather than the velocity change dv/v because the velocity in the natural frame is inversely proportional to the travel time, and the velocity change can be expressed in terms of travel time change in this frame.

7.3 Experimental validation design and parameters for signal processing

Following the introduction of the simulation method for obtaining velocity changes of diffuse bulk waves in Section 7.2, this chapter will focus on designing a set of Experiments to investigate the acoustoelastic effect of bulk waves in the diffuse regime.

The specimen employed in this chapter is a cylindrical sample with a diameter of 300 mm and a height of 500 mm, the same size as the one shown in Figure 4.1 in Chapter 4. The

mixture composition of this specimen can be found in Table 6.3 in Chapter 6. Two tests are conducted on this sample, where axial loads are applied on the top and bottom surfaces of the cylinder. The chosen compressive stress range varies from 1 MPa to 7 MPa. In Test I, the load is applied from 100 kN (1.41 MPa) to 500 kN (7.07 MPa) and then back to 200 kN (2.83 MPa) with a 20 kN (0.28 MPa) interval. In Test II, the load is applied from 100 kN (1.41 MPa) to 500 kN (7.07 MPa) and then back to 100 kN (1.41 MPa) with the same interval. The load interval is designed based on the observation in Section 4.2.4.3. The loading and unloading processes are depicted in Figure 7.4. It is worth noting that Test I took place approximately two months after the concrete was cast, with a 40-day interval between Test I and Test II.

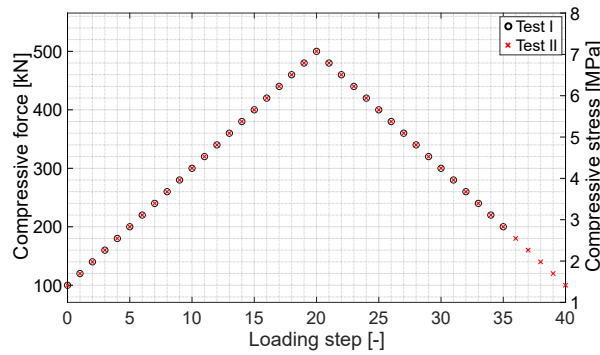
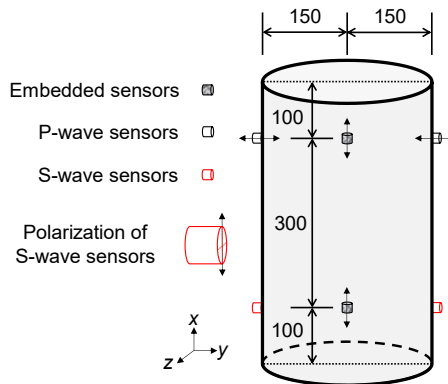


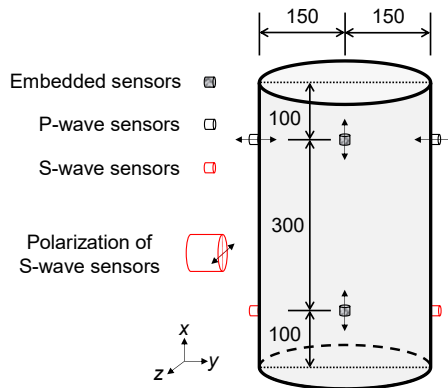
Figure 7.4 Loading protocol.

In both tests, three pairs of ultrasonic sensors are employed to generate and detect bulk waves in concrete. These pairs include one embedded longitudinal wave sensor pair, one longitudinal wave sensor pair on the surface, and one transverse wave sensor pair on the surface. The embedded sensors are aligned with their polarization directions parallel to the load direction. This longitudinal wave sensor pair is used to determine the acoustoelastic parameter A_{1111} . The polarization direction of longitudinal wave sensors on the surface is perpendicular to the load direction, and these sensors are utilized in both Test I and II to determine the acoustoelastic parameter A_{2211} . The polarization direction of transverse wave sensors on the surface is aligned parallel to the load direction in Test I, and this transverse wave sensor pair is used to determine the acoustoelastic parameter A_{2111} . In Test II, their polarization directions are rotated by 90 degrees to determine the acoustoelastic parameter A_{2311} . The sensor layout and polarization directions are illustrated in Figure 7.5. As mentioned in Section 5.4.2, the velocity changes obtained through the WI techniques are linked to the acoustoelasticity in the natural frame, where A_{2111} is equal to A_{1211} . Therefore, the transverse waves propagating along the x -axis with polarization along the y - or z -axis are not investigated in the experiment, as these scenarios can theoretically be represented by transverse waves propagating along the y - or z -axis with polarization along the x -axis.

7.3 Experimental validation design and parameters for signal processing



(a) Setup for Test I (longitudinal wave and transverse wave sensors on the surface are polarized in y - and x -directions, respectively).



(b) Setup for Test II (longitudinal wave and transverse wave sensors on the surface are polarized in y - and z -directions, respectively).

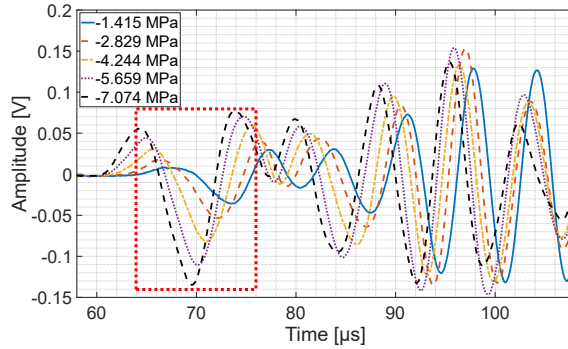
Figure 7.5 The concrete cylindrical sample with sensor locations and setups for two tests (note that there is some vertical exaggeration; the polarization of embedded sensors and the load direction are along the x-direction).

Considering the frequency of interest being higher than 50 kHz, a squared pulse with a frequency of 54 kHz is utilized as the excitation signal. For the longitudinal wave and transverse wave sensors on the surface, the sampling rate is set at 10 MHz, and only their ballistic wave parts are used in the subsequent analysis. For embedded sensors, signals are acquired using sampling rates of 1 MHz and 10 MHz, respectively. The signal with a sampling rate of 10 MHz is employed for the analysis of the ballistic wave part, while the one with 1 MHz is used for the diffuse wave analysis.

The ballistic waves and diffuse waves are analysed using the stretching technique and the WCS technique introduced in Chapter 4, respectively. The stretching technique is applied within a time window that encompasses approximately one cycle of the signal, around 15 μs (corresponds to 66.7 kHz), as shown in Figure 7.6. The utilization of such short time

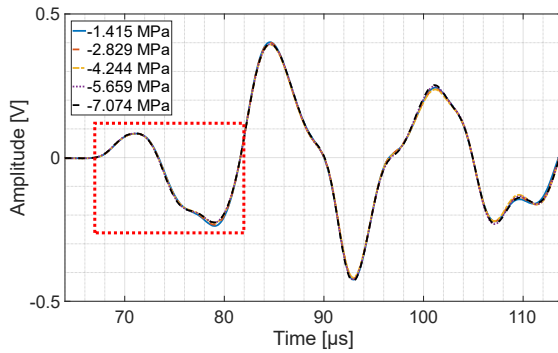
windows is essential for capturing travel times changes of pure wave modes while minimizing the influence of possible wave mode conversions on the results. Additionally, using a short time window can help reduce the impact of Rayleigh waves on measurements. In the cylindrical sample shown in Figure 7.5, the shortest path for Rayleigh waves traveling from the sender to the receiver is half the perimeter, approximately 0.47 m. Given that the Rayleigh wave velocity in concrete is about 2300 m/s (Shin, Yun et al. 2007), the arrival time of these waves is approximately 204 μs , which is significantly later than the time windows selected, as will be shown in Figure 7.6.

The wavelet cross-spectrum (WCS) technique is operated with a moving window with a length of 200 μs starting from 70 μs . For details on this technique, see Section 4.2.2.2 for more information. The frequency of interest is chosen from 50 kHz to 80 kHz, aligned with the resonant frequency of smart aggregates. The adjacent time windows overlap by 100 μs (50% overlap) to ensure the continuity of the obtained travel time change. Considering the low signal-to-noise ratio in the late coda, only the time windows before 6000 μs are used for the analysis. In addition, only the dv/v of time windows with CC higher than 0.9 is adopted in the following calculation. The results of applying WCS will be presented in Section 7.6.

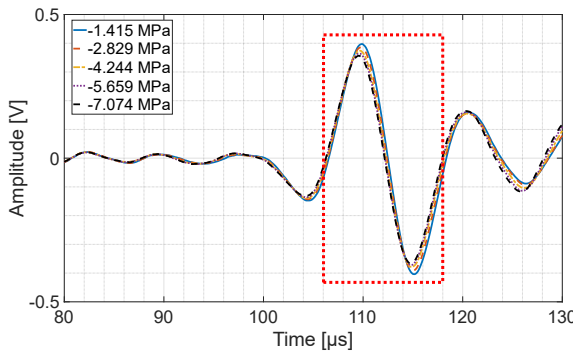


(a) Longitudinal waves with propagation directions parallel to the uniaxial stress direction received from embedded P-wave sensors in Test I. The longitudinal wave velocity calculated using the beginning of the time window is around 4688 m/s.

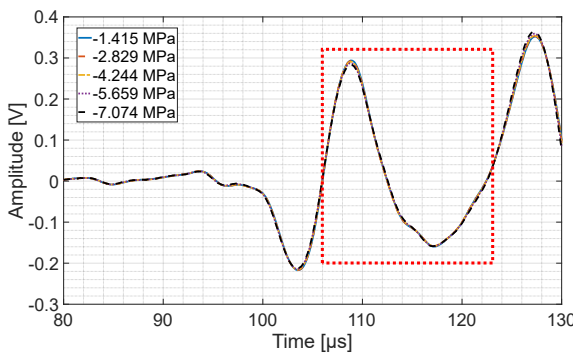
7.3 Experimental validation design and parameters for signal processing



(b) Longitudinal waves with propagation directions perpendicular to the uniaxial stress direction received from surface-bonded P-wave sensors in Test I. The longitudinal wave velocity calculated using the beginning of the time window is around 4478 m/s.



(c) Transverse waves with polarization directions parallel to the uniaxial stress direction received from surface-bonded S-wave sensors in Test I. The transverse wave velocity calculated using the beginning of the time window is around 2830 m/s.



(d) Transverse waves with polarization directions perpendicular to the uniaxial stress direction received from surface-bonded S-wave sensors in Test II. The transverse wave velocity calculated using the beginning of the time window is around 2830 m/s.

Figure 7.6 Signals received by sensors in Test I and II. Locations of time window for operating the stretching technique are indicated as red dotted rectangles.

7.4 Estimation of equilibration time and equilibrated ratio using the bulk wave energy transport model

In this section, we aim to calculate the equilibrated energy ratio and determine the equilibration time using the bulk wave energy transport model as delineated in Chapter 6.

To deduce the energy evolution of bulk waves during transport, we employ a longitudinal wave source, signifying that the principal energy contribution originates from longitudinal waves. This choice in utilizing a longitudinal wave source directly corresponds to the sensor employed for diffuse wave collection - the compressive mode smart aggregate (SA). This particular sensor predominantly generates longitudinal waves upon vibration. Figure 7.7 illustrates the evolution of the energy ratio for a longitudinal wave source calculated using Equation (6.49), where the scattering cross-section Σ_{PS} is calculated based on wave frequency of 65 kHz, aligning with the centre frequency of the frequency band utilized in the WCS technique. As depicted, the energy ratio attains equilibration at approximately 100 μs . Notably, this time is within the first time window, from 70 μs to 270 μs . In conjunction with the accelerated attainment of equilibration facilitated by dissipation, it is expected that the bulk wave energy within the second time window will reach equilibration, regardless of whether dissipation is considered.

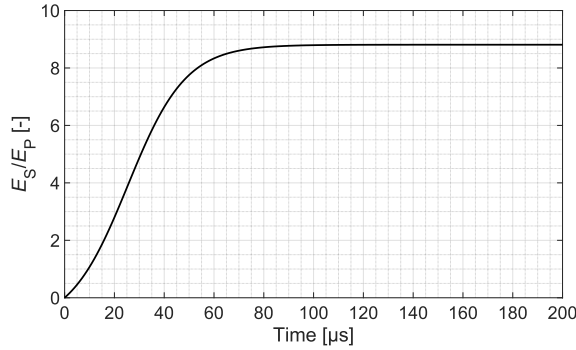


Figure 7.7 Evolution of the energy ratio for a longitudinal wave source predicted by the fitted model using Equation (6.49).

The equilibration ratio, depicted in Figure 7.7, remains consistently at approximately 8.81 across all three cases in the absence of dissipation. Accordingly, the proportion of longitudinal wave energy within the overall energy is 10.2%. Upon introducing the dissipation of transverse waves, which is approximately equal to 9000 s^{-1} at 65 kHz according to Figure 4.27, and the dissipation of longitudinal waves, which can be estimated through the dissipation of transverse waves using the relationship of $\tau^{(a)}_P/\tau^{(a)}_S=10/3$ (Margerin, van Tiggelen et al. 2001), the equilibration ratio can be calculated numerically by solving the eigenvectors in Equation (6.23). In this case, the equilibration ratio is equal to 8.18, equivalent to a 10.9% proportion of longitudinal wave energy. It is important to acknowledge

7.5 Estimation of travel time changes of diffuse bulk waves

here that the impact of dissipation on the proportion of longitudinal wave energy within the total energy is limited. In subsequent chapter, we will utilize the 10.90% proportion for further calculations.

7.5 Estimation of travel time changes of diffuse bulk waves

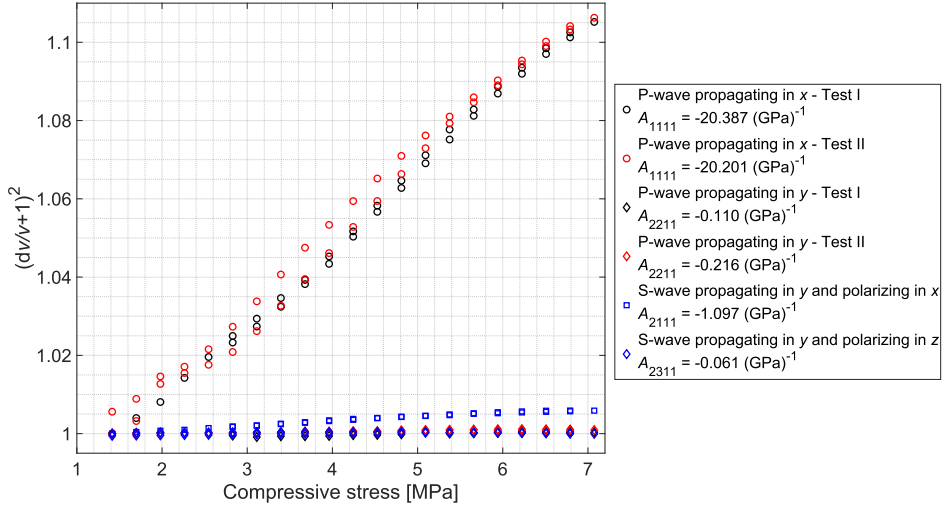
7.5.1 Inputs of the response function

In Section 7.2.2, we introduced the response functions, designed to estimate the velocity change of spatially isotropic longitudinal or transverse waves. The calculation of these response functions requires the determination of five acoustoelastic parameters. These parameters can be obtained by fitting the stress-velocity relationship obtained from experiments, as illustrated in Section 5.6.2.

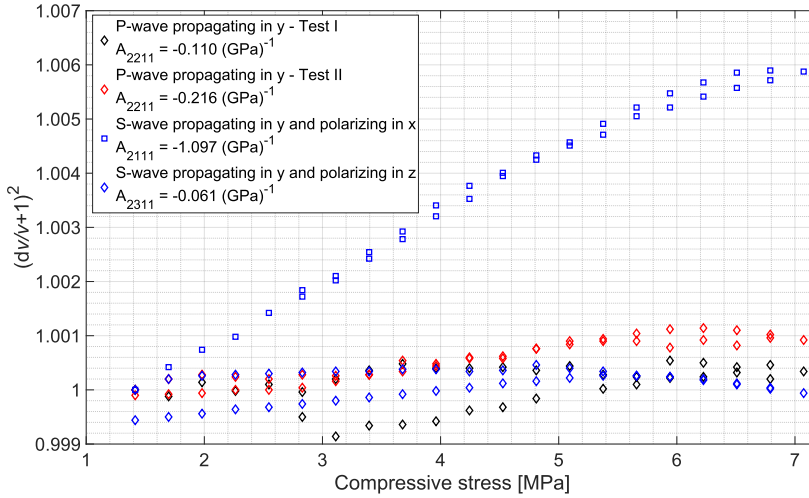
The compressive stress-square of relative velocity relationships for the four wave modes obtained in experiments are illustrated in Figure 7.8. Acoustoelastic parameters in this figure are acquired using the following equation:

$$A_{ij11} = \frac{s}{1 - s\sigma_{1,1}} \quad , \quad (7.6)$$

where i and j represent the wave propagation and polarization directions, respectively. The term $\sigma_{1,1}$ denotes the principal compressive stress in the x -direction, as shown in Figure 7.5, at the first stress level of -1.41 MPa. The slope s is determined by performing a linear fit of the square of relative velocity, $(dv/v+1)^2$, with respect to the compressive stress. As depicted, longitudinal waves propagating parallel to the uniaxial stress direction acquired using embedded sensors exhibit the most significant acoustoelastic effect, with consistent experimental results from two tests. Acoustoelastic parameters acquired from experiments are shown in Table 7.2. Notably, the difference in magnitudes of A_{1111} acquired in Test I and Test II is 0.186 GPa^{-1} (approximately 0.9% of the magnitude of A_{1111}), which is comparable to the observation in Section 5.7, where the fluctuation from Test I to Test II with a time interval of one month is 0.260 GPa^{-1} . However, magnitudes of A_{1111} in Test I and II are approximately 10 times greater than those reported in Table 5.4. This will be further discussed in Section 7.7.1. In subsequent calculations, we utilize the mean value of A_{1111} and A_{2211} acquired from two tests. The acoustoelastic parameters used in the follow-up study in this section can be found in Table 7.2.



(a) All four wave modes.



(b) Three wave modes except longitudinal waves propagating parallel to uniaxial principal stress direction.

Figure 7.8 Compressive stress-square of relative velocity relationship of four wave modes acquired in experiments.

Table 7.2 Acoustoelastic parameters acquired from experiments used in the follow-up study in this section.

Acoustoelastic parameter	A_{1111}	A_{2211}/A_{3311}	A_{2111}/A_{3111}	A_{2311}/A_{3211}	A_{1211}/A_{1311}
Value [GPa ⁻¹]	-20.294	-0.163	-1.097	-0.061	-1.097

7.5.2 Travel time changes determined from the Monte Carlo simulation

This section presents Monte Carlo simulation results illustrating travel time changes of diffuse bulk waves, utilizing response functions shown in Equation (7.5) and acoustoelastic parameters in Table 7.2. To ensure comparability with travel time changes of diffuse waves acquired from experiments, identical loading steps as those employed in the experiment are utilized, and the travel time change is computed relative to the travel time at the previous load step. It is important to note that this section focuses solely on the loading process; nevertheless, the conclusion drawn is equally applicable to the unloading process. The calculation follows steps listed in Algorithm 7.4.

Algorithm 7.4 Estimating observed travel time changes of longitudinal and transverse waves propagating in arbitrary directions using Monte Carlo simulation and simplified response function

```

Initialization:
1: Initialize acoustoelastic parameters,  $A_{ijkk}$ , from Table 7.2
2: Initialize stress matrix for iteration:
    $\sigma_{(p)} \leftarrow [\sigma_{11,p} \ 0 \ 0 \ 0 \ 0 \ 0 \ 0 \ 0 \ 0 \ 0 \ 0 \ 0]$ ,  $\sigma_{11,p} = [-1.41\text{e}6; -0.28\text{e}6; -7.07\text{e}6]$ ,  $p \in [1, 21]$ 
3: Repeat for each principal stress matrix  $\sigma_{(p)}$ 
4:   Generate  $10^6$  random sets for  $(\alpha, \beta, \gamma)$  values, where  $\alpha, \beta$ , and  $\gamma \in [0, 2\pi]$ 
5:   Repeat for each random set of  $(\alpha_k, \beta_k, \gamma_k)$ ,  $k \in [1, 10^6]$ 
6:     Compute transformation matrix based on rotation angles:
        $\mathbf{Q} \leftarrow \text{Eq. 7.2}((\alpha_k, \beta_k, \gamma_k))$ 
7:     Compute reference stress matrix based on transformation matrix:
        $\sigma'_{(p)} \leftarrow \text{Eq. 7.1}(\sigma_{(p)}, \mathbf{Q})$ 
8:     Compute current stress matrix based on transformation matrix:
        $\sigma'_{(p+1)} \leftarrow \text{Eq. 7.1}(\sigma_{(p+1)}, \mathbf{Q})$ 
9:     Compute normal stress components required in Eq. 7.5:
        $\sigma_{11}^{(r)} \leftarrow \sigma'_{11,p+1}$ 
        $\sigma_{22}^{(r)} \leftarrow \sigma'_{22,p+1}$ 
        $\sigma_{33}^{(r)} \leftarrow \sigma'_{33,p+1}$ 
        $\sigma_{11}^{(0)} \leftarrow \sigma'_{11,p}$ 
        $\sigma_{22}^{(0)} \leftarrow \sigma'_{22,p}$ 
        $\sigma_{33}^{(0)} \leftarrow \sigma'_{33,p}$ 
10:    Set the wave propagation direction as (1,0,0):
        $\mathbf{N} \leftarrow (1, 0, 0)$ 
11:    Compute travel time changes:
        $(dv/v)^{(P)}_k \leftarrow \text{Eq. 7.5(a)}$ 
        $(dv/v)^{(S1)}_k \leftarrow \text{Eq. 7.5(b)}$ 
        $(dv/v)^{(S2)}_k \leftarrow \text{Eq. 7.5(c)}$ 
12:    Until all  $(\alpha, \beta, \gamma)$  sets are iterated over
13:    Compute the average of longitudinal wave velocity change in each stress case:
        $(dt/t)^{(P, \text{ob})}_p \leftarrow \text{average}((dv/v)^{(P)}_k)$ 
        $(dt/t)^{(S, \text{ob})}_p \leftarrow \text{average}([(dv/v)^{(S1)}_k; (dv/v)^{(S2)}_k])$ 
14:  Until all  $\sigma_{(p)}$  sets are iterated over
15:  Result: Return observed velocity changes in  $20 \times 1$  vectors for longitudinal wave,  $(dt/t)^{(P, \text{ob})}$ , and
    transverse waves,  $(dt/t)^{(S, \text{ob})}$ .

```

Figure 7.9 depicts Monte Carlo simulation results of spatially isotropic longitudinal and transverse waves, with two noteworthy observations. Firstly, the travel time change is not constant despite identical loading intervals. This variability arises from the non-linear correlation between normal stresses and travel time change, as indicated in Equation (5.86). Furthermore, there are some minor fluctuations in the results from Monte Carlo simulation, i.e., around -4.8 MPa for transverse waves in Figure 7.9. This variability is

likely due to the fact that the samples used in the simulation are randomly generated. Although the large number of data points (10^6) helps to reduce this effect, some minor variations remain. Additionally, the travel time change of longitudinal waves is higher than that of transverse waves, which is attributed to the much more pronounced acousto-elastic effect of longitudinal waves propagating parallel to the stress direction, as shown in Table 7.2.

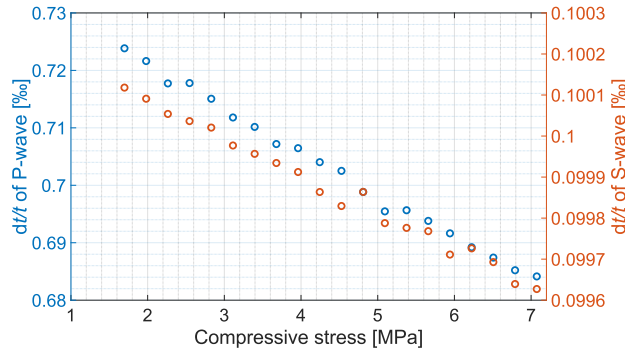


Figure 7.9 Travel time changes of spatially isotropic longitudinal and transverse waves acquired through Monte Carlo simulation. The calculation steps can be found in Algorithm 7.4.

To estimate the travel time change of diffuse bulk waves due to stresses change, we weight the travel time changes of longitudinal and transverse waves in Figure 7.9 using the equilibrated energy ratio given in Section 7.4. In this context, longitudinal waves contribute to a total travel time change of 10.9%, with the remaining portion attributed to transverse waves. The weighted results are presented in Figure 7.10. Please note that while travel time changes do vary across different load levels, the extent of this variation is minimal, with a maximum difference of only 4.6×10^{-6} . The travel time changes of diffuse bulk waves can be used to construct effective acoustoelastic parameters for diffuse waves, which will be shown in the next section.

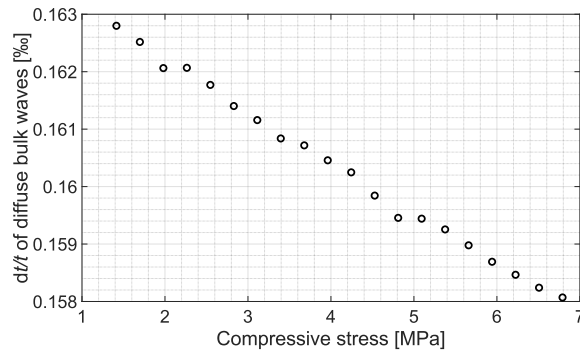


Figure 7.10 Travel time changes of diffuse bulk waves.

7.6 Effective acoustoelastic parameters of diffuse waves

In Section 7.4, we determined the time required for bulk wave energy to reach equilibration and established the equilibrated energy ratio using the bulk wave energy transport model. Building upon this energy ratio, Section 7.5 involved calculating travel time changes of diffuse bulk waves through a Monte Carlo simulation grounded in acoustoelastic theory. In this section, we will leverage the results from these two sections to formulate the time-lapse effective acoustoelastic parameters of diffuse bulk waves.

It is crucial to reiterate that the applied stress change first induces velocity changes in the medium due to the acoustoelastic effect. Subsequently, these velocity changes result in travel time changes of bulk waves. As the waves propagate, the travel time changes accumulate along their paths, with longer wave paths resulting in more significant travel time changes. In practice, waves traveling along longer paths are typically detected in later time windows. Once the bulk waves reach the diffusive regime, the travel time difference per unit lag time, dt/t , becomes constant, as discussed in Section 7.5. In this section, t in the denominator represents the centre time of the time window. It is also important to note that the time windows in this study are distributed uniformly along the lag time. Therefore, in the diffusive regime under a specific load interval, the travel time difference between two consecutive time windows should remain constant. This difference in travel time is referred to as the net travel time difference in this section.

To examine the net travel time difference $dt^{(\text{net})}$ in each time window, we subtract the travel time difference in the previous window from that in the current window using the following equation:

$$dt_i^{(\text{net})} = dt_i - dt_{i-1} , \quad (7.7)$$

where i denotes the i th time window. The net travel time difference in Test I is presented in Figure 7.11, exhibiting substantial fluctuations. When bulk waves reach the diffusive regime, also implying the energy equilibration, we anticipate that the net travel time difference should fluctuate around the theoretical value for spatially isotropic diffuse bulk waves obtained in Section 7.5.2. This theoretical result, averaged across different load steps, is depicted as a dotted black line in Figure 7.11. However, due to the considerable fluctuation across different load steps, drawing a direct conclusion from this figure is challenging.

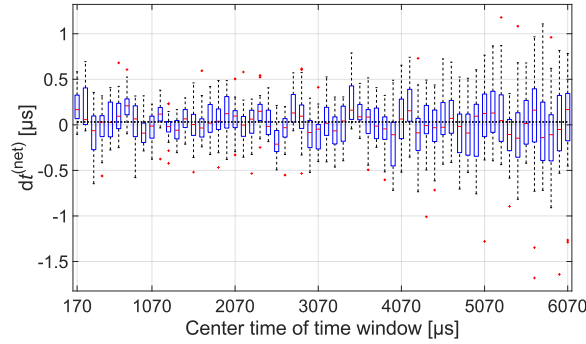


Figure 7.11 Box plot of the net travel time difference $dt^{(net)}$ in each time window during the loading process in Test I (black dotted line indicates the theoretical net travel time difference of diffuse bulk waves).

The significant fluctuations seen in Figure 7.11 are also evident in the travel time differences, dt , in each time window, as shown in Figure 7.12. Each box in Figure 7.12 represents travel time differences in the same time window at different load steps with the same interval during the loading process. Consequently, the observed fluctuation in the individual boxplots stem from variations in travel time differences among different loading steps. These variations may stem from the nonlinear behaviour of travel time changes at different load levels, as shown in Figure 7.9 and Figure 7.10, or from noise-induced fluctuations during the application of the WCS technique. However, given that the travel time changes across different load levels exhibit minimal variation—e.g., the theoretical fluctuation at 1070 μs is approximately $1070 \mu s \times 4.6 \times 10^{-6} = 0.0049 \mu s$, which is much smaller than the fluctuations observed in Figure 7.12—the observed fluctuations are likely due to the latter factor.

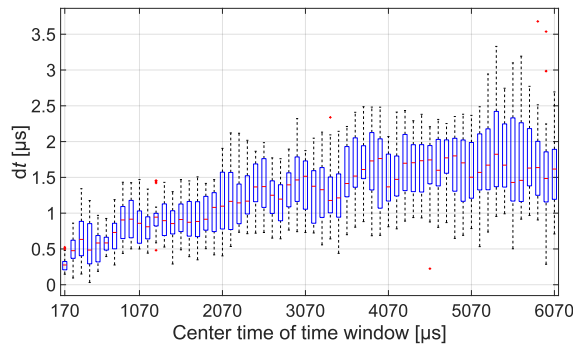


Figure 7.12 Box plot of the travel time difference dt in each time window during the loading process in Test I.

As previously mentioned, the significant fluctuation of travel time differences observed in Figure 7.12 is attributed to their fluctuations among load steps. To mitigate this impact

7.6 Effective acoustoelastic parameters of diffuse waves

on observations, we calculate the effective acoustoelastic parameter, representing the change in wave velocity within a specific time window concerning the applied stress. This computation is based on the travel time change, or equivalently, velocity change within the respective time window. Figure 7.13 shows the relationship between square of relative velocity and compressive stress for time windows with centre time of 170 μs , 1070 μs , 2070 μs , 3070 μs , 4070 μs , 5070 μs , and 6070 μs in Test I. Two symbols at the same load level indicate two measurements: one during loading and the other during unloading. Coefficients of determination for linear fits of the relationship between the square of relative velocity and compressive stress across different time windows are shown in Figure 7.14. It is important to note that all coefficients of determination exceed 0.93, indicating the linear relationship between the square of relative velocity and compressive stress. Notably, the slopes during both loading and unloading phases exhibit consistency. Consequently, the subsequent analysis of effective acoustoelastic parameters focuses solely on the loading phase, with implications equally relevant to the unloading process.

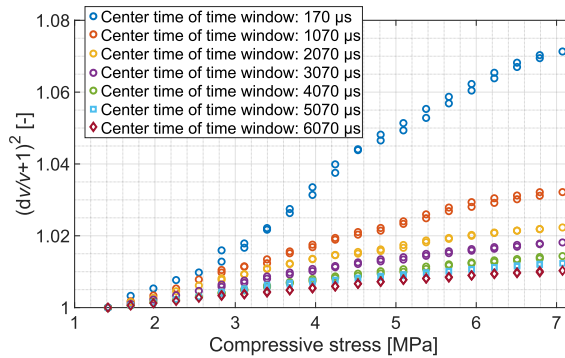


Figure 7.13 Square of relative velocity vs. compressive stress for time windows with centre time of 170 μs , 1070 μs , 2070 μs , 3070 μs , 4070 μs , 5070 μs , and 6070 μs in Test I during loading and unloading stages, as shown in Figure 7.4. Two symbols at the same load level indicate two measurements: one during loading and the other during unloading.

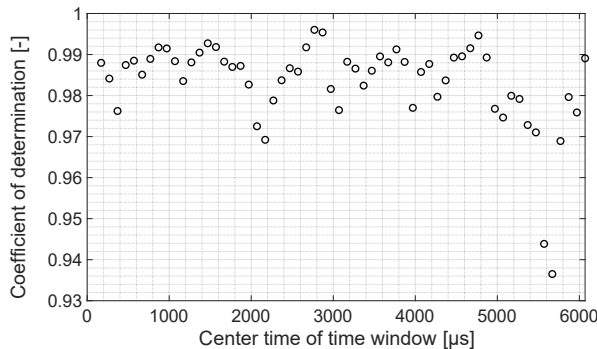


Figure 7.14 Coefficients of determination for linear fits of the relationship between the square of relative velocity and compressive stress across different time windows.

The effective acoustoelastic parameters from two tests are presented in Figure 7.15, as represented by black circles and black diamond, respectively. In accordance with Section 7.4, energy equilibration occurs in the second time window, as indicated by the red dotted line. Consequently, it becomes feasible to predict the evolution of time-lapse effective acoustoelastic parameters by utilizing theoretical travel time changes of diffuse bulk waves provided in Figure 7.10. When bulk waves reach equilibrium, the travel time change between two consecutive load steps should remain constant. As a result, in the diffusive regime, the travel time difference becomes linearly proportional to the centre time of the time window. This travel time difference can be accumulated to the travel time difference in the initial time windows to predict travel time changes in later time windows after reaching equilibration and, ultimately, determine the effective acoustoelastic parameters for diffuse waves. The use of effective acoustoelastic parameters also helps to mitigate fluctuations in travel time differences, as observed in Figure 7.12. This is because the fitting process, which determines these parameters, involves a set of data that averages out individual fluctuations. The pseudocode for this calculation is presented in Algorithm 7.5.

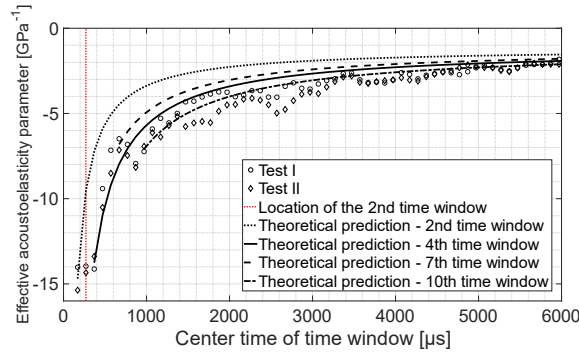


Figure 7.15 Effective acoustoelastic parameters in each time window together with theoretical predictions. The calculation steps can be found in Algorithm 7.5.

Algorithm 7.5 Estimating time-lapse effective acoustoelastic parameters of diffuse bulk waves

Initialization:

- 1: Initialize theoretical travel time changes of diffuse bulk waves at each load step (Figure 7.10)
 $(dt/t)_i \leftarrow$ Theoretical travel time changes of diffuse bulk waves at each load step $i, i \in [1, 20]$
 (only loading process is considered here)
- 2: Initialize travel time changes in different time windows acquired using WCS at each load step
- 3: Determine the travel time difference at different load steps in the n -th time window, after which the energy flux of bulk waves are spatially isotropic:
 $t_n \leftarrow$ Centre time of the n -th time window
 $(dt_n/t_n)_i \leftarrow$ Travel time change in the n -th time window retrieved using the WCS technique at load step $i, i \in [1, 20]$ (only loading process is considered here; the travel time change is averaged across Test I and Test II)
 $(dt_n)_i \leftarrow t_n \times (dt_n/t_n)_i$
- 4: **Repeat** for each time window $j, j \in [n+1, 60]$ (60 time windows in total)
- 5: Compute the centre time of time window j :
 $t_j \leftarrow$ Centre time of time window j

7.7 Discussion

```
6:          Compute the theoretical travel time difference of diffuse bulk waves between time window
           n and j at each load step i:
            $(dt)_i \leftarrow (t_j - t_n) \times (dt/t)_i$ 
7:          Repeat for each load step i,  $i \in [1, 20]$ 
8:          Compute the theoretical velocity change of diffuse bulk waves:
            $(dv/v)_i \leftarrow [(dt)_i + (dt_n)_i]/t_j$ 
9:          Until all load steps are iterated over
10:         Compute the theoretical effective acoustoelastic parameters in time window j:
            $A_j \leftarrow \text{Eq. 7.6}$ 
11:        Until all time windows are iterated over
12:        Result: Return theoretical effective acoustoelastic parameters in a  $(61-n) \times 1$  vector.
```

According to the theoretical prediction in Section 7.4, energy equilibration occurs in the second time window. Consequently, the calculation begins with the first time window, corresponding to $n=1$ in Algorithm 7.5. These predicted results are depicted as red circles in Figure 7.15. However, as evident in the figure, the magnitudes of effective acoustoelastic parameters in the second and third time windows are considerably larger than the theoretical result. This observation implies an underestimation of the quantity of longitudinal waves propagating parallel to the principal stress direction, which exhibits the most significant acoustoelastic effect. A possible explanation is that the wavefield becoming isotropic lags behind energy being equilibrated (Paul, Campillo et al. 2005). Hence, even after energy equilibration between longitudinal and transverse waves, a substantial presence of longitudinal waves propagating parallel to the stress direction persists within the longitudinal wave component, which results in the effective acoustoelastic parameters remaining at a high magnitude.

Therefore, we construct effective acoustoelastic parameters in later time windows by assuming a fully isotropic wavefield starting from the fourth time window ($n=3$), seventh time window ($n=6$), and tenth time window ($n=9$), respectively. These predictions are represented as red diamonds, red plus sign, and red cross in Figure 7.15, and they align well with the experimental results. Hence, it becomes conceivable to predict the effective acoustoelastic parameters of diffuse bulk waves through the utilization of acoustoelastic parameters of pure wave modes calibrated using ballistic waves.

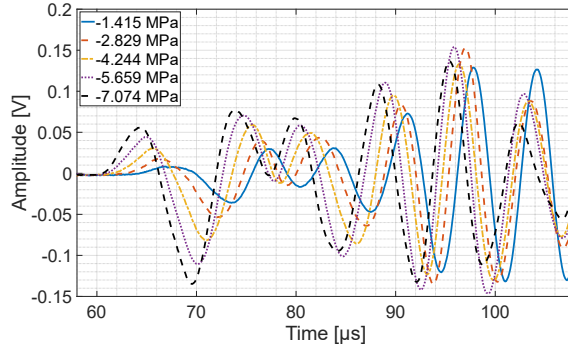
7.7 Discussion

7.7.1 Inconsistencies in acoustoelastic parameters obtained using embedded sensors and surface-bonded sensors

The acoustoelastic parameters presented in Table 7.2 for longitudinal waves traveling parallel to the uniaxial stress direction exhibit greater magnitudes compared to those listed in Table 5.4. In Table 7.2, the parameter is -20.294 GPa^{-1} , whereas in Table 5.4, it is around -2.7 GPa^{-1} . This discrepancy complicates the calculation of the Murnaghan constants from the acoustoelastic parameters, as it becomes difficult to find constants that align with all the parameters listed in Table 7.2. This is why the Murnaghan constants from other researchers were used in Section 7.2. The experiments detailed in Chapter 5

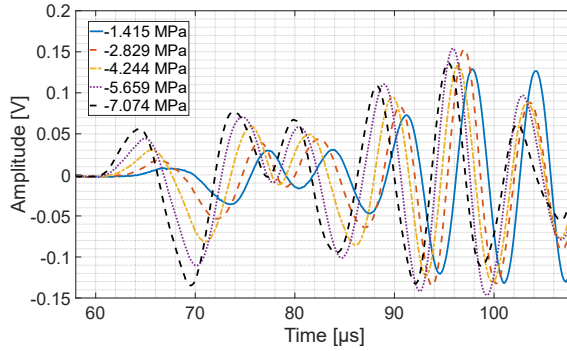
and 7 were conducted on the same sample but on different dates and with sensors installed at different locations. The longitudinal waves in Table 7.2 are acquired using the embedded sensors, while those in Table 5.4 are based on the surface-bonded sensors. Considering the magnitude of difference between these two results are much higher than the possible errors induced by the stretching technique, as discussed in Section 5.9.2, the emergence of this phenomenon may stem from two aspects.

Firstly, the age of the concrete may have an impact on the measurements. To assess this impact, an additional test was conducted after Test I and II. In Figure 7.16, we present the longitudinal wave signals received by embedded sensors at 106 days (Test I), 147 days (Test II), and 385 days (additional test). It is important to note that the tests conducted in Chapter 5 were carried out at 463 days (Test 1), 496 days (Test 2), and 497 days (Test 3) on the same sample using surface-bonded sensors. The acoustoelastic parameters for longitudinal waves traveling parallel to the uniaxial stress direction are -20.387 GPa^{-1} , -20.201 GPa^{-1} , and -12.526 GPa^{-1} for Test I, Test II, and the additional test, respectively. While there are indeed some changes in the acoustoelastic parameters during concrete hydration, the magnitude of these changes is not significant enough to account for the observed discrepancy between Table 5.4 and Table 7.2.

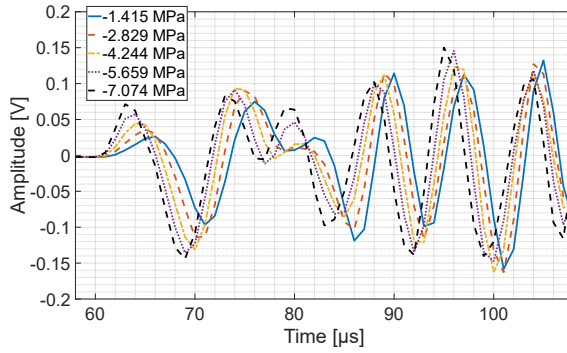


(a) Received signal during Test I (concrete age: 106 days; acoustoelastic parameter A_{1111} : -20.387 GPa^{-1}).

7.7 Discussion



(b) Received signal during Test II (concrete age: 147 days; acoustoelastic parameter A_{1111} : -20.201 GPa^{-1}).



(c) Received signal during the additional test (concrete age: 385 days; acoustoelastic parameter A_{1111} : -12.526 GPa^{-1}).

Figure 7.16 Longitudinal waves propagating parallel to the uniaxial stress direction received by embedded sensors on different concrete age.

Second, it is likely that the measurements from the embedded sensors are much more sensitive to the stress change than the surface-bonded sensors in concrete, which can also be observed from the waveforms shown in Figure 5.12 and Figure 7.6. This is an inaugural instance of observing such a phenomenon, with no pertinent literature to reference. In this chapter, acoustoelastic parameters for transverse waves are determined utilizing surface-bonded sensors. Given the information presented in this paragraph, acoustoelastic parameters for transverse waves employed in constructing effective acoustoelastic parameters for diffuse waves might be underestimated. Even if acoustoelastic parameters are indeed underestimated, this discrepancy will not affect the validity of the method proposed in this chapter for constructing effective acoustoelastic parameters. To demonstrate this argument, we present another representation of the constructed acoustoelastic parameters in Figure 7.17. The key distinction between Figure 7.15 and Figure 7.17 lies in the magnitude of A_{2311} and A_{2111}/A_{1211} , which in this calculation is assumed to be 5 times

greater than those measured from surface-bonded sensors as detailed in Table 7.2. Additionally, the construction process commences from the 4th time window. As depicted in this figure, even in this extreme scenario, the constructed result remains reasonable, albeit with relatively higher errors evident in the later coda after 4000 μs . From this discussion, it is clear that while the acoustoelastic parameters measured using surface and embedded sensors may differ, these differences do not impact the effectiveness of the proposed method in constructing the effective acoustoelastic parameters.

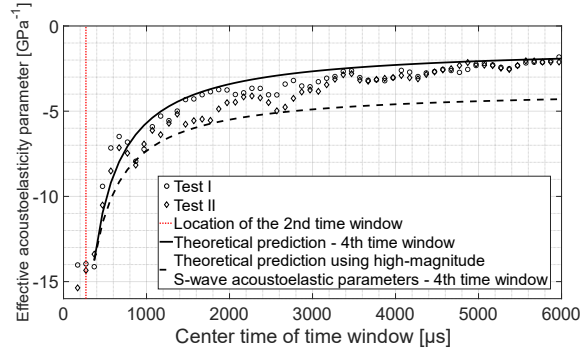


Figure 7.17 Effective acoustoelastic parameters in each time window together with theoretical predictions using the acoustoelastic parameters of transverse waves with higher magnitudes.

7.7.2 Fluctuations of effective acoustoelastic parameters among different samples

This dissertation involves three cylinders, each detailed in Table 7.3. Cylinders 2 and 3 share the same mixture, while Cylinder 1 is cast using an unknown commercial mixture. It is important to note that the measurements of Cylinder 3 has not been utilized in previous chapters; its loading protocol is outlined in Figure 7.18. Effective acoustoelastic parameters for these three samples across five experiments are provided in Figure 7.19. Significantly, the additional test for Cylinder 2 highlights notable discrepancies in effective acoustoelastic parameters during the initial time windows when compared to Tests I and II. A possible explanation is that the additional test shows a lower A_{1111} magnitude than Tests I and II, as shown in Figure 7.16. The reduced magnitude of the acoustoelastic parameter for longitudinal waves has a significant influence on the initial time windows, given the substantial longitudinal wave energy they contain. However, effective acoustoelastic parameters across these three tests on Cylinder 2 converge in the later coda, particularly after 1000 μs , indicating repeatability in diffuse wave scenarios. Despite of the different mixture compositions, tests on Cylinder 1 and 3 demonstrate similar effective acoustoelastic parameters in the coda. This similarity is currently difficult to explain, particularly with only two tests conducted. Since Cylinders 2 and 3 have the same mixture composition but were subjected to different loading protocols and magnitudes, the variations in their effective acoustoelastic parameters may be attributed to these differences.

7.7 Discussion

Therefore, to ensure accuracy, it is recommended not to extrapolate effective acoustoelastic parameters obtained from a specific stress range to ranges beyond that in future research.

Table 7.3 Concrete cylinders employed in this dissertation.

Sample name	Related chapter(s)	Mixture composition	Loading protocol	Test date
Cylinder 1	Section 4.2	Commercial mixture (unknown)	See Figure 4.3	2021/03/25
Cylinder 2	Section 4.3.5; Section 5.6; Chapter 7	See Table 6.3	Test I: See Figure 7.4	2021/07/09
			Test II: See Figure 7.4	2021/08/19
			Additional test: See Figure 7.4	2022/04/14
Cylinder 3	Section 7.7.2	See Table 6.3	See Figure 7.18	2021/05/20

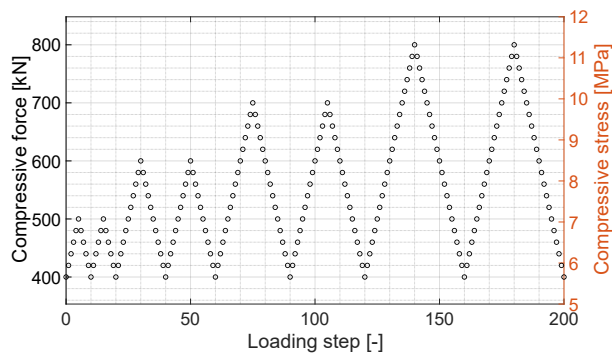


Figure 7.18 Loading protocol for Cylinder 3.

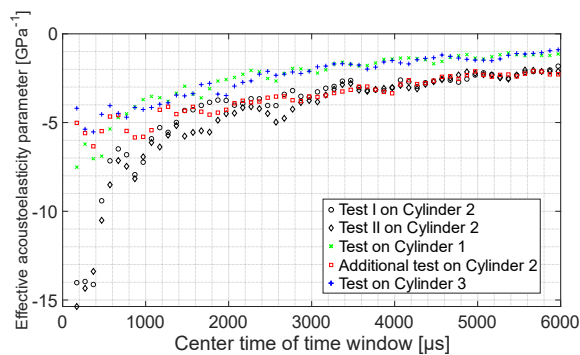


Figure 7.19 Effective acoustoelastic parameters in each time window among different samples.

Due to the limited number of samples, mixtures, and experiments discussed in this section, it is challenging to draw definitive conclusions about the impact of materials and

load steps on effective acoustoelastic parameters. In the future, further testing is necessary to evaluate their impact on these parameters in concrete samples.

7.7.3 Travel time change of diffuse longitudinal and transverse waves in biaxial or triaxial stress states

In Section 7.5, we demonstrated how to obtain the travel time change of diffuse longitudinal and transverse waves using the Monte Carlo simulation, as outlined in Algorithm 7.4. The proposed method can be extended to biaxial or triaxial stress states by modifying the initial stress matrix, denoted as $\sigma(p)$ in Algorithm 7.4. However, we have not validated the effectiveness of this method under biaxial or triaxial stress conditions. Therefore, we recommend experimentally validating its performance in these stress states using embedded sensors before applying it to such scenarios.

7.7.4 Long-lasting anisotropy of the wavefield

In Section 7.6, we observed that the effective acoustoelastic parameters based on theoretical equilibration time do not fully align with experimental results. We suggest that this discrepancy is due to the prolonged presence of spatially anisotropic wave energy, which lags behind the equilibration of the overall energy.

In seismology, a possible explanation for long-lasting wavefield anisotropy is the uneven distribution of epicentres (Paul, Campillo et al. 2005), leading to a preferential energy flow direction in diffuse waves. In this dissertation, SAs are used as both transducers and receivers. However, as indicated by Zhao et al. (2020), smart aggregates are not equally sensitive to spatial changes in all directions, showing a preference for deformations from certain directions. To better understand the long-lasting anisotropy of the wavefield in concrete using smart aggregates, this directional preference must be considered.

7.8 Summary

In this chapter, we introduce a framework that integrates theories and models introduced in Chapter 5 and 6 to interpret the changes in travel time of diffuse waves in uniaxially stressed concrete. We proposed the following steps to estimate the effective acoustoelastic parameters for diffuse waves:

- Estimate the energy ratio of equilibrated longitudinal and transverse waves in concrete, as well as the time required for equilibration, using the bulk wave energy transport model introduced in Chapter 6.
- Obtain four acoustoelastic parameters from experiments: two for longitudinal waves and two for transverse waves.
- Use Monte Carlo simulations, combined with the acoustoelastic parameters, to estimate travel time changes in diffuse longitudinal and transverse waves.

7.8 Summary

- Weight the travel time changes of diffuse longitudinal and transverse waves by the equilibrated wave energy from the energy transport model to predict the travel time change for diffuse bulk waves.
- Utilize the travel time changes of diffuse bulk waves to derive time-lapse effective acoustoelastic parameters for diffuse waves.

8. Recommendations for applications in concrete structures

8.1 Introduction

In previous chapters, we have laid out the theoretical frameworks concerning acoustoelasticity and the energy equilibration process of bulk waves in concrete. Now, our focus shifts towards exploring the practical applications of these frameworks in monitoring stress changes in concrete structures.

8.2 Estimating stress-induced velocity changes in concrete using the stretching technique and the WCS technique

The stretching technique can be used to retrieve velocity changes in both ballistic and coda waves. When applying this technique to ballistic waves for determining acoustoelastic parameters, the time window should include at least one period of the signal but no more than three. Longer time windows may contain multiply scattered waves, reducing the accuracy of the measured acoustoelastic parameters compared to shorter windows. For applications of the stretching technique in the coda waves, it is recommended to determine the time window length by considering the frequency of interest. The time window should encompass at least ten periods (the reciprocal of the frequency of interest) to mitigate cycle skipping in the coda. Additionally, the stress difference between consecutive measurements should be kept low. In the case reported in Section 4.2.4.3, this difference was 0.57 MPa.

For the WCS technique, this technique can be used to retrieve velocity changes in coda waves. It is recommended to determine the operational frequency band by considering the expected magnitude of travel time differences and the energy present within the frequency band. The maximum travel time difference at the frequency of interest should be less than half a period (the reciprocal of the frequency of interest). Furthermore, velocity changes should be averaged over a time window spanning at least ten periods (the reciprocal of the frequency of interest) to reduce fluctuations in the measured velocity changes at different lag times. Additionally, the energy within the operational frequency band should be significantly higher than the noise level, as shown in Figure 4.5. To reduce the risk of cycle skipping in the coda, the stress difference between consecutive measurements should be kept low, particularly for waves in the high-frequency range, such as those above 80 kHz, as noted in Section 4.2.4.3. Given that the computational efficiency of the WCS technique is much higher than that of the stretching technique, it is also suitable for quickly calculating velocity changes in concrete.

8.3 Estimating diffusive properties in concrete members with boundaries

For future acquisitions of diffusivity and dissipation in concrete, the following steps are recommended:

8.4 Estimating bulk wave energy transport properties in concrete members

1. Filter the raw signals obtained from experiments to focus on the frequency of interest. In this dissertation, we utilized the continuous wavelet transform (CWT) for this purpose.
2. Determine the appropriate time window length for acquiring ensemble-averaged energy. The time window should be at least the reciprocal of the frequency of interest.
3. Determine the ending time window based on the declining trend of the logarithmic energy, which should exhibit linearity or approximate linearity.
4. Determine the locations of time windows to ensure that data points in the maximum energy arrival and energy decay portions are comparable.
5. Calculate the logarithm of ensemble-averaged energy in each time window.
6. Evaluate the maximum contribution of reflected energy from image sources by using $\exp\{-[(r')^2 - r^2]/(4Dt)\}$ (refer to Section 4.3.2.2). Image sources with low contribution can be neglected. In the case shown in Section 4.3.4.2, the threshold was 0.30.
7. Construct the new diffusion equation using Equation (4.19) and (4.25).
8. Fit the constructed diffusion equation to the logarithm of ensemble-averaged energy to determine the diffusivity and dissipation.
9. Verify the arrival time of maximum energy using Equation (4.12) to avoid anomalous results.

Given the significant fluctuations in diffusivity and dissipation, it is essential to analyse their characteristics statistically, as individual observations may hold limited significance.

8.4 Estimating bulk wave energy transport properties in concrete members

For future applications of bulk wave energy transport model, the following steps are recommended:

1. Determine the frequency of interest, the characteristic radius of coarse aggregates (through Equation (6.42b)), the volume fraction of coarse aggregates, and the average longitudinal and transverse wave velocities.
2. Calculate the total scattering cross-sections and weighted total scattering cross-sections using Equations (6.43) and (6.44).
3. Fit the model using the approach mentioned in Section 6.7.4 if it is necessary.

4. Estimate energy evolution using Equation (6.20). The time required to reach bulk wave energy equilibration can be predicted through this energy evolution.
5. Determine the equilibrated energy ratio using Equation (6.23), taking into account the dissipation fitted through the diffusion equation in Section 8.3.

8.5 Determining acoustoelastic parameters for ballistic waves and effective acoustoelastic parameters for diffuse waves

In this section, we outline the key steps and considerations to determine acoustoelastic parameters from ballistic waves and effective acoustoelastic parameters from diffuse waves in future studies:

1. Sample and sensor preparation:
 - a. The sample can be either cylindrical or prismatic in shape, with dimensions tailored to the frequency of interest. The dimensions should be at least twice the wavelength to accommodate the propagation of transverse waves at this frequency. For a transverse wave frequency of 50 kHz and a velocity of 2700 m/s, the wavelength is 54 mm. Thus, the diameter and height of the cylindrical sample, or the width and height of the prismatic sample, should be at least 108 mm.
 - b. Compression mode (d_{33} mode) piezoelectric-based embedded sensors are recommended to reduce the influence of Rayleigh waves. The distance between sensors should be at least twice the wavelength of the transverse waves at the frequency of interest. Given a transverse wave frequency of 50 kHz and a velocity of 2700 m/s, the wavelength is 54 mm, so the sensor spacing should be at least 108 mm.
 - c. The compressive load should be applied uniaxially. Four pairs of ultrasonic sensors are required (refer to Figure 7.5):
 - i. One longitudinal wave sensor pair with a propagation direction parallel to the uniaxial load direction.
 - ii. One longitudinal wave sensor pair with a propagation direction perpendicular to the uniaxial load direction.
 - iii. One transverse wave sensor pair with a propagation direction perpendicular to the uniaxial load direction and a polarization direction parallel to the uniaxial load direction.
 - iv. One transverse wave sensor pair with propagation direction perpendicular to the uniaxial load direction while polarization direction perpendicular to the uniaxial load direction.

8.5 Determining acoustoelastic parameters for ballistic waves and effective acoustoelastic parameters for diffuse waves

2. Loading protocol and testing:
 - a. The loading protocol should be designed according to the stress range relevant to the concrete structure. As mentioned in Section 8.2, the stress difference between consecutive measurements should be kept less than 0.57 MPa.
 - b. There is no strict requirement on the loading speed. Signals should be collected at each load step when the load is stabilized, which can be ensured by checking the load cell in the jack.
3. Diffusivity (will be utilized in Step 4 for model validation):
 - a. Diffusivity can be determined from the signals obtained during loading, following the procedures outlined in Section 8.3.
4. Equilibrated ratio for bulk waves(will be used in Step 6 to weight the travel time changes of longitudinal and transverse waves) and the time required for the equilibration (will be used in Step 7 to determine the if the wavefield has become isotropic):
 - a. The equilibrated ratio for bulk waves and the time required for the equilibration can be obtained using the methodology described in Section 8.4.
5. Acoustoelastic parameters for ballistic waves:
 - a. Acoustoelastic parameters can be calculated using Equation (7.6).
 - b. The slope s in Equation (7.6) can be acquired by performing a linear fit of the square of relative velocity, $(dv/v+1)^2$, with respect to the compressive stress. Please note that the relative velocities include those retrieved from two longitudinal wave sensor pairs and two transverse wave sensor pairs, as previously mentioned.
6. Travel time changes of diffuse bulk waves:
 - a. Travel time changes of diffuse bulk waves can be obtained by weighting the travel time changes of spatially isotropic longitudinal and transverse waves using the Monte Carlo simulation outlined in Algorithm 7.4.
7. Effective acoustoelastic parameters:
 - a. Determine if the wavefield has become isotropic by checking the energy equilibration time.
 - b. Effective acoustoelastic parameters can be acquired using the method described in Algorithm 7.5.

8.6 Estimating biaxial principal stress changes in concrete members

One of the potential applications of the proposed theories in this dissertation is monitoring changes in principal stresses under the plane stress state. In Equation (5.77), we introduced the acoustoelastic expression for the longitudinal wave propagating parallel to the principal stress direction as:

$$v_{11}^{\text{natural}} = v_{11}^{(0)} \sqrt{1 + A_{1111} \sigma_1} . \quad (8.1)$$

The velocity change for longitudinal waves propagating in the same direction as the principal stress direction with the uniaxial stress changing from $\sigma_{1,1}$ to $\sigma_{1,2}$, is shown as:

$$\begin{aligned} \frac{v_{11,2}^{\text{natural}} - v_{11,1}^{\text{natural}}}{v_{11,1}^{\text{natural}}} &= \frac{\sqrt{1 + A_{1111} \sigma_{1,2}} - \sqrt{1 + A_{1111} \sigma_{1,1}}}{\sqrt{1 + A_{1111} \sigma_{1,1}}} \\ &\simeq \frac{\frac{1}{2} A_{1111} (\sigma_{1,2} - \sigma_{1,1})}{1 + \frac{1}{2} A_{1111} \sigma_{1,1}} \\ &\approx \frac{1}{2} A_{1111} (\sigma_{1,2} - \sigma_{1,1}) , \end{aligned} \quad (8.2)$$

where $v_{11,1}^{\text{natural}}$ and $v_{11,2}^{\text{natural}}$ indicate the velocity of longitudinal waves in the natural frame at the first stress level, $\sigma_{1,1}$, and the second stress level, $\sigma_{1,2}$, respectively. Please note that the subscripts before and after comma represent the tensor index and the load step, respectively. For example, $\sigma_{1,1}$ denotes the principal stress in the 1 (or x) direction at load step 1, while $v_{11,2}$ represents the wave velocity with both propagating and polarization in the 1 (or x) direction at load step 2. Taylor expansion is utilized in the derivation from step 1 to step 2 in Equation (8.2), and the approximation from step 2 to step 3 is based on the assumption that the term $A_{1111} \sigma_{1,1}/2$ is much smaller than 1, a condition deemed valid except when $\sigma_{1,1}$ holds considerable magnitude.

Similarly, for the case that longitudinal waves propagating perpendicular to the uniaxial stress direction, a similar expression as to Equation (8.2) can be obtained as

$$\begin{aligned} \frac{v_{11,2}^{\text{natural}} - v_{11,1}^{\text{natural}}}{v_{11,1}^{\text{natural}}} &= \frac{\sqrt{1 + A_{1122} \sigma_{2,2}} - \sqrt{1 + A_{1122} \sigma_{2,1}}}{\sqrt{1 + A_{1122} \sigma_{2,1}}} \\ &\simeq \frac{\frac{1}{2} A_{1122} (\sigma_{2,2} - \sigma_{2,1})}{1 + \frac{1}{2} A_{1122} \sigma_{2,1}} \\ &\approx \frac{1}{2} A_{1122} (\sigma_{2,2} - \sigma_{2,1}) , \end{aligned} \quad (8.3)$$

where $\sigma_{2,1}$ and $\sigma_{2,2}$ denote the uniaxial stresses applied along the y -axis in the first and second load levels, respectively. Equation (8.2) and (8.3) can be utilized to calibrated the acoustoelastic parameters A_{1111} and A_{1122} through laboratory tests.

8.6 Estimating biaxial principal stress changes in concrete members

Equation (8.2) and (8.3) are acoustoelastic expressions for longitudinal waves under uniaxial stress conditions. The acoustoelastic expression for biaxial stress conditions is presented in Equation (5.82). This equation can be formatted similarly to Equation (5.77) and (5.79) as:

$$\begin{aligned} v_{11}^{\text{natural}} &= v_{11}^{(0)} \sqrt{1 + [\cos^2(\theta) \sigma_1 + \sin^2(\theta) \sigma_2] A_{1111} + [\sin^2(\theta) \sigma_1 + \cos^2(\theta) \sigma_2] A_{1122}} \\ &= v_{11}^{(0)} \sqrt{1 + [\cos^2(\theta) A_{1111} + \sin^2(\theta) A_{1122}] \sigma_1 + [\sin^2(\theta) A_{1111} + \cos^2(\theta) A_{1122}] \sigma_2} . \end{aligned} \quad (8.4)$$

The velocity change of longitudinal waves propagating in an inclined direction shown in Figure 5.9(b) while the biaxial stresses are applied in the y - and x -axis shown in Figure 5.9(a) is then:

$$\begin{aligned} \frac{v_{11,2}^{\text{natural}} - v_{11,1}^{\text{natural}}}{v_{11,1}^{\text{natural}}} &= \frac{\sqrt{1 + [\cos^2(\theta_2) A_{1111} + \sin^2(\theta_2) A_{1122}] \sigma_{1,2} + [\sin^2(\theta_2) A_{1111} + \cos^2(\theta_2) A_{1122}] \sigma_{2,2}}}{\sqrt{1 + [\cos^2(\theta_1) A_{1111} + \sin^2(\theta_1) A_{1122}] \sigma_{1,1} + [\sin^2(\theta_1) A_{1111} + \cos^2(\theta_1) A_{1122}] \sigma_{2,1}}} - 1 \\ &= \frac{\frac{1}{2} [\cos^2(\theta_2) \sigma_{1,2} - \cos^2(\theta_1) \sigma_{1,1}] A_{1111} + \frac{1}{2} [\sin^2(\theta_2) \sigma_{2,2} - \sin^2(\theta_1) \sigma_{2,1}] A_{1122}}{1 + \frac{1}{2} \{ [\cos^2(\theta_1) A_{1111} + \sin^2(\theta_1) A_{1122}] \sigma_{1,1} + [\sin^2(\theta_1) A_{1111} + \cos^2(\theta_1) A_{1122}] \sigma_{2,1} \}} \\ &\approx \frac{1}{2} [\cos^2(\theta_2) \sigma_{1,2} - \cos^2(\theta_1) \sigma_{1,1}] A_{1111} + \frac{1}{2} [\sin^2(\theta_2) \sigma_{2,2} - \sin^2(\theta_1) \sigma_{2,1}] A_{1122} , \end{aligned} \quad (8.5)$$

where $\sigma_{i,1}$ and $\sigma_{i,2}$ indicate the principal stresses in the i direction at the first stress level, and the second stress level, respectively. Following the calibration to obtain the acoustoelastic parameters A_{1111} and A_{1122} , Equation (8.5) involves six unknowns. Theoretically, a system of six equations is necessary to determine all unknowns, achievable by adjusting sensor configurations in various inclinations. In practice, given that the magnitude of A_{1122} is significantly smaller than that of A_{1111} , as demonstrated in earlier chapters, the term involving A_{1122} can be disregarded. This simplification reduces the number of unknowns to four, allowing for the theoretical determination of changes in principal stress magnitudes and their orientations in a biaxial stress state. It is important to note that this approach can only detect changes in principal stresses and cannot be used to determine their absolute magnitudes or orientation.

Furthermore, it is important to note that (i) the principal stresses estimated through the ballistic wave portion represent mean principal stresses along the ballistic wave trajectory, and (ii) the preceding equations in this chapter are solely applicable to the elastic stage of concrete, where no visible crack exists in the medium under examination.

8.7 Applications in monitoring concrete infrastructures

The methodology proposed in this dissertation is designed for monitoring stress changes in concrete infrastructures. Depending on the specific monitoring goals, these applications can be categorized into two primary types:

1. monitoring changes in magnitudes and directions of principal stresses;
2. mapping spatial variations of stress in a given area.

The first application utilizes the ballistic wave component and is relatively straightforward in its implementation. A simplified approach for monitoring a biaxial principal stress state is presented in Section 8.6. For concrete bridges, which typically operate under a plane stress state, the proposed approach can be directly applied.

For cases requiring analysis of stress changes in a triaxial state, additional sensor pairs are necessary. In such scenarios, Equation (7.1) should be employed to compute the stress matrix. However, due to the complexity of the acoustoelastic equations in a triaxial stress state, analytical solutions may not always be feasible. In these instances, numerical calculations are recommended.

Unlike the first application, which utilizes ballistic waves, the second application relies on diffuse waves. Diffuse waves have the advantage of traveling longer distances and exhibiting higher sensitivity to subtle changes in the medium. This dissertation investigates diffuse wave acoustoelasticity under a uniaxial stress state. While the proposed framework can theoretically be extended to biaxial and triaxial stress states by modifying the stress matrix in Equation (7.1), experimental validation for these scenarios remains incomplete. Consequently, further experimental work is necessary before applying the method to real-world structures.

To effectively map spatial stress changes, the diffuse wave acoustoelasticity should be combined with the sensitivity kernel (Larose, Planes et al. 2010). However, this dissertation does not include experimental work incorporating the sensitivity kernel, and its performance in conjunction with diffuse wave acoustoelasticity is yet to be determined. Two potential strategies for translating velocity change maps into stress change maps are proposed:

1. Use the sensitivity kernel to generate a velocity change map, which is then converted to a stress change map using the diffuse wave acoustoelasticity.
2. Convert velocity changes into stress changes directly using diffuse wave acoustoelasticity, then map these stress changes spatially using the sensitivity kernel.

As neither approach has been implemented by the authors, the most effective method for concrete structures remains undetermined.

8.7 Applications in monitoring concrete infrastructures

While the proposed methodology is promising, several challenges must be addressed before applying to in-situ monitoring of concrete infrastructures. The first challenge is the sensitivity to environmental factors. The high sensitivity of the stretching and WCS techniques can be a double-edged sword. In addition to detecting stress changes, they are significantly affected by environmental factors such as temperature and humidity, leading to potential inaccuracies during in-situ monitoring. Additionally, the resonant frequency of sensors may introduce non-negligible effects on monitoring results, necessitating careful calibration, testing and interpretation.

These challenges are difficult to fully resolve in a controlled laboratory environment, highlighting the importance of practical applications to refine the methodology. To validate and enhance the proposed methodology in this dissertation, several ongoing projects focus on the monitoring of concrete infrastructure using smart aggregates and bulk waves. These projects include:

- Monitoring the Maastunnel in Rotterdam, the Netherlands.
- Monitoring the N69 bridges near Dommelen, the Netherlands.
- Monitoring the Kowebrêge road bridge in Friesland, the Netherlands.
- Monitoring the Fehmarn Belt fixed link between Denmark and Germany.
- Monitoring the bridge on Balladelaan in Amersfoort, the Netherlands.
- Monitoring prestressed inverted T-girders in the Netherlands.

The results of these long-term monitoring efforts are not included in this dissertation, and some of the findings are unpublished. These developments will be presented in future publications.

9. Conclusions and recommendations for the future work

9.1 Conclusions

The main objective of this study is to improve the knowledge about the mechanism and evolution of velocity changes in concrete retrieved from bulk waves. Given that such velocity changes may result from a combination of concrete heterogeneity and the acoustoelastic effect, this study aims to develop a means-end approach grounded in acoustoelasticity and scattering theory. To facilitate the problem-solving process, the main objective is divided into five specific sub-goals: 1. tailoring data processing techniques (Chapter 4); 2. refining the acoustoelastic theory (Chapter 5); 3. interpreting velocity changes in stressed concrete retrieved via ballistic bulk waves (Chapter 5); 4. modelling bulk wave propagation in concrete (Chapter 6); and 5. interpreting velocity changes in stressed concrete retrieved via diffuse bulk waves (Chapter 7).

The conclusions of this dissertation are summarized as follows:

A comparison of the stretching technique and the WCS technique for retrieving stress-induced velocity changes in concrete shows that both methods demonstrate comparable accuracy, underscoring their reliability and effectiveness for precise velocity change measurements. (Sub-goal 1)

- In the experiment detailed in Section 4.2, the stabilities of the stretching technique and the WCS technique are comparable for wave frequencies ranging from 50 kHz to 80 kHz.
- The stretching technique is more effective when handling signals with short duration.
- It is recommended to determine the suitable time window length for the stretching technique by considering both the wave frequency and the expected magnitude of velocity change.
- For the WCS technique, it is advisable to determine the operational frequency band by considering the expected magnitude of velocity change and the energy present within the frequency band.

The diffusion equation for an infinite medium is modified to account for the influence of boundaries on the diffusive properties of elastic bulk waves in concrete by incorporating boundary-reflected energy. This adjustment improves the accuracy of measuring both diffusivity and dissipation in concrete structures. (Sub-goal 1)

- Neglecting reflected energy during the fitting process leads to underestimated diffusivity and dissipation.

9.1 Conclusions

- In concrete, as wave frequency increases, diffusivity decreases while dissipation increases.
- Determining the amount of reflected energy to be included in the diffusion equation requires evaluating its contribution to the main energy.

The theoretical framework of acoustoelasticity is refined to include bulk waves propagating in arbitrary directions. The modes and velocities of these waves are determined by solving the equation of motion with the specified propagation direction and the updated acoustoelastic modulus matrix, derived from the stress matrix. The refined framework provides a tool for comprehensively understanding wave behaviour under complex stress conditions. (Sub-goal 2)

- In concrete, the polarization direction of longitudinal waves is relatively unaffected by the stress matrix, whereas the polarization direction of transverse waves is highly sensitive to it.
- The magnitudes of normal strains have a significant impact on the velocities of both longitudinal and transverse waves in concrete.
- The magnitudes of shear strains have a minimal effect on longitudinal wave velocities in concrete but significantly influence the velocities of transverse waves.

The acoustoelastic effect on ballistic waves is characterized by two distinct parameters—one for longitudinal waves propagating parallel to the uniaxial stress direction and another for those propagating perpendicular to it—providing a comprehensive understanding of how stress influences ballistic wave velocity depending on its propagation direction. (Sub-goal 3)

- This approach is based on the theoretical analysis indicating that shear strains have a minimal impact on longitudinal wave velocities in concrete.
- The acoustoelastic parameters should be defined in the natural frame to account for the static deformation resulting from the static stress.
- Although there may be some transverse waves in the ballistic wave regime, it is predominantly dominated by longitudinal waves.

A new approach is proposed for modelling the energy transport of bulk waves in concrete by incorporating scattering theory into a probability-based energy equilibration model, considering bulk wave frequency, the characteristic radius of coarse aggregates, and their volume fraction. The proposed modelling approach provides a reasonable representation of wave energy evolution in concrete. (Sub-goal 4)

- The time required for S-S equilibration is notably shorter than that required for P-S equilibration.
- Presence of dissipation accelerates P-S equilibration and alters the equilibrated energy ratio between longitudinal and transverse waves.
- Actual time for energy equilibration may exceed theoretically predicted global equilibration time significantly.

The acoustoelastic effect on diffuse waves is characterized by four distinct parameters—two for longitudinal waves and two for transverse waves—offering a detailed framework for understanding how stress affects diffuse wave velocity. Travel time changes for diffuse waves can be estimated by weighting those for diffuse longitudinal and transverse waves according to the equilibrated energy ratio, offering a method for predicting travel time changes in diffuse waves. (Sub-goal 5)

- For isotropic materials in the natural frame, there are five independent acoustoelastic parameters; however, two of these parameters for transverse waves share the same theoretical expression.
- The acoustoelastic effect on diffuse longitudinal or transverse waves can be estimated using Monte Carlo simulation.

The theoretical framework proposed in this dissertation can potentially be applied to the structural health monitoring of concrete structures, such as bridges and tunnels, to track stress or strain changes using bulk waves detected by embedded ultrasonic sensors.

9.2 Recommendations for the future work

9.2.1 Minimum resolution of the stretching technique and the WCS technique

In Section 4.2, we conducted a comparison between the stretching technique and the WCS technique. Following this, in Section 5.9.2, we carried out an error analysis to assess the precision of the stretching technique. From these initial analyses, it became evident that the error magnitude associated with the stretching technique significantly impacts the measured velocity change, particularly at low magnitudes around 0.1%. Notably, this magnitude is comparable to the stress-induced velocity change observed when longitudinal waves propagate perpendicular to uniaxial stress. The error utilized in this analysis was estimated based on reported errors in the literature. Currently, there is a lack of research specific to concrete in this regard. Future experimental investigations on determining the minimum resolution of both the stretching and WCS techniques in retrieving velocity changes of the medium can aid in disregarding unreliable measurements with low

9.2 Recommendations for the future work

velocity change magnitudes. For guidance on the design of experimental investigations, we recommend the work by Weaver et al. (2011).

9.2.2 Mitigation of cycle skipping effect while using the WI techniques

As demonstrated in Section 4.2.4.3, the cycle skipping effect inevitably arises when employing WI techniques. This effect can significantly compromise the reliability of the retrieved velocity changes, potentially leading to erroneous conclusions regarding the integrity of monitored concrete structures. Thus, enhancing the algorithms of WI techniques holds importance for their application in real structure monitoring.

Mao et al. (2020) propose the utilization of phase unwrapping to mitigate the cycle skipping effect. Phase unwrapping is a signal processing technique designed to eliminate discontinuities (or ‘wraps’) in signal phase. Typically, signal phases are measured within a range of $-\pi$ to π , resulting in wrapping around once these boundaries are reached. This wrapping, often associated with the cycle skipping effect in the WCS technique, complicates the accurate interpretation of phase information. Phase unwrapping seeks to reconstruct the original, continuous phase by identifying and rectifying these discontinuities. It involves determining the appropriate integer multiples of 2π to add or subtract from wrapped phase values, ensuring continuity. Numerous studies exist detailing algorithms for phase unwrapping, such as those outlined by Wang and Houseman (1998). However, no research has explored incorporating phase unwrapping into the WCS technique to enhance its stability against cycle skipping when applied to concrete. Further research should investigate the reliability of retrieved velocity changes in concrete utilizing the WCS technique incorporating phase unwrapping.

Regarding the stretching technique, there is currently a dearth of literature addressing this aspect. Further investigations are needed to propose an enhanced stretching technique to mitigate the cycle skipping effect.

9.2.3 Response of diffusive properties of bulk waves to stresses

In Section 4.3, we explored the diffusive properties of bulk waves in concrete. Throughout this examination, we did not account for the potential influence of applied stress on these diffusive properties, diffusivity and dissipation. However, understanding the response of diffusive properties to stresses is crucial for enhancing the accuracy of stress mapping using the sensitivity kernel-based technique. This is because the sensitivity kernel relies on the diffusion equation for its construction (Pacheco and Snieder 2005).

Based on findings from previous chapters, stress has a limited impact on wave velocity during the elastic stage of concrete. Given the close relationship between diffusivity and wave velocity, as depicted in Equation (6.48), we do not anticipate a significant effect of applied stress on diffusivity in concrete. Regarding dissipation, it is essential to note that the response of dissipations, arising from viscoelasticity and internal friction, to stress

may exhibit distinct behaviours (Brunet, Jia et al. 2008). Therefore, an experiment is necessary to assess the response of dissipation to stress changes in concrete. The concrete sample used can be the same cylindrical specimen from Section 4.2.

9.2.4 Determination of Murnaghan constants of concrete

Another potential avenue for future research involves the precise determination of Murnaghan constants for concrete. This endeavour must address three crucial considerations. Firstly, the fitting of Murnaghan constants should be accurately performed using expressions of acoustoelasticity in the natural frame. This is essential because stress-induced deformations are not accounted for in the expressions of acoustoelasticity in the initial frame, despite their presence in experimental conditions. The second key point pertains to dynamic and static Lamé parameters. The acoustoelastic theory encompasses two types of deformations: static deformations and dynamic deformations. To accurately determine static deformations, one should utilize the static elastic modulus and Poisson's ratio obtained from experiments. Conversely, dynamic deformations, represented as wave velocities in acoustoelastic theory, require the use of dynamic Lamé parameters for their determination. Thirdly, the spatial variation of concrete's mechanical properties must be considered, which necessitates averaging measurements from multiple sensor pairs. Future researchers are recommended to design their test setups and curve fitting processes in line with these recommendations.

9.2.5 Mapping stress change field using ballistic waves and tomography

Mapping the stress field using ballistic wave acoustoelasticity involves a mapping technique known as the tomography. Tomography is a data processing technique that generates cross-sectional images, a method that has been extensively developed in geophysics (Dines and Lytle 1979) and medical imaging (Kak and Slaney 2001) over the years. Tomography can be implemented in three primary forms: (i) parallel-scanning, commonly used in medical computerized tomography (CT); (ii) two-sided transmission employing two linear arrays of sensors; and (iii) four-sided transmission. The theoretical foundations of this mapping technique can be found in the literature (Bond, Kepler et al. 2000, Martins, Soares et al. 2007, Pursiainen and Kaasalainen 2014, Tant, Galetti et al. 2018), with its limitations reviewed by Santamarina and Gheshlaghi (1995). However, due to scope limitations, the theoretical background and limitations will not be extensively discussed in this section. By employing tomography, one can generate a velocity map of the specimen, as depicted in Fig. 4 of Kepler's work (2000). This velocity map can be translated into a stress map by integrating Equation (8.5) into the mapping process, solving it for each individual element divided for tomography. The proper integration of acoustoelasticity into the tomography process remains an open topic for exploration.

9.2.6 Mapping stress change field using diffuse waves and sensitivity kernel

Similar to the tomography technique, another mapping technique capable of mapping velocity changes in the medium is the sensitivity kernel-based mapping technique (Pacheco and Snieder 2005, Rossetto, Margerin et al. 2011, Obermann, Froment et al. 2014). This technique has been effectively employed in concrete to map velocity changes retrieved from diffuse coda waves (Zhang, Planes et al. 2016, Clauss, Epple et al. 2020, Jiang, Zhan et al. 2020). Consequently, it is feasible to obtain a stress field map by integrating the acoustoelastic effect of diffuse waves, as discussed in Chapter 7, into the inversion process of the sensitivity kernel-based technique.

One of the key challenges in incorporating the acoustoelastic effect of diffuse waves into the inversion process of the sensitivity kernel-based technique is interpreting stress changes from travel time changes, particularly in biaxial or triaxial stress states. While theoretically, these stress states can be accounted for by adjusting the principal stress matrix prior to Monte Carlo simulations, experimental studies involving biaxial or triaxial loads are required to validate the simulation results first.

Notations

Roman upper case

A	Total cross-section of the characteristic medium
\mathbf{A}	Dissipation matrix
A_{eff}	Effective acoustoelastic parameter for inclined propagating longitudinal waves in the natural frame
A_I	Amplitude spectrum of time-domain signal u_I (I can refer to the unperturbed signal or signal after perturbation)
A_{ij}	Contrast of the properties for the two phases (i and j can be the material parameters ρ , μ and λ)
A_{ijkl}	Acoustoelastic parameter for body waves in the natural frame ($i, j, k, l \in \{1,2,3\}$)
$A_{ijkl}^{(i)}$	Acoustoelastic parameter for body waves in the initial frame ($i, j, k, l \in \{1,2,3\}$)
$A_i^{(m)}$	Magnitude of the material property of the matrix (i can be ρ , μ and λ)
$A_i^{(s)}$	Magnitude of the material property of the scatterer (i can be ρ , μ and λ)
$A_{\text{scatterers}}$	Total cross-section of scatterers in the characteristic medium
B_i	Eigenvalue of the acoustoelastic modulus matrix ($i \in \{1,2,3\}$)
B_{ijkl}	Acoustoelastic modulus in the initial frame ($i, j, k, l \in \{1,2,3\}$)
B_{ijkl}^0	Acoustoelastic modulus in the initial frame before coordinate rotation ($i, j, k, l \in \{1,2,3\}$)
C_{ijkl}	Second-order elastic coefficient ($i, j, k, l \in \{1,2,3\}$)
C_{ijklmn}	Third-order elastic constants ($i, j, k, l, m, n \in \{1,2,3\}$)
D	Diffusivity
$D_{\xi\beta k\delta}$	Acoustoelastic modulus in the natural frame ($\xi, \beta, k, \delta \in \{1,2,3\}$)
E	Transport energy
E_0	Deposited energy at initial location at time $t=0$
$E_{\text{high-frequency}}$	Wave energy of the frequency band in the high-frequency regime
E_M	Transport energy of wave mode M (M should be either longitudinal waves or transverse waves)
$E_M^{(0)}$	Deposited energy of wave mode M at initial location at time $t=0$ (M should be either longitudinal waves or transverse waves)
$E_{\text{low-frequency}}$	Wave energy of the frequency band in the low-frequency regime
E_s	Static elastic modulus
E_{SH}	Transport energy of horizontal transverse waves
E_{SV}	Transport energy of vertical transverse waves
E_{total}	Total transport energy considering the reflected energy from boundaries
H	Characteristic correlation length
$H(\cdot)$	The Heaviside step function

Notations

I_m	Random field of matrix phase
I_s	Random field of scatterer phase
\mathbf{J}	Mode conversion matrix
K_m	Matrix phase in the two-phase medium
K_s	Scatterer phase in the two-phase medium
N_λ	Unit vector normal to the plane wave ($\lambda \in \{1,2,3\}$)
\mathbf{Q}	Transformation matrix for stress/strain matrix
R	Normalized correlation function
R_C	Diameter of the cylinder
R_{ij}	Correlation function of material property fluctuation between i and j (i and j can be the material parameters ρ , μ and λ)
\tilde{R}_{ij}^{KL}	Power spectral density (PSD) of material property fluctuation between i and j (i and j can be the material parameters ρ , μ and λ) for incident wave mode K and scattered wave mode L (K and L should be either longitudinal waves or transverse waves)
S	The scale function in the wavelet filter bank
S_{ij}^{final}	Second Piola-Kirchhoff stress tensor in the final state ($i, j \in \{1,2,3\}$)
$S_{ij}^{\text{incremental}}$	Incremental second Piola-Kirchhoff stress tensor ($i, j \in \{1,2,3\}$)
S_{ij}^{initial}	Second Piola-Kirchhoff stress tensor in the initial state ($i, j \in \{1,2,3\}$)
T	Half-length of the time window when operating the stretching technique
T_{ij}^{final}	Cauchy stress tensor in the final state ($i, j \in \{1,2,3\}$)
T_{ij}^{initial}	Cauchy stress tensor in the initial state ($i, j \in \{1,2,3\}$)
U_I	Fourier transforms of the time-domain signal u_I (I can refer to the unperturbed signal or signal after perturbation)
U_γ	Amplitude vector of the plane wave function ($\gamma \in \{1,2,3\}$)
V	Total volume of coarse aggregates in concrete
\mathbf{V}_i	Eigenvector of the mode conversion matrix ($i \in \{1,2\}$)
W	Strain energy function
W_I	Wavelet spectrum of the time-domain signal u_I (I can refer to the unperturbed signal or signal after perturbation)
\mathbf{X}, X_I	Final coordinates

Roman lower case

a	Normalization coefficient in the equation to account for the energy contribution of the image source
\mathbf{a}, a_α	Natural coordinates ($\alpha \in \{1,2,3\}$)
b	Coefficient that is related to the nature of the boundary condition in the equation to account for the energy contribution of the image source
d	Distance between the source and receiver in the cylindrical sample

d_1	Distance between the source to the planar boundary
d_2	Distance between the receiver to the planar boundary
dt	Travel time difference
$dt^{(net)}$	Net travel time difference in a time window
dt/t	Travel time change
dv/v	Velocity change
$dv/v^{(i)}$	Velocity change in the initial frame of acoustoelasticity
$dv/v_{P,app}$	Approximate velocity changes of longitudinal wave using the first diagonal element in the acoustoelastic modulus matrix in the initial frame
$dv/v_{P,exa}$	Exact velocity changes of longitudinal wave calculated using the first eigenvalue of the acoustoelastic modulus matrix in the initial frame
$dv/v_{S,app}$	Approximate velocity changes of transverse wave using the second diagonal element in the acoustoelastic modulus matrix in the initial frame
$dv/v_{S,exa}$	Exact velocity changes of transverse wave calculated using the second eigenvalue of the acoustoelastic modulus matrix in the initial frame
$dv/v_{unp,per}$	Velocity change spectrum retrieved using the wavelet cross-spectrum technique
e_i	Principal strain ($i \in \{1,2,3\}$)
$\text{erf}(\cdot)$	The error function
$e_{\alpha\beta}^{initial}, e_{\alpha\beta}$	Lagrangian finite strain tensors in the initial state ($\alpha, \beta \in \{1,2,3\}$)
$e_{\alpha\beta}^{final}$	Lagrangian finite strain tensors in the final state ($\alpha, \beta \in \{1,2,3\}$)
$e_{\alpha\beta}^{incremental}$	Lagrangian finite incremental strain tensors ($\alpha, \beta \in \{1,2,3\}$)
f	Hertz frequency
$f^{(c)}$	The centre frequency of the Gaussian filter when operating wavelet transform using the analytical Morlet wavelet
f_n	Frequency components (n is the number of sampling points in the time domain)
$f_{Nyquist}$	The Nyquist frequency
g	Total amount of grading intervals for coarse aggregates
k_M	Wavenumber of wave mode M (M should be either longitudinal waves or transverse waves)
\mathbf{k}_K	Incident wave vector (K should be either longitudinal waves or transverse waves)
\mathbf{k}_L	Scattered wave vector (L should be either longitudinal waves or transverse waves)
l^s	Scattering mean free path
l^*	Transport mean free path
l	Murnaghan first constant
m	Murnaghan second constant
n	Murnaghan third constant (dimension of diffusion equation in Chapter 4)

Notations

n_d	Dimension of the diffusion equation
n_i	Volume ratio of coarse aggregate within the grading interval i
n_s	Density of scatterers
p	Fraction of total cross-section that is blocked by the scatterers
p_M	Probability of wave mode M converting to other wave modes (M should be either longitudinal waves or transverse waves)
p_{KL}	Probability of incident wave mode K converting to scattered wave mode L (K and L should be either longitudinal waves or transverse waves)
r	Distance between the source and receiver
r'	Distance between the image source and receiver
r_a	Radius of a single scatterer
r_s	Characteristic radius of coarse aggregates
r_i	Characteristic radius of coarse aggregates within the grading interval i
s	Wavelet scale
s	Fitted slope on the square of relative velocity-stress relationship
t_c	Centre time of the time window when operating the stretching technique
$t_{\text{maximum energy}}$	Arrival time of the maximum energy
t_n	Samples in the time domain (n is the number of sampling points in the time domain)
u_I	Time-domain signal (I can refer to the unperturbed signal or signal after perturbation)
$\mathbf{u}^{\text{final}}, u_i^{\text{final}}$	Displacement from the natural to the final state ($i \in \{1,2,3\}$)
$\mathbf{u}^{\text{incremental}}, u_i^{\text{incremental}}$	Incremental displacement from the initial to the final state ($i \in \{1,2,3\}$)
$\mathbf{u}^{\text{initial}}, u_i^{\text{initial}}$	Displacement from the natural state to the initial state ($i \in \{1,2,3\}$)
v_{ij}^0	Velocity of the body wave propagating in the i -direction while polarizing in the j -direction without external load applied ($i, j \in \{1,2,3\}$)
$v_{ij,k}$	Velocity of the body wave propagating in the i -direction while polarizing in the j -direction measured at the k th stress level ($i, j \in \{1,2,3\}$)
$v_{ij}^{(\text{natural})}$	Velocity of the body wave propagating in the i -direction while polarizing in the j -direction in the natural frame ($i, j \in \{1,2,3\}$)
v_M	Velocity of wave mode M (M should be either longitudinal waves or transverse waves)
v^{initial}	Wave velocity in the initial frame
v^{natural}	Wave velocity in the natural frame
\mathbf{x}, x_i	initial coordinates ($i \in \{1,2,3\}$)
x_a	Mean distance between two adjacent total cross-sections with scatterers
x_M	Dimensionless frequency for wave mode M (M should be either longitudinal waves or transverse waves)

Greek upper case

I	Wavelet cross-coherency
ΔA_{eff}	Error in the effective acoustoelastic parameters
Δs	Error in the fitted slope on the square of relative velocity-stress relationship
Σ_M	Total scattering cross-section for wave mode M (M should be either longitudinal waves or transverse waves)
Σ_{KL}	Total scattering cross-section associated with mode transition from incident wave mode K to scattered wave mode L (K and L should be either longitudinal waves or transverse waves)
Σ_M'	Weighted total scattering cross-section for wave mode M (M should be either longitudinal waves or transverse waves)
Σ_{KL}'	Weighted total scattering cross-section associated with mode transition from incident wave mode K to scattered wave mode L (K and L should be either longitudinal waves or transverse waves)
Φ	Wavelet filter bank

Greek lower case

α	Dissipation
δ_{ij}	The Kronecker delta ($i, j \in \{1,2,3\}$)
$\delta t_{\text{unp,per}}$	Time difference spectrum obtained through the wavelet cross-spectrum technique
ε	Stretching factor when operating the stretching technique
ε_{max}	Stretching factor that maximizes the correlation coefficient
$\varsigma\{\cdot\}$	The smoothing operator for both time and frequency scales
θ	Rotation angle
λ	Lamé first constant
λ_i	Eigenvalue of the mode conversion matrix ($i \in \{1,2\}$)
μ	Lamé second constant
ν	Static Poisson ratio
ρ^0	Mass density in the natural state
ρ^{final}	Mass density in the final state
ρ^{initial}	Mass density in the initial state
σ	Stress matrix in the original stress state
σ'	Stress matrix in the stress state after coordinate rotation
σ_i	Principal stress ($i \in \{1,2,3\}$)
σ_{ij}	Stress tensor ($i, j \in \{1,2,3\}$)
$\sigma_{i,k}$	Principal stress in the i -direction at the stress level at which the measurement k is taken ($i \in \{1,2,3\}$)
σ_{KL}	Scattering cross-section associated with mode transition from incident wave mode K to scattered wave mode L (K and L should be either longitudinal waves or transverse waves)

Notations

$\sigma_{ij}^{(0)}$	Stress tensor in the original stress state ($i, j \in \{1,2,3\}$)
$\sigma_{ij}^{(r)}$	Stress tensor in the stress state after coordinate rotation ($i, j \in \{1,2,3\}$)
$\tau^{(a)}_P$	Characteristic dissipation time for longitudinal wave energy
$\tau^{(a)}_S$	Characteristic dissipation time for transverse wave energy
τ_{PS}	Characteristic equilibration time between P-S equilibration
τ_{SS}	Characteristic equilibration time between S-S equilibration
ϕ_I	Phase spectrum of time-domain signal u_I (I can refer to the unperturbed signal or signal after perturbation)
χ	Cosine of the scattering angle
ϕ_m	Volume fraction of matrix
ϕ_s	Volume fraction of scatterers
$\phi_{\text{unp,per}}$	Phase difference spectrum obtained through the wavelet cross-spectrum technique
ω	Angular frequency
ω_0	Constant used in designing the wavelet filter bank

Appendix A. Derivation of acoustoelastic moduli in the initial frame

The derivation details of elements in B -matrix is shown in this appendix. The elements in the B -matrix is given by:

$$B_{ijkl} := C_{jlmn} e_{mn}^{\text{initial}} \delta_{ik} + C_{ijkl} + C_{ijklmn} e_{mn}^{\text{initial}} + C_{mjkl} \frac{\partial u_i^{\text{initial}}}{\partial a_m} + C_{imkl} \frac{\partial u_j^{\text{initial}}}{\partial a_m} + C_{ijml} \frac{\partial u_k^{\text{initial}}}{\partial a_m} + C_{ijkml} \frac{\partial u_l^{\text{initial}}}{\partial a_m} . \quad (5.33)$$

In the following derivation, the linear part of the strain will be used to simplify the expressions:

$$e_{\alpha\beta}^{\text{initial}} = \frac{1}{2} \left(\frac{\partial u_\beta^{\text{initial}}}{\partial a_\alpha} + \frac{\partial u_\alpha^{\text{initial}}}{\partial a_\beta} \right) . \quad (A.1)$$

Additionally, the second- and third-order elastic coefficients will be represented using Voigt notation. Here are the derivation details:

$$\begin{aligned} B_{1111} &= C_{11mn} e_{mn}^{\text{initial}} \delta_{11} + C_{1111} + C_{1111mn} e_{mn}^{\text{initial}} \\ &\quad + C_{m111} \frac{\partial u_1^{\text{initial}}}{\partial a_m} + C_{1m11} \frac{\partial u_1^{\text{initial}}}{\partial a_m} + C_{11m1} \frac{\partial u_1^{\text{initial}}}{\partial a_m} + C_{111m} \frac{\partial u_1^{\text{initial}}}{\partial a_m} \\ &= C_{1111} + C_{1111} e_{11}^{\text{initial}} + C_{1122} e_{22}^{\text{initial}} + C_{1133} e_{33}^{\text{initial}} + C_{111111} e_{11}^{\text{initial}} + C_{111122} e_{22}^{\text{initial}} + C_{111133} e_{33}^{\text{initial}} \\ &\quad + C_{1111} \frac{\partial u_1^{\text{initial}}}{\partial a_1} + C_{1111} \frac{\partial u_1^{\text{initial}}}{\partial a_1} + C_{1111} \frac{\partial u_1^{\text{initial}}}{\partial a_1} + C_{1111} \frac{\partial u_1^{\text{initial}}}{\partial a_1} \\ &= C_{11} + (5C_{11} + C_{111}) e_{11}^{\text{initial}} + (C_{12} + C_{112}) e_{22}^{\text{initial}} + (C_{13} + C_{113}) e_{33}^{\text{initial}} . \end{aligned} \quad (A.2)$$

$$\begin{aligned} B_{2121} &= C_{11mn} e_{mn}^{\text{initial}} \delta_{22} + C_{2121} + C_{2121mn} e_{mn}^{\text{initial}} \\ &\quad + C_{m121} \frac{\partial u_2^{\text{initial}}}{\partial a_m} + C_{2m12} \frac{\partial u_1^{\text{initial}}}{\partial a_m} + C_{21m1} \frac{\partial u_2^{\text{initial}}}{\partial a_m} + C_{212m} \frac{\partial u_1^{\text{initial}}}{\partial a_m} \\ &= C_{2121} + C_{1111} e_{11}^{\text{initial}} + C_{1122} e_{22}^{\text{initial}} + C_{1133} e_{33}^{\text{initial}} + C_{212111} e_{11}^{\text{initial}} + C_{212122} e_{22}^{\text{initial}} + C_{212133} e_{33}^{\text{initial}} \\ &\quad + C_{2121} \frac{\partial u_2^{\text{initial}}}{\partial a_2} + C_{2121} \frac{\partial u_1^{\text{initial}}}{\partial a_1} + C_{2121} \frac{\partial u_2^{\text{initial}}}{\partial a_2} + C_{2121} \frac{\partial u_1^{\text{initial}}}{\partial a_1} \\ &= C_{66} + (C_{11} + 2C_{66} + C_{661}) e_{11}^{\text{initial}} + (C_{12} + 2C_{66} + C_{662}) e_{22}^{\text{initial}} + (C_{13} + C_{663}) e_{33}^{\text{initial}} . \end{aligned} \quad (A.3)$$

$$\begin{aligned} B_{3131} &= C_{11mn} e_{mn}^{\text{initial}} \delta_{33} + C_{3131} + C_{3131mn} e_{mn}^{\text{initial}} \\ &\quad + C_{m131} \frac{\partial u_3^{\text{initial}}}{\partial a_m} + C_{3m13} \frac{\partial u_1^{\text{initial}}}{\partial a_m} + C_{31m1} \frac{\partial u_3^{\text{initial}}}{\partial a_m} + C_{313m} \frac{\partial u_1^{\text{initial}}}{\partial a_m} \\ &= C_{3131} + C_{1111} e_{11}^{\text{initial}} + C_{1122} e_{22}^{\text{initial}} + C_{1133} e_{33}^{\text{initial}} + C_{313111} e_{11}^{\text{initial}} + C_{313122} e_{22}^{\text{initial}} + C_{313133} e_{33}^{\text{initial}} \\ &\quad + C_{3131} \frac{\partial u_3^{\text{initial}}}{\partial a_3} + C_{3131} \frac{\partial u_1^{\text{initial}}}{\partial a_1} + C_{3131} \frac{\partial u_3^{\text{initial}}}{\partial a_3} + C_{3131} \frac{\partial u_1^{\text{initial}}}{\partial a_1} \\ &= C_{55} + (C_{11} + 2C_{55} + C_{551}) e_{11}^{\text{initial}} + (C_{12} + C_{552}) e_{22}^{\text{initial}} + (C_{13} + 2C_{55} + C_{553}) e_{33}^{\text{initial}} . \end{aligned} \quad (A.4)$$

Appendix A

$$\begin{aligned}
B_{1121} &= C_{11mn} e_{mn}^{\text{initial}} \delta_{12} + C_{1121} + C_{1121mn} e_{mn}^{\text{initial}} \\
&\quad + C_{m121} \frac{\partial u_1^{\text{initial}}}{\partial a_m} + C_{1m21} \frac{\partial u_1^{\text{initial}}}{\partial a_m} + C_{11m1} \frac{\partial u_2^{\text{initial}}}{\partial a_m} + C_{112m} \frac{\partial u_1^{\text{initial}}}{\partial a_m} \\
&= C_{112112} e_{12}^{\text{initial}} + C_{112121} e_{21}^{\text{initial}} + C_{2121} \frac{\partial u_1^{\text{initial}}}{\partial a_2} + C_{1221} \frac{\partial u_1^{\text{initial}}}{\partial a_2} + C_{1111} \frac{\partial u_2^{\text{initial}}}{\partial a_1} + C_{1122} \frac{\partial u_1^{\text{initial}}}{\partial a_2} \\
&= (2C_{166} + 2C_{11}) e_{12}^{\text{initial}} = B_{2111} \quad .
\end{aligned} \tag{A.5}$$

$$\begin{aligned}
B_{1131} &= C_{11mn} e_{mn}^{\text{initial}} \delta_{13} + C_{1131} + C_{1131mn} e_{mn}^{\text{initial}} \\
&\quad + C_{m131} \frac{\partial u_1^{\text{initial}}}{\partial a_m} + C_{1m31} \frac{\partial u_1^{\text{initial}}}{\partial a_m} + C_{11m1} \frac{\partial u_3^{\text{initial}}}{\partial a_m} + C_{113m} \frac{\partial u_1^{\text{initial}}}{\partial a_m} \\
&= C_{113113} e_{13}^{\text{initial}} + C_{113131} e_{31}^{\text{initial}} + C_{3131} \frac{\partial u_1^{\text{initial}}}{\partial a_3} + C_{1331} \frac{\partial u_1^{\text{initial}}}{\partial a_3} + C_{1111} \frac{\partial u_3^{\text{initial}}}{\partial a_1} + C_{1133} \frac{\partial u_1^{\text{initial}}}{\partial a_3} \\
&= (2C_{155} + 2C_{11}) e_{13}^{\text{initial}} = B_{3111} \quad .
\end{aligned} \tag{A.6}$$

$$\begin{aligned}
B_{2131} &= C_{11mn} e_{mn}^{\text{initial}} \delta_{23} + C_{2131} + C_{2131mn} e_{mn}^{\text{initial}} \\
&\quad + C_{m131} \frac{\partial u_2^{\text{initial}}}{\partial a_m} + C_{2m31} \frac{\partial u_1^{\text{initial}}}{\partial a_m} + C_{21m1} \frac{\partial u_3^{\text{initial}}}{\partial a_m} + C_{213m} \frac{\partial u_1^{\text{initial}}}{\partial a_m} \\
&= C_{213123} e_{23}^{\text{initial}} + C_{213132} e_{32}^{\text{initial}} + C_{3131} \frac{\partial u_2^{\text{initial}}}{\partial a_3} + C_{2121} \frac{\partial u_3^{\text{initial}}}{\partial a_2} \\
&= (2C_{654} + 2C_{44}) e_{23}^{\text{initial}} = B_{3121} \quad .
\end{aligned} \tag{A.7}$$

Appendix B. Derivation of acoustoelastic moduli in the natural frame

The derivation details of elements in D -matrix is shown in this appendix. The elements in the D -matrix is given by:

$$D_{\xi\beta k\delta} := C_{\beta\delta\epsilon\eta} e_{\epsilon\eta}^{\text{initial}} \delta_{k\xi} + C_{\xi\beta k\delta} + C_{\xi\beta k\delta\epsilon\eta} e_{\epsilon\eta}^{\text{initial}} + C_{\alpha\beta k\delta} \frac{\partial u_{\xi}^{\text{initial}}}{\partial a_{\alpha}} + C_{\xi\beta\gamma\delta} \frac{\partial u_k^{\text{initial}}}{\partial a_{\gamma}}. \quad (5.43)$$

In the following derivation, the linear part of the strain will be used to simplify the expressions:

$$e_{\alpha\beta}^{\text{initial}} = \frac{1}{2} \left(\frac{\partial u_{\beta}^{\text{initial}}}{\partial a_{\alpha}} + \frac{\partial u_{\alpha}^{\text{initial}}}{\partial a_{\beta}} \right). \quad (B.1)$$

Additionally, the second- and third-order elastic coefficients will be represented using Voigt notation. Here are the derivation details:

$$\begin{aligned} D_{1111} &= C_{11\epsilon\eta} e_{\epsilon\eta}^{\text{initial}} \delta_{11} + C_{1111} + C_{1111\epsilon\eta} e_{\epsilon\eta}^{\text{initial}} + C_{\alpha 111} \frac{\partial u_1^{\text{initial}}}{\partial a_{\alpha}} + C_{11\gamma 1} \frac{\partial u_1^{\text{initial}}}{\partial a_{\gamma}} \\ &= C_{1111} + C_{1111} e_{11}^{\text{initial}} + C_{1122} e_{22}^{\text{initial}} + C_{1133} e_{33}^{\text{initial}} + C_{111111} e_{11}^{\text{initial}} + C_{111122} e_{22}^{\text{initial}} + C_{111133} e_{33}^{\text{initial}} \\ &\quad + C_{1111} \frac{\partial u_1^{\text{initial}}}{\partial a_1} + C_{1111} \frac{\partial u_1^{\text{initial}}}{\partial a_1} \\ &= C_{11} + (3C_{11} + C_{111}) e_{11}^{\text{initial}} + (C_{12} + C_{112}) e_{22}^{\text{initial}} + (C_{13} + C_{113}) e_{33}^{\text{initial}}. \end{aligned} \quad (B.2)$$

$$\begin{aligned} D_{2121} &= C_{11\epsilon\eta} e_{\epsilon\eta}^{\text{initial}} \delta_{22} + C_{2121} + C_{2121\epsilon\eta} e_{\epsilon\eta}^{\text{initial}} + C_{\alpha 121} \frac{\partial u_2^{\text{initial}}}{\partial a_{\alpha}} + C_{21\gamma 1} \frac{\partial u_2^{\text{initial}}}{\partial a_{\gamma}} \\ &= C_{2121} + C_{1111} e_{11}^{\text{initial}} + C_{1122} e_{22}^{\text{initial}} + C_{1133} e_{33}^{\text{initial}} + C_{212111} e_{11}^{\text{initial}} + C_{212122} e_{22}^{\text{initial}} + C_{212133} e_{33}^{\text{initial}} \\ &\quad + C_{2121} \frac{\partial u_2^{\text{initial}}}{\partial a_2} + C_{2121} \frac{\partial u_2^{\text{initial}}}{\partial a_2} \\ &= C_{66} + (C_{11} + C_{661}) e_{11}^{\text{initial}} + (C_{12} + 2C_{66} + C_{662}) e_{22}^{\text{initial}} + (C_{13} + C_{663}) e_{33}^{\text{initial}}. \end{aligned} \quad (B.3)$$

$$\begin{aligned} D_{3131} &= C_{11\epsilon\eta} e_{\epsilon\eta}^{\text{initial}} \delta_{33} + C_{3131} + C_{3131\epsilon\eta} e_{\epsilon\eta}^{\text{initial}} + C_{\alpha 131} \frac{\partial u_3^{\text{initial}}}{\partial a_{\alpha}} + C_{31\gamma 1} \frac{\partial u_3^{\text{initial}}}{\partial a_{\gamma}} \\ &= C_{3131} + C_{1111} e_{11}^{\text{initial}} + C_{1122} e_{22}^{\text{initial}} + C_{1133} e_{33}^{\text{initial}} + C_{313111} e_{11}^{\text{initial}} + C_{313122} e_{22}^{\text{initial}} + C_{313133} e_{33}^{\text{initial}} \\ &\quad + C_{3131} \frac{\partial u_3^{\text{initial}}}{\partial a_3} + C_{3131} \frac{\partial u_3^{\text{initial}}}{\partial a_3} \\ &= C_{55} + (C_{11} + C_{551}) e_{11}^{\text{initial}} + (C_{12} + C_{552}) e_{22}^{\text{initial}} + (C_{13} + 2C_{55} + C_{553}) e_{33}^{\text{initial}}. \end{aligned} \quad (B.4)$$

$$\begin{aligned} D_{1121} &= C_{11\epsilon\eta} e_{\epsilon\eta}^{\text{initial}} \delta_{12} + C_{1121} + C_{1121\epsilon\eta} e_{\epsilon\eta}^{\text{initial}} + C_{\alpha 121} \frac{\partial u_1^{\text{initial}}}{\partial a_{\alpha}} + C_{11\gamma 1} \frac{\partial u_2^{\text{initial}}}{\partial a_{\gamma}} \\ &= C_{112112} e_{12}^{\text{initial}} + C_{112121} e_{21}^{\text{initial}} + C_{2121} \frac{\partial u_1^{\text{initial}}}{\partial a_2} + C_{1111} \frac{\partial u_2^{\text{initial}}}{\partial a_1} \\ &= 2C_{166} e_{12}^{\text{initial}} + C_{66} \frac{\partial u_1^{\text{initial}}}{\partial a_2} + C_{11} \frac{\partial u_2^{\text{initial}}}{\partial a_1} = D_{2111}. \end{aligned} \quad (B.5)$$

Appendix B

$$\begin{aligned}
D_{1131} &= C_{11\varepsilon\eta} e_{\varepsilon\eta}^{\text{initial}} \delta_{13} + C_{1131} + C_{1131\varepsilon\eta} e_{\varepsilon\eta}^{\text{initial}} + C_{\alpha 131} \frac{\partial u_1^{\text{initial}}}{\partial a_\alpha} + C_{11\gamma 1} \frac{\partial u_3^{\text{initial}}}{\partial a_\gamma} \\
&= C_{113113} e_{13}^{\text{initial}} + C_{113131} e_{31}^{\text{initial}} + C_{3131} \frac{\partial u_1^{\text{initial}}}{\partial a_3} + C_{1111} \frac{\partial u_3^{\text{initial}}}{\partial a_1} \\
&= 2C_{155} e_{13}^{\text{initial}} + C_{55} \frac{\partial u_1^{\text{initial}}}{\partial a_3} + C_{11} \frac{\partial u_3^{\text{initial}}}{\partial a_1} = D_{3111} \quad .
\end{aligned} \tag{B.6}$$

$$\begin{aligned}
D_{2131} &= C_{11\varepsilon\eta} e_{\varepsilon\eta}^{\text{initial}} \delta_{23} + C_{2131} + C_{2131\varepsilon\eta} e_{\varepsilon\eta}^{\text{initial}} + C_{m131} \frac{\partial u_2^{\text{initial}}}{\partial a_m} + C_{21m1} \frac{\partial u_3^{\text{initial}}}{\partial a_m} \\
&= C_{213123} e_{23}^{\text{initial}} + C_{213132} e_{32}^{\text{initial}} + C_{3131} \frac{\partial u_2^{\text{initial}}}{\partial a_3} + C_{2121} \frac{\partial u_3^{\text{initial}}}{\partial a_2} \\
&= 2(C_{654} + C_{44}) e_{23}^{\text{initial}} = D_{3121} \quad .
\end{aligned} \tag{B.7}$$

Appendix C. Numerical results of velocity change using the material properties of other specimens reported by Nogueira and Rens (2019)

In this appendix, we will demonstrate the theoretical calculation of velocity changes for quasi-longitudinal and quasi-transverse waves. These velocity changes are computed using Equation (5.75), taking into account the material properties of concrete, including Lamé parameters and Murnaghan constants, which are reported by Nogueira and Rens (2019).

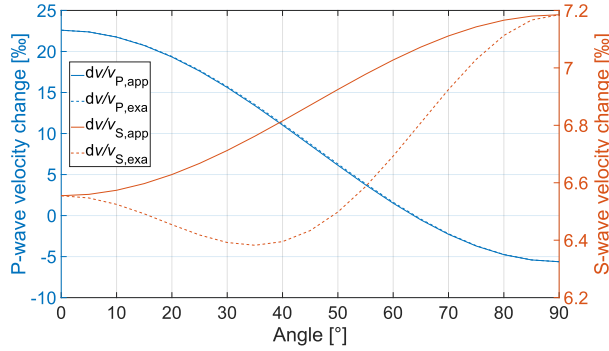


Figure C.1 Same as Figure 5.8 but calculated using the properties of Specimen 2.

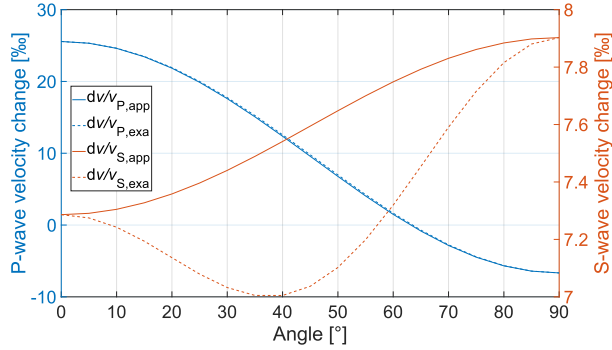


Figure C.2 Same as Figure 5.8 but calculated using the properties of Specimen 3.

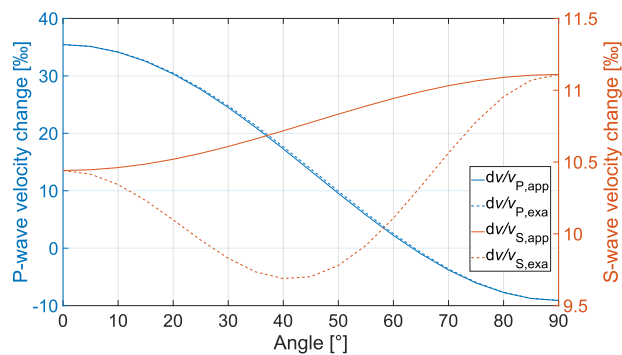


Figure C.3 Same as Figure 5.8 but calculated using the properties of Specimen 4.

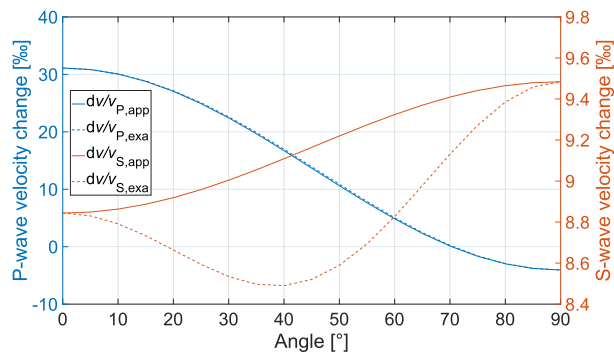


Figure C.4 Same as Figure 5.8 but calculated using the properties of Specimen 5.

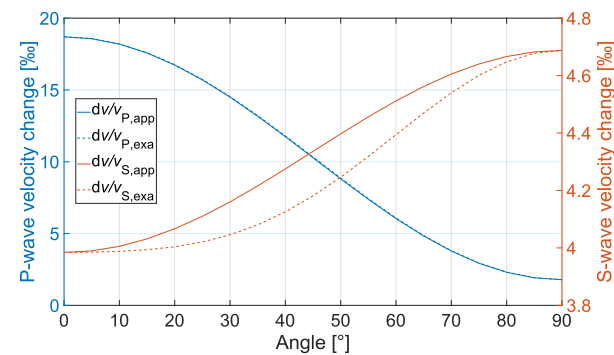


Figure C.5 Same as Figure 5.8 but calculated using the properties of Specimen 6.

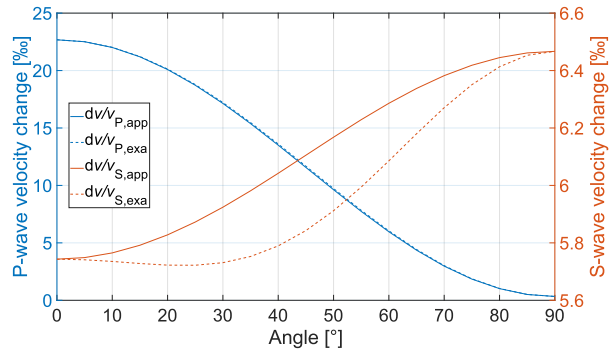


Figure C.6 Same as Figure 5.8 but calculated using the properties of Specimen 7.

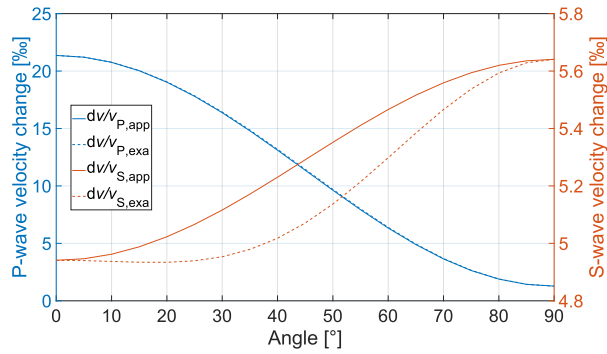


Figure C.7 Same as Figure 5.8 but calculated using the properties of Specimen 8.

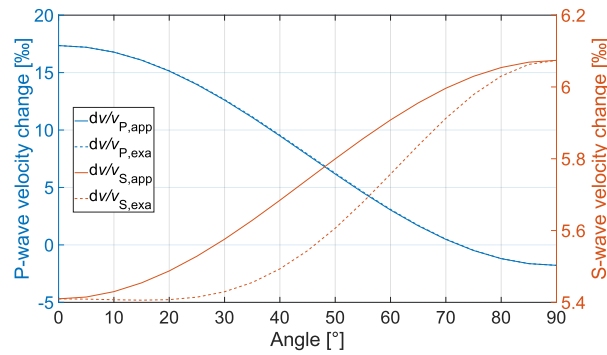


Figure C.8 Same as Figure 5.8 but calculated using the properties of Specimen 9.

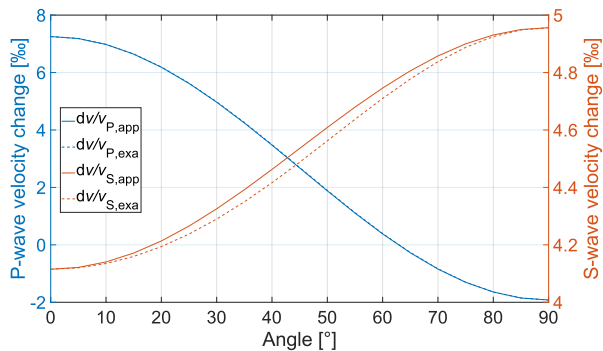


Figure C.9 Same as Figure 5.8 but calculated using the properties of Specimen 10.

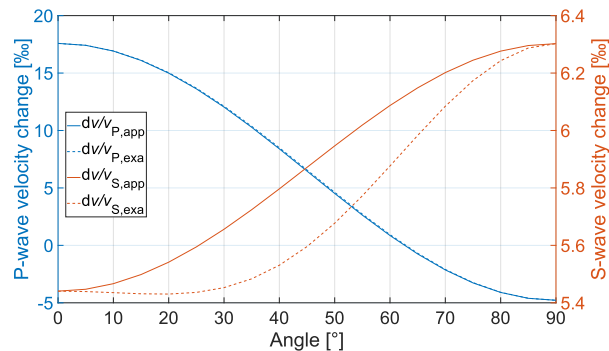


Figure C.10 Same as Figure 5.8 but calculated using the properties of Specimen 11.

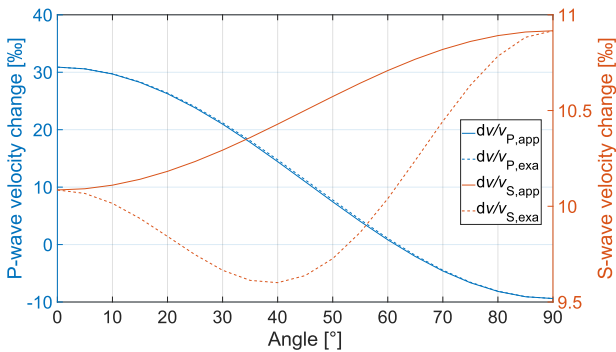


Figure C.11 Same as Figure 5.8 but calculated using the properties of Specimen 12.

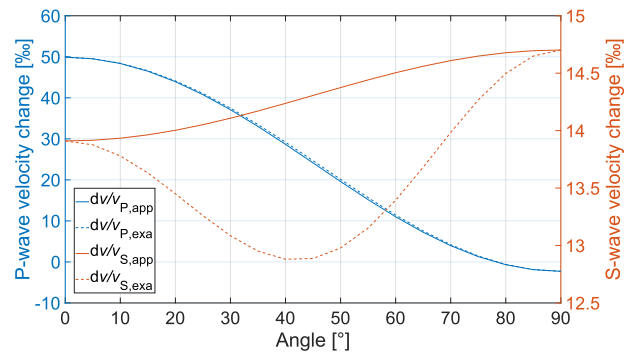


Figure C.12 Same as Figure 5.8 but calculated using the properties of Specimen 13.

Appendix D. Acoustoelastic parameters in isotropic materials when bulk waves propagating along one of the principal deformation directions

When the bulk wave propagates along one of the principal deformation directions, the relationship between bulk wave velocity and applied principal stresses in the natural frame-based acoustoelasticity can be expressed as:

$$v_{ij} = v_{ij}^0 \sqrt{1 + A_{ijkk} \sigma_k} \quad , \quad (\text{D.1})$$

where i and j represent wave propagation and polarization directions, respectively. The parameter σ_k denotes the principal stress in direction k , and the subscript k follows Einstein's summation convention. The acoustoelastic parameters in the natural frame A_{ijkk} are:

$$A_{1111} = A_{2222} = A_{3333} = \frac{3\lambda + 6\mu + 2l + 4m - \nu(2\lambda + 4l)}{E(\lambda + 2\mu)} \quad , \quad (\text{D.2a})$$

$$A_{2211} = A_{3311} = A_{1122} = \frac{\lambda + 2l - \nu(4\lambda + 6\mu + 4l + 4m)}{E(\lambda + 2\mu)} \quad , \quad (\text{D.2b})$$

$$A_{1211} = A_{1311} = A_{2122} = \frac{\lambda + 2\mu + m - \nu\left(2\lambda + 2\mu + 2m - \frac{n}{2}\right)}{E\mu} \quad , \quad (\text{D.2c})$$

$$A_{2111} = A_{3111} = A_{1211} = \frac{\lambda + 2\mu + m - \nu\left(2\lambda + 2\mu + 2m - \frac{n}{2}\right)}{E\mu} \quad , \quad (\text{D.2d})$$

$$A_{2311} = A_{3211} = A_{1233} = \frac{\lambda + m - \frac{n}{2} - \nu(2\lambda + 4\mu + 2m)}{E\mu} \quad . \quad (\text{D.2e})$$

Please note that A_{2111} is equal to A_{1211} in the natural frame.

In the initial frame, Equation (D.1) can be expressed into the following form by introducing the acoustoelastic parameters in the initial frame $A_{ijkk}^{(i)}$:

$$v_{ij} = v_{ij}^0 \sqrt{1 + A_{ijkk}^{(i)} \sigma_k} \quad , \quad (\text{D.3})$$

Where the acoustoelastic parameters in the initial frame are:

$$A_{1111}^{(i)} = A_{2222}^{(i)} = A_{3333}^{(i)} = \frac{5\lambda + 10\mu + 2l + 4m - \nu(2\lambda + 4l)}{E(\lambda + 2\mu)} \quad , \quad (\text{D.4a})$$

$$A_{2211}^{(i)} = A_{3311}^{(i)} = A_{1122}^{(i)} = \frac{\lambda + 2l - \nu(6\lambda + 10\mu + 4l + 4m)}{E(\lambda + 2\mu)} \quad , \quad (\text{D.4b})$$

Appendix D

$$A_{1211}^{(i)} = A_{1311}^{(i)} = A_{2122}^{(i)} = \frac{\lambda + 4\mu + m - \nu \left(2\lambda + 2\mu + 2m - \frac{n}{2} \right)}{E\mu}, \quad (\text{D.4c})$$

$$A_{2111}^{(i)} = A_{3111}^{(i)} = A_{1222}^{(i)} = \frac{\lambda + 2\mu + m - \nu \left(2\lambda + 4\mu + 2m - \frac{n}{2} \right)}{E\mu}, \quad (\text{D.4d})$$

$$A_{2311}^{(i)} = A_{3211}^{(i)} = A_{1233}^{(i)} = \frac{\lambda + m - \frac{n}{2} - \nu (2\lambda + 6\mu + 2m)}{E\mu}. \quad (\text{D.4e})$$

Appendix E. Correlation function of material property fluctuations in two phase material

For a two-phase material, the entirely occupied three-dimensional space can be divided into two nonintersecting phases: Phase 1, K_1 , and Phase 2, K_2 . The random field of Phase 1 is:

$$I_1(\mathbf{x}) = \begin{cases} 1, & \text{if } \mathbf{x} \in K_1 \\ 0, & \text{otherwise} \end{cases} . \quad (\text{E.1})$$

Obviously, the random field of Phase 2 is $I_2(\mathbf{x})=1-I_1(\mathbf{x})$. The ensemble average of $I_1(\mathbf{x})$ and $I_2(\mathbf{x})$ are equivalent to the volume fraction of scatterers ϕ_1 and matrix ϕ_2 :

$$\langle I_1(\mathbf{x}) \rangle = \phi_1 , \quad (\text{E.2})$$

$$\langle I_2(\mathbf{x}) \rangle = \phi_2 = 1 - \phi_1 . \quad (\text{E.3})$$

The material density, ρ , and Lamé parameters, λ and μ , are assumed to vary spatially and to have the form (Turner and Anugonda 2001):

$$\rho(\mathbf{x}) = \bar{\rho} [1 + \delta\rho(\mathbf{x})] , \quad (\text{E.4a})$$

$$\lambda(\mathbf{x}) = \bar{\lambda} [1 + \delta\lambda(\mathbf{x})] , \quad (\text{E.4b})$$

$$\mu(\mathbf{x}) = \bar{\mu} [1 + \delta\mu(\mathbf{x})] , \quad (\text{E.4c})$$

where terms with δ represent a dimensionless measure of the spatial fluctuations about the average. The over-bar terms are the average quantities. For example, the average density in the two-phase materials can be written as:

$$\begin{aligned} \bar{\rho} &= \langle I_1(\mathbf{x}) \rangle \rho_1 + \langle I_2(\mathbf{x}) \rangle \rho_2 \\ &= \phi_1 \rho_1 + \phi_2 \rho_2 , \end{aligned} \quad (\text{E.5})$$

where ρ_1 and ρ_2 are densities in Phase 1 and Phase 2, respectively. The average Lamé parameters are in the same form as the density shown in Equation (E.5). Then, the spatial density of the two-phase material can be represented using the densities of Phase 1 and Phase 2 in the following form:

$$\rho(\mathbf{x}) = I_1(\mathbf{x}) \rho_1 + I_2(\mathbf{x}) \rho_2 . \quad (\text{E.6})$$

The following derivation will use the auto-correlation of density as an example, but the entire process applies equally to the auto-correlations of Lamé parameters or the cross-correlations of Lamé parameters and densities. The auto-correlation of the density is given by (Turner and Anugonda 2001):

$$R_{\rho\rho}(\mathbf{x}-\mathbf{y}) = \langle \delta\rho(\mathbf{x}) \delta\rho(\mathbf{y}) \rangle . \quad (\text{E.7})$$

Appendix E

The average medium is assumed statistically isotropic and statistically homogeneous (Turner and Anugonda 2001). These assumptions imply that the correlation functions depend only on the magnitude of the difference of the two positions. Therefore, Equation (E.7) can be written as:

$$R_{\rho\rho}(\mathbf{x}-\mathbf{y}) = R_{\rho\rho}(|\mathbf{x}-\mathbf{y}|) = R_{\rho\rho}(r) = \langle \delta\rho(\mathbf{x})\delta\rho(\mathbf{y}) \rangle, \quad (\text{E.8})$$

where r represents the distance between two locations \mathbf{x} and \mathbf{y} . Based on Equation (E.4a), the spatial fluctuations of density can be written as:

$$\delta\rho(\mathbf{x}) = \frac{\rho(\mathbf{x}) - \bar{\rho}}{\bar{\rho}}. \quad (\text{E.9})$$

Substituting Equation (E.9) into Equation (E.8) gives:

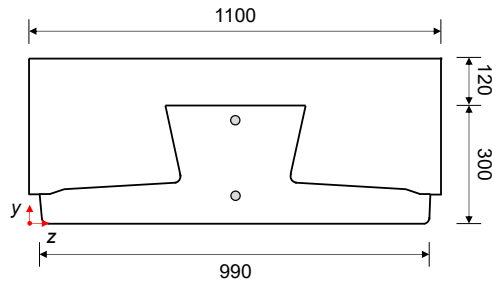
$$\begin{aligned} R_{\rho\rho}(r) &= \langle \delta\rho(\mathbf{x})\delta\rho(\mathbf{y}) \rangle \\ &= \frac{\langle [\rho(\mathbf{x}) - \bar{\rho}][\rho(\mathbf{y}) - \bar{\rho}] \rangle}{\bar{\rho}^2} \\ &= \frac{\langle [\rho_1 I_1(\mathbf{x}) + \rho_2 I_2(\mathbf{x}) - \bar{\rho}][\rho_1 I_1(\mathbf{y}) + \rho_2 I_2(\mathbf{y}) - \bar{\rho}] \rangle}{\bar{\rho}^2} \\ &= \frac{\langle \rho_1^2 I_1(\mathbf{x}) I_1(\mathbf{y}) + \rho_2^2 I_2(\mathbf{x}) I_2(\mathbf{y}) + \rho_1 \rho_2 [I_1(\mathbf{x}) I_2(\mathbf{y}) + I_1(\mathbf{y}) I_2(\mathbf{x})] \rangle}{\bar{\rho}^2} \\ &\quad - \frac{\bar{\rho} [\rho_1 \langle I_1(\mathbf{x}) \rangle + \rho_2 \langle I_2(\mathbf{x}) \rangle] + \bar{\rho} [\rho_1 \langle I_1(\mathbf{y}) \rangle + \rho_2 \langle I_2(\mathbf{y}) \rangle] - \bar{\rho}^2}{\bar{\rho}^2} \\ &= \frac{\langle \rho_1^2 I_1(\mathbf{x}) I_1(\mathbf{y}) + \rho_2^2 I_2(\mathbf{x}) I_2(\mathbf{y}) + \rho_1 \rho_2 [I_1(\mathbf{x}) I_2(\mathbf{y}) + I_1(\mathbf{y}) I_2(\mathbf{x})] - \bar{\rho}^2 \rangle}{\bar{\rho}^2} \\ &= \frac{\langle \rho_1^2 I_1(\mathbf{x}) I_1(\mathbf{y}) + \rho_2^2 [1 - I_1(\mathbf{x})][1 - I_1(\mathbf{y})] \rangle}{\bar{\rho}^2} \\ &\quad + \frac{\langle \rho_1 \rho_2 \{ I_1(\mathbf{x})[1 - I_1(\mathbf{y})] + I_1(\mathbf{y})[1 - I_1(\mathbf{x})] \} - \bar{\rho}^2 \rangle}{\bar{\rho}^2} \\ &= \frac{\langle (\rho_1 - \rho_2)^2 I_1(\mathbf{x}) I_1(\mathbf{y}) + \rho_2^2 + 2\rho_1 \rho_2 \phi_1 - 2\rho_2^2 \phi_1 - [\phi_1 \rho_1 + (1 - \phi_1) \rho_2]^2 \rangle}{\bar{\rho}^2} \\ &= \frac{(\rho_1 - \rho_2)^2}{\bar{\rho}^2} \langle I_1(\mathbf{x}) I_1(\mathbf{y}) - \phi_1^2 \rangle. \end{aligned} \quad (\text{E.10})$$

Equation (E.10) can be found at Eq. (8) in the article by Liu and Turner (Liu and Turner 2008). The general form of Equation (E.10) refers to Equation (6.30) in Section 6.4.1.1.

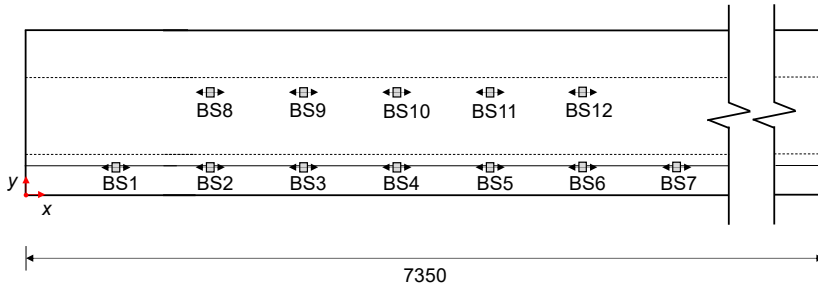
Appendix F. Geometries and sensor layouts in geopolymer members

This dissertation involves three geopolymer members. In Section 4.3.4, one beam was introduced and used to demonstrate the extraction of diffusive properties in a medium with planar boundaries. In this appendix, the remaining geopolymer members will be presented. These members are utilized in Chapter 6 to validate the total scattering cross-sections.

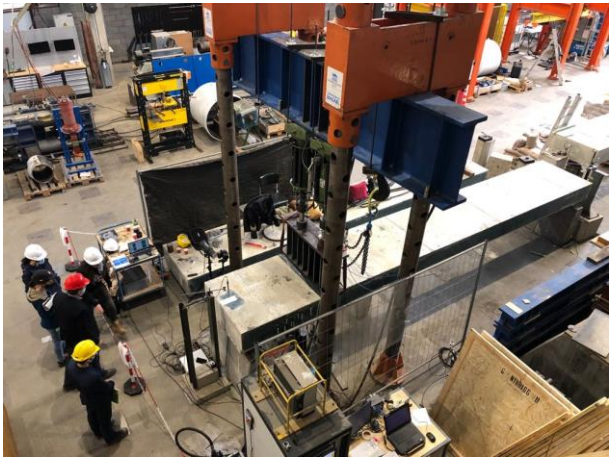
In the second beam, sensors are positioned close to the end of the beam. This specific beam encompasses 12 SAs labelled from BS1 to BS12, as shown in Figure F.1. Exact sensor locations are detailed in Table F.1. Similar to the first beam introduced in Section 4.3.4, measurements are performed between adjacent SAs within each row, resulting in a total of ten SA pairs. Therefore, a total of 20 measurements are carried out in this beam.



(a) Cross-sectional view.



(b) Front view.



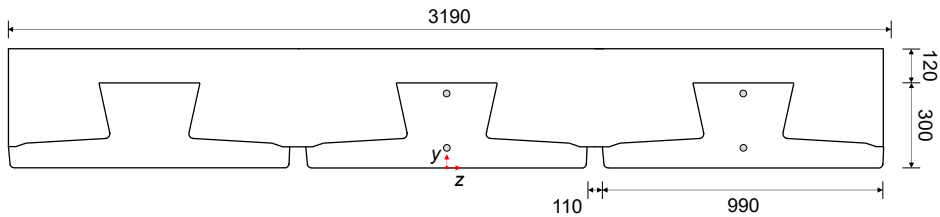
(c) Photo of the second beam.

Figure F.1 Dimensions and photo of the second geopolymer concrete beam and the sensor layout (unit: mm; black arrow on the SA indicates the polarization direction of the sensor).

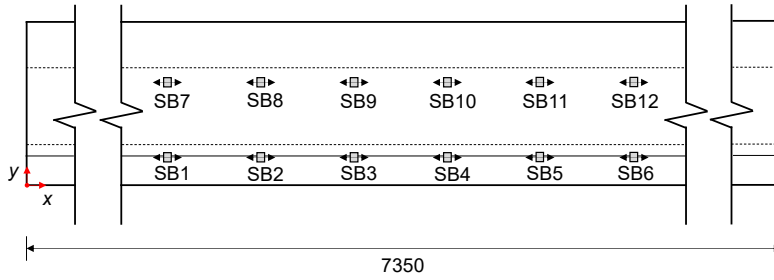
Table F.1 Locations of SAs relative to the coordinates in Figure F.1(a) and F.1(b).

Sensor	BS1	BS2	BS3	BS4	BS5	BS6	BS7	BS8	BS9	BS10	BS11	BS12
x [mm]	260	505	760	1015	1270	1550	1810	505	760	1015	1270	1550
y [mm]	77	77	77	77	77	77	77	277	277	277	277	277
z [mm]	550	550	550	550	550	550	550	550	550	550	550	550

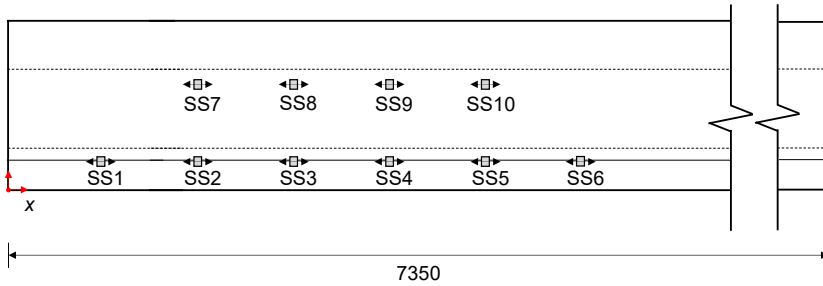
The third member is a geopolymer concrete slab. This slab comprises three beams, with sensors installed in both the middle beam and one of the edge beams. In the middle beam, there are 12 SAs labelled from SB1 to SB12, illustrated in Figure F.2. Sensor locations for the middle beam can be found in Table F.2. The edge beam incorporates sensors labelled from SS1 to SS10, with their respective locations detailed in Table F.3. Similar to the previous beam setups, measurements are performed between adjacent SAs within each row.



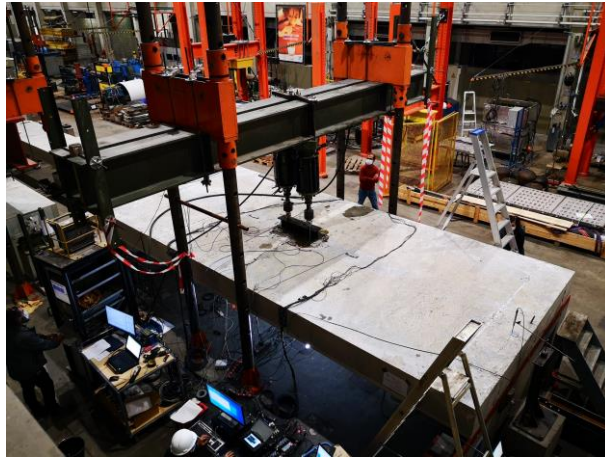
(a) Cross-sectional view of the slab.



(b) Front view of the middle beam.



(c) Front view of the edge beam.



(d) Photo of the geopolymer concrete slab.

Figure F.2 Dimensions and photo of the geopolymer concrete slab and the sensor layout (unit: mm; black arrow on the SA indicates the polarization direction of the sensor).

Table F.2 Locations of SAs in the middle beam relative to the coordinates in Figure F.2(a) and F.2(b).

Sensor	SB1	SB2	SB3	SB4	SB5	SB6	SB7	SB8	SB9	SB10	SB11	SB12
x [mm]	3030	3290	3550	3795	4050	4300	3030	3290	3550	3795	4050	4300
y [mm]	77	77	77	77	77	77	77	277	277	277	277	277
z [mm]	0	0	0	0	0	0	0	0	0	0	0	0

Appendix F

Table F.3 Locations of SAs in the edge beam relative to the coordinates in Figure F.2(a) and F.2(c).

Sensor	SS1	SS2	SS3	SS4	SS5	SS6	SS7	SS8	SS9	SS10
<i>x</i> [mm]	275	535	795	1015	1265	1535	535	795	1015	1265
<i>y</i> [mm]	77	77	77	77	77	77	277	277	277	277
<i>z</i> [mm]	1100	1100	1100	1100	1100	1100	1100	1100	1100	1100

Appendix G. Comparison between the performance of the exact response functions and approximate response functions using the material properties of other specimens reported by Nogueira and Rens (2019)

In this appendix, we will demonstrate the comparison of exact velocity change obtained from the exact response functions of Equation (5.52) and approximate velocity change obtained from approximate response functions of Equation (7.3) and (7.4) in 21 uniaxial stress cases ranging from 0 MPa to 10 MPa, taking into account the material properties of concrete, including Lamé parameters and Murnaghan constants, which are reported by Nogueira and Rens (2019).

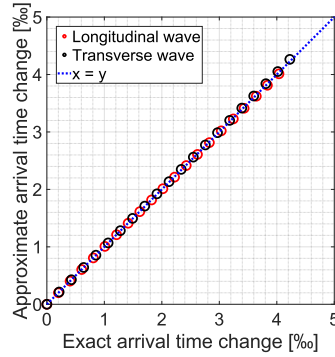


Figure G.1 Same as Figure 7.3 but calculated using the properties of Specimen 2.

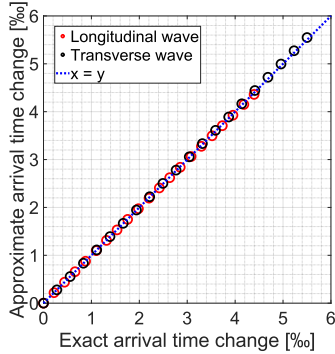


Figure G.2 Same as Figure 7.3 but calculated using the properties of Specimen 3.

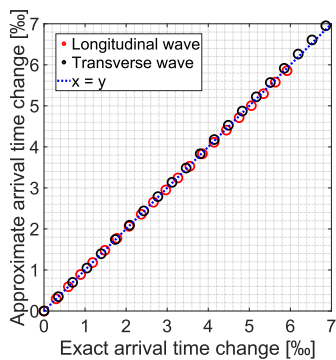


Figure G.3 Same as Figure 7.3 but calculated using the properties of Specimen 4.

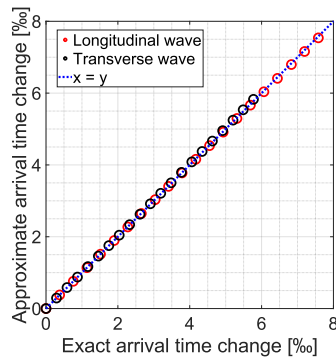


Figure G.4 Same as Figure 7.3 but calculated using the properties of Specimen 5.

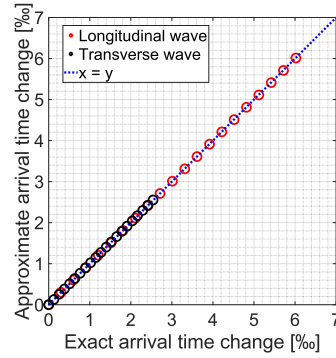


Figure G.5 Same as Figure 7.3 but calculated using the properties of Specimen 6.

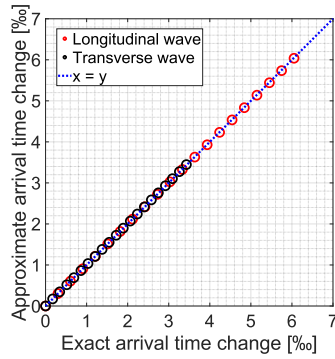


Figure G.6 Same as Figure 7.3 but calculated using the properties of Specimen 7.

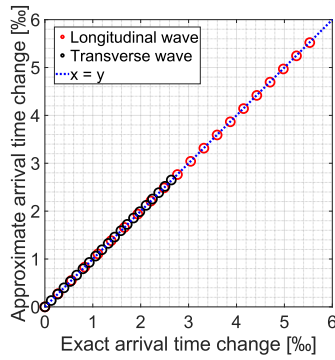


Figure G.7 Same as Figure 7.3 but calculated using the properties of Specimen 8.

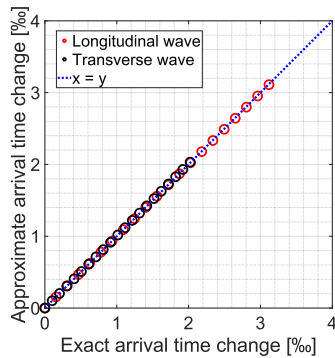


Figure G.8 Same as Figure 7.3 but calculated using the properties of Specimen 9.

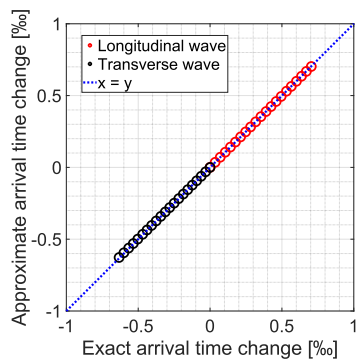


Figure G.9 Same as Figure 7.3 but calculated using the properties of Specimen 10.

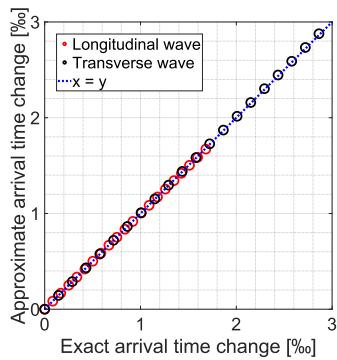


Figure G.10 Same as Figure 7.3 but calculated using the properties of Specimen 11.

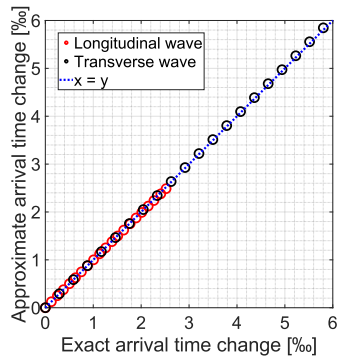


Figure G.11 Same as Figure 7.3 but calculated using the properties of Specimen 12.

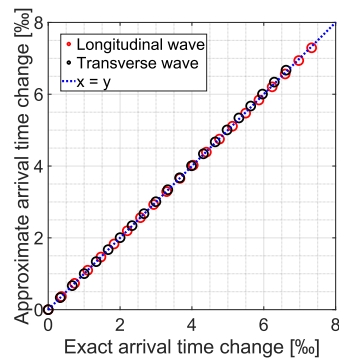


Figure G.12 Same as Figure 7.3 but calculated using the properties of Specimen 13.

REFERENCE

- Abbasi, Z. and D. Ozevin (2016). "Acoustoelastic coefficients in thick steel plates under normal and shear stresses." Experimental Mechanics **56**(9): 1559-1575.
- Abiza, Z., M. Destrade and R. W. Ogden (2012). "Large acoustoelastic effect." Wave Motion **49**(2): 364-374.
- Ahmed, S. and R. B. Thompson (1996). "Propagation of elastic waves in equiaxed stainless-steel polycrystals with aligned [001] axes." Journal of the Acoustical Society of America **99**(4): 2086-2096.
- Ahn, E., M. Shin and J. S. Popovics (2022). "Air-coupled ultrasonic diffuse-wave techniques to evaluate distributed cracking damage in concrete." Ultrasonics **125**: 106800.
- Ahn, E., M. Shin, J. S. Popovics and R. L. Weaver (2019). "Effectiveness of diffuse ultrasound for evaluation of micro-cracking damage in concrete." Cement and Concrete Research **124**: 105862.
- Aki, K. (1969). "Analysis of the seismic coda of local earthquakes as scattered waves." Journal of Geophysical Research **74**(2): 615-631.
- Aki, K. and B. Chouet (1975). "Origin of coda waves: source, attenuation, and scattering effects." Journal of Geophysical Research **80**(23): 3322-3342.
- Aki, K. and P. G. Richards (2002). Quantitative seismology.
- Alderliesten, M. (2005). "Mean particle diameters. Part V: Theoretical derivation of the proper type of mean particle diameter describing a product or process property." Particle & Particle Systems Characterization **22**(4): 233-245.
- Allen, J. B. and D. A. Berkley (1979). "Image method for efficiently simulating small-room acoustics." Journal of the Acoustical Society of America **65**(4): 943-950.
- Anderson, P. W. (1985). "The question of classical localization A theory of white paint?" Philosophical Magazine B **52**(3): 505-509.
- Anugonda, P., J. S. Wiehn and J. A. Turner (2001). "Diffusion of ultrasound in concrete." Ultrasonics **39**(6): 429-435.
- ASTM (2017). "ASTM C469-02: Standard test method for static modulus of elasticity and Poisson's ratio of concrete in compression." ASTM International.
- Baniassadi, M., H. Garmestani, D. S. Li, S. Ahzi, M. Khaleel and X. Sun (2011). "Three-phase solid oxide fuel cell anode microstructure realization using two-point correlation functions." Acta Materialia **59**(1): 30-43.

Reference

- Barrias, A., J. R. Casas and S. Villalba (2016). "A Review of distributed optical fiber sensors for civil engineering applications." Sensors **16**(5): 748.
- Becker, J., L. J. Jacobs and J. M. Qu (2003). "Characterization of cement-based materials using diffuse ultrasound." Journal of Engineering Mechanics **129**(12): 1478-1484.
- Bing, L., R. Park and H. Tanaka (2001). "Stress-strain behavior of high-strength concrete confined by ultra-high-and normal-strength transverse reinforcements." ACI Structural journal **98**(3): 395-406.
- Biot, M. A. (1940). "The influence of initial stress on elastic waves." Journal of Applied Physics **11**(8): 522-530.
- Birch, F. (1938). "The effect of pressure upon the elastic parameters of isotropic solids, according to Murnaghan's theory of finite strain." Journal of Applied Physics **9**(4): 279-288.
- Biswal, S. and A. Ramaswamy (2016). "Measurement of existing prestressing force in concrete structures through an embedded vibrating beam strain gauge." Measurement **83**: 10-19.
- Bobrenko, V. M., A. N. Kutsenko and V. P. Lesnikov (1990). "Elastic-waves in a solid subjected to shear deformation." Soviet Applied Mechanics **26**(1): 67-71.
- Bond, L. J., W. F. Kepler and D. M. Frangopol (2000). "Improved assessment of mass concrete dams using acoustic travel time tomography. Part I—theory." Construction and Building Materials **14**(3): 133-146.
- Boyd, R. W., A. L. Gaeta and E. Giese (2008). Nonlinear Optics. Springer Handbook of Atomic, Molecular, and Optical Physics, Springer: 1097-1110.
- Brillouin, L. (1925). "Sur les tensions de radiation." Ann. Phys. **4**: 528-586.
- Brunet, T., X. Jia and P. Mills (2008). "Mechanisms for acoustic absorption in dry and weakly wet granular media." Physical Review Letters **101**(13): 138001.
- Busch, K., C. M. Soukoulis and E. N. Economou (1994). "Transport and scattering mean free paths of classical waves." Physical Review B **50**(1): 93-98.
- Calvet, M. and L. Margerin (2012). "Velocity and attenuation of scalar and elastic waves in random media: a spectral function approach." Journal of the Acoustical Society of America **131**(3): 1843-1862.
- Calvet, M. and L. Margerin (2018). "Erratum: Velocity and attenuation of scalar and elastic waves in random media: A spectral function approach [J. Acoust. Soc. Am.

- 131(3), 1843-1862 (2012)]." Journal of the Acoustical Society of America **143**(1): 139.
- Cantrell, J. H. and K. Salama (1991). "Acoustoelastic characterization of materials." International Materials Reviews **36**(4): 125-145.
- Carette, J. and S. Staquet (2016). "Monitoring the setting process of eco-binders by ultrasonic P-wave and S-wave transmission velocity measurement: Mortar vs concrete." Construction and Building Materials **110**: 32-41.
- Cauchy, A.-L. (1829). "Sur l'équilibre et le mouvement intérieur des corps considérés comme des masses continues." Ex. de Math **4**: 293-319.
- Chandrasekhar, S. (2013). Radiative Transfer, Courier Corporation.
- Chen, F. (1984). Introduction to Plasma Physics and Controlled Fusion, Springer.
- Clauss, F., N. Epple, M. A. Ahrens, E. Niederleithinger and P. Mark (2020). "Comparison of experimentally determined two-dimensional strain fields and mapped ultrasonic data processed by coda wave interferometry." Sensors **20**(14): 4023.
- Clotfelter, W. and E. Risch (1974). "Ultrasonic measurement of stress in railroad wheels and in long lengths of welded rail." No. NASA-TM-X-64863. 1974.
- Connor, P. and R. W. Ogden (1995). "The effect of shear on the propagation of elastic surface-waves." International Journal of Engineering Science **33**(7): 973-982.
- Connor, P. and R. W. Ogden (1996). "The influence of shear strain and hydrostatic stress on stability and elastic waves in a layer." International Journal of Engineering Science **34**(4): 375-397.
- Crank, J. (1979). The Mathematics of Diffusion, Oxford University Press.
- Crecraft, D. (1967). "The measurement of applied and residual stresses in metals using ultrasonic waves." Journal of Sound and Vibration **5**(1): 173-192.
- Crecraft, D. I. (1962). "Ultrasonic wave velocities in stressed Nickel steel." Nature **195**(4847): 1193-&.
- Curtis, A., P. Gerstoft, H. Sato, R. Snieder and K. Wapenaar (2006). "Seismic interferometry—turning noise into signal." The Leading Edge **25**(9): 1082-1092.
- De Abajo, F. G., M. Van Hove and C. Fadley (2001). "Multiple scattering of electrons in solids and molecules: A cluster-model approach." Physical Review B **63**(7): 075404.

Reference

- de Hoop, A. T. (2001). *Handbook of Radiation and Scattering of Waves: Acoustic Waves in Fluids, Elastic Waves in Solids, Electromagnetic Waves*, Acoustical Society of America.
- Debye, P., H. Anderson Jr and H. Brumberger (1957). "Scattering by an inhomogeneous solid. II. The correlation function and its application." Journal of Applied Physics **28**(6): 679-683.
- Debye, P. and A. M. Bueche (1949). "Scattering by an inhomogeneous solid." Journal of Applied Physics **20**(6): 518-525.
- Degtyar, A. and S. Rokhlin (1995). "Absolute stress determination in orthotropic materials from angular dependences of ultrasonic velocities." Journal of Applied Physics **78**(3): 1547-1556.
- Derode, A., A. Tourin and M. Fink (2001). "Random multiple scattering of ultrasound. I. Coherent and ballistic waves." Physical Review E **64**(3 Pt 2): 036605.
- Deroo, F., J. Y. Kim, J. Qu, K. Sabra and L. J. Jacobs (2010). "Detection of damage in concrete using diffuse ultrasound." Journal of the Acoustical Society of America **127**(6): 3315-3318.
- Destrade, M. and R. W. Ogden (2005). "Surface waves in a stretched and sheared incompressible elastic material." International Journal of Non-Linear Mechanics **40**(2-3): 241-253.
- Diewald, F., N. Epple, T. Kraenkel, C. Gehlen and E. Niederleithinger (2022). "Impact of external mechanical loads on coda waves in concrete." Materials **15**(16).
- Dines, K. A. and R. J. Lytle (1979). "Computerized geophysical tomography." Proceedings of the IEEE **67**(7): 1065-1073.
- Dowaikh, M. A. (1990). Surface and interfacial waves and deformations in pre-stressed elastic materials, PhD dissertation, University of Glasgow.
- Duquennoy, M., M. Ouaftouh, M. Ourak and W. J. Xu (1999). "Influence of natural and initial acoustoelastic coefficients on residual stress evaluation: Theory and experiment." Journal of Applied Physics **86**(5): 2490-2498.
- Egle, D. and D. Bray (1976). "Measurement of acoustoelastic and third-order elastic constants for rail steel." Journal of the Acoustical Society of America **60**(3): 741-744.
- Egle, D. M. (1981). "Diffuse wave fields in solid media." Journal of the Acoustical Society of America **70**(2): 476-480.

- Elaloufi, R., W. Carminati and J. J. Greffet (2002). "Time-dependent transport through scattering media: from radiative transfer to diffusion." Journal of Optics a-Pure and Applied Optics **4**(5): S103-S108.
- Eurocode 2 (2005). "Eurocode 2: design of concrete structures-part 1–1: general rules and rules for buildings." British Standard Institution, London.
- Farge, M. (1992). "Wavelet transforms and their applications to turbulence." Annual Review of Fluid Mechanics **24**(1): 395-457.
- Fayyadh, M. M. and H. Abdul Razak (2011). "Detection of damage location using mode shape deviation: Numerical study." International Journal of Physical Sciences **6**(24): 5688-5698.
- Fehler, M., M. Hoshiaba, H. Sato and K. Obara (1992). "Separation of scattering and intrinsic attenuation for the Kanto-Tokai region, Japan, using measurements of S-wave energy versus hypocentral distance." Geophysical Journal International **108**(3): 787-800.
- Frechet, J., L. Martel, L. Nikolla and G. Poupinet (1989). "Application of the cross-spectral moving-window technique (CSMWT) to the seismic monitoring of forced fluid migration in a rock mass." International Journal of Rock Mechanics and Mining Sciences & Geomechanics Abstracts **26**(3-4): 221-233.
- Freund, I. I., M. Kaveh and M. Rosenbluh (1988). "Dynamic multiple scattering: Ballistic photons and the breakdown of the photon-diffusion approximation." Physical Review Letters **60**(12): 1130-1133.
- Frisch, H. (1965). "Statistics of random media." Transactions of the Society of Rheology **9**(1): 293-312.
- Gabor, D. (1947). "Acoustical quanta and the theory of hearing." Nature **159**(4044): 591-594.
- Gandhi, N. (2010). Determination of dispersion curves for acoustoelastic lamb wave propagation, Master Thesis, Georgia Institute of Technology.
- Ganghoffer, J.-F. (2018). Constitutive models of soft and hard living tissues. Multiscale Biomechanics, Elsevier: 149-186.
- Giurgiutiu, V., J. Bao and W. Zhao (2001). Active sensor wave propagation health monitoring of beam and plate structures. Smart Structures and Materials 2001: Smart Structures and Integrated Systems, International Society for Optics and Photonics.

Reference

- Glangeaud, F. (1981). "Signal-processing for magnetic pulsations." Journal of Atmospheric and Terrestrial Physics **43**(9): 981-+.
- Golewski, G. L. (2023). "The phenomenon of cracking in cement concretes and reinforced concrete structures: the mechanism of cracks formation, causes of their initiation, types and places of occurrence, and methods of detection—a review." Buildings **13**(3): 765.
- Grabke, S., F. Clauss, K. U. Bletzinger, M. A. Ahrens, P. Mark and R. Wuchner (2021). "Damage detection at a reinforced concrete specimen with coda wave interferometry." Materials **14**(17): 15.
- Green, A. E. (1963). "A note on wave propagation in initially deformed bodies." Journal of the Mechanics and Physics of Solids **11**(2): 119-126.
- Grêt, A., R. Snieder and U. Özbay (2006). "Monitoring in situ stress changes in a mining environment with coda wave interferometry." Geophysical Journal International **167**(2): 504-508.
- Guz, A. N. and F. G. Makhort (2000). "The physical fundamentals of the ultrasonic non-destructive stress analysis of solids." International Applied Mechanics **36**(9): 1119-1149.
- Guz, A. N. (2002). "Elastic waves in bodies with initial (residual) stresses." International Applied Mechanics **38**(1): 23-59.
- Habets, E. A. (2006). "Room impulse response generator." Technische Universiteit Eindhoven, Tech. Rep **2**(2.4): 1.
- Hasegawa, M. and Y. Sasaki (2004). "Acoustoelastic birefringence effect in wood I: effect of applied stresses on the velocities of ultrasonic shear waves propagating transversely to the stress direction." Journal of Wood Science **50**(1): 47-52.
- Hasegawa, M. and Y. Sasaki (2004). "Acoustoelastic birefringence effect in wood II: influence of texture anisotropy on the polarization direction of shear wave in wood." Journal of Wood Science **50**(2): 101-107.
- Hasegawa, M. and Y. Sasaki (2004). "Acoustoelastic birefringence effect in wood III: ultrasonic stress determination of wood by acoustoelastic birefringence method." Journal of Wood Science **50**(2): 108-114.
- Hasegawa, M., Y. Sasaki and T. Iwata (2000). "Acoustoelastic effect of wood III: effect of applied stresses on the velocity of ultrasonic waves propagating normal to the direction of the applied stress." Journal of Wood Science **46**(2): 102-108.

- Hayes, M. (1963). "Wave propagation and uniqueness in prestressed elastic solids." Proceedings of the Royal Society of London Series A-Mathematical and Physical Sciences **274**(1356): 500-+.
- Hayes, M. and R. S. Rivlin (1961). "Propagation of a plane wave in an isotropic elastic material subjected to pure homogeneous deformation." Archive for Rational Mechanics and Analysis **8**(1): 15-22.
- He, Y., L. Song, K. Xue, S. Liu, H. Li, W. Yang and J. Huang (2022). "Ultrasonic coda wave experiment and simulation of concrete damage process under uniaxial compression." Buildings **12**(5).
- Heller, G., L. Margerin, O. Sèbe, J. Mayor and M. Calvet (2022). "Revisiting multiple-scattering principles in a crustal waveguide: equipartition, depolarization and coda normalization." Pure and Applied Geophysics **179**(6-7): 2031-2065.
- Hennino, R., N. Tregoures, N. M. Shapiro, L. Margerin, M. Campillo, B. A. van Tiggelen and R. L. Weaver (2001). "Observation of equipartition of seismic waves." Physical Review Letters **86**(15): 3447-3450.
- Hilloulin, B., J. B. Legland, E. Lys, O. Abraham, A. Loukili, F. Grondin, O. Durand and V. Tournat (2016). "Monitoring of autogenous crack healing in cementitious materials by the nonlinear modulation of ultrasonic coda waves, 3D microscopy and X-ray microtomography." Construction and Building Materials **123**: 143-152.
- Hinkley, D. V. (1971). "Inference about the change-point from cumulative sum tests." Biometrika **58**(3): 509-523.
- Hirao, M., H. Fukuoka and K. Hori (1981). "Acoustoelastic effect of Rayleigh surface-wave in isotropic material." Journal of Applied Mechanics-Transactions of the ASME **48**(1): 119-124.
- Hirao, M. and H. Ogi (2017). Acoustoelastic stress measurements. Electromagnetic Acoustic Transducers: Noncontacting Ultrasonic Measurements Using EMATs, 2nd Edition. Tokyo, Springer Japan: 233-269.
- Hsu, N. N. (1974). "Acoustical birefringence and the use of ultrasonic waves for experimental stress analysis." Experimental Mechanics **14**(5): 169-176.
- Hu, H., D. Li, L. Wang, R. Chen and X. Xu (2021). "An improved ultrasonic coda wave method for concrete behavior monitoring under various loading conditions." Ultrasonics **116**: 106498.
- Hughes, D. S. and J. Kelly (1953). "Second-order elastic deformation of solids." Physical Review **92**(5): 1145.

Reference

- Imanishi, E., M. Sasabe and Y. Iwashimizu (1982). "Experimental-study on acoustical birefringence in stressed and slightly anisotropic materials." Journal of the Acoustical Society of America **71**(3): 565-572.
- In, C. W., K. Arne, J. Y. Kim, K. E. Kurtis and L. J. Jacobs (2017). "Estimation of crack depth in concrete using diffuse ultrasound: validation in cracked concrete beams." Journal of Nondestructive Evaluation **36**(1): 1-9.
- In, C. W., R. B. Holland, J. Y. Kim, K. E. Kurtis, L. F. Kahn and L. J. Jacobs (2013). "Monitoring and evaluation of self-healing in concrete using diffuse ultrasound." NDT & E International **57**: 36-44.
- Ioffe, A. and A. Regel (1960). Non-crystalline, amorphous, and liquid electronic semi-conductors. Progress in Semiconductors: 237-291.
- Iwashimizu, Y. and K. Kubomura (1973). "Stress-induced rotation of polarization directions of elastic waves in slightly anisotropic materials." International Journal of Solids and Structures **9**(1): 99-114.
- Janssen, M. (1994). "Acoustoelastic stress evaluation in metal plate using absolute shear and longitudinal time-of-flight data." PhD dissertation, Delft University of Technology.
- Jia, X. (2004). "Codalike multiple scattering of elastic waves in dense granular media." Physical Review Letters **93**(15): 154303.
- Jiang, H., H. Zhan, Z. Ma and R. Jiang (2020). "Comparative study of three-dimensional stress and crack imaging in concrete by application of inverse algorithms to coda wave measurements." Sensors **20**(17): 4899.
- Jiang, H., H. Zhan, J. Zhang and R. Jiang (2019). "Diffusion coefficient estimation and its application in interior change evaluation of full-size reinforced concrete structures." Journal of Materials in Civil Engineering **31**(3): 04018398.
- Jiang, H., H. Zhan, J. Zhang, R. Jiang, C. Zhuang and P. Fan (2021). "Detecting stress changes and damage in full-size concrete T-beam and slab with ultrasonic coda waves." Journal of Structural Engineering **147**(9): 11.
- Jiang, H., J. Zhang and R. Jiang (2017). "Stress evaluation for rocks and structural concrete members through ultrasonic wave analysis: Review." Journal of Materials in Civil Engineering **29**(10): 10.
- Johnson, G. C. (1981). "Acoustoelastic theory for elastic-plastic materials." Journal of the Acoustical Society of America **70**(2): 591-595.

- Kak, A. C. and M. Slaney (2001). "Principles of computerized tomographic imaging", Society for Industrial and Applied Mathematics.
- Karaikos, G., A. Deraemaeker, D. G. Aggelis and D. Van Hemelrijck (2015). "Monitoring of concrete structures using the ultrasonic pulse velocity method." Smart Materials and Structures **24**(11): 18.
- Keinde, D., S. Kamali-Bernard, F. Bernard and I. Cisse (2014). "Effect of the interfacial transition zone and the nature of the matrix-aggregate interface on the overall elastic and inelastic behaviour of concrete under compression: a 3D numerical study." European Journal of Environmental and Civil Engineering **18**(10): 1167-1176.
- Kepler, W. F., L. J. Bond and D. M. Frangopol (2000). "Improved assessment of mass concrete dams using acoustic travel time tomography. Part II—application." Construction and Building Materials **14**(3): 147-156.
- King, R. and C. Fortunko (1983). "Determination of in-plane residual stress states in plates using horizontally polarized shear waves." Journal of Applied Physics **54**(6): 3027-3035.
- Kong, Q. (2015). Innovation in Piezoceramic Based Structural Health Monitoring. PhD dissertation, University of Houston.
- Königsberger, M., M. Hlobil, B. Delsaute, S. Staquet, C. Hellmich and B. Pichler (2018). "Hydrate failure in ITZ governs concrete strength: A micro-to-macro validated engineering mechanics model." Cement and Concrete Research **103**: 77-94.
- Kop, R. H. J., P. deVries, R. Sprik and A. Lagendijk (1997). "Observation of anomalous transport of strongly multiple scattered light in thin disordered slabs." Physical Review Letters **79**(22): 4369-4372.
- Koutsourelakis, P. S. and G. Deodatis (2005). "Simulation of binary random fields with applications to two-phase random media." Journal of Engineering Mechanics **131**(4): 397-412.
- Kurz, J. H., C. U. Grosse and H. W. Reinhardt (2005). "Strategies for reliable automatic onset time picking of acoustic emissions and of ultrasound signals in concrete." Ultrasonics **43**(7): 538-546.
- Lai, Y., S. K. Cheung and Z. Zhang (2005). "Wave transport in two-dimensional random media: the ballistic to diffusive transition and the extrapolation length." Physical Review E **72**(3 Pt 2): 036606.
- Landau, L. D., E. M. Lifshitz, A. M. Kosevich and L. P. Pitaevskii (1986). Theory of Elasticity: Volume 7, Elsevier.

Reference

- Larose, E. and S. Hall (2009). "Monitoring stress related velocity variation in concrete with a 2×10^{-5} relative resolution using diffuse ultrasound." Journal of the Acoustical Society of America **125**(4): 1853-1856.
- Larose, E., T. Planes, V. Rossetto and L. Margerin (2010). "Locating a small change in a multiple scattering environment." Applied Physics Letters **96**(20): 204101.
- Li, G., Y. Zhao and S. Pang (1999). "Four-phase sphere modeling of effective bulk modulus of concrete." Cement and Concrete Research **29**(6): 839-845.
- Li, Y., Y. Li and R. Wang (2019). "Quantitative evaluation of elastic modulus of concrete with nanoidentation and homogenization method." Construction and Building Materials **212**: 295-303.
- Lifshits, I. and G. Parkhomovski (1950). "On the theory of ultrasonic wave propagation in polycrystals." Zh. Eksp. Teor. Fiz **20**(1): 175-182.
- Lillamand, I., J. F. Chaix, M. A. Ploix and V. Garnier (2010). "Acoustoelastic effect in concrete material under uni-axial compressive loading." NDT & E International **43**(8): 655-660.
- Liu, D. and J. A. Turner (2008). "Influence of spatial correlation function on attenuation of ultrasonic waves in two-phase materials." Journal of the Acoustical Society of America **123**(5): 2570-2576.
- Liu, P. (1994). Wavelet spectrum analysis and ocean wind waves. Wavelet Analysis and Its Applications, Elsevier. **4**: 151-166.
- Lobkis, O. I. and R. L. Weaver (2003). "Coda-wave interferometry in finite solids: recovery of P-to-S conversion rates in an elastodynamic billiard." Physical Review Letters **90**(25 Pt 1): 254302.
- Love, A. E. H. (1911). Some Problems of Geodynamics: Being an Essay to which the Adams Prize in the University of Cambridge was Adjudged in 1911, University Press.
- Love, A. E. H. (2013). A Treatise on the Mathematical Theory of Elasticity, Cambridge University Press.
- Lutz, M. P., P. J. M. Monteiro and R. W. Zimmerman (1997). "Inhomogeneous interfacial transition zone model for the bulk modulus of mortar." Cement and Concrete Research **27**(7): 1113-1122.
- Maeda, N. (1985). "A method for reading and checking phase times in autoproccessing system of seismic wave data." Zisin **38**: 365-379.

- Majumder, M., T. K. Gangopadhyay, A. K. Chakraborty, K. Dasgupta and D. K. Bhattacharya (2008). "Fibre Bragg gratings in structural health monitoring - Present status and applications." Sensors and Actuators A-Physical **147**(1): 150-164.
- Man, C. S. and W. Y. Lu (1987). "Towards an acoustoelastic theory for measurement of residual-stress." Journal of Elasticity **17**(2): 159-182.
- Mao, S. J., A. Mordret, M. Campillo, H. J. Fang and R. D. van der Hilst (2020). "On the measurement of seismic traveltimes changes in the time-frequency domain with wavelet cross-spectrum analysis." Geophysical Journal International **221**(1): 550-568.
- Margerin, L. (2017). "Breakdown of equipartition in diffuse fields caused by energy leakage." European Physical Journal **226**(7): 1353-1370.
- Margerin, L., M. Campillo and B. Van Tiggelen (2000). "Monte Carlo simulation of multiple scattering of elastic waves." Journal of Geophysical Research-Solid Earth **105**(B4): 7873-7892.
- Margerin, L., B. van Tiggelen and M. Campillo (2001). "Effect of absorption on energy partition of elastic waves in the seismic coda." Bulletin of the Seismological Society of America **91**(3): 624-627.
- Martins, J. L., J. A. Soares and J. C. da Silva (2007). "Ultrasonic travel-time tomography in core plugs." Journal of Geophysics and Engineering **4**(2): 117-127.
- Mason, W. and H. McSkimin (1948). "Energy losses of sound waves in metals due to scattering and diffusion." Journal of Applied Physics **19**(10): 940-946.
- Mason, W. P. and H. J. McSkimin (1947). "Attenuation and scattering of high frequency sound waves in metals and glasses." Journal of the Acoustical Society of America **19**(3): 464-473.
- Mayeda, K., F. Su and K. Aki (1991). "Seismic albedo from the total seismic energy-dependence on hypocentral distance in Southern California." Physics of the Earth and Planetary Interiors **67**(1-2): 104-114.
- Mcsweeney, T. J., N. N. Biswas, K. Mayeda and K. Aki (1991). "Scattering and anelastic attenuation of seismic energy in Central and South-Central Alaska." Physics of the Earth and Planetary Interiors **67**(1-2): 115-122.
- Merkulov, L. G. (1956). "Investigation of ultrasonic scattering in metals." Soviet Physics-Technical Physics **1**(1): 59-69.
- Metropolis, N. and S. Ulam (1949). "The monte carlo method." Journal of the American Statistical Association **44**(247): 335-341.

Reference

- Mi, B., J. E. Michaels and T. E. Michaels (2006). "An ultrasonic method for dynamic monitoring of fatigue crack initiation and growth." Journal of the Acoustical Society of America **119**(1): 74-85.
- Mikesell, T. D., A. E. Malcolm, D. Yang and M. M. Haney (2015). "A comparison of methods to estimate seismic phase delays: numerical examples for coda wave interferometry." Geophysical Journal International **202**(1): 347-360.
- Mondal, P., S. P. Shah and L. D. Marks (2009). "Nanomechanical properties of interfacial transition zone in concrete." Nanotechnology in Construction 3, Proceedings **3**: 315-+.
- Morlet, J., G. Arens, E. Fourgeau and D. Giard (1982). "Wave propagation and sampling theory; Part II, Sampling theory and complex waves." Geophysics **47**(2): 222-236.
- Morlet, J., G. Arens, E. Fourgeau and D. Glard (1982). "Wave propagation and sampling theory—Part I: Complex signal and scattering in multilayered media." Geophysics **47**(2): 203-221.
- Morse, P. M. and H. Feshbach (1954). "Methods of theoretical physics." American Journal of Physics **22**(6): 410-413.
- Mosley, W. H., J. H. Bungey and R. Hulse (1999). Reinforced Concrete Design, Springer.
- Muir, D. D. (2009). One-sided ultrasonic determination of third order elastic constants using angle-beam acoustoelasticity measurements, PhD dissertation, Georgia Institute of Technology.
- Murnaghan, F. D. (1937). "Finite deformations of an elastic solid." American Journal of Mathematics **59**(2): 235-260.
- Newton, R. G. (2013). Scattering theory of waves and particles, Springer Science & Business Media.
- Nguyen, N. T., Z.-M. Sbartaï, J.-F. Lataste, D. Breyse and F. Bos (2013). "Assessing the spatial variability of concrete structures using NDT techniques—Laboratory tests and case study." Construction and Building Materials **49**: 240-250.
- Nogueira, C. L. and K. L. Rens (2019). "Acoustoelastic response of concrete under uniaxial compression." ACI Materials Journal **116**(3): 21-33.
- Obermann, A., B. Froment, M. Campillo, E. Larose, T. Planès, B. Valette, J. Chen and Q. Liu (2014). "Seismic noise correlations to image structural and mechanical changes associated with the 7.9 2008 Wenchuan earthquake." Journal of Geophysical Research-Solid Earth **119**(4): 3155-3168.

- Ogden, R. W. (1970). "Waves in isotropic elastic materials of Hadamard, Green, or Harmonic type." Journal of the Mechanics and Physics of Solids **18**(2): 149-&.
- Ogden, R. W. (1997). Non-Linear Elastic Deformations, Courier Corporation.
- Pacheco, C. and R. Snieder (2005). "Time-lapse travel time change of multiply scattered acoustic waves." Journal of the Acoustical Society of America **118**(3): 1300-1310.
- Pao, Y. H. (1987). Theory of acoustoelasticity and acoustoplasticity. Solid Mechanics Research for Quantitative Non-destructive Evaluation, Springer: 257-273.
- Pao, Y. H. and U. Gamer (1985). "Acoustoelastic waves in orthotropic media." Journal of the Acoustical Society of America **77**(3): 806-812.
- Papadakis, E. P. (1965). "Ultrasonic attenuation caused by scattering in polycrystalline metals." Journal of the Acoustical Society of America **37**(4): 711-717.
- Pau, A. and F. Vestroni (2019). "The role of material and geometric nonlinearities in acoustoelasticity." Wave Motion **86**: 79-90.
- Paufler, P. (1988). Landolt-Börnstein. Numerical data and functional relationships in science and technology. New Series. Group III: Crystal and Solid State Physics. Vol. 22: Semiconductors. Subvolume a: Intrinsic Properties of Group IV Elements and III-V, II-VI and I-VII Compounds. Ed. by O. Madelung Springer-Verlag Berlin-Heidelberg-New York-London-Paris-Tokyo 1987. XII+ 451 pp. Hard cover DM 1120.—, ISBN 3-540-16609-2, Wiley Online Library.
- Paul, A., M. Campillo, L. Margerin, E. Larose and A. Derode (2005). "Empirical synthesis of time-asymmetrical Green functions from the correlation of coda waves." Journal of Geophysical Research-Solid Earth **110**(B8).
- Payan, C., V. Garnier and J. Moysan (2010). "Potential of nonlinear ultrasonic indicators for non-destructive testing of concrete." Advances in Civil Engineering **2010**: 8.
- Payan, C., V. Garnier and J. Moysan (2011). "Determination of nonlinear elastic constants and stress monitoring in concrete by coda waves analysis." European Journal of Environmental and Civil Engineering **15**(4): 519-531.
- Payan, C., V. Garnier, J. Moysan and P. A. Johnson (2009). "Determination of third order elastic constants in a complex solid applying coda wave interferometry." Applied Physics Letters **94**(1): 3.
- Planès, T. and E. Larose (2013). "A review of ultrasonic Coda Wave Interferometry in concrete." Cement and Concrete Research **53**: 248-255.

Reference

- Poupinet, G., W. L. Ellsworth and J. Frechet (1984). "Monitoring velocity variations in the crust using earthquake doublets - an application to the Calaveras fault, California." Journal of Geophysical Research **89**(Nb7): 5719-5731.
- Prokopski, G. and J. Halbiniak (2000). "Interfacial transition zone in cementitious materials." Cement and Concrete Research **30**(4): 579-583.
- Punurai, W., J. Jarzynski, J. Qu, J. Y. Kim, L. J. Jacobs and K. E. Kurtis (2007). "Characterization of multi-scale porosity in cement paste by advanced ultrasonic techniques." Cement and Concrete Research **37**(1): 38-46.
- Pursiainen, S. and M. Kaasalainen (2014). "Sparse source travel-time tomography of a laboratory target: accuracy and robustness of anomaly detection." Inverse Problems **30**(11): 114016.
- Qi, K. and Z. Tan (2018). "Experimental study on acoustoelastic character of rock under uniaxial compression." Geotechnical and Geological Engineering **36**(1): 247-256.
- Quiviger, A., C. Payan, J. F. Chaix, V. Garnier and J. Salin (2012). "Effect of the presence and size of a real macro-crack on diffuse ultrasound in concrete." NDT & E International **45**(1): 128-132.
- Ramamoorthy, S. K., Y. Kane and J. A. Turner (2004). "Ultrasound diffusion for crack depth determination in concrete." Journal of the Acoustical Society of America **115**(2): 523-529.
- Ramaniraka, M., S. Rakotonarivo, C. Payan and V. Garnier (2019). "Effect of the Interfacial Transition Zone on ultrasonic wave attenuation and velocity in concrete." Cement and Concrete Research **124**: 105809.
- Ramaniraka, M., S. Rakotonarivo, C. Payan and V. Garnier (2022). "Effect of Interfacial Transition Zone on diffuse ultrasound in thermally damaged concrete." Cement and Concrete Research **152**: 106680.
- Rayleigh (1906). "On the dilatational stability of the earth." Proceedings of the Royal Society of London Series a-Containing Papers of a Mathematical and Physical Character **77**(519): 486-499.
- Rayleigh, J. W. S. B. (1896). The Theory of Sound, Macmillan.
- Rijswaterstaat (2007). "Inventarisatie Kunstwerken." Brief aan de Voorzitter.
- Rossetto, V., L. Margerin, T. Planès and É. Larose (2011). "Locating a weak change using diffuse waves: Theoretical approach and inversion procedure." Journal of Applied Physics **109**(3): 034903.

- Rozman, M. G. and M. Utz (2001). "Efficient reconstruction of multiphase morphologies from correlation functions." Physical Review E **63**(6 Pt 2): 066701.
- Ryzhik, L., G. Papanicolaou and J. B. Keller (1996). "Transport equations for elastic and other waves in random media." Wave Motion **24**(4): 327-370.
- Sakurai, J. J. and J. Napolitano (2020). Modern Quantum Mechanics, Cambridge University Press.
- Salawu, O. S. (1997). "Detection of structural damage through changes in frequency: a review." Engineering Structures **19**(9): 718-723.
- Santamarina, J. C. and F. Gheshlaghi (1995). "Tomographic imaging: potential and limitations." Nondestructive Evaluation of Aging Structures and Dams **2457**: 67-78.
- Sasaki, Y. and M. Hasegawa (2007). "Effect of anisotropy on acoustoelastic birefringence in wood." Ultrasonics **46**(2): 184-190.
- Sasaki, Y., T. Iwata and K. Ando (1998). "Acoustoelastic effect of wood - II: Effect of compressive stress on the velocity of ultrasonic longitudinal waves parallel to the transverse direction of the wood." Journal of Wood Science **44**(1): 21-27.
- Sato, H. (1994). "Multiple isotropic scattering model including PS conversions for the seismogram envelope formation." Geophysical Journal International **117**(2): 487-494.
- Schubert, F. and B. Koehler (2004). "Numerical time-domain simulation of diffusive ultrasound in concrete." Ultrasonics **42**(1-9): 781-786.
- Schurr, D. P., J. Y. Kim, K. G. Sabra and L. J. Jacobs (2011). "Damage detection in concrete using coda wave interferometry." NDT & E International **44**(8): 728-735.
- Seher, M., C. W. In, J. Y. Kim, K. E. Kurtis and L. J. Jacobs (2013). "Numerical and experimental study of crack depth measurement in concrete using diffuse ultrasound." Journal of Nondestructive Evaluation **32**(1): 81-92.
- Sens-Schönfelder, C. and U. Wegler (2006). "Passive image interferometry and seasonal variations of seismic velocities at Merapi Volcano, Indonesia." Geophysical Research Letters **33**(21): 5.
- Shams, M., M. Destrade and R. W. Ogden (2011). "Initial stresses in elastic solids: Constitutive laws and acoustoelasticity." Wave Motion **48**(7): 552-567.
- Shapiro, N. M., M. Campillo, L. Margerin, S. K. Singh, V. Kostoglodov and J. Pacheco (2000). "The energy partitioning and the diffusive character of the seismic coda." Bulletin of the Seismological Society of America **90**(3): 655-665.

Reference

- Sheng, P. (2006). Introduction to Wave Scattering, Localization and Mesoscopic Phenomena, Springer Science & Business Media.
- Shi, F., J. E. Michaels and S. J. Lee (2013). "In situ estimation of applied biaxial loads with Lamb waves." Journal of the Acoustical Society of America **133**(2): 677-687.
- Shin, S. W., C.-B. Yun, J. S. Popovics and J. H. Kim (2007). "Improved Rayleigh wave velocity measurement for nondestructive early-age concrete monitoring." Research in Nondestructive Evaluation **18**(1): 45-68.
- Sierra, P. L., M. Poliotti, Y. Yang, X. M. García and R. Chacón (2023). Dynamic characterization of a real-scale prestressed concrete beam tested until failure. International Symposium of the International Federation for Structural Concrete, Springer.
- Singh, B., G. Ishwarya, M. Gupta and S. Bhattacharyya (2015). "Geopolymer concrete: A review of some recent developments." Construction and Building Materials **85**: 78-90.
- Smith, R. (1963). "Stress-induced anisotropy in solids—the acousto-elastic effect." Ultrasonics **1**(3): 135-147.
- Smith, R. T., R. Stern and R. W. Stephens (1966). "Third-order elastic moduli of polycrystalline metals from ultrasonic velocity measurements." Journal of the Acoustical Society of America **40**(5): 1002-&.
- Snieder, R. (2002). "Coda wave interferometry and the equilibration of energy in elastic media." Physical Review E **66**(4 Pt 2): 046615.
- Snieder, R. (2006). "The theory of coda wave interferometry." Pure and Applied Geophysics **163**(2-3): 455-473.
- Snieder, R., A. Gret, H. Douma and J. Scales (2002). "Coda wave interferometry for estimating nonlinear behavior in seismic velocity." Science **295**(5563): 2253-2255.
- Stahler, S. C., C. Sens-Schonfelder and E. Niederleithinger (2011). "Monitoring stress changes in a concrete bridge with coda wave interferometry." Journal of the Acoustical Society of America **129**(4): 1945-1952.
- Stanke, F. E. (1986). "Spatial autocorrelation functions for calculations of effective propagation constants in polycrystalline materials." Journal of the Acoustical Society of America **80**(5): 1479-1485.

- Stanke, F. E. and G. S. Kino (1984). "A unified theory for elastic wave-propagation in polycrystalline materials." Journal of the Acoustical Society of America **75**(3): 665-681.
- Sutton, M. A., J. J. Orteu and H. W. Schreier (2009). Image correlation for shape, motion and deformation measurements: Basic concepts, theory and applications. New York, Springer.
- Tallon, B., T. Brunet and J. H. Page (2017). "Impact of strong scattering resonances on ballistic and diffusive wave transport." Physical Review Letters **119**(16): 164301.
- Tang, S. (1967). "Wave propagation in initially-stressed elastic solids." Acta Mechanica **4**(1): 92-106.
- Tant, K. M. M., E. Galetti, A. J. Mulholland, A. Curtis and A. Gachagan (2018). "A transdimensional Bayesian approach to ultrasonic travel-time tomography for non-destructive testing." Inverse Problems **34**(9): 29.
- Tatsuo, T. and I. Yukio (1968). "Acoustical birefringence of ultrasonic waves in deformed isotropic elastic materials." International Journal of Solids and Structures **4**(3): 383-389.
- Taylor, R. E. (1991). "Deep inelastic scattering: The early years." Reviews of Modern Physics **63**(3): 573.
- Thompson, R., S. Lee and J. Smith (1983). Suppression of microstructural influences on the acoustoelastic measurement of stress by interchanging shear wave propagation and polarization directions. 1983 Ultrasonics Symposium, IEEE.
- Thurston, R. (1974). "Waves in solids." In: Mechanics of solids IV (Festkoerpermechanik IV). Berlin **4**: 109-308.
- Thurston, R. and K. Brugger (1964). "Third-order elastic constants and the velocity of small amplitude elastic waves in homogeneously stressed media." Physical Review **133**(6A): A1604.
- Tinoco, I. V. and R. C. A. Pinto (2021). "Evaluation of stiffness loss of reinforced concrete beams using the diffuse ultrasound method." Ultrasonics **117**: 106540.
- Tokuoka, T. and M. Saito (1969). "Elastic wave propagations and acoustical birefringence in stressed crystals." Journal of the Acoustical Society of America **45**(5): 1241-&.
- Torquato, S. (1999). "Exact conditions on physically realizable correlation functions of random media." Journal of Chemical Physics **111**(19): 8832-8837.

Reference

- Torrence, C. and G. P. Compo (1998). "A practical guide to wavelet analysis." Bulletin of the American Meteorological Society **79**(1): 61-78.
- Torrence, C. and P. J. Webster (1999). "Interdecadal changes in the ENSO-monsoon system." Journal of Climate **12**(8): 2679-2690.
- Toupin, R. A. and B. Bernstein (1961). "Sound waves in deformed perfectly elastic materials - Acoustoelastic effect." Journal of the Acoustical Society of America **33**(2): 216-&.
- Tourin, A., A. Derode, A. Peyre and M. Fink (2000). "Transport parameters for an ultrasonic pulsed wave propagating in a multiple scattering medium." Journal of the Acoustical Society of America **108**(2): 503-512.
- Trégourès, N. P. and B. A. van Tiggelen (2001). "Generalized diffusion equation for multiple scattered elastic waves." Waves in Random Media **12**(1): 21.
- Truesdell, C. (1952). "The mechanical foundations of elasticity and fluid dynamics." Journal of Rational Mechanics and Analysis **1**(2): 125-291.
- Tsao, Y. (1984). "Uncertainty principle in frequency-time methods." The Journal of the Acoustical Society of America **75**(5): 1532-1540.
- Turner, J. A. (1998). "Scattering and diffusion of seismic waves." Bulletin of the Seismological Society of America **88**(1): 276-283.
- Turner, J. A. (1999). "Elastic wave propagation and scattering in heterogeneous, anisotropic media: Textured polycrystalline materials." Journal of the Acoustical Society of America **106**(2): 541-552.
- Turner, J. A. and P. Anugonda (2001). "Scattering of elastic waves in heterogeneous media with local isotropy." Journal of the Acoustical Society of America **109**(5 Pt 1): 1787-1795.
- Turner, J. A. and R. L. Weaver (1994). "Radiative-transfer and multiple-scattering of diffuse ultrasound in polycrystalline media." Journal of the Acoustical Society of America **96**(6): 3675-3683.
- Turner, J. A. and R. L. Weaver (1994). "Radiative transfer of ultrasound." The Journal of the Acoustical Society of America **96**(6): 3654-3674.
- Tverdokhlebov, A. (1983). "On the acoustoelastic effect." Journal of the Acoustical Society of America **73**(6): 2006-2012.
- Wan, Y., Y. Wu and Z. Zhang (2009). "Steady state and time-dependent energy equilibration in two-dimensional random elastic slabs." Journal of the Acoustical Society of America **126**(4): 1807-1816.

- Wang, X., J. Chakraborty, A. Bassil and E. Niederleithinger (2020). "Detection of multiple cracks in four-point bending tests using the coda wave interferometry method." Sensors **20**(7): 1986.
- Wang, X., J. Chakraborty and E. Niederleithinger (2021). "Noise reduction for improvement of ultrasonic monitoring using coda wave interferometry on a real bridge." Journal of Nondestructive Evaluation **40**(1): 14.
- Wang, Y. and G. Houseman (1998). "Continuous unwrapped phase." Journal of Seismic Exploration **7**(2): 109-116.
- Watson, G. H., Jr., P. A. Fleury and S. L. McCall (1987). "Searching for photon localization in the time domain." Physical Review Letters **58**(9): 945-948.
- Weaver, R. (1998). "Ultrasonics in an aluminum foam." Ultrasonics **36**(1-5): 435-442.
- Weaver, R. L. (1982). "On diffuse waves in solid media." Journal of the Acoustical Society of America **71**(6): 1608-1609.
- Weaver, R. L. (1990). "Anderson localization of ultrasound." Wave Motion **12**(2): 129-142.
- Weaver, R. L. (1990). "Diffusivity of ultrasound in polycrystals." Journal of the Mechanics and Physics of Solids **38**(1): 55-86.
- Weaver, R. L., C. Hadziioannou, E. Larose and M. Campillo (2011). "On the precision of noise correlation interferometry." Geophysical Journal International **185**(3): 1384-1392.
- Weaver, R. L. and W. Sachse (1995). "Diffusion of ultrasound in a glass bead slurry." Journal of the Acoustical Society of America **97**(4): 2094-2102.
- Weitz, D. A., D. J. Pine, P. N. Pusey and R. J. Tough (1989). "Nondiffusive Brownian motion studied by diffusing-wave spectroscopy." Physical Review Letters **63**(16): 1747-1750.
- Wesley, J. P. (1965). "Diffusion of seismic energy in the near range." Journal of Geophysical Research **70**(20): 5099-5106.
- Wu, R. (1985). "Multiple scattering and energy transfer of seismic waves—separation of scattering effect from intrinsic attenuation—I. Theoretical modelling." Geophysical Journal International **82**(1): 57-80.
- Wu, Y., Y. Lai, Y. Wan and Z. Zhang (2008). "Wave propagation in strongly scattered random elastic media: Energy equilibration and crossover from ballistic to diffusive behavior." Physical Review B **77**(12): 10.

Reference

- Xue, Q., E. Larose, L. Moreau, R. Thery, O. Abraham and J. M. Henault (2022). "Ultrasonic monitoring of stress and cracks of the 1/3 scale mock-up of nuclear reactor concrete containment structure." Structural Health Monitoring-an International Journal **21**(4): 1474-1482.
- Yeong, C. and S. Torquato (1998). "Reconstructing random media." Physical Review E **57**(1): 495.
- Yim, H. J., Y. K. An and J. H. Kim (2016). "Water depercolation of setting cement paste evaluated by diffuse ultrasound." Cement and Concrete Composites **71**: 10-19.
- Yoo, K., F. Liu and R. Alfano (1990). "When does the diffusion approximation fail to describe photon transport in random media?" Physical Review Letters **64**(22): 2647.
- Yuan, C., J. Bryan and M. Denolle (2021). "Numerical comparison of time-, frequency- and wavelet-domain methods for coda wave interferometry." Geophysical Journal International **226**(2): 828-846.
- Zarate Garnica, G. I., E. O. L. Lantsoght and Y. Yang (2022). "Monitoring structural responses during load testing of reinforced concrete bridges: A review." Structure and Infrastructure Engineering **18**(10-11): 1558-1580.
- Zavattieri, P. D., P. V. Raghuram and H. D. Espinosa (2001). "A computational model of ceramic microstructures subjected to multi-axial dynamic loading." Journal of the Mechanics and Physics of Solids **49**(1): 27-68.
- Zeng, Y. (1993). "Theory of scattered P-and S-wave energy in a random isotropic scattering medium." Bulletin of the Seismological Society of America **83**(4): 1264-1276.
- Zhan, H., H. Jiang, J. Zhang and R. Jiang (2020). "Condition evaluation of an existing T-beam bridge based on neutral axis variation monitored with ultrasonic coda waves in a network of sensors." Sensors **20**(14): 3895.
- Zhan, H., H. Jiang, C. Zhuang, J. Zhang and R. Jiang (2020). "Estimation of stresses in concrete by using coda wave interferometry to establish an acoustoelastic mDatabase." Sensors **20**(14): 11.
- Zhan, H., H. Jiang and R. Jiang (2020). "Three-dimensional images generated from diffuse ultrasound wave: detections of multiple cracks in concrete structures." Structural Health Monitoring-an International Journal **19**(1): 12-25.
- Zhan, Z., V. C. Tsai and R. W. Clayton (2013). "Spurious velocity changes caused by temporal variations in ambient noise frequency content." Geophysical Journal International **194**(3): 1574-1581.

- Zhang, J., B. Han, H. Xie, L. Zhu, G. Zheng and W. Wang (2018). "Correlation between coda wave and stresses in uni-axial compression concrete." Applied Sciences **8**(9).
- Zhang, X. and Z. Zhang (2002). "Wave transport through thin slabs of random media with internal reflection: Ballistic to diffusive transition." Physical Review E **66**(1): 016612.
- Zhang, Y., O. Abraham, F. Grondin, A. Loukili, V. Tournat, A. Le Duff, B. Lascoup and O. Durand (2012). "Study of stress-induced velocity variation in concrete under direct tensile force and monitoring of the damage level by using thermally-compensated Coda Wave Interferometry." Ultrasonics **52**(8): 1038-1045.
- Zhang, Y., O. Abraham, V. Tournat, A. Le Duff, B. Lascoup, A. Loukili, F. Grondin and O. Durand (2013). "Validation of a thermal bias control technique for Coda Wave Interferometry (CWI)." Ultrasonics **53**(3): 658-664.
- Zhang, Y., T. Planes, E. Larose, A. Obermann, C. Rospars and G. Moreau (2016). "Diffuse ultrasound monitoring of stress and damage development on a 15-ton concrete beam." Journal of the Acoustical Society of America **139**(4): 1691.
- Zhang, Y., E. Larose, L. Moreau and G. d'Ozouville (2018). "Three-dimensional in-situ imaging of cracks in concrete using diffuse ultrasound." Structural Health Monitoring-an International Journal **17**(2): 279-284.
- Zhang, Z., I. P. Jones, H. P. Schriemer, J. H. Page, D. A. Weitz and P. Sheng (1999). "Wave transport in random media: the ballistic to diffusive transition." Physical Review E **60**(4 Pt B): 4843-4850.
- Zhao, S., S. Fan, J. Yang and S. Kitipornchai (2020). "Numerical and experimental investigation of electro-mechanical impedance based concrete quantitative damage assessment." Smart Materials and Structures **29**(5): 055025.
- Zhong, B. and J. Zhu (2022). "Applications of stretching technique and time window effects on ultrasonic velocity monitoring in concrete." Applied Sciences **12**(14).
- Zhong, B., J. Zhu and G. Morcoux (2021). "Measuring acoustoelastic coefficients for stress evaluation in concrete." Construction and Building Materials **309**: 125127.

Reference

Acknowledgement

Embarking on the journey to complete a PhD has been a transformative and profoundly rewarding experience. I am deeply grateful to all those who have supported and guided me along the way.

First and foremost, I wish to express my deepest gratitude to my promoter, Prof. Max Hendriks, for his guidance, patience, and encouragement throughout this research journey. Your passion and dedication have not only deeply impacted my work throughout my PhD, but have also illuminated the path toward becoming an exceptional researcher in the future.

I am profoundly thankful to my promoter, Dr. Yuguang Yang, for his steadfast support, insightful guidance, and constructive feedback. Your expertise and commitment have consistently inspired me, and your belief in my potential has driven me to strive for excellence. Bringing me to TU Delft, challenging me to grow, and encouraging me to aim higher have had a transformative effect on both my academic and personal development.

I extend my heartfelt gratitude to my copromoter, Dr. Katrin Löer, for her guidance and support during the final, most demanding phase of my PhD journey. This period, centred around writing and refining my dissertation based on feedback, was undoubtedly the most challenging. I am deeply fortunate to have benefitted from your expertise, meticulous quality checks, and thoughtful advice, not only on academic matters but also on planning for my future career.

My sincere thanks go to Dr. Cornelis Weemstra, whose insightful discussions and thoughtful feedback greatly enriched my research. Your depth of knowledge significantly contributed to my academic growth, and your support played a vital role in helping me navigate the complexities of this journey. I am truly grateful for the time and effort you dedicated to our conversations.

I am also deeply appreciative of the members of my dissertation committee, Prof. Andrei Metrikine, Prof. Laurence Jacobs, Prof. Erik Saenger, and Prof. Evert Slob, for their constructive feedback and invaluable suggestions. Your thoughtful critiques have not only greatly enhanced the quality of my dissertation but have also played a vital role in shaping my research interests for future endeavours. I am sincerely grateful for your time and expertise.

A special thank you goes to my master's thesis supervisors, Prof. Gangbing Song from the University of Houston and Prof. Linsheng Huo from Dalian University of Technology, for introducing me to the fascinating field of structural health monitoring. Your guidance and support during the early stages of my academic journey laid a solid foundation for the progress I achieved during my PhD work.

Acknowledgement

I would also like to extend my gratitude to the technicians at TU Delft, particularly Kees van Beek, Albert Bosman, Jaap Elstgeest, Hugo de Fraiture, Sam Reus, and Ake Blom, for their assistance and support. I could not have completed my laboratory and in-situ work without your expertise and dedication.

My heartfelt thanks also go to the secretaries of Concrete Structures, Claire de Bruin and Jacqueline Barnhoorn, for their exceptional support and dedication. Both of your efficiencies and commitments have made our office work significantly easier and more organized.

A special thank you to one of my paronyms, Dr. Mauro Poliotti, with whom I shared an office for three years. Thank you for introducing me to the authentic calabash gourd maté and bombilla, an entirely new experience for me that I quickly grew to enjoy. I still remember the delightful aroma of maté in our office. Sharing an office with you was a pleasure, and your incredible personality made the experience truly enjoyable.

Another special thank you goes to my other paronym, Dr. Alberto Stella. I am deeply grateful for your friendship. You are an amazing friend, always willing to travel from Italy to the Netherlands just to spend a weekend with us. When I asked you to be my paronym, you agreed without hesitation, despite the inconvenience of flying to the Netherlands and taking time off. May our friendship last forever.

I am especially thankful to Jakub Pawłowicz and Gabriela Zárte Garnica for their support during the early phase of my PhD. Arriving in the Netherlands during the pandemic in 2020 was challenging, as I was far from family and friends and struggled to meet new people. Jakub and Gabriela helped me by including me in conversations, parties, and outdoor activities, allowing me to connect with others. I deeply appreciate their kindness.

To Shozab Mustafa, Mohammed Sirage Ibrahim, and Dr. Beyazit B. Aydin, thank you for the countless engaging, insightful, and intense evening discussions, accompanied by good “food” and drinks. Thank you all for making this journey memorable. May our friendship last forever.

A heartfelt thank you to Dr. Shizhe Zhang, my “driver” and travel companion during our year-long commutes between Friesland and Ghent for the geopolymer project. Your humour, music, and companionship made these trips not only productive but also genuinely enjoyable.

I am also grateful to my wonderful friends, Dr. Fengqiao Zhang, Dr. Lichao Wu, Yitao Huang, Jiandong Lu, Zhenxu Qian, and Dr. Weikang Feng, for the memorable travels and cherished moments we have shared. Your friendship has been an invaluable part of this journey.

To Dr. Sebastiaan Ensink, thank you for joining Mohammed and me for the special Saturday coffee breaks. While I am thrilled about your success in completing your dissertation, I must admit that I have missed your presence at these unique gatherings since your graduation.

A special thank you to Dr. Rafael Sanabria Díaz and Gianmarco Addonizio for our Saturday evening beers. I firmly believe that those relaxed conversations over a “few” cups of beer not only brought fresh perspectives but also played a part in sharpening my research mindset.

To Dr. Minkook Park, thank you for your warm hospitality during my conference trip to South Korea. I had the privilege of enjoying the best Korean BBQ of my life so far, and I sincerely hope we can meet again, whether in Korea or China.

I would like to express my heartfelt gratitude to my office mates during my final year, Yubao Zhou, Emilia Andrade Borges, and Dr. Jesper Harrild Sørensen, for their camaraderie, support, and countless moments of laughter. Your encouragement and shared experiences brought joy and inspiration to this journey.

To my colleagues in the Section of Concrete Structures, Dr. Eva Lantsoght, Dr. Mladena Luković, Dr. Sandra Nunes, Dr. Kees Blom, Dr. Marco Roosen, Rein de Vries, Jelle Bezemer, Laura Gómez Jaramillo, and Juan Felipe Garzón Amórtegui, thank you for your support and thought-provoking discussions. Your collaborative spirit has enriched my experience and made this journey truly fulfilling.

A sincere thank you to Hendrik Herder and Klaas Ellens from Haitsma Beton. Hendrik, your generosity, especially the food and beer after long days at the plant, was deeply appreciated. Klaas, thank you for always picking me up on your way to work, which made those early starts so much easier.

I extend my heartfelt thanks to Floris Besseling, Janno de Bruijn, and Coen Kortendijk from Witteveen+Bos. Traveling to Denmark with Floris and Janno was a delightful experience, and I am grateful for the chance to contribute to such an impactful project. Coen, thank you for your support on the Balladelaan project, and it was a pleasure collaborating with you.

I would like to express my gratitude to Dr. Yubo Sun and Dr. Minfei Liang, with whom I had the pleasure of collaborating to expand my knowledge in the concrete materials domain. Working alongside such talented and dedicated individuals has been an enriching experience, and I am truly grateful for the knowledge I gained from both of you.

A heartfelt thank you to my dear friends from high school, Xiang Lyu and Bowen Wang, for their mental and emotional support throughout my PhD journey. Though we have only

Acknowledgement

met a few times since graduating high school—and it has been years since our last reunion—our friendship has remained strong despite the distance. I sincerely hope we can see each other soon and share moments together, just as we did during those high school days.

To my basketball friends, Luiz Miranda de Lima, Dr. Chao Ma, Dr. Hanqing Liu, Dr. Dingshan Sun, Dr. Jianing Zhu, Zichao Li, Dawei Fu, Dr. Yang Wu, Jiaxiang Yi, Prof. Zhenming Li, Dr. Hu Shi, Chen Liu, and Xuhui Liang, thank you for the “physical” support on the court. I may not be able to name each one of you, but I deeply appreciate the games we played at the X.

I am profoundly grateful to my parents and family for their selfless support and unwavering love throughout my life. No matter the challenges I face, your strength empowers me and inspires me to confront each obstacle with courage. Your understanding, patience, and love are the forces that drive me forward and remain my unshakable foundation. In the days ahead, I will strive even harder to live up to your expectations, becoming a person who embodies gratitude, bravery, and resilience. Thank you for everything, I love you forever! (感谢我的父母和家人一直以来对我的无私支持与关爱。无论我遇到什么困难，都是你们给我力量，让我勇敢地面对一切挑战。你们的理解、宽容和爱，是我前进的动力，也是我永远的依靠。在未来的日子里，我会更加努力，不辜负你们的期望，做一个懂得感恩、勇敢坚强的人。谢谢你们，永远爱你们！)

To my dear girlfriend: over these four years, despite being separated by thousands of miles and living in different countries, your unwavering understanding and support have been the driving force behind my progress. You have patiently endured the demands of my busy studies and overwhelming pressures, offering boundless comfort and solace during my setbacks. Thank you for always standing by me, giving me the courage to chase my dreams and the confidence to face the future. (致我亲爱的女朋友：在这四年的时光里，虽然我们相隔千里，身处异国他乡，但你的理解与支持始终是我不断前行的动力。你不仅包容了我忙碌的学业和巨大的压力，更在我遭遇挫折时，给予我无尽的安慰与温暖。感谢你在我身边，给我勇气追求梦想，给我信心迎接未来。)

Due to space limitations, I am unable to mention everyone who has supported me in this acknowledgment. Thank you all for being part of this journey and for your contributions to the completion of this dissertation. To everyone I have met in the Netherlands, I wish you all the very best in your future endeavours!

Hao Cheng/成昊

January 1st, 2025 in Delft

2025年1月1日，于代尔夫特

Curriculum vitae

Personal information:

Name: Hao Cheng

Date of Birth: 06 March 1995

Place of Birth: Qingdao, Shandong Province, People's Republic of China



Academic Qualifications:

10/2020-02/2025 Ph.D., Section of Concrete Structures
Faculty of Civil Engineering and Geosciences
Delft University of Technology, The Netherlands

09/2017-06/2020 M.Sc., Institute of Structural Control and Monitoring
School of Infrastructure Engineering
Dalian University of Technology, China

09/2013-06/2017 B.Sc. in Civil Engineering
School of Civil Engineering
Qingdao University of Technology, China